SPIN ORBIT SPLITTING IN

III-V ALLOYS

by

ORAZIO BEROLO

Dissertation submitted to the Faculty of the Graduate School
of the University of Ottawa in partial fulfillment
of the requirements for the degree
Doctor of Philosophy

1973

ABSTRACT

Room temperature Reflectrance Electrolytic Electroreflectance (EER) and Surface Barrier Electroflectance (SBER) measurements have been made on a number of alloy systems (such as (Ga,Al)As, (Ga,In)As, In(As,Sb), Ga(As,P) and In(As,P) in an attempt to measure transition energies between the valence and the conduction band over energy ranges involving the direct gap E_o and the split-off valence band to conduction band gap $E_o + \Delta_o$ as a function of alloy composition.

In the case of the (Ga,Al)As alloy system transitions such as $E_1(1)$, $(E_1 + \Delta_1)(1)$, $E_1(2)$, $(E_1 + \Delta_1)(2)$, E_o' $E_o' + \Delta_o$ and E_2 are observed by the EER. All these measurements are least-square fitted to a quadratic equation and the coefficients compared to the theory of Van Vechten and Bergestresser.

The measured values of the E_o and $E_o + \Delta_o$ for the alloy systems are used to obtain the dependence on composition of the spin-orbit splitting Δ_o.

These results are analysed conjointly with results of Δ_1 obtained elsewhere. Two approaches are used. First, an expression with a term proportional to the aperiodic part of the potential is used to fit the results. The one free parameter used is then found to depend quadratically on the difference of the atomic splitting of the mixed elements in the pseudo-binary alloy system. From this theory Δ_o and Δ_1 is predicted for a number of other alloy systems. Second, these same results are then discussed in terms of mixing of states within a band (intraband) and mixing of states between two bands (interband), due to the matrix elements proportional to the aperiodic part of the potential. Each term contributes

to the virtual crystal value an amount depending on the difference in electronegativity of the constituents, the alloy composition and the direct gap associated with the splitting in the virtual crystal approximation. A successful explanation of the results is obtained.

This last approach is then used to develop modifications to the Kane model in terms of interband mixing to explain the behaviour of the bottom of the conduction band effective mass reported in the literature. The inconsistencies between experiment and the predicted values by the Kane model are explained.

It is further shown experimentally that the spin orbit splitting is not affected by temperature when SBER measurements are taken on GaAs by a Ni - Al_2O_3 - GaAs configuration.

The phase diagram of the (Pb,Sn)Se alloy system has been investigated. The optical properties at room temperature of the (PbSn)Te alloy system have been studied for optical transitions above the fundamental gap as a function of alloy composition. These two items are not an integral part of the thesis. They are to be found in appendix I.

ACKNOWLEDGMENTS

I would like to express my sincere gratitude to my supervisor, Professor J.C. Woolley, who suggested this project, for his constant guidance, the fruitful discussions I have had with him and his encouragement throughout the progress of this work.

I am grateful to Dr. M. Rubenstein of Westinghouse Research Laboratories for providing me with the Ga(AsP) and the In(AsP) samples, Dr. A. Casey and Dr. Panish for their epitaxy Ga(AlAs) samples.

I wish to thank in particular Dr. J. Van Vechten whose useful suggestions prompted the analysis of some of the results. My thanks go equally to Dr. K. Song, Dr. S.S. Vishnubathla, Mr. R. Senechal for the discussions I have had with them. I also wish to thank Mr. R. Glinski and Mr. P. Prat for their collaboration. My sincere thanks go to the staff members of the machine shop for the assistance I have received from them during the course of this work.

I wish to thank Miss D. Dubé for typing this thesis.

I want to acknowledge the financial support of the National Research Council of Canada and that of my supervisor.

STATEMENT OF ORIGINALITY

So far as the author is aware, the following parts of the present work are original:

1. The determination of transition energies versus composition for the (Ga,Al)As alloy system from electrolytic electroreflectance measurement over the energy range from 1.4 eV to 5 eV (at 300°K).
2. The determination of transition energies versus composition from surface barrier electroreflectance measurement in the vicinity of the fundamental gap (including spin-orbit splitting effects) for the alloy systems In(As,Sb) and In(as,P) (at 300°K).
3. The determination of transition energies versus composition from surface barrier electroreflectance in the vicinity of the fundamental gap (including spin-orbit splitting effects) for the alloy systems In(Ga,As) and Ga(As,P). In(Ga,As) had been investigated previously on a few samples only (3W68). Ga(As,P) had been investigated by electrolytic electroreflectance (2T66). Both systems are investigated here in more detail (at 300°K).
4. The determination of transition energies by reflectance on the alloy system (Pb,Sn)Te in the energy range from 0.8 eV to 5.5 eV at 300°K.
5. The study of the T - x phase diagram of the (Pb,Sn)Se alloy system by a quench anneal technique.
6. The measurement of E_o and $E_o + \Delta_o$ for GaAs at 4.2°K by the surface barrier electroreflectance technique using Al_2O_3 oxide layers obtained by a pyrolysis technique.

7. The derivation of a disorder-perturbed virtual crystal expression for the spin-orbit splitting at the $\vec{k}$ = (0,0,0) point, (Δ_o) and in the $\vec{k}$ = (111) direction, (Δ_1), relating the alloying effect to both locations in the Brillouin zone.

8. Contributions to the interpretation of the composition dependence of transition energies by way of a band-mixing concept.

9. Utilization of the band mixing concept to derive an expression for a disorder perturbed effective mass at the bottom of the conduction band (at $\vec{k}$ = (0,0,0)) which verifies previously established data.

10. The analysis of the effect of thin films on the lineshape of SBER measurements. This study is in collaboration with R.Glinski and some of his suggestions are part of this analysis.

For the sake of convenience the following abbreviations have been adopted throughout this work.

B.Z.	Brillouin Zone
x	Composition (mole %)
c.b.	Conduction band
EER	Electrolytic Electroreflectance
E_o	Fundamental gap (direct)
s-o	Spin orbit splitting
SBER	Surface barrier electroreflectance
v.b.	Valence band
VCA	Virtual crystal Approximation
ZnS	Zinc-blende
wf	Wave-function
S.E.	Schrödinger equation
K-K	Kramers-Kroenig
I.R.	Infrared
U.V.	Ultra-violet
k,r	(are usually vectors, the vector notation is dropped, unless otherwise indicated).
C_FG, C_{AB}	the two different notations are equivalent

LIST OF FIGURES

Page

LIST OF TABLES

TABLE OF CONTENTS

INTRODUCTION

The technological applications of semiconductors in communications, information, medicine and research is ever expanding. Therefore detailed information on the parameters describing the behaviour of these materials under various laboratory conditions is necessary. Such information prescribes the conditions required for the particular application, performance and its long-term reliability, sometimes under uncontrollable external conditions.

Even since the early 1950's, when most work done was on silicon and germanium, Welker and others (1W56) were investigating the properties of III-V compounds. Analogs to the group IV semiconductors (1C57), providing perhaps a wider selection in applicability, the compounds were soon amalgamated into alloys, generally covering a continuous range of solubility (1W62). This new possibility provided a larger field for the basic parameters.

The last few years have witnessed the emergence of theoretical techniques for the calculation of band structures of real solids with an accuracy comparable to that of the available experimental data. Clearly, it would be desirable to perform such calculations from first principles. Such calculations however, have not been able to predict the band structure entirely from first principles, and for the time being, more realistic approaches have found greater utility (2W67).

It is unfortunate that the first principlesapproach to the mixed crystal systems lags considerably behind both the above semi-empirical theories and experimental information. In fact, the complexity of dealing with alloy structures from first principles is so overwhelming, that forthe present it can only be hoped that semi-empirical considerations which are in good agreement with experiment will be a reliable guideline to the theoretician as to the possible new approaches to the problem.

It is therefore the purpose of this work to investigate and then to explain even if in part, the variation with alloy composition of specific band structure parameters such as spin orbit splitting (s.o.) and the fundamental gap (E_o). It is found that, this way, other parameters such as the effective mass at the conduction band minimum (m_c^*) can be predicted.

CHAPTER I BAND STRUCTURE AND ALLOYS.

1.1 Introduction.

1.2 Energy band concept.

1.3 Crystal structure of diamond and zinc blende materials.

1.4 Energy band representation.

1.5 Determination of band structure.

1.6 Band Structure results on diamond and zinc blende materials.

1.7 Semiconductor alloys.

1.8 The virtual crystal approximation.

1.9 Review of relevant alloy systems.

1.1 INTRODUCTION

It is proposed in this chapter to review briefly the concept of energy bands and how they are related to the crystalline structure of the material. Further, a short description is given of the formal calculation of band structures, with importance given to those models that are relevant to this work. A brief description of the overall band characteristics and the results of these calculations are discussed for a typical III-V compound.

The virtual crystal model is explained and a brief review of the results of theoretical calculations is given. A resume on the general state of results on alloys of III-V compounds is then given.

1.2 ENERGY-BAND CONCEPT

The easiest way to visualize the energy band picture for a solid is by first considering its atoms separated so that no interaction occurs between their electrons. The energy levels of the electron states are then atomic levels. With the N atoms constituting the solid, the degeneracy for each non-interacting energy level is therefore N fold. As the distance between the atoms decreases (see fig. 1.1a), the N separate levels under the perturbation of the neighbouring atoms will spread into an N level, closely spaced quasi-continuum of energy: an energy band.

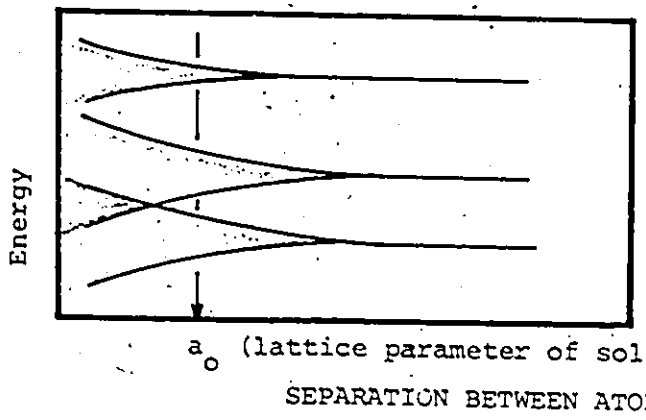

Figure 1.1a Simplified diagram showing the formation of bands from atomic states as the atoms merge to form a solid.

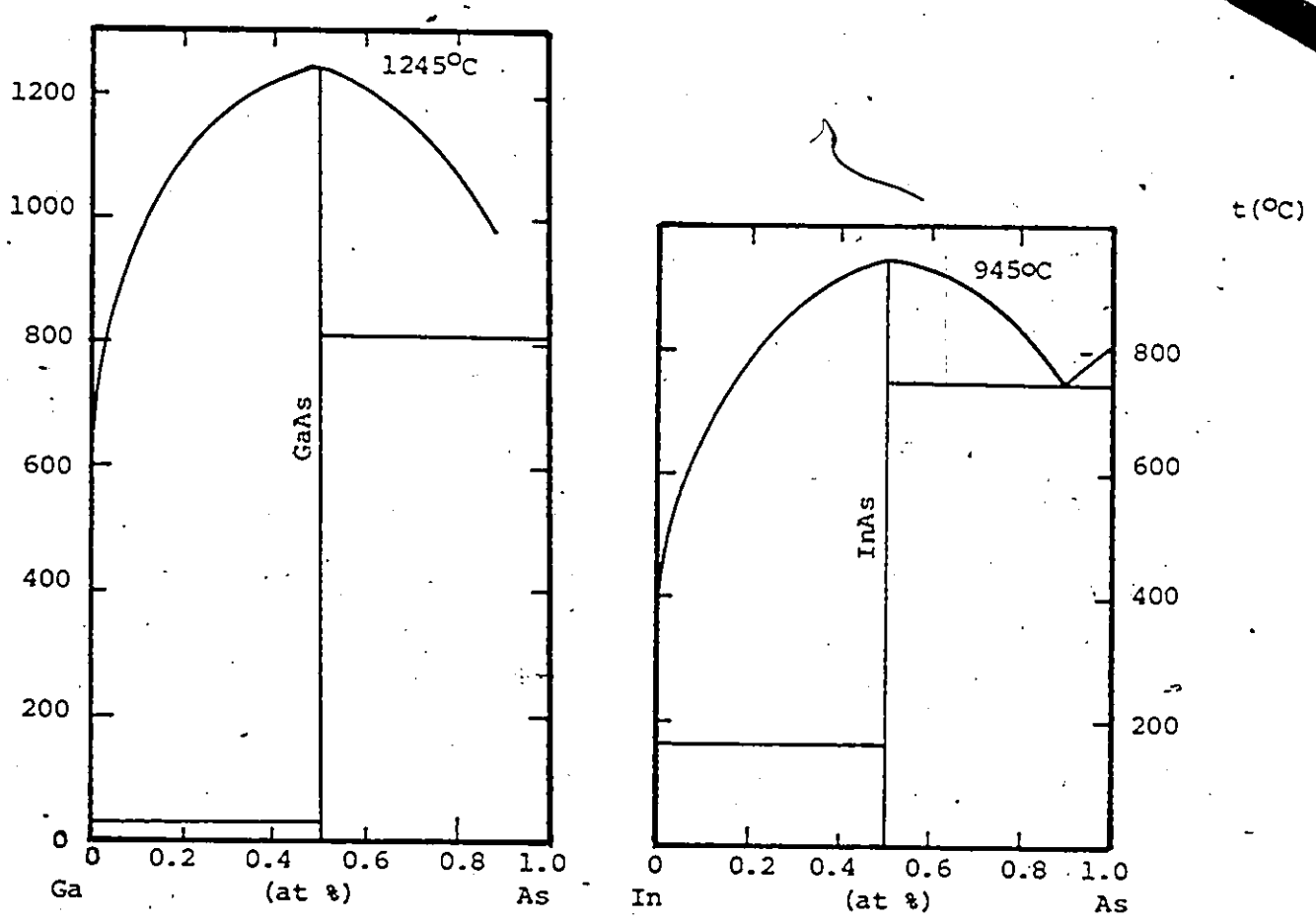

Figure 1.1b Showing Ga-As and In-As phase-diagram, representing the stoichiometric formation of III-V compounds from the elements

For core states, this perturbation is much smaller. The structure of the crystal, whose atoms have just been brought together, depends on the quantum state in which the valence electrons are to be found (table 1.2). The extent to which electrons are shared on these bonds as well as their orientation determine more than one property of the material in question (2W71, 1P70).

1.3 CRYSTAL STRUCTURE OF DIAMOND-LIKE AND ZINC-BLENDE SEMICONDUCTORS

As it was just stated, the valence electrons, their number and their free atomic quantum states determine the type of crystal structure and the bonding.

Atoms that fall into column IV of the periodic table, as well as compounds formed from elements from column III and V (and therefore their alloys), have electron valence states with second quantum numbers s and p. It has been shown (1P60) that these orbitals hybridize into sp^3 states because these represent lower energy states than the free atomic states. (See table 1.1)

TABLE 1.1	ATOMIC STATES			BEFORE BONDING				AFTER BONDING			
ELEMENT	III	IV	V	IV	IV	III	V	IV	IV	III	V
p	·	·	·				·	·	·	·	·
	·	··	··	··	··	·	··	··	··	··	··
s	··	··	··	··	··	··	··	·	·	·	·

The hybridization states form from a linear combination of the atomic states

$$\left(\begin{array}{ll} s = 1 & \\ p_x = \sqrt{3} & \sin\phi\cos\theta \\ p_y = \sqrt{3} & \sin\phi\sin\theta \\ p_z = \sqrt{3} & \cos\phi \end{array}\right] \Rightarrow \left[\begin{array}{l} \Phi = s+p_x+p_y+p_z \\ \Phi = s-p_x-p_y+p_z \\ \Phi = s+p_x-p_y-p_z \\ \Phi = s-p_x+p_y-p_z \end{array}\right) \quad (1.1)$$

where ϕ and θ are the spherical polar coordinates and the radial part of the function is normalized to unity.

The bonding in tetrahedral directions for diamond and zinc-blende material is crystallographically represented by two interpenetrating face centered cubic lattices (f.c.c.). The displacement of one sublattice with respect to the other is by 1/4 the body diagonal (fig. 1.2a). In the case of diamond like semiconductors all the atoms are the same. However due to the hybridization scheme, when III-V compounds (and their alloys) are considered, the elements of like atomic valency crystallize out on the same f.c.c. sublattice. The occupation of adjacent sites by different atoms reduces the symmetry of the crystal (1C57). The loss of the inversion center from diamond like to ZnS structure introduces important modifications to the band structure.

1.4 ENERGY BAND REPRESENTATION

It has been long argued (1D00, 1L05) that electrons in semiconductor crystals are in some sense free to move. They form a kind of a gas within the

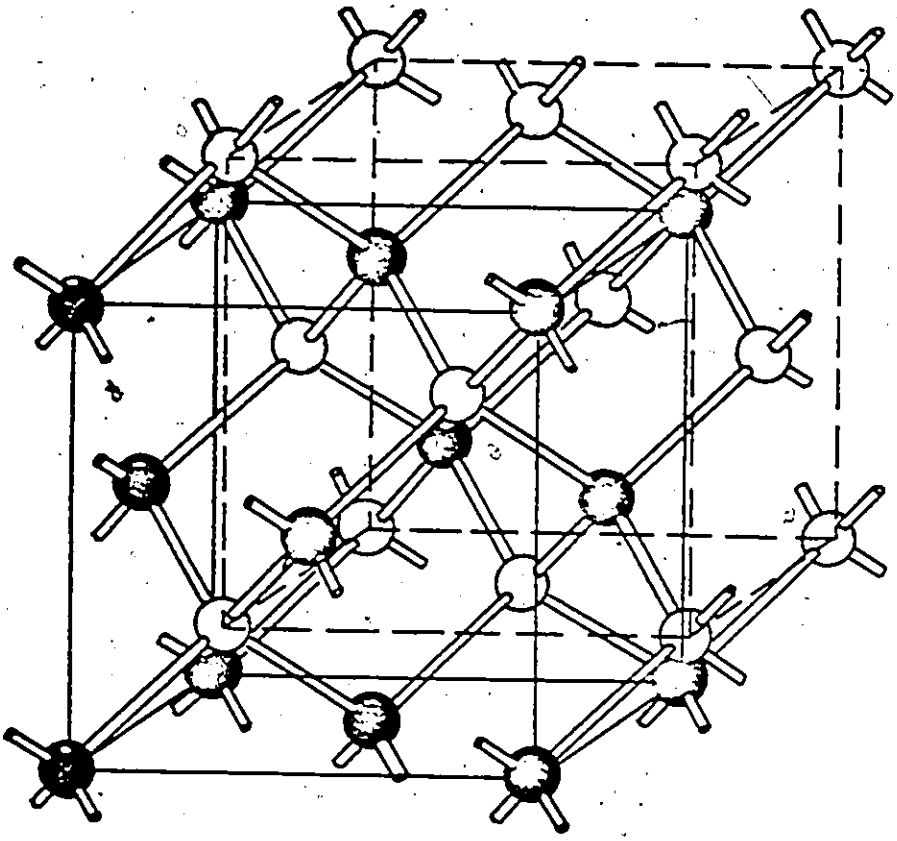

Figure 1.2a Showing a zinc-blende unit cell.

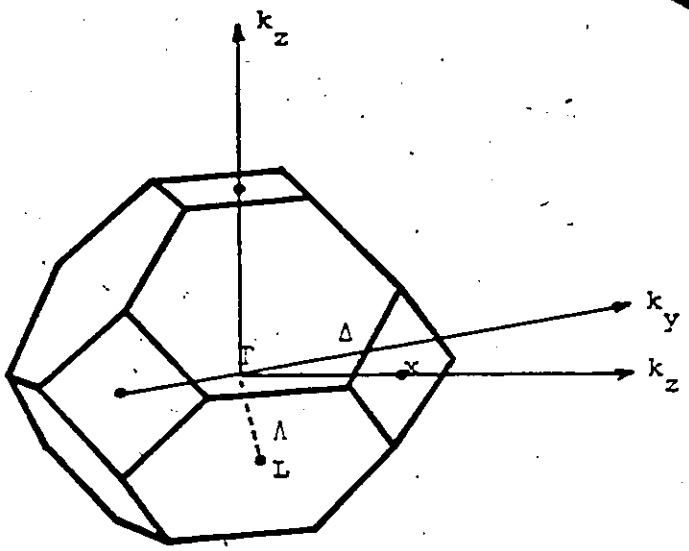

Figure 1.2b Showing the first Brillouin zone for a face-centered cubic lattice.

Table 1.2

Principal q. n.	I	II	III	IV	V	VI	VII	VIII
n	S	S^2	P	P^2	P^3	P^4	P^5	P^6
2	(1) (2) ATOM (3) (4)		5 (.20) B .88	6 (.15) C .77 (2.6)	7 (.11) N .70 1.48	8 (.09) O .66 1.35	9 (.07) F .64 1.33	10 N_e
3			13 .55 Al 1.26	14 .40 Si 1.17	15 (.34) P 1.10 1.86	16 (.31) S 1.04 1.82	17 (.26) Cl .99 1.80	18 Ar
4	29 Cu	30 Zn	31 .65 Ga 1.26	32 .55 Ge 1.22	33 (.47) As 1.18 1.91	34 (.42) Se 1.14 1.93	35 (.39) Br 1.11 1.96	36 Kr
5	47 Ag	48 Cd	49 .95 In 1.44	50 .65 Sn 1.40	51 (.62) Sb 1.36 2.08	52 (.56) Te 1.32 2.12	53 (.50) I 1.28 2.20	54 Xe
6	79 Au	80 Hg	81 (.95) Te	82 .70 Pb	83 (.74) Bi 2.13	84 Po	85 At	86 Rn

(1) Atomic # (2) Ionic radius (+) (3) Covalent radius (4) Ionic radius (-)

boundaries of the solid. This picture is far from being perfect, since the electrons must strongly interact with each other and the nuclei which are screened by closed shells of electrons.

Such a complex picture cannot be analysed without some simplifying assumptions. The effect of one electron on all the others can be averaged and thus one can treat each electron separately and independently as moving in an average field of all the other electrons and the field of positive ions (one electron approximation (1H70)). These positive ions are considered stationary at the locations described by the crystalline structure as a further simplification of the problem. (Born-Oppenheimer approximation).

The simplest treatment for the solution of the Schrödinger equation (S.E.) in order to obtain the energy levels for electrons, is by assuming the potential inside the crystal to be constant (i.e. zero)

i.e.

$$-\frac{\hbar^2}{2m}\nabla_k^2\,\psi(k) = E(k)\,\psi(k) \qquad (1.2)$$

where $\psi(k) = A\,e^{i\vec{k}.\vec{r}}$ is the wavefunction (wf) with wavevector k and a normalizing parameter A. This is Sommerfeld's (1S25) model. Quantum mechanics predicts a quasi continuous range of energy levels for this type of smooth potential. The solution to this equation is $E(k) = \frac{\hbar^2}{2m_e}k^2$ where m_e is the mass of the electron. While this theory is capable of explaining many properties of metals, it fails to distinguish between the categories of material having such a wide range in electrical conductivities. Bloch (1B28) modified the problem by replacing the constant potential by one representing the lattice:

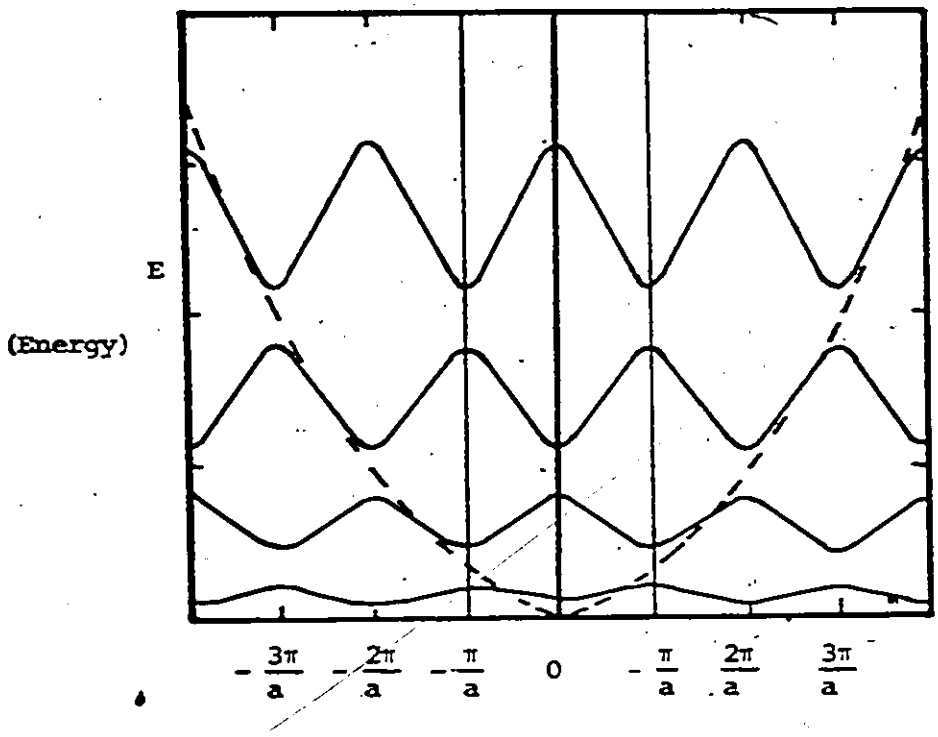

Figure 1.3 Plot of energy E vs wavenumber k for a one dimensional periodic lattice.

——— Free electron model

_____ Bloch model

$$\left[-\frac{\hbar^2}{2m}\nabla_k^2 + V(r)\right]\ \psi(k) = E(k)\ \psi(k) \qquad (1.3)$$

where $\psi(k) = u(k)\ e^{ik.r}$ and $u(k) = \sum_k a(k_j)\ e^{ik_j.r}$ is a function having the periodicity of the lattice. In fact he points out that the electron states which in the Sommerfeld model could be represented by plane waves will now be modulated by the function $u(k)$ and therefore adopt the periodicity of the lattice. This causes the energy states which in the Sommerfeld model were continuously dependent on k (fig. 1.3 dashed lines) to undergo discontinuities in energy at certain values of k (fig. 1.3 full lines). This discontinuity in the dispersion of energy spectrum as a function of the wave vector k is physically viewed as corresponding to the energies associated with plane waves of electrons which are completely scattered or distorted by the lattice.

However, since the lattice is periodic, these conditions will occur periodically as well. In the one dimensional periodic lattice (fig. 1.3) the discontinuities in the energy occur at values of $k \pm \frac{n\Pi}{a}$ where n is an integer, a is the lattice parameter.

Since for any band the energy is a periodic function of k, the above described conditions will have the same recurrence. It is then possible to translate by the appropriate lattice vector the information on the $E(k)$ curve within each period into the first zone: This first zone of $-\frac{\Pi}{a} < k < \frac{\Pi}{a}$ is called the first Brillouin zone (1B30) in the

reduced zone scheme and it combines all the necessary information on the E-k dispersion curves. The E vs k dependance in the 1st Brillouin zone represents the band structure and the region of energy where electron states are not allowed is called an energy gap.

This whole argument can be expanded into a three dimensional case. The independent one dimensional k cases are taken as cartesian coordinates and span the three dimensional k-space representative of a three dimensional lattice. The first B.Z. for an f.c.c. lattice is a truncated octahedron (fig. 1-2b). The E-k dispersion curves are usually drawn along high symmetry directions of k-space since the Schroedinger equation can be solved more easily (the secular determinant is easily diagonalized) and because the Van Hove singularities (lV53) which are involved with measurable electron transitions appear along these directions.

If the crystal has the primitive translation vectors $\vec{a}_1$, $\vec{a}_2$, $\vec{a}_3$, then these form the basis vectors which define the point f.c.c. lattice. This can be represented by the row or column vectors of the matrix

$$A = \begin{pmatrix} 0 & a/2 & a/2 \\ a/2 & 0 & a/2 \\ a/2 & a/2 & 0 \end{pmatrix} \qquad 1.4$$

with a the lattice constant. (For ZnS and diamond structure this represents one of the sublattices). The reciprocal space in which $\vec{k}$ is defined is

therefore spun by row or column vectors of the matrix B, such that

$$B.A = 2\pi I \qquad \text{I.5a}$$

i.e. $$k_i = \frac{2\pi\ (\vec{a}_j \times \vec{a}_k)}{\vec{a}_i.(\vec{a}_j \times \vec{a}_k)} \quad \text{(i,j,k in sequence rotation)} \qquad \text{1.5b}$$

The number of k vectors, or states, in each band is equal (in the reduced zone scheme) to N times the number of lattice points in the primitive unit cell taken twice to account for spin. The B.Z. for diamond and ZnS like semiconductors is represented by a truncated octahedron (fig. 1.2b). The letters shown identify various symmetry points and directions in the B.Z. and are the group theoretical notation introduced by B.S.W. (1B36).

1.5 DETERMINATION OF BAND STRUCTURE

It has been seen in the previous section how the overwhelming problem of dealing with a large number of electrons and nuclei in a crystal can be simplified by way of some initial approximations (Born-Oppenheimer approximation and the one electron approximation). The crystal is now viewed as composed of single, non interacting electrons responding to "frozen-in" periodic screened potentials. However the problem is stilla many electron problem and the complete wavefunction (wf) of the system is described by the product of non-interacting single-one electron states. The electron states are then filled by available

electrons up to the Fermi level. The higher states are available for extra electrons or optical transitions.

Although the qualitative band picture relies mainly on the symmetry of the lattice, a choice for a potential is needed for the Hamiltonian of the system. The various methods of band calculation differ in the model for the potential adopted and in the procedure for the solution of the S.e. (1P59).

The determination of band structure can be approached from two different directions: from first-principles or from semi-empirical methods. The semi-empirical approach is a scheme whereby some experimental information about the band structure at some locations in the B,Z. is used to calculate it over the whole of k space. On the other hand, a first-principle calculation starts off from fundamental considerations about the S.e. and the electron wf. The crystal symmetry and the chemical nature of the atoms occupying the lattice sites are used to simplify the solving of the S.e. The spin property of the electron is initially neglected and is subsequently annexed to the calculation in form of a perturbation on the system.

However, before proceeding with either form, the consideration of a free electron band structure usually gives valuable information as to the general shape of the bands, their energy levels and their degeneracies without actually predicting any energy values. This calculation bases itself on the application of orthogonalized plane waves to an empty crystal

lattice (zero potential) where the actual translational properties of the lattice are retained (1J60, 2C64, 2S65). Group theoretical arguments classify the symmetries of the points and symmetry axes of the B.Z. The neglected periodic potential can at this point be considered as a perturbation, whereby lifting some degeneracies of the empty lattice energy levels.

1.5a FIRST PRINCIPLES

OPW (orthogonalized-plane-wave). In this calculation the crystal potential is approximated in terms of the sum of local atomic like wave-functions of core states at the lattice sites. Plane waves orthogonal to these inner states are used to represent electron states. The inner states are in terms of some LCAO (linear combination of atomic orbitals). The electron states are symmetrized consistently with the lattice. The final wavefunction will be representative of atomic orbitals only in the vicinity of the atoms and will otherwise be smooth functions.

In covalently bonded material, which is of interest in this thesis, the electron wf distribution varies quite widely from point to point in the unit cell (2S65) with a similar variation for the resulting potential (1J60). The above method has therefore been found useful for such materials and it originated with Herring (1H40). Spin-orbit (s-o) splitting was eventually included in these calculations (1H69).

Accurate band structure calculations from first principles are a long and complicated procedure to perform. If accurate experimental

information is available, the predicted values from a first principle calculation agree only qualitatively. The OPW method briefly described above is here given only as an example : it is accompanied by other techniques such as the Wigner-Seitz (2W67), the tin muffin (2W67), APW (1K71) and the tight-binding calculations (2W67). These are all limited in some aspects for their prediction of band structures.

Since it is always possible to obtain experimentally a few reliable parameters, these can be used in semi-empirical band calculations. Such techniques are then tested in their predictions of other band parameters by the extent of their agreement with experimental information. The semi-empirical methods so developed are the pseudo-potential, the k.p and the dielectric methods.

1.5b SEMI-EMPIRICAL METHODS: Pseudopotential scheme.

The OPW was described in some detail because the empirical pseudo-potential scheme is a modification of it.

It has been seen that for the OPW, the wf's are represented as smooth functions which have core state form near the nuclei.

$$\Psi(r,k) = \Phi(r,k) - \sum_c (\Psi_c,\Phi)\, \Psi_c(r,k) \qquad 1.6$$

where Φ is the smooth plane wave like Bloch function and Ψ_c is the atomic core function. (Ψ_c,Φ) will be a rapidly varying function in the vicinity of nuclei. Replacing (1.6) into the Schroedinger equation,

$$(\frac{p^2}{2m} + V_c)\Phi + \sum_c (E - E_c)\ (\Psi_c\Phi)\ \Psi_c = E\Phi \qquad 1.7$$

which can be rewritten as

$$(\frac{p^2}{2m} + V_c)\ \Phi + V_r\Phi = E\Phi \qquad 1.8$$

and V_r will now represent the pseudo-potential, (2B71). The pseudopotential is expanded in reciprocal lattice vectors. The expansion coefficients, called form factors, are required to calculate band structures of some simple crystal structures. Phillips (2P58) showed that for Si and Ge only a few of these terms were necessary. He further suggested (1P58, 1P59, 2P58), that the V_r term be now considered a disposable quantity that can be used to fit experimental data on an interpolation scheme. Cohen and Bergestresser (1C66) have calculated the band structure of several diamond and ZnS structure materials obtaining the pseudopotentials from well established optical data.

The k.p method- The energy eigenvalue equation including spin is now represented as

$$[\frac{p^2}{2m} + V(r) + \frac{\hbar}{4m^2c^2}\ (\vec{\nabla}V(r) \times \vec{p}).\vec{\sigma}]\ \Psi(k) = E(k)\ \Psi(k) \qquad 1.9$$

where $p = -\frac{\hbar}{i}\nabla_k$ is the electron momentum, σ is the spin operator. If the solutions are written in the Bloch form $\psi(k) = u(k)\, e^{ik.r}$ then 1.9 can be rewritten in the vicinity of k = 0 as

$$\left[\frac{1}{2m}(p+\hbar\vec{k})^2 + V(r) + \frac{\hbar}{4m^2c^2}(\vec{\nabla}V(r) \times (\vec{p}+\hbar\vec{k})).\vec{\sigma}\right] u(k)e^{ik.r} = E(k)u(k)e^{ik.r} \qquad 1.10a$$

or

$$(H_o + H_1 + H_2 + H_3)\, u(k) = E'(k)\, u(k) \qquad 1.10b$$

with

$$H_o = \frac{p^2}{2m} + V(r) \qquad H_1 = \frac{\hbar}{m}\vec{k}.\vec{p}$$

$$H_2 = \frac{\hbar}{4m^2c^2}(\nabla V \times \vec{p}).\sigma \qquad H_3 = \frac{\hbar^2}{4m^2c^2}(\nabla V \times \vec{k}).\sigma$$

and $E'(k) = E(k) - \frac{\hbar^2k^2}{2m}$. H_o is considered as the hamiltonian of the unperturbed problem. H_1 for small k's is a spin independent term, H_2 a spin dependent term and H_3 is believed negligible.

The unperturbed base functions used by Kane (1K56, 2K56) for the expansion of the wf of the perturbed states are thw two $s_{\pm}$ functions and the six p functions $X_{\pm}$, $Y_{\pm}$ and $Z_{\pm}$, (+ spin up, - spin down). These are derived under the assumption that the unperturbed problem results from a conduction band edge of symmetry Γ_1 and a valence band edge with Γ_{15} symmetry. The consideration of only eight wavefunctions indicates the assumption that interactions from other bands is negligible.

An 8 x 8 determinant is then obtained, with elements that treat the H_1 and H_2 terms exactly and not as a perturbation. The solutions to the secular determinant are then the solutions E' of

$$E'\left[E'(E'-E_g)(E'+\Delta) - k^2P^2(E' + \frac{2}{3}\Delta)\right] = 0 \qquad 1.11$$

where

$$P = -\frac{i\hbar}{m} \langle S|p_z|Z\rangle$$

$$\Delta = \frac{3\hbar i}{4m^2c^2} \langle X|\ (\nabla V \times p)_z|Y\rangle$$

and E_g is the unperturbed eigenstate. The influence of higher and lower bands can be included by second order perturbation (1C63). At k = 0 eq. 1.11 clearly has four solutions, with $E_c = E_g + E_{V1,2}$, $E_{V1,2} = 0$ $E_{V3} = E_{V1,2} - \Delta$. These are the conduction and three valence bands.

When only small terms in k are considered in the solution of eq. 1.11, the conduction band E_c can be approximated to a parabolic behaviour in k near its minimum at Γ_{1c}, because the non-parabolic terms in the solution become negligible. With increasing k, the effect of higher and lower bands results in a shift of the band to higher energies (see fig. 1.4). V_1, the top most "heavy hole", (E_{V1}) band is not influenced by the conduction band but apparently it is strongly affected by other bands (1, 2K56). The maxima of the band lie on the [111] axes away from $\vec{k} = 0$. This is due to the fact the w.f. is antisymmetric and therefore the loss in inversion symmetry from group IV to III-V compounds prevents the first order energy shift

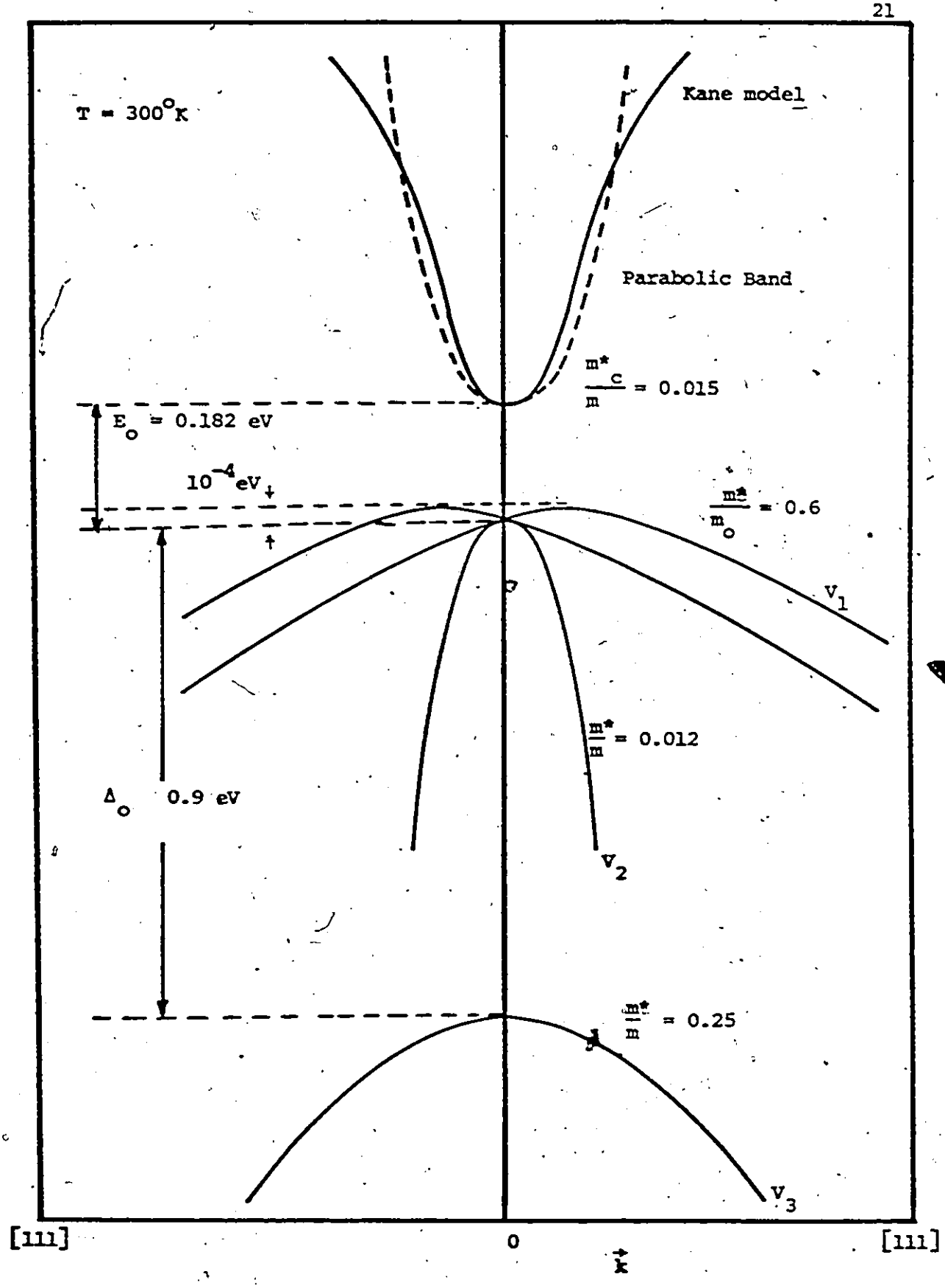

Figure 1.4 The band structure for InSb as found by E.O. Kane (2K56).

$\frac{\hbar}{m}$ k. $\langle s|P|Z\rangle$ from vanishing. It vanishes for diamond like material (3C66) V_2 is the next v.b., degenerate with the V_1 band at $\vec{k} = 0$. It is strongly non-parabolic as it is similar to the c.b. It contains terms in k that lift the spin degeneracy at $\vec{k} \neq 0$. The V_3 band is separated from the V_1 and the V_2 bands at k = 0 by the values of the spin orbit splitting Δ ($\equiv \Delta_o$), and is otherwise similar to the V_2 band except for the absence of linear terms in k, (1B68,3P66).

The effective mass in the Kane model can be derived if the solution to the secular determinant is expanded into terms in second order perturbation.

$$E_i(k) = E_{io} + \frac{\hbar^2 k^2}{2m} + \frac{\hbar^2}{m^2} \sum_{i \neq j} \frac{|k.\langle s|P|Z\rangle|^2}{E_{io} - E_{jo}} \qquad (1.12)$$

Then eq. 1.12 can be rewritten as

$$E_i(k)' = E_{io} + \frac{\hbar^2}{2m} \vec{k}. \left|\left(\frac{m}{m^*}\right)_i\right| .\vec{k} \qquad (1.13)$$

where now the elements of the effective mass tensor may be written as

$$\left(\frac{m}{m^*}\right)_i^{\ell,n} = \delta_{\rho,m}^{\ell,n} + \frac{2}{m} \sum_{i \neq j} \frac{|\langle s|P|Z\rangle|^2}{E_{io} - E_{jo}} \qquad (1.14)$$

This equation, for example, gives rise to the familiar effective mass expression at the bottom of the conduction band :

$$\frac{1}{m_c} = \frac{2}{3}\frac{P^2}{m}\left[\frac{2}{E_g} + \frac{1}{E_g + \Delta_o}\right] + 1 \qquad (1.15)$$

where

$$P^2 = \frac{1}{3}|\langle s|p|z\rangle|^2$$

The k.p method was used by Kane to calculate energy bands for Ge and InSb at the Γ point. It has been successfully extended by Cordona and others to the calculation of several III-V compounds over the entire B.Z. (1C63, 1P66, 1B69, 1P68).

Dielectric Method (1P70)

A more recent method of band structure calculation is based on the theory of electronegativity differences by Phillips (1P70). It involves fewer parameters than any of the above methods. It was used by Phillips and Van Vechten to determine the band structures of several semiconductors, thus claiming a better accuracy in their predictions.

An average gap E_g for a semiconductor is considered as due to contributions from a homopolar or covalent part E_h and a heteropolar or ionic part C

$$E_g^2 = E_h^2 + C^2 \qquad (1.16)$$

whereby the ionicity in defined as $f_i = C^2/E_g^2$.

The heteropolar part of the gap is defined by a screened electronegativity difference as defined by Phillips (1P70) between the constituents

$$C = C_{AB} = b\, e^2 \left| \frac{Z_A}{r_A} - \frac{Z_B}{r_B} \right| e^{-k_s \cdot \left[\frac{r_A + r_B}{2}\right]} \qquad (1.17)$$

Here k_s is the Thomas Fermi screening wavenumber, r_A is the covalent radius of atom A (see Table 1-2) and Z_A is the atom's valence number. b is a factor correcting the short range screening of the Thomas Fermi approximation.

The homopolar part of the gap E_h and all other homopolar variables are assumed to be a simple power law function of nearest neighbour distances d (= $\frac{\sqrt{3}}{4}\, a_o$) only determined by the value obtained in Si.

$$E_{hi} = E_{hi}\,(Si) \left[\frac{d}{d_{Si}}\right]^n \qquad (1.18)$$

where n is a parameter and i labels the gaps in question (i.e. i = 0 for E_o (at Γ) and i = 1 for E_1 (at Λ)).

When the perturbative effect of the d band on s like levels (Γ_{1c} and Λ_{1c}) is included the value of the gap at Γ (i = 0) and Λ (i = 1) are given by

$$E_i = (E_{ih} - (D-1)\,\Delta E_i) \left[1 - \left[\frac{C_{AB}}{E_{ih}}\right]^2\right]^{1/2} \qquad (1.19)$$

where ΔE_i is a parameter which is a function of d only as of eq. 1.18 and D represents the effect that d bands have on the conduction band whether i = 0 or 1.

Most of the other energy transitions observable in optical work can be predicted and compared to experimental results by formulae analogous to the above ones.

1.6 BAND STRUCTURE OF DIAMOND AND ZINC BLENDE MATERIALS.

The most extensively studied and best understood semiconductor energy band structures are thoseof elemental Si and Ge, both of which form diamond cubic crystals and the simple binary compounds (therefore their alloys) formed between elements of group IIIA and VA of the periodic table. These compounds crystallize in the zinc-blende cubic structure and their bands are anologous in many respects to those of Si and Ge.

As seen in fig. 1.5, the band structures of Ge and Si are qualitatively similar. The main difference lies in the relative minima of the lowest conduction band. In Ge these are located on the eight [111] axes at the B.Z. boundaries, in Si they are located on the six [100] axes, just inside the zone boundary. Figure 1.5 shows the band structure of both Si and Ge as calculated by Herman (2H66) without the effect of spin orbit splitting.

The valence bands for Ge and Si are essentially identical. The band is triply degenerate at the B.Z. center (Γ point). Because of the S-O

Table 1-3

	E_g (eV) (direct)	Δ_o (6) (eV)	Δ_1 (6) (eV)	$m_{\Gamma_{1c}}$	$m_{\parallel}(\Lambda)$	$m_{\perp}(\Lambda)$	ε_o (4)	f_i (5)	M.P. (°C)	a_o (Å)
Si	4.06	0.04					10.8	0		5.428
Ge	.798	0.29	0.19		1.588 (3)	0.0815 (3)	15.7	0		5.658
AlAs		0.28	0.20					0.274	1600	5.63
GaP	2.74	0.10	0.10	0.135 (1)	1.184 (1)	0.150 (1)	8.4	0.374	1525	5.450
GaAs	1.42	0.34	0.23	0.065 (1)	0.97 (1)	0.166 (1)	11.1	0.310	1237	5.653
GaSb	.68	0.77	0.46	0.045 (2)	3.51 (2)	0.255 (2)	14.5	0.261	712	6.095
InP	1.34	0.11	0.15	0.0545 (1)	1.208 (1)	0.112 (1)	9.8	0.421	1062	5.869
InAs	0.35	0.40	0.28	0.026 (2)	-4.65 (2)	0.339 (2)	13.2	0.357	942	6.058
InSb	0.18	0.80	0.50	0.0178 (2)	1.92 (2)	0.286 (2)	15.7	0.321	533	6.479

(From k.p calculations (1) (1P66), (2) (1H68), (3) (1L68), (4) (1R71), (5) (1P70), (6) (2C69).

(A)

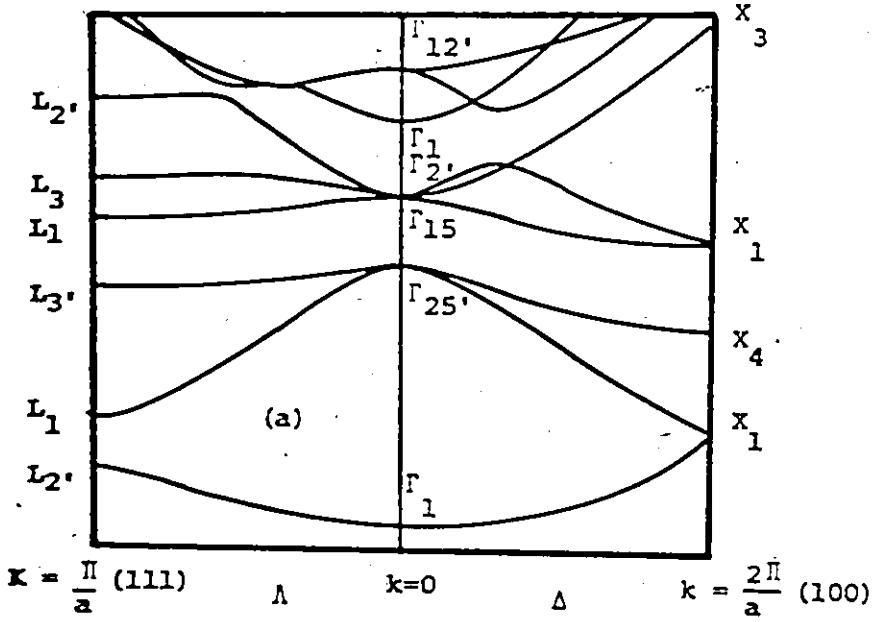

(B)

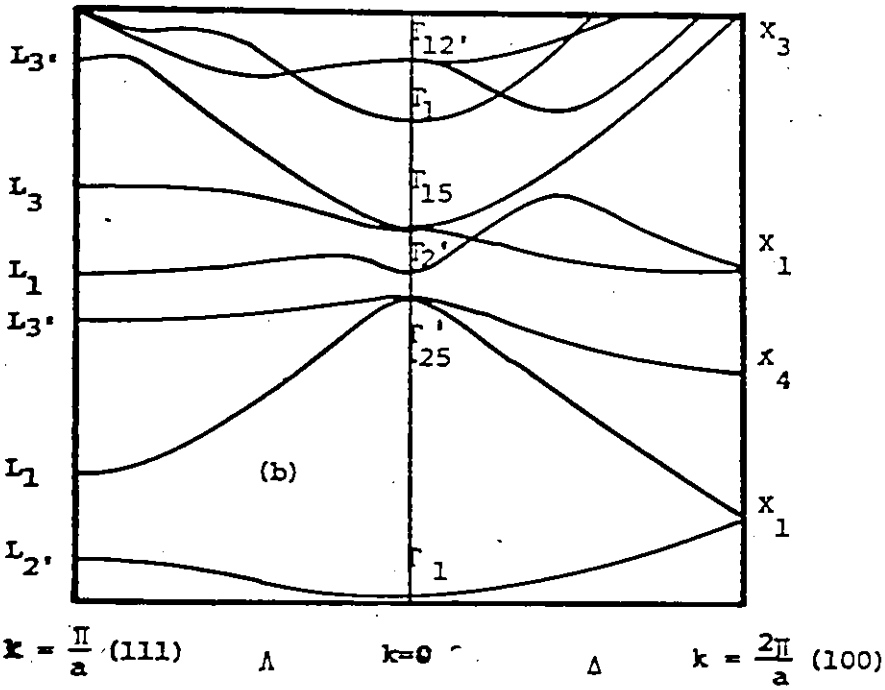

Figure 1.5 a)b) Band Structure of silicon (A) and germanium (B) Without Spin Effects.

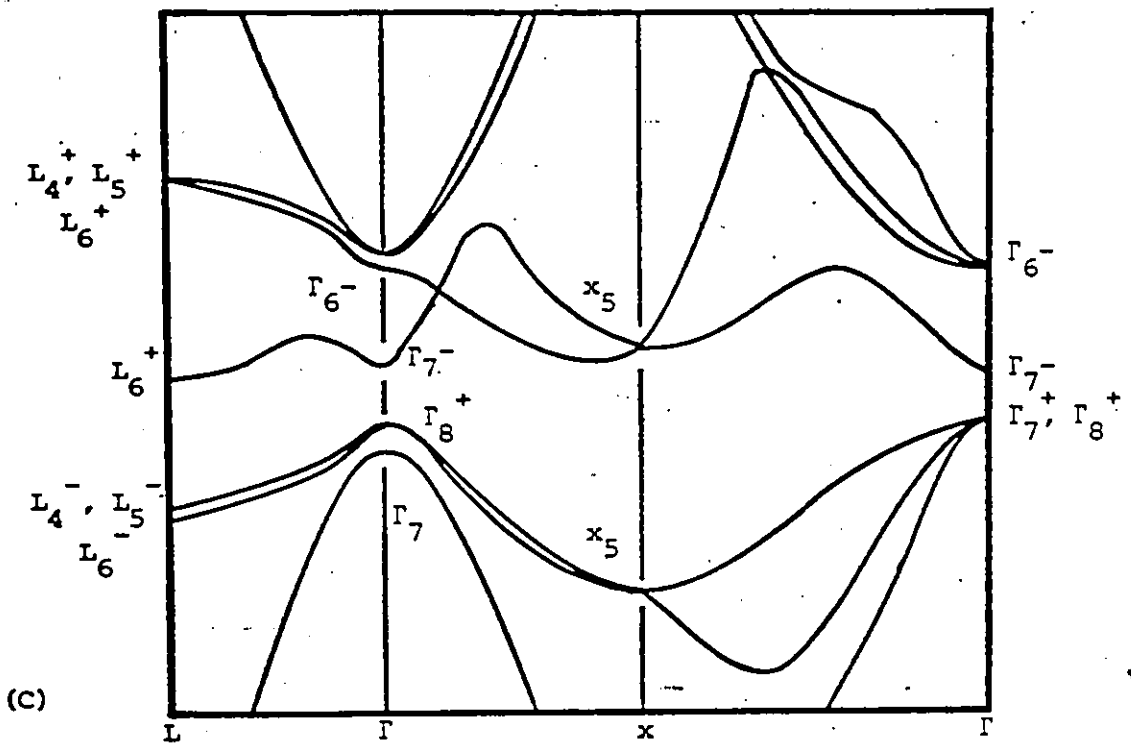

Figure 1-5 c) Band structure of Germanium, spin-orbit splitting included.

interaction, however, one of these bands is split-off from the other two by an amount Δ_o (see table 5.1 for values of energy gap E_o, Δ_o for Si and Ge as well as most III-V compounds and figure 1.5b compared to figure 1.5c where spin orbit interaction has been included). The wave-functions representing these states are reduced in symmetry and the usual group theoretical notation is replaced by the double group notation (fig. 1.5b and 1.5c). The split-off band is found to have spherical constant energy surfaces, while the two degenerate bands have warped surfaces. Such warped surfaces are replaced for convenience by two constant energy surfaces having different effective masses m_{v1} (heavy) and m_{v2} (light) holes. (1D55). When the top degenerate bands are located in either the Λ or Δ directions, the degeneracy at Γ is lifted.

The conduction band edge for both Ge and Si have prolate spheroidal constant energy surfaces leading to two effective masses m_{c1} and m_{c11}. The conduction band minimum at $k \equiv (ooo)$ is higher in energy than either minima at Λ or Δ for Ge and Si respectively. Values of the various effective masses are given in (1S59, p. 347). The conduction band minimum at Γ in Ge has spherical surfaces of constant energy. However Si has a conduction band minimum Γ_{15} in the single group notation, different from that of Ge ($\Gamma_{2'}$) indicating that the origin of the two minima for Si and Ge is different.

When spin is not considered, the only difference between the diamond and the zinc blende band structures in a qualitative sense is the spin splitting of the degenerate X point (see figure 1.5, 1.6). The detailed

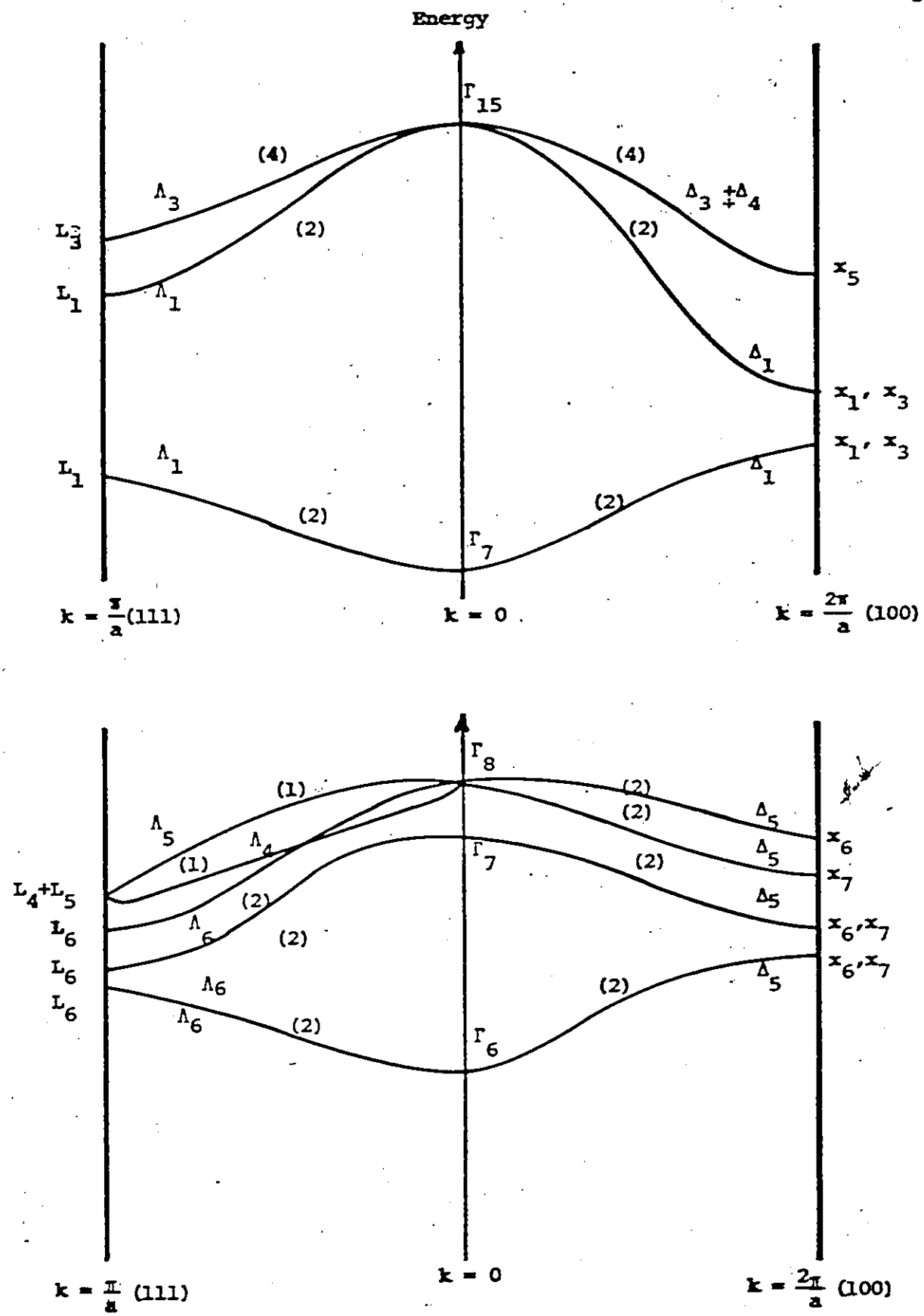

ure 1-6. A qualitative diagram of the valence band schemes of zinc blende materials from symmetry considerations (a) without and (b) with spin effects (2M64) Numbers in brackets represent number of single spin states.

structure of the valence band of zinc blende materials with and without spin effects is seen in fig. 1.6. As it is apparent, the S-O effects greatly complicate the structure. The true maxima of the valence band is expected from theory to be located on the [111] axes in k-space (8 in number). Each of these maxima occur at ~3% of the Γ to L distance in the Λ direction and are apparently only 10^{-3}eV above the edge at k = 0 (1B66). Because of the closeness of these maxima in both energy and wave number to the zone center, the valence band of III-V compounds is usually considered like that of Si or Ge (see fig. 1.7). The 3rd valence band (V3) is depressed from the top valence band edge by the spin-orbit interaction (Δ_o). The minima of the conduction band and the maximum of the split-off band still lies at $\vec{k}$ = (o,o,o) when the S-O interactions are included. The spin orbit splitting is the result of the separation which must occur between $P_{1/2}$ and $P_{3/2}$ states since L and S are antiparallel for the $P_{1/2}$ states but parallel for the $P_{3/2}$ states. It can be shown that the Δ_o energy is a result of the $P_{3/2}$ states to move up by an energy $\Delta_o/3$ from the position in the absence of the interaction and $P_{1/2}$ states move down by $2\Delta_o/3$. In addition the degeneracy at Γ of the $P_{3/2}$ states is lifted where k is away from the Γ point. Of particular interest is what happens in the Λ direction for these bands. The Kane model (1,2K56) shows clearly that the top, heavy hole, valence band is literally unaltered in energy by the interaction, however the "light hole" band moves down by an amount $2\Delta_o/3$. This effect gives rise to the 2/3 approximation relating Δ_o to Δ_1 the splitting between the V1 and V2 bands ($2/3\ \Delta_o = \Delta_1$).

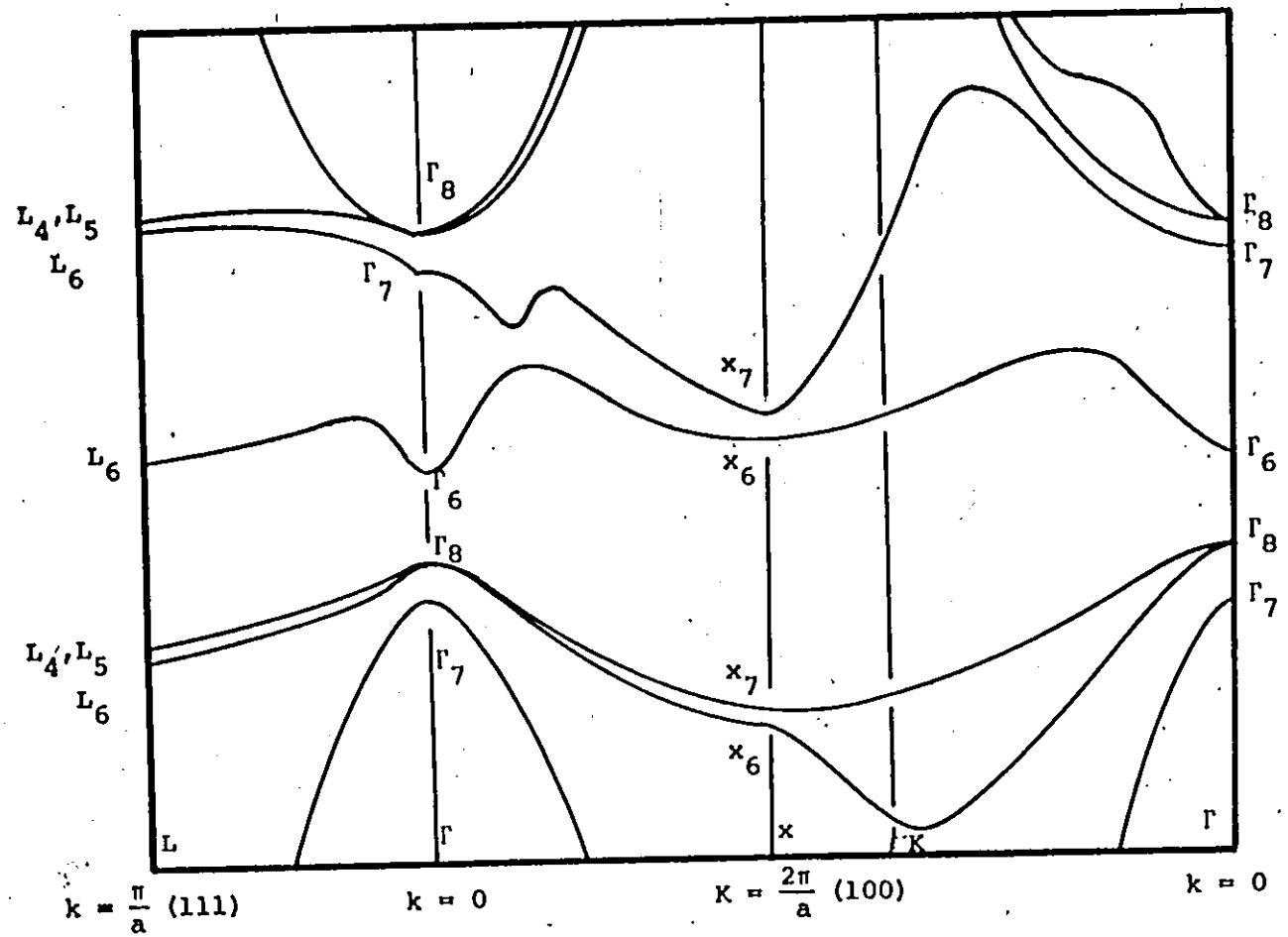

Figure 1-7 Band Structure Diagram of a III-V compound spin-orbit interaction included.

It has been reliably established from experiment that the lowest point of the conduction band for all III-V compounds except for GaP, AlSb, AlP, and AlAs, is at Γ_{1c} (Γ_6).

The constant energy surfaces at Γ_{1c} are spherical. A considerable deviation from parabolicity in the Evs k curve occurs as the value of the direct gap at Γ decreases (see fig. 1.4). The conduction-band minimum of AlAs, AlP, GaP and AlSb make part of the collection of semiconductor compounds having a many valley conduction band edges, similar to that of Si, ie. the lowest points are located on the six (1oo) or Δ axes. By alloying such materials with direct gap compounds, it is possible at some composition to produce alloys having the same direct and indirect energy gap.

However, the minimum in the conduction band at Γ is the general rule in these semiconductors. The deviations from parabolicity in narrow gap semiconductors such as InSb lead to significant changes in the interpretation of experimental results. It has been shown that the electron effective mass varies according to the degree the band is filled and different definitions of effective mass give different values. Also the value of optical gap varies as a function of impurity concentration of the specimen. This Burnstein (1B54) shift is often used as a correction on the rapidly filling low density of states, narrow band gap material.

Experimental information either assists in determining band structure with better accuracy or it may confirm it. One of the key

parameters (1K56) is spin orbit splitting. Optical measurements yield information about this quantity specifically with electric field modulation. From it, other parameters such as effective mass may be predicted (1C63). Recently several band structure calculations have been attempted for whole ranges of crystal alloys (1O71, 1H71, 1S70). It is hoped that the work presented here, that is the measurements and the analysis of the results of Δ_o over several alloy systems, will be of some assistance in future band calculations.

1.7 ALLOY SEMICONDUCTORS

An alloy is the result of the amalgamation of atoms of different types in known proportions. In the case of alloy systems formed from diamond like semiconductors as constituents, with x mole percent of element A and 1-x mole percent of element B (viz A_xB_{1-x}), one type of atom substitutionally replaces the other on the crystal lattice sites in a random manner. This type of system is called binary. A representative example is the Si-Ge (1S39, 1J54) alloy system. With this type of alloy, whose constitutents are elements from column IV A of the periodic table, the condition of homogeneous solid solubility is controlled by the sizes of the atoms alone. It has been shown (1H62) that in binary systems of the type Si-Ge, all compositions are possible when the lattice parameters of the solvent and the solute constitutents do not differ by more than ~8% and when the chemical properties of the constituents do not provide the formation of intermediate compounds (1W62).

When in this type of alloy systems the constituents are replaced by IIIA-VA compounds (viz $(AC)_x(BC)_{1-x}$), the solid crystallizes out into the zinc-blende structure fig (1.2a). The structure freezes out with the like valence atoms of the constituents arrayed on one of the f.c.c. sublattices (sec 1.3, lW62). The unlike atoms of the same valence substitutionally replace one another on the crystal sites associated with the same f.c.c. sublattice in a random manner. Because of this analogous behaviour to binary systems, such alloys are referred to as pseudo-binary (lW62).

While the nature of the bonding between atoms forming the binary systems discussed above is strictly covalent, alloys between III-V compounds have in addition to the covalent bonding a certain ionic character. Therefore in addition to the condition that the lattice parameters of the constituents should not differ by more than ∿8%, the difference in ionicity plays an important part in determining the homogeneity of the solid solutions over the whole composition range (see Table 1.4) (lF58, lM64). Homogeneity is an important aspect in mixed crystal growth if single phase solid solutions are to be studied. If this condition is not satisfied the interpretation of measured properties is difficult and misleading.

A study of the physical properties of binary and pseudo-binary alloys adds to the understanding of terminal materials and provides

	AlP	AlAs	AlSb	GaP	GaAs	GaSb	InP	InAs	InSb
AlP									
AlAs	0.34								
AlSb	.119	.153							
GaP	.067	.101	.052						
GaAs	.003	.037	.116	.064					
GaSb	.046	.012	.165	.113	.049				
InP	.114	.148	.005	.047	.110	.160			
InAs	.05	.084	.069	.017	.047	.096	.064		
InSb	.014	.048	.105	.053	.011	.060	.10	.036	

SOLUTE →

SOLVENT ↓

Difference in f_i

AlP									
AlAs	3.02								
AlSb	10.9	8.15							
GaP	0.2	3.30	12.4						
GaAs	3.41	0.41	8.43	3.59					
GaSb	10.4	7.62	0.57	10.58	7.25				
InP	6.98	4.07	4.44	7.13	3.68	3.85			
InAs	9.87	7.06	1.18	10.03	6.68	0.61	3.12		
InSb	15.72	13.10	5.38	15.8	12.75	5.92	9.41	6.49	

% Difference in a_o

Table 1-4 The darkened regions are related to alloy systems where no miscibility over the alloy range has been reported (4W68).

information on the composition dependance of physical properties of interest. A good number of semiconductor alloys have been studied experimentally, and some semiempirical calculations using the pseudo-potential (1B63, 1J69, 3V70) and dielectric (3V70) methods have been partially successful in explaining the available experimental information. The obvious difficulty in the alloy problem is the treatment of the aperiodic part of the potential. The concept of virtual crystal (VCA) introduced by Nordheim(1N31) and later developed by Muto (1M35) and Parmenter (1P55 etc) is a valuable calculation in alloy studies.

1.8 THE VIRTUAL CRYSTAL APPROXIMATION (VCA)

The virtual crystal approximation (VCA) is perhaps the first model which has been used in an attempt to describe mechanisms affecting the band parameters in substitutional semiconductor alloys.

In 1931 Nordheim (1N31) and later Muto (1M38) proposed to view the crystal alloy as one composed of average potentials, each constituent contributing to it an amount proportional to its composition.

The alloy $(AC)_x(BC)_{1-x}$ (where x is the % mole composition) that crystallizes into the zinc blende structure freezes out with all the like valency atoms of the constituents arrayed on one of the f.c.c. sublattices (Ch. 1, sec 1.3) and (1W62). The sublattice with like atoms (C) is considered as contributing a constant quantity to the crystal potential. The sublattice with unlike atoms from the same column of the periodic table (A,B) contains information about disorder

and must therefore be considered more carefully. The potential in this latter case is usually separated out into a periodic (V_p) and an aperiodic V_a part. In most cases V_a is small and it can be treated as a perturbation (1P55, 2P55). This requirement is quite logical when one considers that a large aperiodic part indicates a large free energy and therefore the immissibility of the constituents.

$$V_{per}(\vec{r}) = x\,V_A(\vec{r}) + (1-x)\,V_B(\vec{r})$$
$$V_{aper}(\vec{r}) = \delta V = V(\vec{r}) - V_{per}(\vec{r}) \qquad (1.20)$$

where $V(\vec{r})$ is $V_A(\vec{r})$ if $\vec{r}$ is positioned on an atom type A;

$V(\vec{r})$ is $V_B(\vec{r})$ if $\vec{r}$ is positioned on an atom type B.

When the aperiodic potential V_a is neglected, the problem represents the VCA. The total potential being essentially periodic with the lattice, standard band structure calculations are now possible (1P55, 3V70).

When treating δV by the perturbation method, Muto (1M35) and later Parmenter (1P55, 2P55) found that the first order term

$$E_1 = \langle\psi|\delta V|\psi\rangle \qquad (1.21)$$

vanishes. However, the contribution of the second order term

$$E_2 = \sum_{\ell\neq k} \frac{|\langle\psi_k|\delta V|\psi_\ell\rangle|^2}{E_o(k)-E_o(\ell)} \qquad (1.22)$$

does not. It has been argued by these authors that the effect of this intraband interaction was to move the band extrema closer as well as to diffuse the band edges (tailing) into the forbidden gap. As a result, the effect of the aperiodic potential was to decrease the energy gap as a function of composition with a dominant effect at x = 0.50. The VCA therefore interpolates the energy gap non linearly (3V70) over the whole composition range with the E_2 term making the appropriate correction. However, experimental evidence suggests that if there is any tailing of the bands into the forbidden gap it is small enough that it cannot be specifically observed by experiment (3W68, 4V72).

In the dielectric method of band calculation for alloys suggested by Van Vechten and Bergestresser (3V70), it is proposed to estimate by a simple method the size of the bowing effect due to disorder. The bowing parameter c is the coefficient of the quadratic term in composition x which describes the behaviour of a band gap with alloy composition (see eq. (4.1), page 142). c is considered as due to the contribution from two effects, the virtual crystal approximation (c_i) and the effects of aperiodicity (c_e):

$$c = c_i + c_e \qquad (1.23)$$

The aperiodic potential is a short range effect. If the substitution of atoms on the one sublattice is perfectly random, the range of the effect is one unit cell. Therefore the aperiodic potential does not distinguish

between various k's in the B.Z. and C_e is approximately constant for a given pair of bands. The VCA potential, being periodic throughout the crystal, affects the band gap differently at various points in k space.

The averaged potentials which describe the alloy are those of Phillipp's electronegativity theory (1P70, 3V70) E_h and C. If it is assumed that in the alloy all bond lengths are equal, so that one has a perfect zinc-blende lattice, then the homopolar part of the gap E_h, which is a function of nearest neighbour distance only (3V70) is given exactly in the VCA and the only fluctuations in the potential arise from differences in the asymmetric part C (see eq. 1.17, 1.19). If the bond lengths are not the same then there are fluctuations in E_h also. In the VCA lattice, or equal bond length approximation, the magnitude of the fluctuation is proportional to the valence of the substituted elements, viz., C_{AB} From (1.17) we see that for an alloy $A_xB_{1-x}C$ the magnitude of the fluctuations of the actual potential in the VCA is

$$C_{AB} = be^2 Z \left[\frac{1}{r_A} - \frac{1}{r_B}\right] e^{-k_s\tilde{R}} \qquad (1.24)$$

where $R = \frac{1}{2}[r_C + (1-x)\, r_B + x\, r_A]$ and $Z = Z_A - Z_B$.

From the estimate of C_{AB}, the contribution of the aperiodic potential to the bandgap c_e is taken as

$$c_e = \frac{C_{AB}^2}{A} \qquad (1.25)$$

ALLOY SYSTEM	C_{FG}	c_i (eV)	c_e (eV)	c_{calc} (eV)	c_{exp} (eV)
Ga(AsP)	0.31	0.21	0.09	0.30	0.21
In(AsP)	0.28	0.15	0.08	0.23	0.20
Ga(InSb)	0.48	0.12	0.24	0.26	0.43
(GaIn)As	0.53	0.28	0.29	0.57	0.33,0.56
In(AsSb)	0.81	0.03	0.67	0.70	0.64
(GaAl)As	0.18	0	0.03	0.03	0.20
(GaIn)P	0.56	0.39	0.31	0.70	0.88

Table 1-5 Results of Van Vechten and Bergestresser with quoted experimental results in (3V70).

where A is a band width parameter, $\sim$ 1eV when compared to experiment. When c_i is found by Van Vechten and Bergestresser in the VCA, c, the total bowing effect is calculated and compared to experiment (see Table 1.5).

1.9 REVIEW OF RELEVANT ALLOY SYSTEMS

Since the first preparation of Ge_xSi_{1-x} alloy samples by a compressed powder anneal technique by Stohrand and Klemm (1S39), methods of mixed crystal preparations of III-V alloys have been refined to the growth of single crystals by several techniques such as for example vapour epitaxy, seed pulling, etc., (1W62). However, the bulk of this work is not concerned with materials growth and preparation. The reader is therefore referred to excellent review articles on such techniques in Willardson & Beer vol. 4, (4W68) and (1W62).

It is here wished to briefly review some properties, in particular optical properties, of some alloy systems. Of these, the simplest example of solid solution in the binary Ge_xSi_{1-x} system. The valence band maximum has been established to be at the Γ'_{25} throughout the entire composition range (2B63). However, information about the lowest conduction band minima in Ge (1H51) and Si (1P53) indicated that the indirect gap should suffer a sudden change when Si atoms are mixed with Ge. The Γ, Λ and Δ conduction band minima would increase in energy with respect to the stationary valence band maximum as the composition 1-x is increased. Eventually the lowest Λ minimum in the Ge-rich end would be

overtaken by the minimum of Si for the indirect transition. After Klemm's (1S39) preparation of the Ge-Si alloys, Johnston (1J54) succeeded in preparing homogeneous samples from the melt. The absorption measurements of the forbidden gap show an abrupt change of slope with alloy composition. This is explained in terms of a critical cross over of the indirect transition from the minima at Λ to that at Δ in the conduction band. The band structure calculations of Herman (1H54) and Long (1L62), are in full agreement with this explanation. The critical cross over from the Λ to the Δ minima occurs at $x = 0.15$ of Si. Transitions above the fundamental gap were found from reflectance measurements by Tauc and Abrahams (1T60), (1T61). Electroreflectance measurements by Kline (1K68) have also found the composition dependence of the direct optical transitions and are in good agreement with Abraham's results. The composition behaviour of these transitions is linear. Recently Stroud (1S70) used a (CPA*) model for band calculation of Si_xGe_{1-x} at $x = .37$. Effects of alloy disorder are included and their effect on the density of states calculated (c.f. Parmenter). The variation of the direct gap E_o with composition calculated by Van Vechten and Bergestresser (3V70) is in good agreement with the experimental information.

(Ga,Al)As as Ga(P,As) and (Ga,Al)Sb belong to that particular family of alloy systems which have for one of the constituents an indirect gap semiconductor: AlAs, GaP, AlSb (1M63, 1M62, 3E63). These have their conduction band minima in the Λ direction.

* (1S70, 2V70, 1V68, 1A67).

(GaAl)As: Black and Ku (2B66, 1K66) have prepared this alloy system and measured the optical absorption finding the cross over to a direct gap at ∿40% AlAs. Panish and Sumski (1P69), Rupprecht (1R67) and Panish and Casey (2P69) have obtained fundamental gap and direct gap measurements for various compositions by photoresponse measurements. They find the cross over point at ∿33% AlAs. The liquid epitaxy method used to prepare these samples is described in (1P69). They were also used in the present work. AlAs electroreflectance measurements were reported by Onton (1O70). The obvious problem in preparing alloys with aluminum (the high reactivity with virtually any container at higher temperature) has not permitted the preparation of bulk samples.

Ga(As,P): Folberth (1F55) and Welker (1W56) reported measurements of the optical gap and Ehrenreich (1E61) has reported additional data of this type. The indication is that the cross over point is around 50% of the composition. Spitzer and Mead (1S64) made surface barrier photovoltaic response measurements distinguishing between a direct and indirect transitions. This sensitive method resolved the cross over point to be at (38% GaP). Fenner used high pressure electrical resistivity measurements to find x_c crossover at 44% GaP (1F64). Injection laser measurements by (1H62, 4H63, 1K63 and 1P65) all found x_c ∿45% GaP. Rubenstein (1R65) prepared alloys of good homogeneity by a sealed tube iodide transport method. He measured the optical energy gap by absorption.

Tietjen (3T66) obtained samples also by a vapour deposition technique on which absorption measurements were made. Reflectance measurements were done by Abagyan (1A65) Bergestresser (1B65) Thompson et al (1T66), Woolley et al (1W65) and Williams (2W65). Thompson (2T66) made electroreflectance measurements on the direct and higher optical transitions.

(Al,Ga)Sb: As with the case of (GaAl)As alloys, growth of this alloy system is difficult. It was first prepared by Burdiyan (1B59) and Miller (1M60). The break in the fundamental gap curve with composition is thought to be at $x_c \sim 70\%$ AlSb, from these optical measurements. Transport measurements by Burdiyan (2B59) were less conclusive since the break in the alloy dependance of E_g was found less sharp.

In(As,P): This alloy system, as the remaining ones does not exhibit a sharp change in indirect to direct fundamental transitions. It was one of the first one investigated. (1F55, 1W56, 2W56). The linear variation of the lattice parameter with composition was investigated by Folberth (1F55) and Koster (3K58). In a recent determination of lattice parameter from halogen vapor transport preparation, Thompson (1T69) detected some slight deviations from linearity. The fundamental gap was determined by Oswald (1O59) from optical absorption and by Weiss (3W59) from electrical data. The gap was found to vary linearly in composition. Kioturu (2K66) reflectance measurements above the gap indicated that for all transitions the composition dependance was linear. Thompson (1T69) measured these transitions by electroreflectance and wavelength modulation.

Vishnubathla's (1V70) EER results are in good agreement with Thompson's. These do not depend linearly on composition, but exhibit the familiar quadratic dependence on composition.

(InGa)As; The first phase diagram and lattice parameter determination for this alloy system was done by Woolley and Smith (1W61). Optical measurements of energy gap were made by Abrahams (1A59) and Woolley (1W61) as well as Hockings (1H66). These workers found a disagreement for the alloy behaviour of the gap. Woolley (1W67) resolved this by the preparation of highly homogeneous material grown by the horizontal Bridgeman technique (1W64). Burnstein shift corrections gave a reliable dependence of the gap on composition. This quadratic dependence was further verified by Woolley and Coderre (1C69) by means of Hall effect measurements. Reflectance measurements for optical transitions above the gap were obtained by Woolley and Blasey (4W64) and Conrad (4C66). Energy dependence on composition was found either linear with composition (high energy transitions) or with a small quadratic dependence (lower energy transitions). Thompson and Woolley (2T67) obtained electroreflectance data in the same spectral region. Williams and Rehn (3W68) found fundamental gap and spin orbit splitting values from both SBER and EER as well as some high energy transitions. Although they agree with previous fundamental gap measurements, they have too few samples to give a final argument for the alloy dependence of Δ_o.

In(SbAs): Woolley and Warner (3W64) prepared this alloy system by a slow gradient freeze technique as well as a zone levelling technique. Two phase material in certain portions of the ingot allowed for only partial conclusions on the energy gap dependence. Eventually good material was grown by the Bridgeman (3W64) technique and the energy gap dependence on x was found to depend quadratically on composition, going through a minimum, a smallest value ever attained with III-V alloys. Thompson and Woolley (3T67) obtained electroreflectance spectra for the higher energy transitions. Woolley and Vishnubathla further investigated these transitions in more detail (1V70).

Ga(AsSb): Little information is known on this alloy system because of the tremendous problems associated with its preparation (1W58). Woolley and Rosenbaum (1R72) have prepared good homogeneous material covering a significant range of the alloy system. Results from transport measurements have recently been analysed (1R72).

CHAPTER II OPTICAL PROPERTIES.

2.1 Introduction

2.2 Definition of Optical Parameters

2.3 Optical Absorption process in a solid

2.4 Assignment of optical transitions to band structure

2.5 Modulated reflectance

2.6 Electroreflectance

2.7 Review of electroreflectance results.

2.1 INTRODUCTION

In the previous chapter it has been proposed to investigate some aspects of the band structure of alloys. It is therefore necessary to elaborate on the means by which the relevant parameters can be determined. The response of semiconducting material to electromagnetic radiation seems to have the advantage of enhancing electron transitions over a wide range of energy at different points in the B.Z. These transitions carry with them information about the initial state and the final state as well as the energy involved in the transition and its probability of occurrence. In other words, the optical constants that are involved with the properties of the material can be related to the band structure and contain information about it.

It is therefore proposed in this chapter to define the fundamental optical parameters, to briefly review the absoption processes in semiconductors and relate these in the presence of an alternating electric field, to relevant band structure parameters.

2.2 DEFINITION OF OPTICAL PARAMETERS.

The response of an isotropic material under the influence of a time dependent electric field is governed by Maxwell's equations. This response is not instantaneous and it may lag by a phase factor

which is related to the absorption of the incident electromagnetic field.

In an isotropic material, the linear relation between D and E is

$$D_i = \sum_{j=1}^{3} \varepsilon_{ij} E_j \qquad (2.1)$$

where the non-diagonal terms of the dielectric tensor $\underline{\varepsilon}$ are zero and it has been justifiably assumed that its frequency dependence is small over one B.Z. (2H70).

The phase difference between D and E can be included in the theory by allowing $\underline{\varepsilon}$ to have real and complex components

$$\underline{\varepsilon} = \varepsilon_1 + i\varepsilon_2 \qquad (2.2)$$

where ε_1 and ε_2 are interrelated via the Kramers-Kroenig relations (1,2K29). The average rate of dissipation of electromagnetic energy density averaged over one complete cycle is

$$W = \langle \vec{E} \cdot \vec{J} \rangle = \frac{\omega}{4\pi} (2E_o^2)\, \varepsilon_2 \qquad (2.3)$$

where E_o is the electric field amplitude and ω is the frequency. Therefore the radiation energy dependence of ε_2 contains all the necessary information about interband transitions and it is related to the absorption coefficient of the material α

$$\alpha = \frac{\omega}{nc}\, \varepsilon_2 \qquad (2.4)$$

where ω is the frequency, c is the speed of light and n is the refractive index of the medium. So in order to determine ε_2 from experiments, optical absorption measurements would be the most appropriate. However, in those frequency ranges where there is strong absorption, it becomes inpractical to measure α(3W67). In semiconductors, as with other materials. strong absorption is due to lattice, plasma and electron interband transitions (2H70). Above the fundamental gap, other parameters, such as reflectance (R) carry all the information about ε_2 and contain more detailed structure not available in absorption.

Using Maxwell's equations, it can be shown that the real and imaginary parts of the refractive index N = n+ik are related to the components of the dielectric constant $\underline{\varepsilon}$ as:

$$\begin{aligned} 2nk &= \varepsilon_2 \\ n^2 - k^2 &= \varepsilon_1 \end{aligned} \tag{2.5}$$

In the case of near-normal incidence, the reflectance R is related to both components of either the dielectric constant or the refractive index by the Fresnel equation

$$R = \frac{(1-n)^2 + k^2}{(1+n)^2 + k^2} \tag{2.6a}$$

$$R = \frac{(\varepsilon_1^2 + \varepsilon_2^2)^{1/2} - \{2\varepsilon_1 + 2(\varepsilon_1^2 + \varepsilon_2^2)^{1/2}\}^{1/2} + 1}{(\varepsilon_1^2 + \varepsilon_2^2)^{1/2} + \{2\varepsilon_1 + 2(\varepsilon_1^2 + \varepsilon_2^2)^{1/2}\}^{1/2} + 1} \tag{2.6b}$$

From the above relation it can be seen that is it not possible to separate ε_1 and ε_2 from a single reflectance measurement at near normal incidence.

The reflectance amplitude $\underline{r}$ may however be expressed in terms of a phase factor θ relating the angular difference between incident and reflected $\vec{E}$ vectors

$$\underline{r} = re^{i\theta(\omega_o)} = \frac{1-(n+ik)}{1+(n+ik)} \tag{2.7}$$

where using the K-K relations it can be shown that

$$\theta(\omega_o) = -\frac{\omega_o}{\pi} \int_0^{\infty} \frac{\ell nR(\omega)}{\omega^2-\omega_o^2}\, d\omega \tag{2.8}$$

From a knowledge of R over the frequency spectrum θ and therefore ε_1 and ε_2 may be calculated using

$$\varepsilon_1 = \frac{(1-R)^2 - 4R\sin^2\theta}{(1+R-2\sqrt{R}\cos\theta)^2}$$

$$\varepsilon_2 = \frac{4\sqrt{R}(1-R)\sin\theta}{(1+R-2\sqrt{R}\cos\theta)^2} \tag{2.9}$$

However, the calculation of θ from R necessitates the information over the whole energy range. Since this is often experimentally unavailable, proper extrapolations are used beyond the available range of measurement (3W67) (see Fig. 2.4). on page 65

2.3 OPTICAL ABSORPTION PROCESSES IN SOLIDS

In the solution of the Hamiltonian for the set of one-electron wavefunctions that has been discussed in section (1.2) it has been shown how for N similar atoms brought toghether to form a crystal, each non degenerate energy level of the atom spreads into a bond of N levels.

An isolated atom is known to have a set of characteristic wf's and energy levels emerging into an ionization continuum. All the excited states have a finite lifetime τ for spontaneous transitions to a state of lower energy. It follows from the uncertainty principle that the energy levels have a width of the order of $\hbar/\tau$ ($< 10^{-6}$eV). The frequencies of the absorption lines are governed by the combination rule

$$E_j - E_i = \hbar\omega \qquad E_j > E_i \qquad (2.10$$

and the strength of absorption line is expressed in terms of matrix elements proportional to matrix elements of the dipole moment

$$M_{ij} = \frac{m\omega}{\hbar e} \langle\psi_j|e.r|\psi_i\rangle \qquad (2.11)$$

The situation in a solid is analogous to atomic transitions. When radiation $\hbar\omega$ is incident on a solid, electrons can make transitions between energy "levels" (which have spread into bands) with the emission or absorption of photons

$$E_c - E_v = \hbar\omega \qquad E_c > E_v \qquad (2.12)$$

A simplistic view would be that, under the influence of the electric force of the electromagnetic wave of frequency ω, the electrons will absorb the radiation at that frequency. They will respond to it as sources of secondary waves and therefore influence other particles. The magnetic field component of the photon is thought to vary too rapidly and electrons in the solid are unable to follow oscillations at that frequency due to longer relaxation times (2H70).

The photon electric field depends only on the vector potential and the scalar potential is assumed to be zero, viz

$$\vec{E} = -\frac{1}{c}\frac{\partial \vec{A}}{\partial t} \qquad (2.13)$$

where

$$\vec{A} = A_o \frac{\vec{A}}{|\vec{A}|} \{ e^{i(k.r-\omega t)} + e^{-i(\vec{k}.\vec{r}-\omega t)} \} \qquad (2.14).$$

The Hamiltonian in (eq. 1.3) can be rewritten in the presence of an electromagnetic field as

$$H = \frac{1}{2m} (\vec{p} + e\vec{A})^2 + V(r) \qquad (2.15)$$

Eq. (2.15) is separated into an unperturbed term $H_o = \frac{p^2}{2m} + V(r)$ and the perturbing term $H_{(1)} = \frac{e\hbar}{m_c} \vec{A}.\vec{p}$. The term $\frac{e^2A^2}{2m}$ has been neglected (2H70). Therefore if

$$H = H_{(o)} + H_{(1)} \qquad (2.16)$$

represents the hamiltonian then the interaction of radiation with the solid is by way of the perturbing term

$$H_{(1)} = \frac{\hbar e}{mc} A_o \left\{ \frac{\vec{A}}{|\vec{A}|} \left(e^{i(\vec{k}.\vec{r} - \omega t)} + e^{-i(\vec{k}.\vec{r} - \omega t)}\right). \vec{p} \right. \quad (2.17)$$

The first term in eq. (2.17) represents the transition probability of an electron into an excited state, corresponding to the absorption of radiation, the other a deexcitation viz., emission, at the same rate.

The transition probability for an electron from the v.b. state with wavevector $\vec{k}$ to a c.b. state with wavevector $\vec{k}'$ can be shown to be (1F66)

$$W(\omega,t,\vec{k},\vec{k}') = \frac{e^2}{m^2\hbar^2} \left| \int_o^t dt' \ \langle \psi_c | A.\vec{p} | \psi_v \rangle \right|^2 \quad (2.18)$$

where t is the time taken for the excitation.

Since ψ_i is a Bloch function belonging to eigenvalue E_i (i=c,v) we can write

$$\psi_i = e^{-\frac{iE_i(\vec{k})\ t}{h}} \ e^{i\vec{k}_i.\vec{r}} \ u(\vec{k}_i,\vec{r}) \quad (2.19)$$

When 2.19 is used for ψ_c, ψ_v, (2.18) can be shown to be

$$W(\omega,t,\vec{k},\vec{k}') = -\left(\frac{e}{m}\right)^2 A_o^2 \left| \int_o^t dt' \ e^{\frac{i}{\hbar}(E_c(k')-E_v(k)-\hbar\omega)} \ M_{vc} \right|^2 \quad (2.20a)$$

where

$$M_{vc} = \langle \vec{u}_c(\vec{k},\vec{r}) \ e^{-i(\vec{k}'-\nu).\vec{r}} \ |\vec{e}.\nabla| u_v(k,r) \ e^{i\vec{k}.\vec{r}} \rangle \quad (2.20b)$$

$\vec{e}$ is the unit vector $\frac{\vec{A}}{|\vec{A}|}$

In time dependent perturbation theory this leads to the transition probability per unit time and unit volume:

$$W_{vc}(\omega) = -4\pi^2\hbar\left(\frac{e}{m}\right)^2 A_o^2 \int_\Omega \frac{d\Omega}{4\pi^3} |M_{vc}|^2 \delta(E_c - E_v - \hbar\omega) \qquad (2.21)$$

The delta function in eq. (2.21) represents the first selection rule based on energy conservation: the transition probability is different from zero only if $E_c - E_v = \hbar\omega$ i.e. the photon energy. The second selection rule based on the conservation of momentum follows from (2.20b), where the matrix element M_{vc} will vanish, unless the photon wave vector

$$\vec{v} = \vec{k}' - \vec{k} \qquad (2.22)$$

since in 2.20b u_c and u_v are conserved under translation. Since the wave vector of the photon is much smaller than k' or k, we have that k' = k, indicating that only direct optical transitions are allowed.

If the energy loss per unit volume of the plane wave by absorption is $W_{vc}(\hbar\omega)$, with eq. (2.3) it can be shown that

$$\varepsilon_2 = 4\pi\left(\frac{e\hbar}{\omega m}\right)^2 \int_\Omega |M_{vc}|^2 \delta(E_c - E_v - \hbar\omega) \frac{d\Omega}{4\pi^3} \qquad (2.23)$$

With the assumption that M_{vc} varies slowly throughout the B.Z. and using some properties of δ functions

$$\varepsilon_2 = 4\pi\left(\frac{e\hbar}{\omega m}\right)^2 \left\{\int_S \frac{1}{4\pi^3} \frac{dS}{|\nabla_k(E_c - E_v)|}\right\} |M_{vc}|^2 \qquad (2.24)$$

where dS is now a surface element of the plane $E_c - E_v = \hbar\omega$ in k space (1F66, 2H70).

The joint density of states can now be defined as

$$J_{vc}(\omega) = \int_S \frac{1}{4\pi^3} \frac{dS}{|\nabla_k (E_c - E_v)|} \tag{2.25}$$

and therefore

$$\varepsilon_2 = 4\pi \left(\frac{e\hbar}{\omega m}\right)^2 J_{vc}(\omega) \left|M_{vc}\right|^2 \tag{2.26}$$

Upon inspection, $J_{vc}(\omega)$ is seen to be a strongly varying function of k whenever the denominator of the integrand approaches zero. $E_c - E_v$ is also a periodic function with the lattice and therefore it must also exhibit such a condition. Whenever $J_{vc}(\omega)$ suffers such a discontinuity, the behaviour is called critical, and the location in the B.Z. a critical point or a VanHove singularity (1V53). Such behaviour has been thoroughly discussed by VanHove (1V53) and J.C Phillips (1P56). These critical points occur under two possible conditions:

$$\nabla_k E_c(k) = \nabla_k E_v(k) = 0$$

and (2.27)

$$\nabla_k E_c(k) = \nabla_k E_v(k) \neq 0$$

The first type occurs at high symmetry points in the B.Z., typically at $\vec{k} = 0$ (the Γ point) for diamond and zinc-blende semiconductors, and are recognized as two band extrema occurring at the same k. Critical points

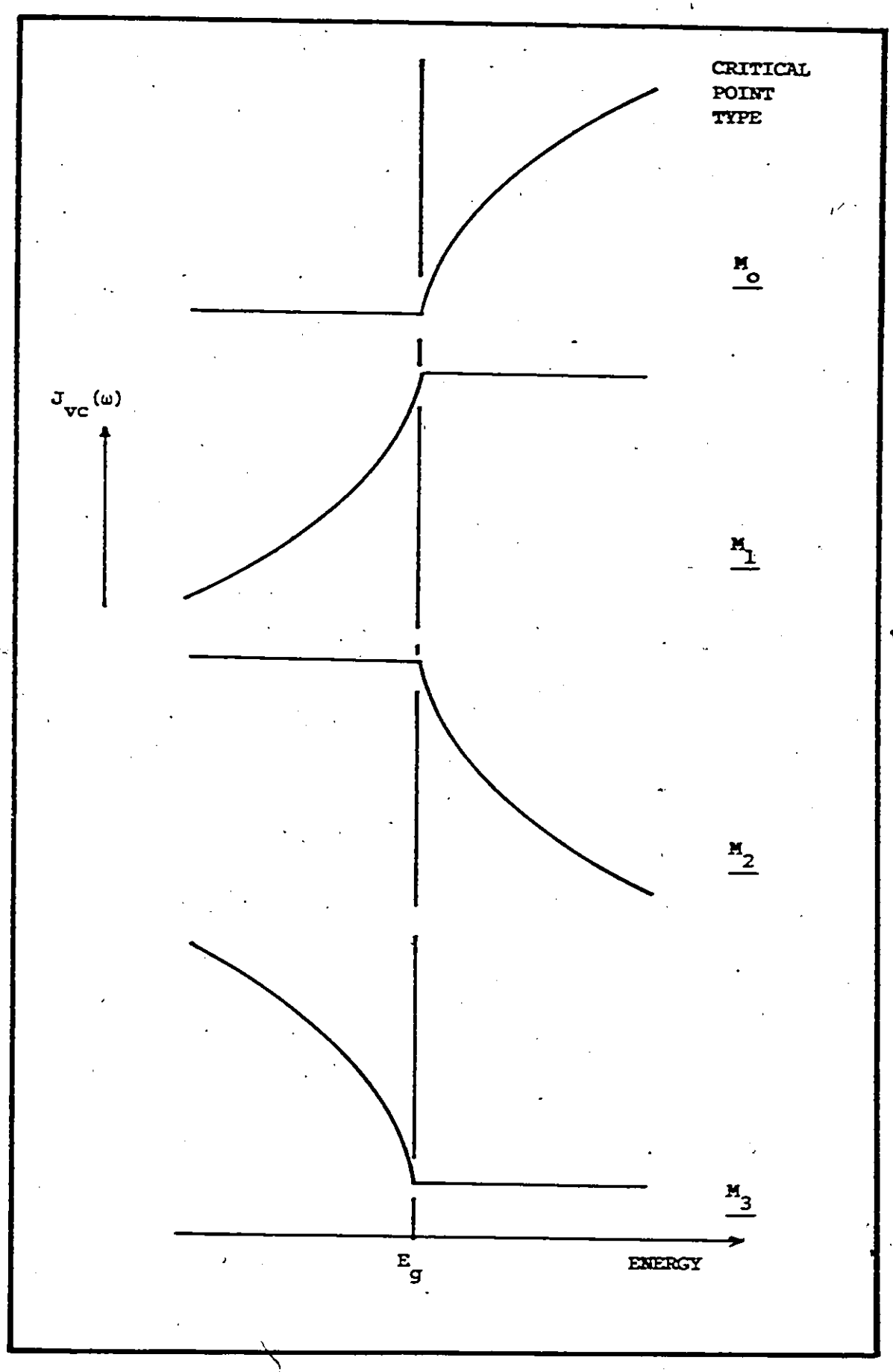

Figure 2-1 Joint density of states function.

of the second type can exist at points or directions of lower symmetry, such as [111] , <111> and <100> for ZnS and diamond semiconductors. While the first transition usually is predicted by symmetry, the second is not. When the analytic behaviour of $J_{vc}(\omega)$ near a critical point is studied, it is usually expanded in a Taylor series about the critical point k_o where $E_g = E_c - E_v$

$$E_c - E_v = E_g + \sum_{i=1}^{3} a_i (k_i - k_{oi})^2 \qquad (2.28)$$

Integrating $J_{vc}(\omega)$ one then obtains four different situations depending on the sign of the a_i's. Since the a_i's are related to the effective masses (2C64) the study of the critical point will give some information on the masses in the bands involved.

Fig. (2-1) shows a plot of $J_{vc}(\omega)$ as a function of energy for these cases. The c_i's in Table (2-1) depend on the absolute value of the a_i's (1F66).

M_o and M_3 give the well known square root dependence of the density of states. M_1, M_3 are dominant critical points in the interband spectra. The behaviour of $J_{vc}(\omega)$ in fig. 2.1 illustrates an other important point: a single critical point does not in itself produce a narrow peak in the density of states thus in ε_2, but only an edge. To obtain a peak due solely to interband transitions, there must be two singularities M_1 and M_2 occurring nearly at the same critical point energy E_g (see fig. 2-3, 2-4).

TABLE 2-1

TYPE OF CRITICAL POINT	a_1	a_2	a_3	NOTATION	J_{vc}	
					$E<E_g$	$E>E_g$
MINIMUM	+	+	+	M_o	0	$c_o(E-E_g)^{1/2}$
SADDLE POINT	+	+	−	M_1	$c_1-c_1'(E_g-E)^{1/2}$	c_1
SADDLE POINT	+	−	−	M_2	c_2	$c_2-c_2'(E-E_g)^{1/2}$
MAXIMUM	−	−	−	M_3	$c_3(E_g-E)^{1/2}$	0

Although this work is not directly concerned with it, we must observe that no maximum in reflectance is observable for certain other types of absorption threshold. It has so far been assumed that $|M_{vc}|$ is constant and non zero in the vicinity of an allowed transition. But if $|M_{vc}| = 0$ at k_o the transition is said to be forbidden. In such cases an expansion of $|M_{vc}|$ near k_o gives terms in $|\vec{k} - \vec{k}_o|$ that will make $|M_{vc}|^2$ proportional to $(E-E_g)$ and $\varepsilon_2 \alpha (E - E_g)^{3/2}$. In such cases a maximum in n or R is not detectable. The same is true for indirect transitions which have not been discussed here. When lattice vibrations are included to assist non vertical transitions, the change in momentum of the electrons will give rise to indirect allowed transitions. Then

$$\varepsilon_2 \alpha (E- E_g)^2$$

for forbidden indirect transitions (2M60)

$$\varepsilon_2 \alpha (E- E_g)^3$$

When characteristic line shapes are available from optical measurements, they are useful to identify the nature of the interband transition experimentally observed and therefore to determine its location in the B.Z. when the band structure is known.

2.4 ASSIGNEMENT OF OPTICAL TRANSITION TO BAND STRUCTURE

To relate the measured experimental quantities R or $\Delta R/R$ in a modulated reflectance study to actual band structure transitions in terms of the joint density of states and band structure of the material is a procedure requiring initially a certain amount of guess-work. The assignment of structure in terms of band structure and experimental information improves depending on the refinement of either.

The materials for which most reliable assignments exist and which have been most exhaustively studied are the ZnS-diamond family. The existence of a number of critical points involving spin-orbit splittings (ie. E_o, E_1) facilitates the assignment of optical transitions. In fact the wide range of Δ_o splittings gives a good method for determining whether the optical structure involves a p-like state at k = 0. The orbital doublet is split by spin orbit splitting interaction into two doublets $|\frac{3}{2}>$ and a singlet $|\frac{1}{2}>$. Away from k = 0, the doublet splits in the valence band of a solid to give Δ_1 in the [111]. (see section 1.5). The two thirds rule (secn. 5-1, 5-2) proves of great utility when the E_1 edge is identified with the $E_1 + \Delta_1$ one in the [111], since the value of Δ_1 may be approximately predicted from Δ_o. In fact it has been shown (1,2K56) that the matrix element (ch. 1 eq. 1-11) is approximately independent of k along the [111]. As fig. (2-2) shows, several optical transitions involve spin-orbit splitting. Since these transitions are accompanied by them, their predicted values are a key to the identification of such high-energy structures as E_o', E_1' and E_2. (see tables 2-2, 2-3).

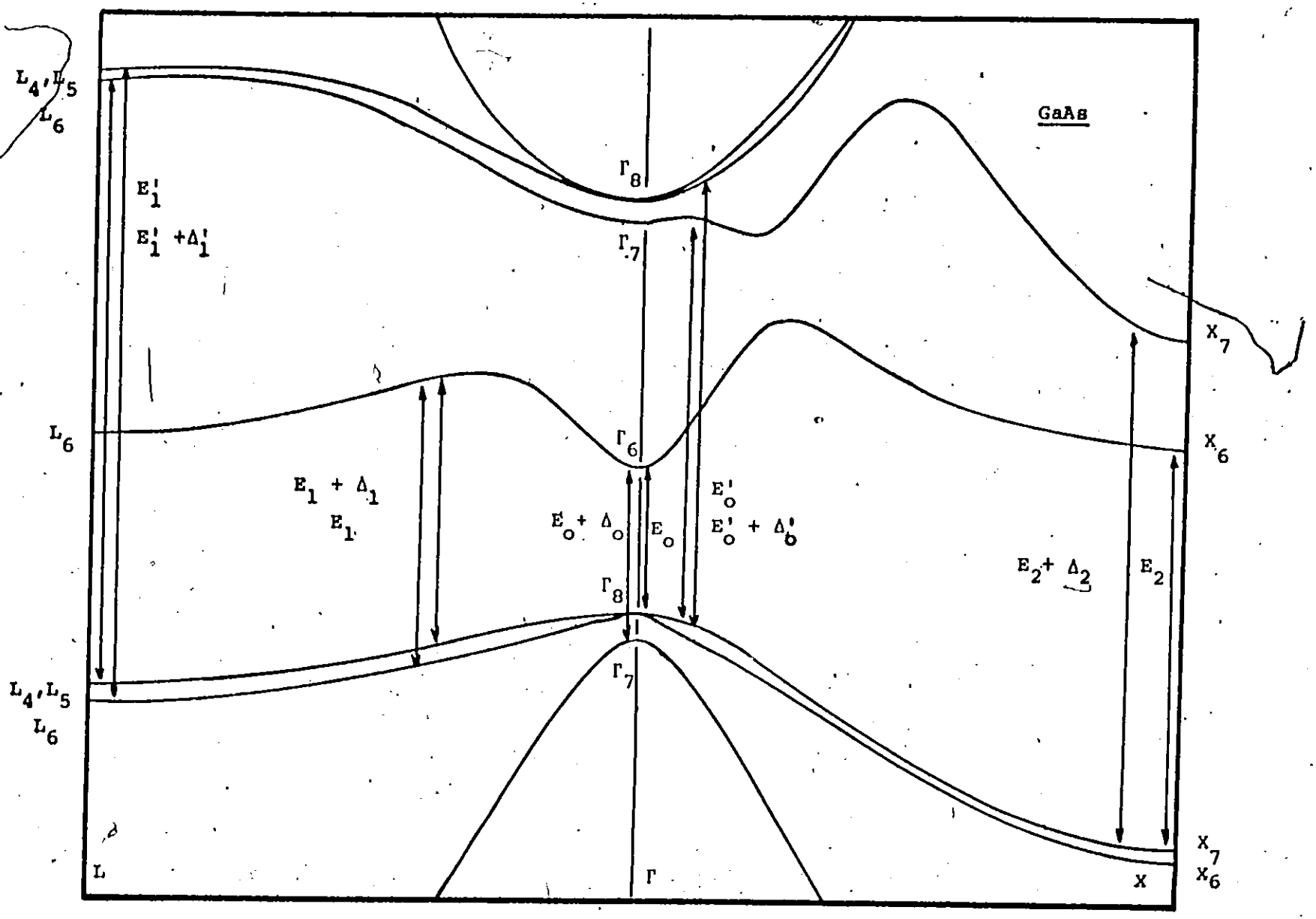

Figure 2-2 Showing the optical transitions that have been studied for semiconductors.

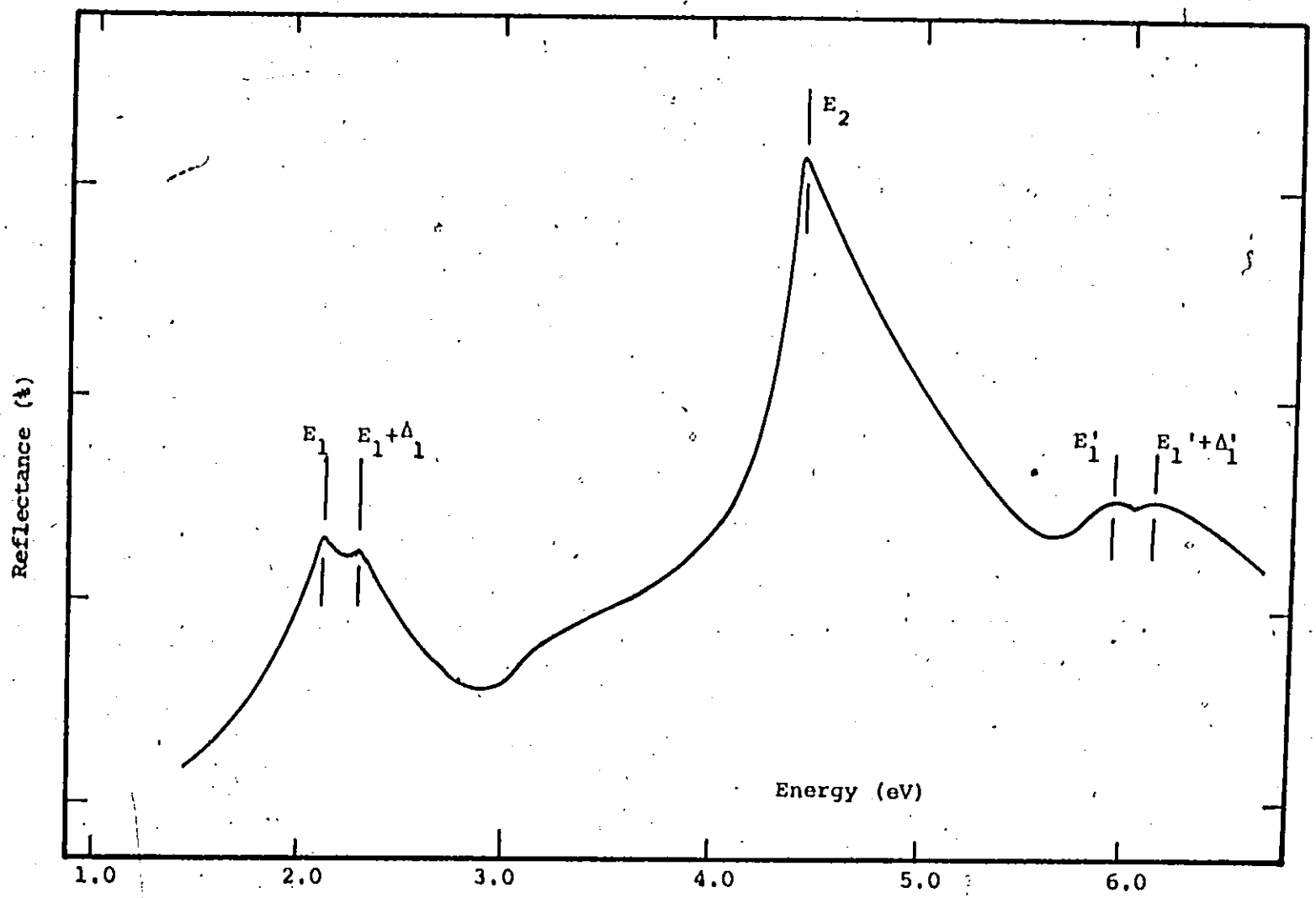

Figure 2-3. Showing the Reflectance spectrum for Ge. (2B62)

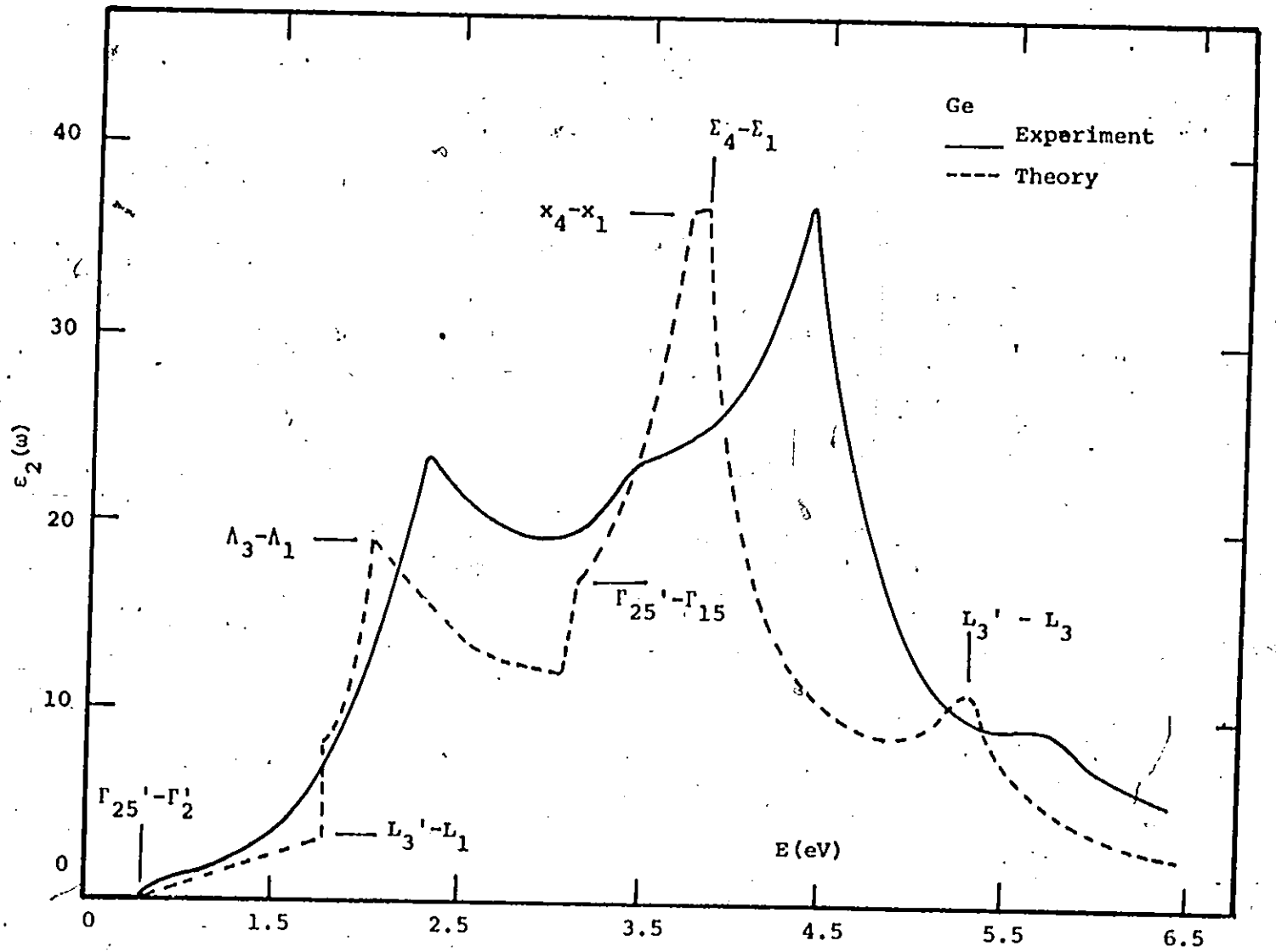

Figure 2-4. Showing calculated and experimental values of $\varepsilon_2(\omega)$ (2B62)

In spite of the guidance of spin orbit splitting, the identification of high symmetry critical points is not always unique. Often lower symmetry critical points involve stronger optical structures due to the increased multiplicity of the density of states (viz., $\Delta R(E_o) < \Delta R(E_1)$).

It is therefore often helpful to compute directly the dielectric constant (1H68) ε_2 from an accurate band structure. (2B62, 1H68, 3B64, 1H67, 1D67). The next procedure is to calculate ε_2 from measured optical constants (eq. 2.9). The comparison of density of states function from experiment to theory is a direct way to identify the edge or peak from reflectance and to relate it to the band-structure. In fig. (2.3) and (2.4) we show this work done for Ge by Brust and Phillips (2B62, 3B64).

The need of more accurate information about both thresholds and band structure has guided the experimentalist to seek more accurate experimental techniques in optical work. Modulation spectroscopy has emerged out of this need.

2.5 MODULATED REFLECTANCE

It has been discussed in the second section in this chapter how the spectrum of ε_2 with frequency does not show clearly fine structure that may be observed in reflectance or absorption alone. Modulated reflectance on the other hand promises to show finer band structure detail associated with optical transitions such as E_o, $E_o + \Delta_o$ (transitions from the valence band and

the split off valence band to the conduction band) which are difficult to see in either absorption or reflection. These are, if one looks at some typical reflectance measurements at high photon energies (fig. 2.3), transitions that often appear as shoulders and are immersed in the background of a bigger structure.

As it has been shown, in (2C69) the dielectric constant $\underline{\varepsilon}$ near a three dimensional critical point can be represented as

$$\underline{\varepsilon} \quad \alpha \quad a\,(\hbar\omega - Eg)^{1/2} + b \tag{2.29}$$

where the constants may be complex numbers.
The constant background in eq. (2.29) may be, and often is, much larger than the singular part, and hence the observation of the singularity may be lost in the noise of the background or the tail contributions from transitions close by. It is therefore advantageous to lift these small changes from the continuum. The easiest device is to look at the change or derivative of $\underline{\varepsilon}$ w.r.t. a parameter Π which may be "modulated" at will. If $\underline{\varepsilon}$ depends on this parameter Π by way of some other band parameter, such as the gap for instance, a response in $\underline{\varepsilon}$ is expected when Π changes in time.

$$\frac{d\varepsilon}{d\Pi} = \frac{a}{2} \frac{1}{(\hbar\omega - E_g)^{1/2}} \frac{d}{d\Pi}(\hbar\omega - E_g) + \frac{da}{d\Pi}(\hbar\omega - E_g)^{1/2} \tag{2.30}$$

while the second term becomes negligible at $\hbar\omega \sim E_g$, the first term blows up at the critical gap E_g and hence it is easily detected.

Two distinct possibilities for the modulating parameter Π appear immediately, the energy $\hbar\omega$ of the energy of the incident radiation, and the gap E_g. The first option is called wavelength modulation (2C69, 1W72, 1Z70) and the second falls into a family of modulation techniques whereby the gap E_g and the parameter Π are shown to depend on each other (such as electric field, temperature, pressure, etc.) (3B66, 4B66, 1M68, 2S70, 2G68,2C69). However, the important point here is that a change in these parameters is not directly measureable, but that changes in reflectance and absorption are now easier to observe. Therefore if in eq. (2.6a) the modulation of the parameter Π induces changes in the real and imaginary components of $\underline{\varepsilon}$, a change ΔR in R is found by differentiating (2.6a) and normalizing it to R.

This has been shown to be (3S65, 3S66, 2C69)

$$\frac{\Delta R}{R} = \alpha(\varepsilon_1,\varepsilon_2)\ \Delta\varepsilon_1 + \beta(\varepsilon_1,\varepsilon_2)\ \Delta\varepsilon_2 \qquad (2.31)$$

where $$\alpha = C_1\left[(\varepsilon_1-1)A_+ + \varepsilon_2 A_-\right]$$

and $$\beta = C_2\left[\frac{(\varepsilon_1-1)}{A_+} - \frac{\varepsilon_2}{A_-}\right]$$

$$A_\pm = \pm\frac{\{2'(\varepsilon_1^2+\varepsilon_2^2)^{1/2} \pm 2\varepsilon_1\}^{1/2}}{(\varepsilon_1^2+\varepsilon_2^2)^{1/2}}$$

and $$C_1 = \left[(\varepsilon_1+1)^2 + \varepsilon_2^2\right]^{-1}$$

$$C_2 = 2\varepsilon_2\left[(\varepsilon_1-1)^2 + \varepsilon_2^2\right]^{-1}(\varepsilon_1^2+\varepsilon_2^2)^{-1}$$

In a modulated reflectance spectrum, which is a trace of $\Delta R/R$ versus photon energy $\hbar\omega$, the components of $\Delta\varepsilon_1$ and $\Delta\varepsilon_2$ are the changes in ε_1 and ε_2 due to the effect of π on the material.

If as an example, the dielectric function at an M_o or M_3 type of critical point (as is the case for E_o) can have an imaginary component as

$$\varepsilon_2(\hbar\omega) = \frac{C}{\hbar\omega^2}(\hbar\omega - E_o)^{1/2} + \text{constant} \qquad (2.32)$$

where C is a constant (see table 2-1), in the energy gap modulation method, of which electroreflectance is an example, the change in ε_2 produced can be obtained from the above equations as

$$\Delta\varepsilon_2 = \frac{C}{2(\hbar\omega)^2} \frac{1}{(\hbar\omega - E_o)^{1/2}} \Delta E_o \qquad (2.33)$$

which has a singularity at $E_o = \hbar\omega$. The second term in the differentiation has been omitted since at $E_o = \hbar\omega$ it is negligible.

This rapidly changing behaviour of $\Delta\varepsilon_2$ at $E_o \sim \hbar\omega$ (eq. 2.33) demonstrates the advantage of modulation experiments over the static reflectance measurements (see fig. 2-9).

The components of $\Delta\varepsilon_1$ and $\Delta\varepsilon_2$ are coupled via the Kramers-Kroenig dispersion relations as ε_1 and ε_2 are thus $\Delta\varepsilon_1$ can be found knowing $\Delta\varepsilon_2$,

$$\Delta\varepsilon_1 = \frac{2}{\hbar} \int_o^\infty \frac{\omega\Delta\varepsilon_2}{\omega_o^2 - \omega^2} d\omega \qquad (2.34)$$

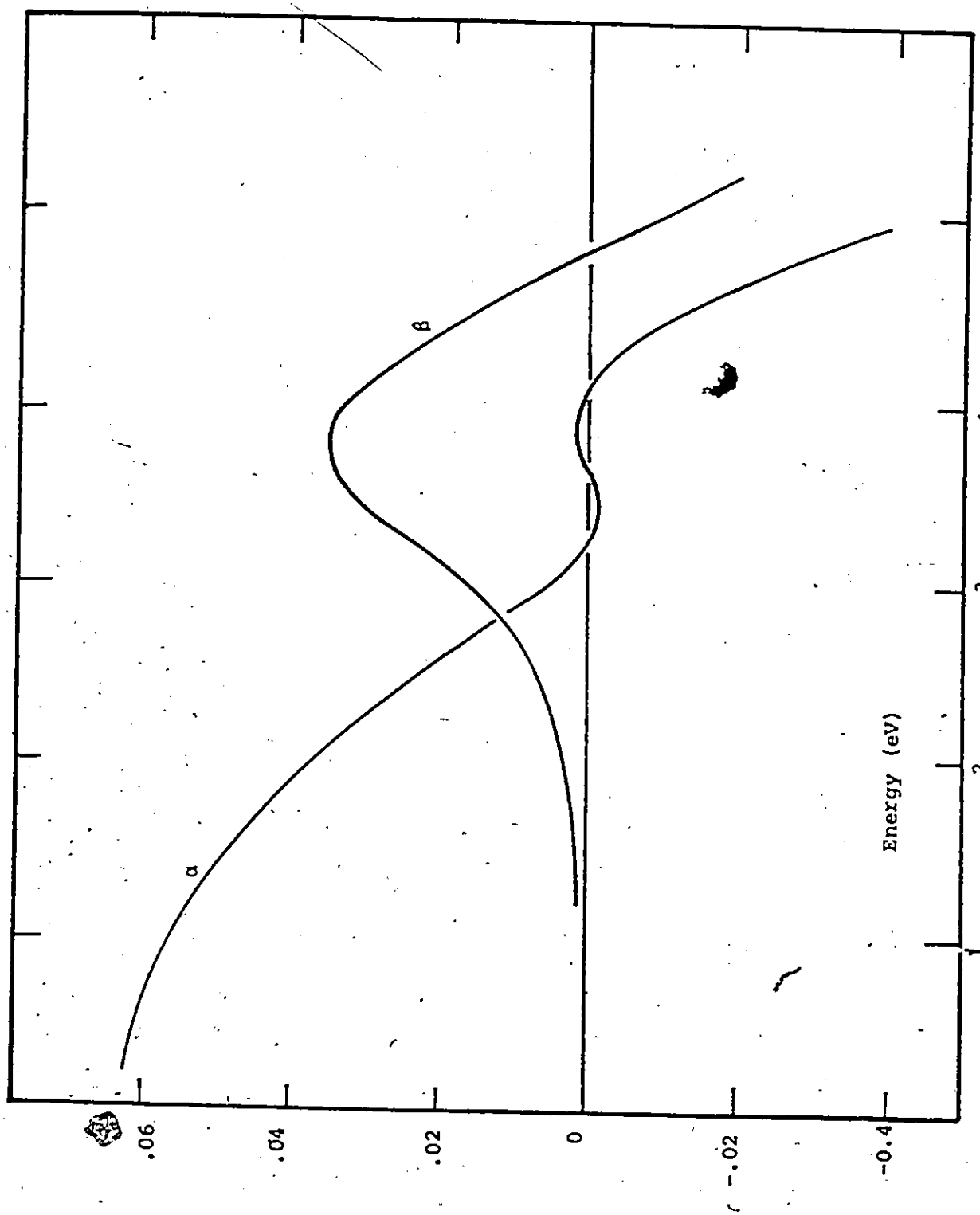

Figure 2-5 Fractional Coefficients α and β as a function of energy, Ge (2C69).

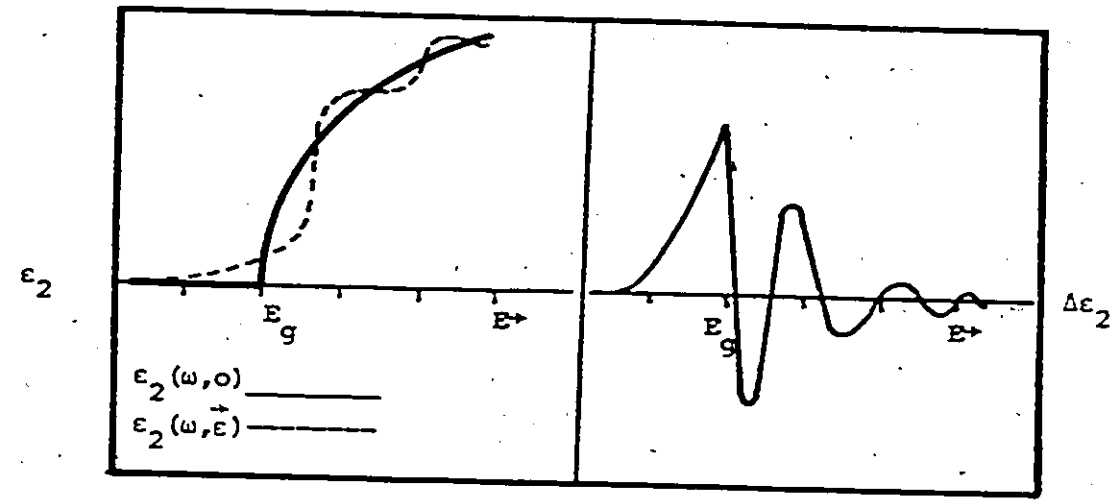

Figure 2-6. Showing the effect of an electric field on ε_2 and the change due to it at an M_o singularity.

In view of eq. (2.31) when ε_1 and ε_2 can be calculated from reflectance measurement by way of eq. (2.9), α and β are found as a function of energy. α and β determine the fractions of $\Delta\varepsilon_1$ and $\Delta\varepsilon_2$ contributing to the whole of the $\Delta R/R$ spectrum. In fig. (2-5), α,β for Ge, found from experimental information are shown. Upon inspection, it is seen that the spectral dependence can be divided into three regions. At low energy α is dominant over β and in the vicinity of the fundamental gap the lineshape of $\Delta R/R$ would be predominantly characteristic of the $\Delta\varepsilon_1$ term in eq. (2.31). This energy region also includes spin-orbit splitting effects (Δ_o). As the photon energy increases, α loses its predominance over β. This region includes the E_1 complex at intermediate energies. The E_o' and E_2 structures and higher energies will see α less than β thus $\Delta\varepsilon_2$ will be predominantly contributing to the $\Delta R/R$ spectrum. The β term goes through a maximum in this energy region. At even higher energies, where E_2 and structures due to d electrons are observable, α and β both turn negative thereby giving a reversal in the direction of the peaks in $\Delta R/R$.

This whole analysis is valid with the restrictions that are inherent in the Fresnel equation (2.6), ie. when normal incidence reflectance measurements are made at an air-sample interface.

2.6 ELECTROREFLECTANCE

It has been first established by Franz (2F58) and Keyldysh (4K58) that the effect of an electric field on the band gap of a semiconductor is to reduce the fundamental edge. According to their results, electrons and holes tunnel into the band gap from the conduction and the valence band edges respectively, thereby narrowing the gap and producing an exponential tail in the absorption coefficient below the band gap energy. Therefore the effect of an electric field on the optical response of a material is generally known as the Franz Keldysh effect.

The effect on the optical properties of a modulating parameter affecting the gap has been discussed in section (2.5). However, the change in ε_2 due to an electric field involves some assumptions that must be considered, the calculations to present date are with non-degenerate bands and neglect interband mixing due to the electric field. An accurate treatment which would not break down under degeneracy is yet to be given.

Two different but equivalent methods have been used for the calculation of the dielectric constant in the neighbourhood of a direct interband critical point in the presence of a uniform electric field. One of those methods (2C63, 3C64, 1A68), involves the calculations of the conduction and valence band wavefunction in presence of an electric field and the evaluation of ε_2 by the use of eq. (2.23). The necessary optical matrix element is found from these wf's. The second method (2A67, 1A66, 1T63) assumes parabolic bands around the vanHove singularities at

k_o and the use of the effective mass approximation. The interband matrix element in the absence of a modulating field is taken constant for allowed transitions.

The first calculation is a generalized theory of the Franz-Keldysh effect at the four kinds of critical points developed by Aspnes (2A67) and Aspnes Handler and Blossey (1A68). They derived a general expression for the imaginary component of the one electron interband dielectric function of a solid in the presence of an electric field on the lines developed by Callaway (2C69, 2C63).

From their results in the weak field approximation, the effect of an electric field on the imaginary part of the dielectric constant ϵ_2 is shown to be for a pair of v. and c. bands (1A68).

$$\epsilon_2(\omega,\vec{\epsilon}) = \frac{4\pi^2 e^2}{m^2\omega^2} \int \frac{2}{(2\pi)^3} |n.p_{vc}|^2 \left[\frac{1}{\hbar\Omega} \, Ai\left[\frac{E_c - E_v - \hbar\omega}{\hbar\Omega}\right]\right] dk^3 \qquad (2.35)$$

where $\hbar\Omega = \left(\frac{e^2 \vec{\epsilon}^2 \hbar^2}{8\mu^*_{ii}}\right)^{1/3}$ and $\frac{1}{\mu^*_{ii}} = \frac{1}{\hbar^2} \frac{\partial^2 (E_c - E_v)}{\partial k_{ii}^2}$

and Ai is the Airy function

$$Ai(x) = \frac{1}{2\pi} \int_{-\infty}^{\infty} ds \, e^{\left(\frac{is^3}{3} + ixs\right)}$$

and the integration in 2.35 is over one B.Z. The electrooptic matrix element $|n.p_{vc}|$ depends only on Bloch functions of the conduction and the valence bands. n is a unit vector in the direction of the $\vec{\epsilon}$ field. No assumptions have been made on the shape of the bands.

Since it is reasonable to assume that the most interesting contributions to $\epsilon_2(\omega,\vec{\epsilon})$ and therefore to $\Delta\epsilon_1$ and $\Delta\epsilon_2$ come from the vicinity of van Hove singularities, the analysis has been confined only to states close to the energy gap (fig. 2-6). The electrooptic matrix element has also been assumed to be constant in this energy region and is therefore taken out of the integration.

The zero field expression for ϵ_2 is given by rewriting eq. (2.23)

$$\epsilon_2(\omega,0) = \frac{4\pi^2 e^2}{m^2\omega^2} \int \frac{2}{(2\pi)^3} \cdot |\vec{e}.p_{vc}|^2 \, \delta(E_c - E_v - \hbar\omega) \, dk^3 \qquad (2.36)$$

Aspnes et al. (2C63) therefore show that in the weak field limit the finite electric field dielectric function $\epsilon_2(\omega,\vec{\epsilon})$ can be approximated by convoluting the zero field dielectric function $(\epsilon_2(\omega,0))$ with an Airy function. From eq. 2.35 and 2.36 an analytic expression for $\Delta\epsilon_2$ can be obtained. For finite values of field at any point $\vec{k}$, the electric field mixes contributions from other points in the neighbourhood of $\vec{k}$ in a direction the electric field is applied. This mixing must vanish as the field is removed.

Seraphin (2S72) explains that this mixing in the presence of an electric field extending over a slope discontinuity in the density of states function (fig. 2.6) is responsible for the large changes observed in $\underline{\epsilon}$ at critical points, while it is small in smoother regions (fig. 2.3).

The effect of the breaking of the symmetry of the lattice by the electric field involves changes in the dielectric function $\underline{\varepsilon}$ as well as in the density of states of the conduction and the valence bands (1R68). The over all effect of the applied field reduces the direct gaps of the material. It will be later argued that an analogous breaking in the symmetry of the mixed crystal by way of the aperiodic potential reduces the gap as a function of alloy composition.

The form of the Airy function is determined by the sign of its arguments. It decays exponentially for positive arguments and has a damped oscillating character for negative arguments. Therefore, as seen in eq. (2.35), the form of $\varepsilon_2(\omega,\vec{\varepsilon})$ will depend on the sign of the reduced effective mass along the application of the electric field. This fact has a significant analytical power in determining the location of optical transitions in the B.Z. and the type of Van Hove singularity involved.

Aspnes (2A67) derived expressions for $\Delta\varepsilon_2(\omega,\vec{\varepsilon})$ at the four types of critical points in terms of two electrooptic functions (see fig. 2-7) F(x) and G(x)

$$\Delta\varepsilon_2(\omega,\vec{\varepsilon}) = \frac{2|p_{vc}.n|^2}{\omega^2(2\mu_{ii})^{3/2}}\left(\frac{\vec{\varepsilon}^2}{2\mu_{ii}}\right)^{1/3} F\left(\frac{E_g-\hbar\omega}{\hbar\Omega}\right)$$

$$\Delta\varepsilon_1(\omega,\vec{\varepsilon}) = \frac{2|p_{vc}.n|^2}{\omega^2(2\mu_{ii})^{3/2}}\left(\frac{\vec{\varepsilon}^2}{2\mu_{ii}}\right)^{1/3} \qquad (2.37)$$

$$\left[G\left(\frac{E_g-\hbar\omega}{\hbar\Omega}\right) + G\left(\frac{E_g+\hbar\omega}{\hbar\Omega}\right) - 2G\left(\frac{\hbar\omega}{\hbar\Omega}\right)\right]$$

where

$$F(x) = \frac{1}{\pi} \left([Ai'(x)]^2 - x[Ai(x)]^2 \right) - (-x)^{1/2} U(x)$$

and

$$G(x) = \frac{1}{\pi} \left(Ai'(x)\, Bi'(x) - x\, Ai(x)\, Bi(x) \right) + (x)^{1/2} U(x)$$

and Ai(x), Bi(x) and Ai'(x), Bi'(x) are Airy functions and their derivatives. U(x) is a unit step function. x is $\frac{E-E_g-\hbar\omega}{\hbar\Omega}$. Six unique distinct lineshapes are obtained at the four types of critical points M_o, M_1, M_2 and M_3 (fig. 2-7). The result of those calculations (1P72) can be seen in (fig. 2-8).

In the formulae given in the preceeding pages, the applied modulating field appears as an argument in the Airy function and in the multiplication factors. A complicated dependence of the electrooptic effect on the orientation of $\vec{\varepsilon}$ is expected. The argument of the Airy function contains the reduced mass along the field direction. For M_1 and M_2 edges, the sign of this mass depends on the direction of $\vec{\varepsilon}$ and therefore as its orientation is varied, the position of the oscillations w.r.t. the gap should vary (2S72). For [111] valleys, the electrooptic effect of allowed transitions is independent of $\vec{n}$ where $\vec{\varepsilon}$ is along the [100] and is strongly anisotropic for $\vec{\varepsilon}$ along [111] (2S72). Airy oscillations then occur both above and below the gap. Since the recognition of lineshapes in the $\Delta R/R$ spectrum leads to an identification of the critical point, proper assignment of optical transitions becomes possible if accurate band

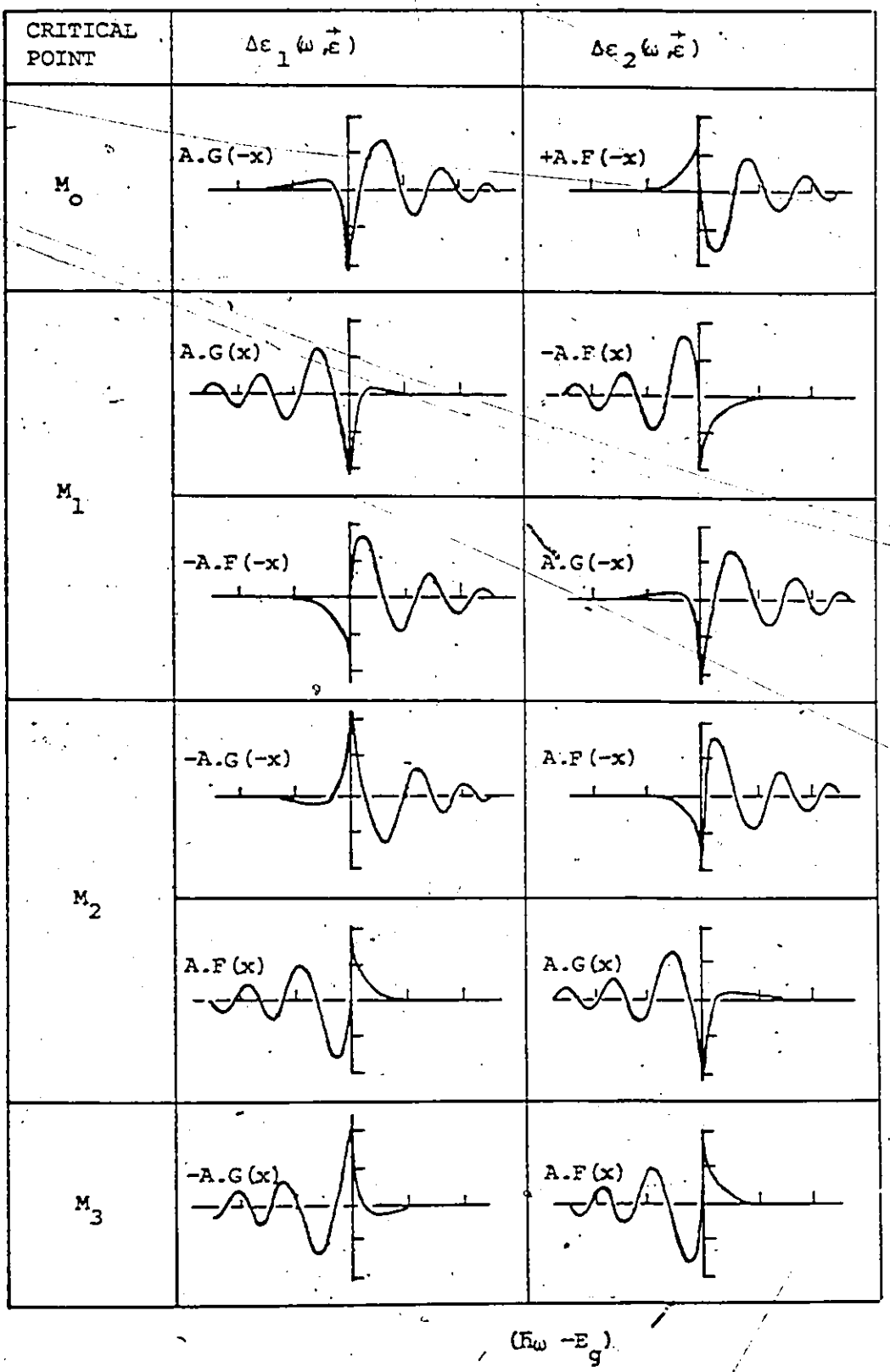

Figure 2-7. Theoretical lineshapes for $\Delta\varepsilon_1$ and $\Delta\varepsilon_2$ at the four types of critical points.

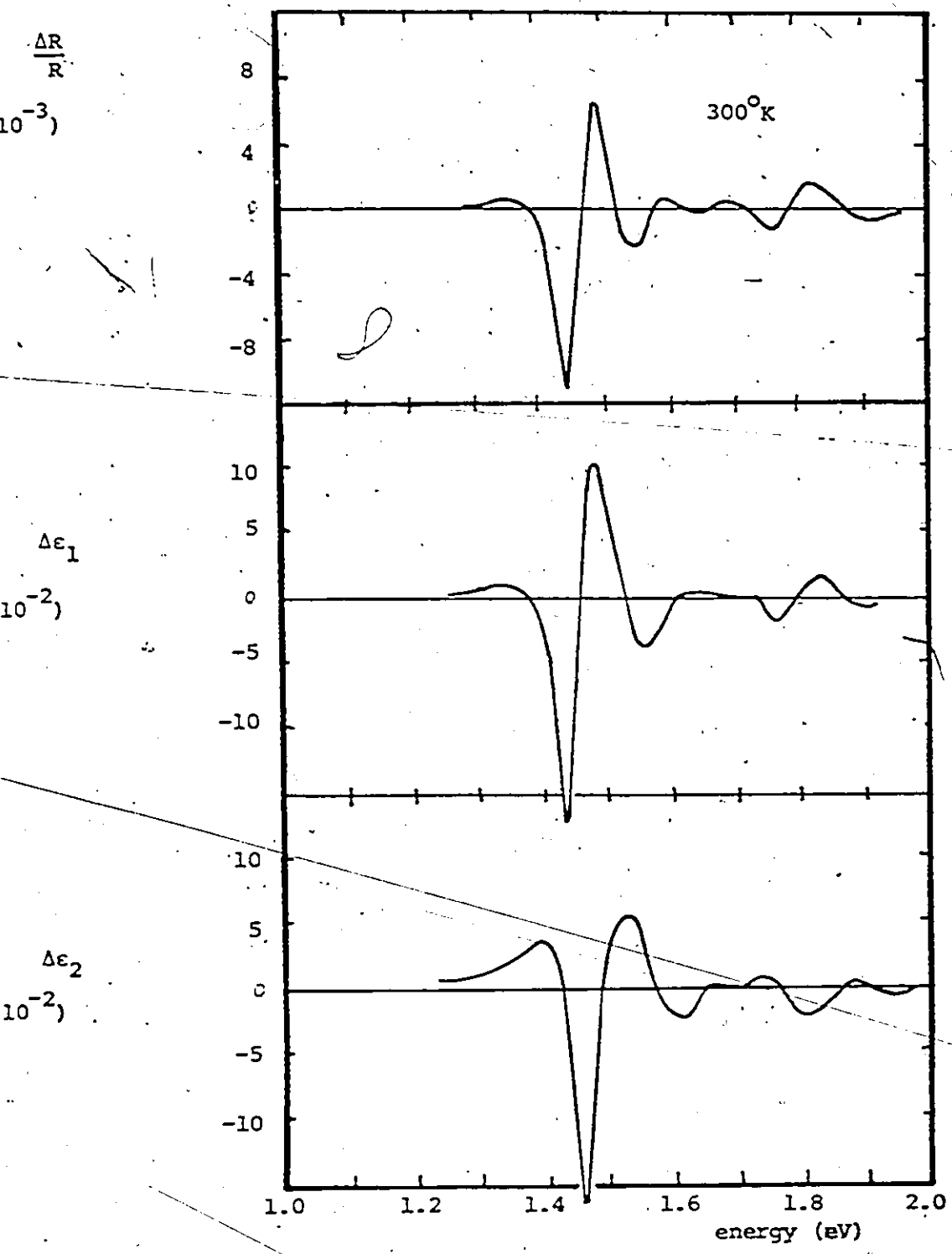

Figure 2-8 $\Delta R/R$ and $\Delta\varepsilon_i$ (i=1,2) for GaAs (1P72).

structure information is available.

However, in real experimentation the line shapes that are predicted by theory are infact broadened by effects of temperature, phonon field, inhomogeneous electric field $\vec{\epsilon}$, space charge effects (2S69) etc. The effect of Lorenzian broadening on the electrooptic functions discussed above has been considered by Aspnes (2A67). A numerical calculation of several particular cases has also been given by Seraphin and Bottka (3S66). Several other treatments are available with respect to resonance broadening (2B71) collision broadening (3A67) and the thermal and electrical broadening (1O72). The effect of alloy broadening has not been treated carefully so far (3W68), (3A72) and may be attributed to effects of alloy inhomogeneity (4V72).

Recently a good experimental correlation between low field electroreflectance spectra and the third derivative of the linear dielectric function which identifies the structure as a resonant third order nonlinear optical susceptibility has been found by Aspnes (1,2A72). This result relates electroreflectance spectra to other types of modulation results. Good experimental agreement is achieved.

2.7 REVIEW OF ELECTROREFLECTANCE RESULTS

The first electroreflectance measurements are due to Seraphin (4S64) by a field effect electroreflectance technique. The electric field is

applied across a thin dielectric material from a semitransparent electrode. Unwanted reflectance caused by mismatches of optical interfaces and changes in electrode configurations by coulomb forces complicate this arrangement. MOS sandwiches, as shall be seen later, are a more apt modification of the surface barrier mode. This technique, as noted by Pidgeon et al., (1P67), lower the temperature range and widens the available spectral range.

The electrolytic electroreflectance technique was developed by Shaklee et al (4S65, 1P67). In this method an electric field is obtained across a liquid electrolyte at the semiconductor-electrolyte interface. The sample is one of the electrodes. The advantage of this technique is that larger fields are obtainable with smaller applied voltages (see ch. 3 section 3.8).

The electroreflectance spectra of Ge, Si and GaAs were obtained by Seraphin using the field effect electro-reflectance technique (4S64). In the Ge spectrum, transitions corresponding to E_o, $E_o + \Delta_o$, E_1, $E_1 + \Delta_1$, the E_o' complex and E_2 are resolved as sharp structures (5S65, 6S65). $E_o + \Delta_o$ structure is usually not resolved by reflectance. In the case of Si (7S65) the three structures observed are attributed to E_o, E_1 transitions with an excitonic peak between the two. The structure found with GaAs (4S66) is in good agreement with previous reflectance data. The field shifts for M_o and M_1 type transitions are measured. The spectra are studied as a function of static surface potential (bias) (2S67). It was found that the signal $\Delta R/R$ at a structure, when observed at the modulation frequency, goes through a minimum when flat-band conditions (2S67) are satisfied. (see also 2H68).

Electroreflectance in the electrolytic configuration requires much less detailed sample preparation and therefore it has been extensively used in the study of semiconductors to determine several critical band gaps in the 0.6 to 6 eV range (1C69). Cardona, with several workers has produced a massive amount of information on diamond, zinc-blende and rocksalt semiconductors (1C67, 1C69, 5C66). The direct gap values as well as spin orbit splittings so obtained have been used in semi-empirical band calculations (2W67) (see Table 2-2, 2-3).

Electrolytic electroreflectance, as well as surface barrier electroreflectance give structure in their spectrum which aresharp and well resolved. Such structures as E_o, $E_o + \Delta_o$ which can only be resolved by absorption are equally seen in electroreflectance. Thompson et al (2T66) have well resolved Δ_o for GaP and Vishnubathla for InP
In fig. (2.g) the electroreflectance and reflectance of InP is shown in the vicinity of the E_1 complex. The figure shows the resolving power of electroreflectance compared to conventional reflectance. The Δ_1 splitting is clearly resolved.

A Kramers-Kroenig analysis in the region around E_o suggests that the lineshape is that of an M_o edge (2C67). The E_1, $E_1 + \Delta_1$ peaks have a lineshape suggesting M_1 critical points. It is thought that the contribution in the $M_{1\perp}$ direction is considerably larger than the one due to $M_{1\parallel}$. The possibility of excitonic contributions to these electroreflectance spectra has been verified for E_o (3B59) and it has been suggested for E_1 (2H68). Transitions above E_1 usually present a broader spectral line.

TABLE 2.2 Energies in eV

	E_o	$E_o+\Delta_o$	$E_1(1)$	$E_1(2)$	$E_1(1)+\Delta_1$	$E_1(2)+\Delta_1$	E_o'	$E_o'+\Delta_o'$	E_2	$E_2+\delta$	E_1'
Si	4.06	4.13					3.32		4.31		
Ge	0.789	1.09	2.12		2.34		3.13	3.32	4.42		
αSn			1.30		1.84		2.28	2.63	3.72		4.11→4.85
AlAs											
AlSb	2.22	3	2.81	2.88	3.22	3.30	3.72	3.99	4.25	4.6	
GaP	2.74	2,84	3.66	3.80			4.78	4.83	5.27	5.74	
GaAs	1.43	1.77	2.89	2.96	3.12	3.19	4.44	4.63	4.99	5.33	
GaSb	.73	1.52	2.03		2.49		2.27	3.56	4.20	4.57	5.50
InP	1.34	1.44	3.12	3.19	3.27	3.24	4.72	4.79	5.04	5.6	
InAs	.36	.75	2.50		2.78		4.40		4.70	5.18	
InSb	.18	.99	1.88		2.38		3.10	3.49	4.08	4.66	5.25

TABLE 2.3 Energies in eV

Material	Δ_o(k.p)	Δ_o(exp)	Δ_1^-(k.p)	Δ_1(exp)	Δ_o'(k.p)	Δ_o'(exp)
Si	0.044	0.044	0.03		0.055	
Ge	0.29	0.29	0.20	0.19	0.30	0.19
αSn	0.72		0.48	0.48	1.06	0.35
AlAs		0.28		0.20		
AlSb	0.75	0.75	0.41	0.40	0.24	0.27
GaP	0.10	0.10	0.073	0.1	0.22	0.05
GaAs	0.34	0.34	0.22	0.23	0.27	0.19
GaSb	0.80	0.73	0.46	0.46	0.39	0.29
InP	0.11	0.11	0.11	0.15	0.82	0.07
InAs	0.43	0.43	0.28	0.28	0.74	
InSb	0.82	0.82	0.48	0.50	0.84	0.33

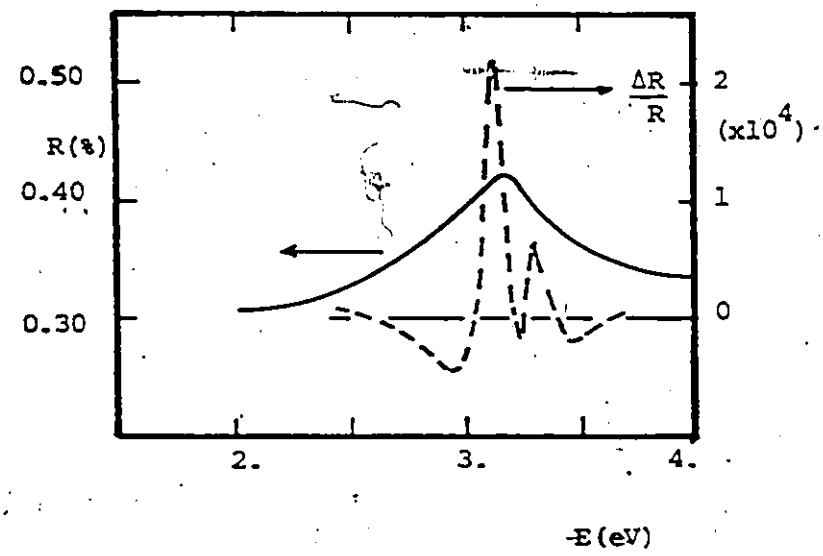

Figure 2-9. Comparison of R and ΔR/R spectra for InP. (2C69).

Line shape determination of ΔE_2, suggest E_o' to be an M_o critical point. (2H68, 3B59).

EER and more recently SBER (surface barrier electroreflectance) have been used to study band gap energies as a function of alloy composition. The Ge-Si alloy system was measured by Klein et al., (2K68). A linear variation of the gap with alloy composition was found. Electro-reflectance studies on (GaIn)As (3W68) Ga(AsP) (2T66, 1B72), GaAlAs (1B71,1B71) and In(AsP) (1A72) have all shown an energy gap dependence which is quadratic in alloy composition. However, only in a few cases (Ga(AsP), (InGa)As) has the spin orbit splitting Δ_o been experimentally determined. We have seen in sections 1-4, 1-6, 2-4 the importance that a study of Δ_o can have in understanding possible future band models in alloys. We believe that together with Δ_1 measurements (1V70) perhaps a comprehensive picture of alloy behaviour of some band parameters such as m_c^* may emerge.

CHAPTER III EXPERIMENTAL

3.1 Introduction

3.2 Experimental conditions on the measurement of optical constants

3.3 Measurement of Reflectance

3.4 Measurement of electroreflectance (EER, SBER)

3.5 Low temperature SBER Measurements

3.6 Sample preparation

3.7 Semiconductor surfaces

3.8 Some properties of MOS films.

3.1 INTRODUCTION

In the previous chapter it has been discussed how measured optical properties can be related to band structures. On the other hand, it has also been discussed how band structure calculations may predict some of the optical characteristics of materials. In this chapter, it is proposed to discuss experimental techniques and how they are used to obtain some of the optical and band structure properties of the material.

Specifically, the methods used in this work, their principle, the apparatus and the experimental details to obtain reproducible measurement of reflectance and electroreflectance are discussed. Most of the III-V compounds and their alloys have been previously prepared in our laboratories (1,2W68, 1C69) or have been obtained commercially (sec 3-8). Materials preparation will therefore not be discussed in great detail.

3.2 EXPERIMENTAL CONDITIONS FOR THE MEASUREMENT OF OPTICAL CONSTANTS

It has been discussed in Chapter II how quantities like reflectance, transmission and modulated reflectance can be related to the fundamental optical parameters of the material. The purpose of optical measurements is therefore to obtain interband transitions energies

which can be tied into the band structure.

When monochromatic light strikes an optically smooth surface, the light is reflected. The ratio of the intensity reflected (I_R) to that incident (I_o) is known as reflectance (R). When some of the incident intensity is transmitted through the sample (I_T), then transmittance is defined as (I_T/I_o). Absolute measurement of these two quantities is experimentally difficult. For an absolute measurement of reflectance or transmission all the light measured as I_o must be focussed on the surface of the sample. All this light must be reflected, transmitted and absorbed by the sample.,

the surfaces of the sample must not scatter light out of the optical path either upon reflection or transmission. Therefore all the light reflected or transmitted must reach the detector. In addition, when it is known that the atmosphere as well as other focussing devices (lenses etc) will absorb some of the radiation around particular photon energies, the optical path of the light must be kept the same for both the measurement of the incident intensity I_o and the reflected (I_R)or transmitted (I_T) intensity. The efficiency of the detecting and the light emitting source must be independent of time. It is clear, that all of these conditions are hard to meet simultaneously and with proper precision over the whole photon energy range. This is why, at best only appropriate extrapolations over unexplored photon ranges will allow a Kramers-Kronig analysis.

Modulated reflectance eliminates some of these problems when $\Delta R/R$ is measured as a function of energy. Any intensity losses reduce both ΔR and R by the same factor.

The experimental configuration is drawn up to satisfy the simple Fresnel conditions (eq. 2.6) and therefore the angle of incidence in this kind of optical work is kept near normal ($\sim 7^{o}$). In this case, the reflectance is independent of the degree of polarization of the incident radiation (2S57). This point is particularly relevant when one considers the polarization effect due to multiple reflections from mirrors, the transmission of the radiation through narrow slits and finally the polarizing effect of high grid gratings.

The equipment used for optical measurement requires a radiation source which covers the photon energy region of interest. This radiation is dispersed into a spectrum by a prism or a diffraction grating. The focussing of the monochromatic light beam is done with mirrors or lenses depending on the type of measurement required. Fig. 3.1 shows the photon ranges covered by various sources and the sensitivity of various detectors. The absorbing power of the atmosphere, which can play an important part in absolute measurements, is also shown. In fig. 3-2 the transmission as a function of photon wavelength for various materials used for prisms, lenses, dielectric insulators (for MOS) or protective coatings for mirrors is shown. This information allows for the choice of the set of light source, detector, filter, cryostat window etc for the measurements.

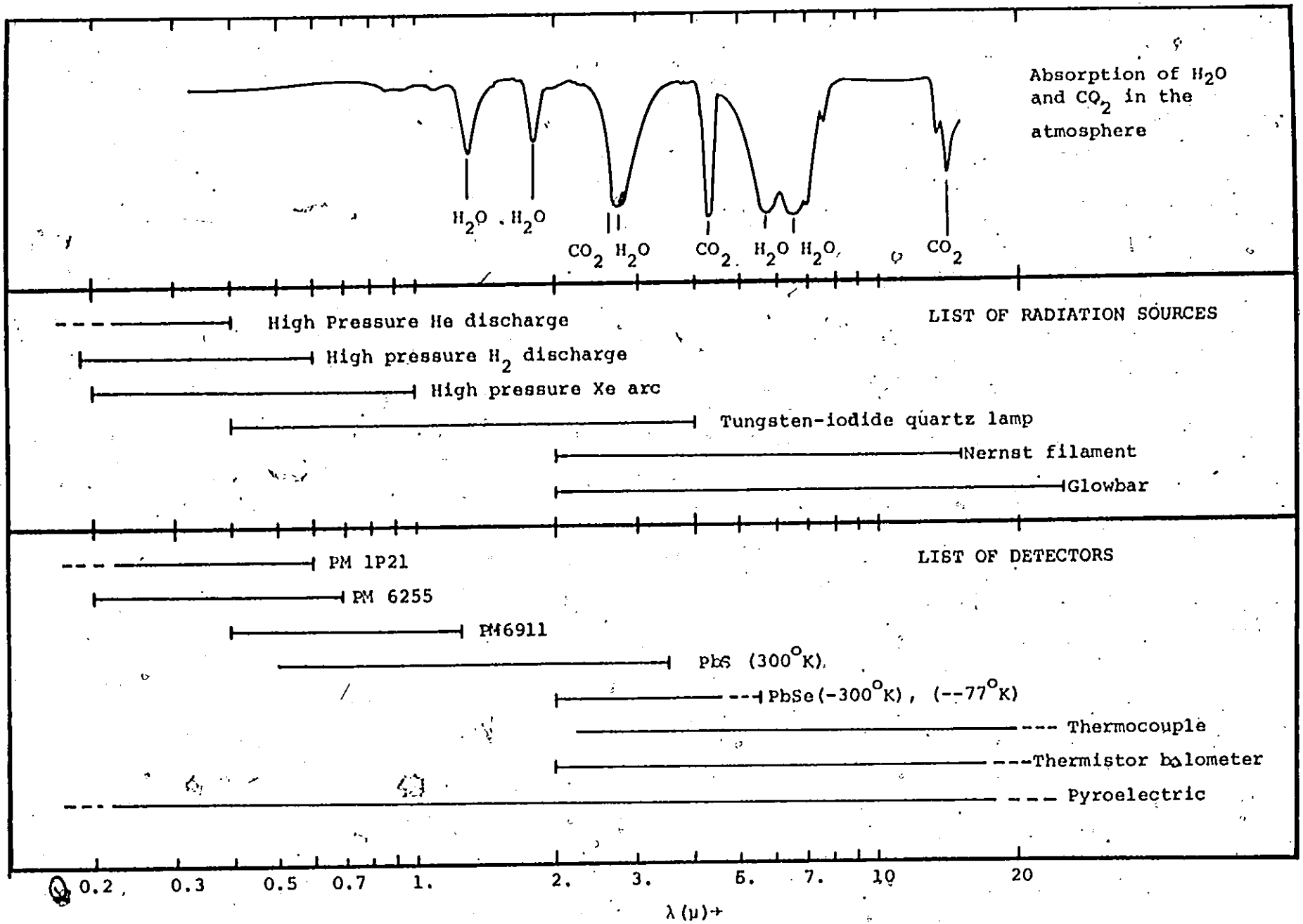

Figure 3.1 Absorption due to the atmosphere, range of radiation sources and detectors.

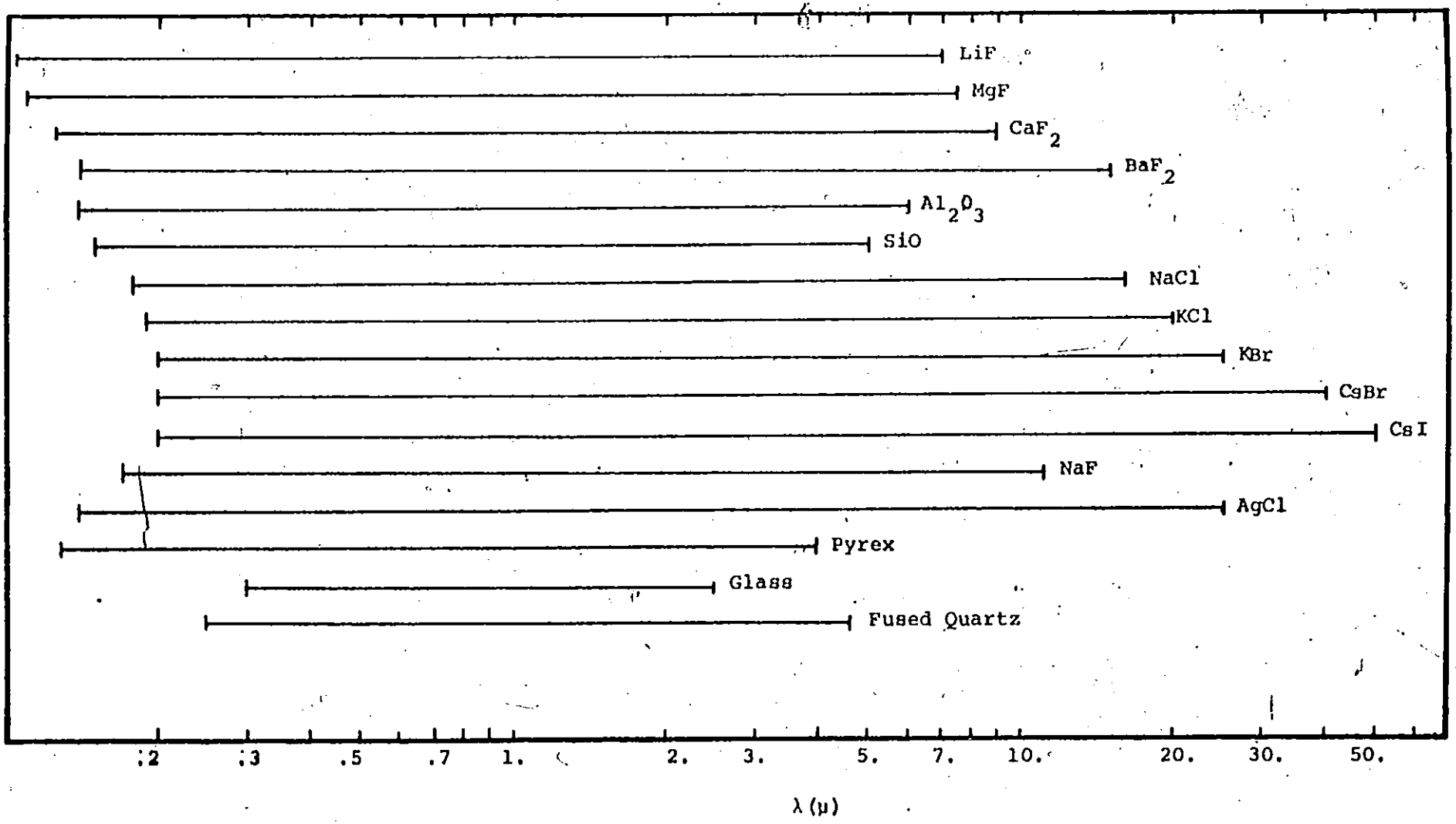

Figure 3-2 Transmission properties of material used as Prisms, insulating oxide layers and protective coatings for front aluminum mirrors. (2H69).

The merit of one type of instrumentation over the other has been discussed in detail by various review articles on the optical properties of materials (2C69, 3W67, 3G68). The stability of both the source and the detecting unit is clearly of importance for reliable measurements.

The measurements which involve this work range over the photon wavelength regions from $\sim 4\mu$ to $\sim 0.2\mu$. Obviously considerable changes are made in both equipment and techniques as the study proceeds from one end of this spectrum to the other.

3.3 MEASUREMENT OF REFLECTANCE

The object of this experiment is to measure the values of reflectance as a function of wavelength or photon energy over an extended range for a semiconductor whose reflecting surface has been prepared with care (see sec. 3-7).

A schematic arrangement of the apparatus for measuring reflectance is shown in fig. 3-3. This particular set up which was used to measure reflectance in the 1 to 5 eV range consists of a Zeiss M4QIII prism monochromator and source. A tungsten halogen lamp and a hydrogen-deuterium (H_2- D_2) discharge tube are available. The 1P28 photomultiplier can be positioned to measure the reflected intensity in one position (B) and the incident beam in the other (A) when the sample is removed from the beam. The angle of incidence is $\sim 7^{\circ}$.

Figure 3-3 The Reflectance Setup

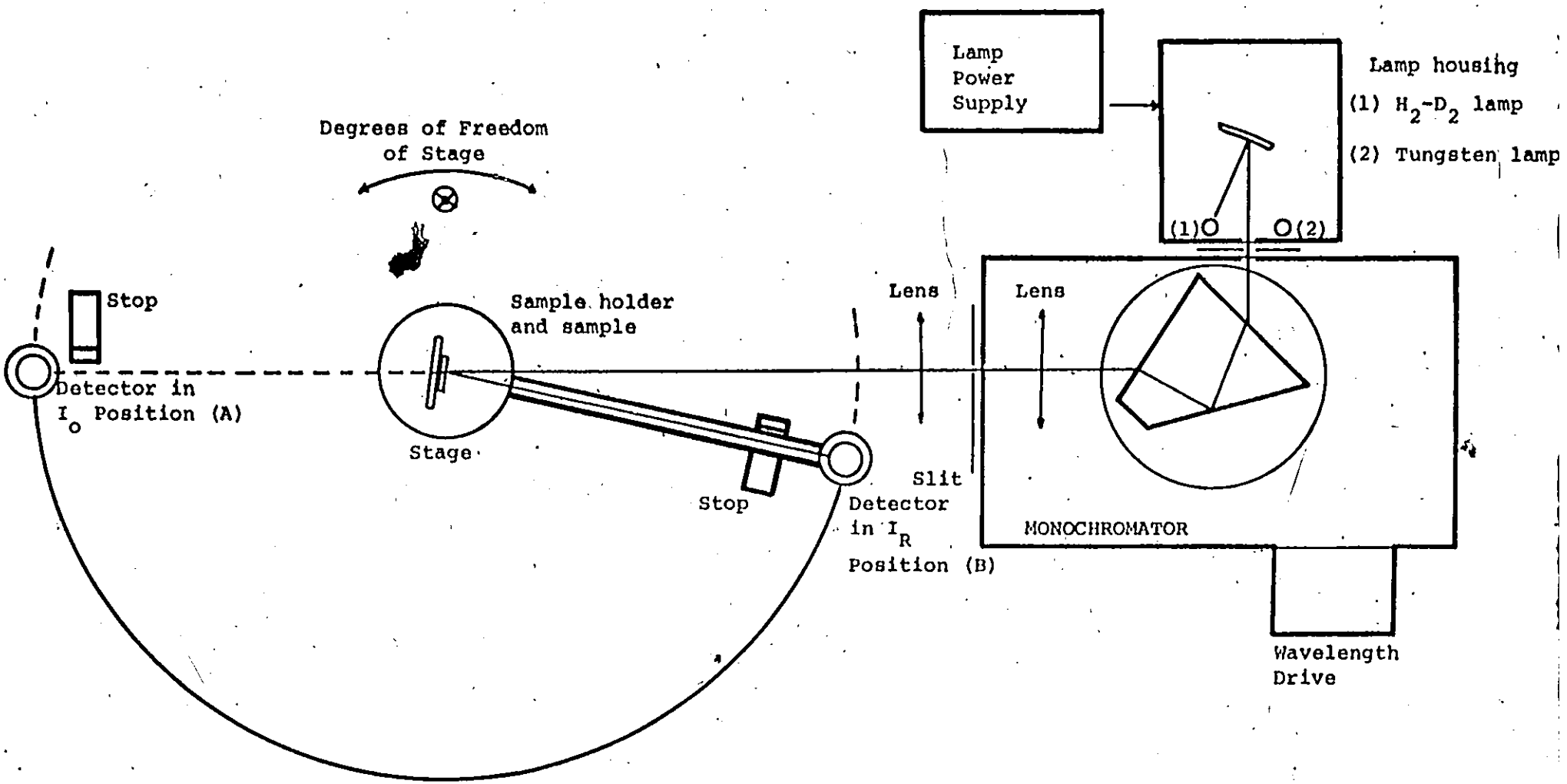

It is possible to obtain a reflectance spectrum by two methods. I_o and I_R may be measured separately over the wavelength spectrum and then R may be calculated, or I_o and I_R are found for each wavelength, thus R, over the spectrum.

The latter technique, although more time-consuming than that of running over the spectrum for each (I_o, I_R) measurement, reduces effects due to fluctuations in the electronics and the lamp intensity. The radial arm upon which the detector is fixed is moved through the same degrees each time (fig. 3-3). Stops are arranged on the radial arm travel to expose the detector to the same sensitive areas for all the measurements. The length of the radial arm is fixed, so that the dimension of the beam falling on the detector is the same for both incident and reflected modes. The sample holder has an angular and a vertical freedom of motion. The angular motion changes the angle of incidence, the vertical removes the sample from the beam for the I_o measurement and replaces the sample for the reflectance position. The point by point measurement was made at wavelength intervals suitable for the particular region of the spectrum investigated. However no obvious differences were detected between the two techniques. The reflectance spectrum then exhibits structure which is associated with interband optical transitions (Ch. II).

3.4A METHODS IN ELECTROREFLECTANCE

Of the several configurations by which a modulating electric field may be achieved on a semiconductor surface (1F67, 3Y66, 2R67, 1P67, 2F67, 1L67, 1F71), the liquid electrolyte (EER) and the transparent solid dielectric (SBER) methods were used in this work.

The method used to obtain surface barrier electroreflectance (SBER) measurements consists of a dry sandwich configuration made up from a dielectric layer which separates the sample from a semitransparent metal electrode which is a metal-oxide-semiconductor or MOS configuration (MOS) (fig. 3-4). The MOS sandwich of Ludecke and Paul eliminates the various technical difficulties inherent in the dry sandwich technique used by Seraphin (4S64) which were discussed in Ch. II. Pidgeon et al (1P67) used an organic photoresist rather than the oxide as dielectric. The increased spectral range and temperature range at which the SBER measurements can be made on these packages have been clearly demonstrated by these workers. In section 3-8 the preparation and the properties of MOS sandwiches in these laboratories is given in detail and the effect of thin film layers on the electroreflectance spectrum is discussed in appendix II.

The second method to obtain electroreflectance which has been used in this work is by the electrolytic method (EER).

The semiconductor electrolyte interface may be viewed as analogous to a p-n junction (fig. 3.4), since the charge carriers have different

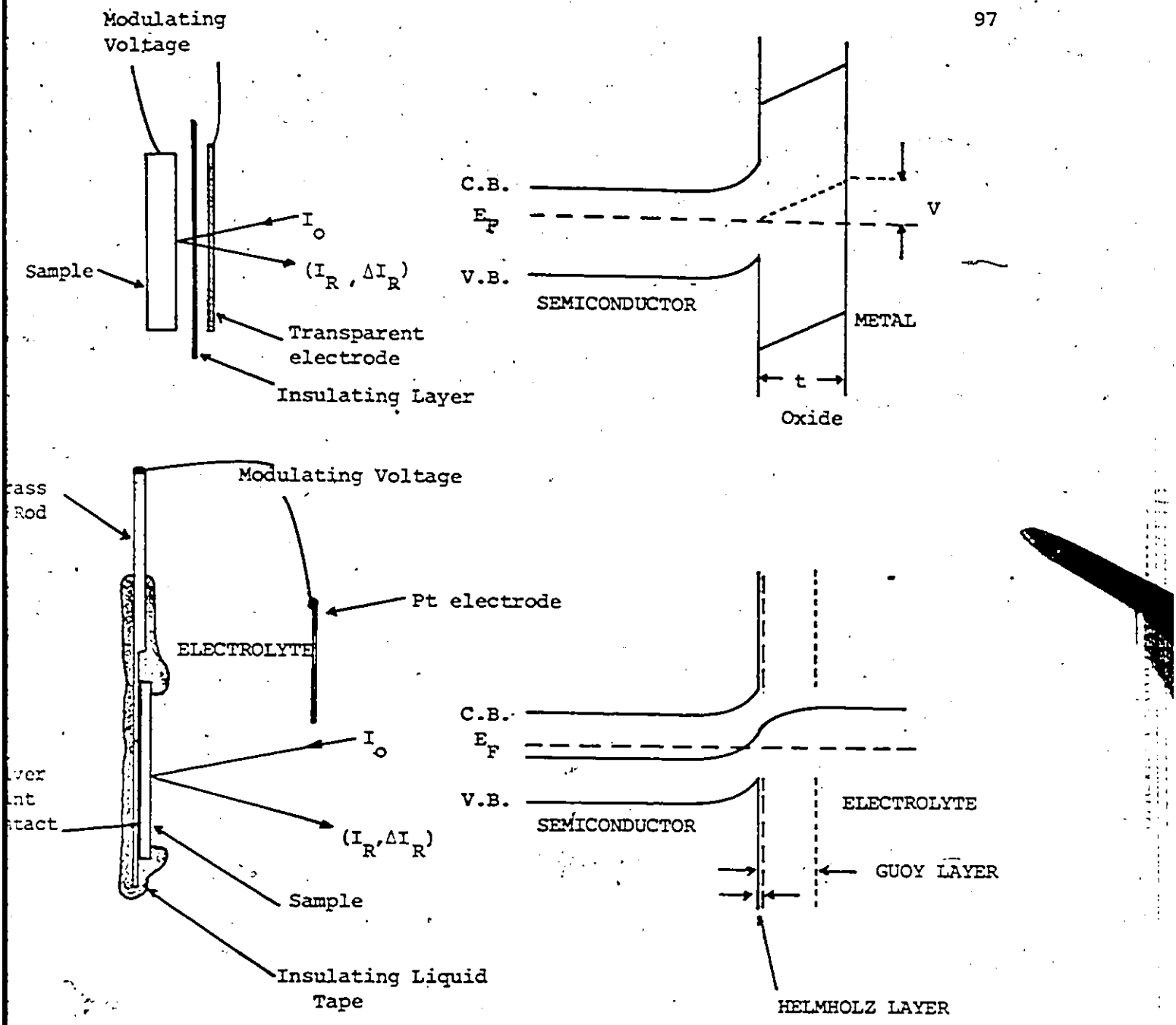

Figure 3-4. Showing field effect configuration due to Seraphin (4S64) and the liquid electrolyte configuration. Appropriate sample mounting and surface conditions are shown.

properties in the electrolyte and in the semiconductor. Upon contact with the electrolyte, the electrochemical potential equalizes with that of the sample and the space charge layer is either established or modified from what it was. The application of a time dependent field on this space charge changes the population in the space charge layer for fast surface states. The effective a.c. impedance for such a cell in aqueous electrolytes is less than in organic ones (1D60, 1T62). The I.V. characteristic curves have been studied (see fig. 3-5) and the ideal working conditions can therefore be established. In the more ionic III-V compounds and their alloys, surface damage has often been seen to result from the application of large + ve biases. In the small bias range a flat portion on the I-V curve is available (fig. 3-5). The conductivity of the interface is here at a minimum. Higher electric fields can therefore be established. Most of the applied field will then drop across the interface. Small a.c. voltages over the narrow interface region results in high a.c. electric fields when the bias in this region is used on the sample.

The choice of electrolyte is governed by its transmission properties (1D60, 1T62, 2C69). Aqueous electrolytes extend from 0.35μ to 1.2μ but organic electrolytes (eg. glycerolpropylene carbonate, acetoniline, etc.,) extend this region into the I.R. Organic electrolytes also allow for measurements down to 150°K (methyl alcohol + KCl).

Figure 3-5 I-V characteristics for an electrolytic cell (2C69).

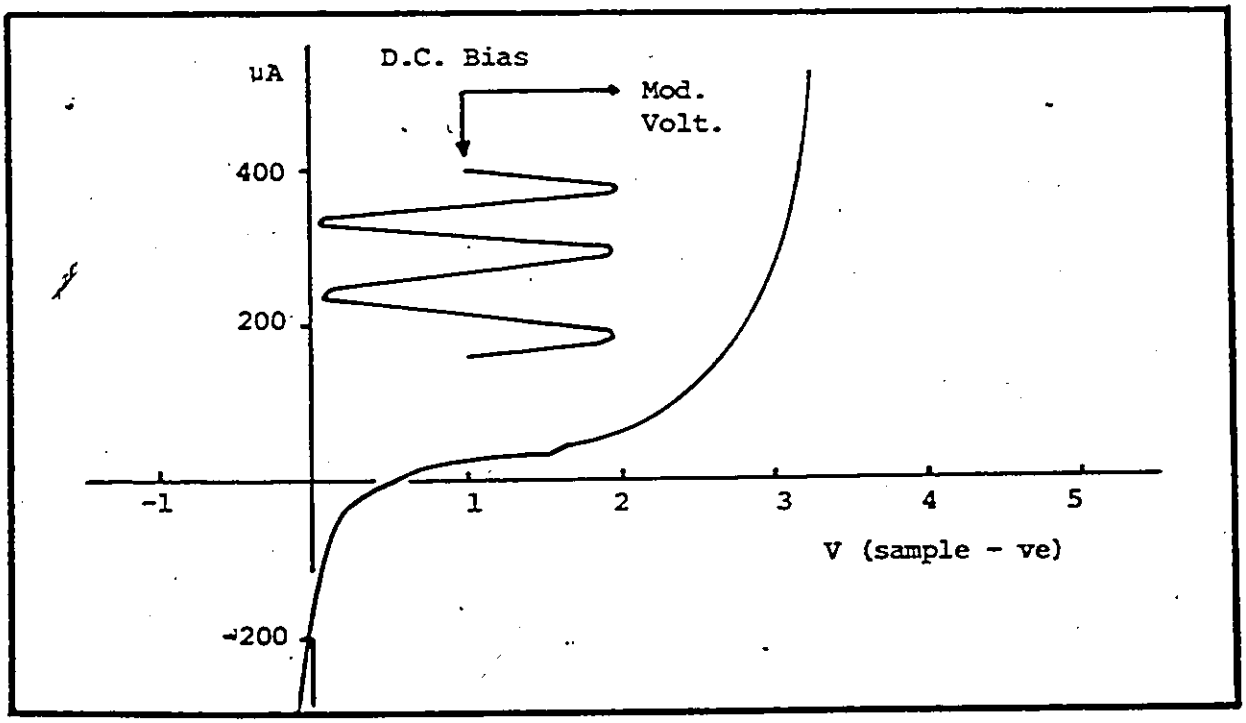

3.4 B MEASUREMENT OF ELECTROREFLECTANCE

In section 2.5 we have seen how the application of an external periodic disturbance on some parameter of a sample will induce a shift of the threshold and enhance changes in the optical properties of the material. We have also seen how the changes of reflectance ΔR can be related, through lineshape analysis, to a particular type of threshold in the joint density of states. In the case of measurement of $\Delta R/R$ as a function of photon energy, it is therefore necessary, in addition to the equipment used in reflectance, to have a source of modulating signal as well as a phase sensitive detecting unit (detector and lock-in amplifier) measuring R at the frequency of modulation.

i) Ultraviolet and Visible Electroreflectance (EER).

A schematic layout of the experimental setup is in fig. 3-6. A Baush and Lomb half meter grating monochromator (1200 groves/mm) disperses the light available from either a Hanovia 907C1, 600 watt high pressure quartz Xe-arc lamp (visible, uv) or a 650 watt Sylvania DWY tungsten filament iodide lamp, run at 75% of its power requirements. The tungsten lamp was found a quieter source when measurements were not too far in the U.V. Wratten 29, Wratten 2A, Glass and Corning 137 u.v. filters are used to eliminate unwanted spectral portions from higher order modes of the grating. The light intensity and resolution are controlled by the entrance and the exit slit. The openings on these are usually kept the same, for

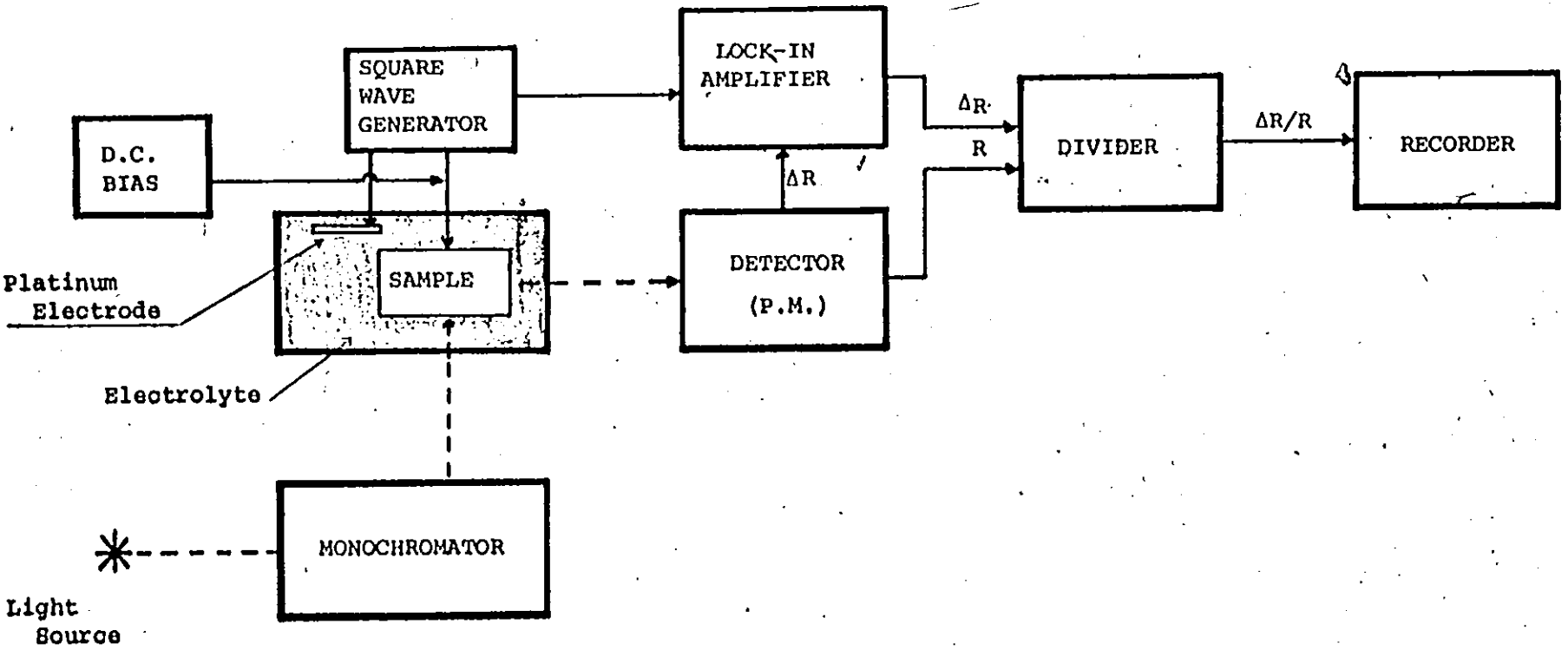

Figure 3-6 Block diagram of EER setup

a maximum of photon energy transmission through the monochromator. The monochromatic beam is focussed at near normal incidence on the surface of the sample by means of a quartz lens.

The sample is held on a brass rod in a Pyrex container filled with the liquid electrolyte and having a flat quartz front plate through which the light beams pass (reflected and incident). The electrolyte used for these measurements is a solution of 7=H_2O: 3= Glycerine. A 4cm^2 platinum electrode is immersed into the full container to carry the a.c. signal across the electrolyte to the sample.

Although some of the advantages of organic electrolytes have been discussed above, some additional advantages are the increase of range of bias voltages without drawing excessive currents through the cell, the reversal of bias conditions without surface damage to the sample and that larger modulating voltages can be used when a good signal is not easily obtained.

The sample and the platinum electrode establish the a.c. voltage across the electrolyte via a Hewlett Packard function generator operating in a square wave mode or by using the reference output from the Par JB6 lock-in amplifier. The amplifier is used to amplify and select the ΔR signal from the reflected beam. In the first instance the lock-in is used in an external reference mode, in the second internal. The bias voltage is established by a unit consisting of a battery and a potentiometer. It essentially raises or lowers the zero of the ac. signal from the oscillator with respect to ground. The desired amount of backoff d.c. bias voltage can then just be tapped off the potentiometer.

The monochromatic light is focussed at near normal incidence on the surface by a quartz short f lens. The reflected light is refocussed by a concave mirror into the phototube detector. A du Mont 6911 is used in the IR region (peaks at 0.7 μ) and an EMI 6255S (peaks at 0.4 μ) in the visible and the u.v. The photomultipliers operate from a Keithly 240 regulated power supply.

The modulated reflectance (at 80 H_Z) consists of two components an a.c. part proportional to the change in reflected intensity and a d.c. component proportional to the reflected intensity. The a.c. component is filtered out of the background by a PAR-JB6 lock-in amplifier. The output is fed into an operational amplifier (Burr-Brown 3263/14). This signal is then divided by the d.c. component which is proportional to the reflected intensity with a Burr Brown 4097/25 differential input divider. The output is then plotted as a function of wavelength on a volt-time Honeywell Electronik 19 chart recorder. The scanning speed and the time constants on the output are chosen in such a way that the division of ΔR by R occurs at the same photon energy. This may be achieved by a slow scan at a fast time constant on the lock-in. (The phototube has a response in the order of nonaseconds). An R-C circuit clears out the noise after the division and therefore the $\Delta R/R$ spectrum is smoothed out. Scanning of the wavelength is motor driven and the wavelength is usually marked at 50 Å intervals. Under ideal signal conditions the estimated resolution in the green (~ 5500 Å) is found to be better than 10 Å. The size of the modulating voltage and bias depend on sample and surface

conditions. The wavelength region of interest is initially scanned. When the location of the structures is established, optimum running conditions are found with respect to resolution (slit width), bias, modulating signal and inphase output from the lock-in. A slow scan follows at ~50 Å/min and 1 to 3 sec timeconstants giving $\Delta R/R$ structure with more than sufficient resolution and signal to noise ratios. When the latter condition is not satisfied, the spectrum is run several times and a noise averaged spectrum is then obtained.

ii) Electroreflectance in the I.R. (SBER):

The experimental layout is shown in fig. 3-7. The light source used is either an a.c. driven Sylvania DWY 650 watt tungsten-iodide lamp for the near U.V., the visible and the near I.R. photon regions, or a Nernst filament covering photon range from the visible to the intermediate IR (~4μ). (see fig. 3-1, 3-2). The image of the source is focussed on the entrance slit of a Spex 1702 Czerny-Turner Scanning Spectrometer, by a front surface aluminium mirror. Plane gratings of different blaze are available (3000Å, 7500Å, 1.6μ , 4μ, 8μ etc). At each exchange from one grating to the other, the spectrometer is recalibrated either by the use of a He-Ne laser or by a precalibrated absorption spectrum of a mylar film. In order of energy cut off, the filters used are Wratten 29, OCLI α-00903-6, OCLI α-01040-8, OCLI α-01900-9A, OCLI α- 62370-9A.

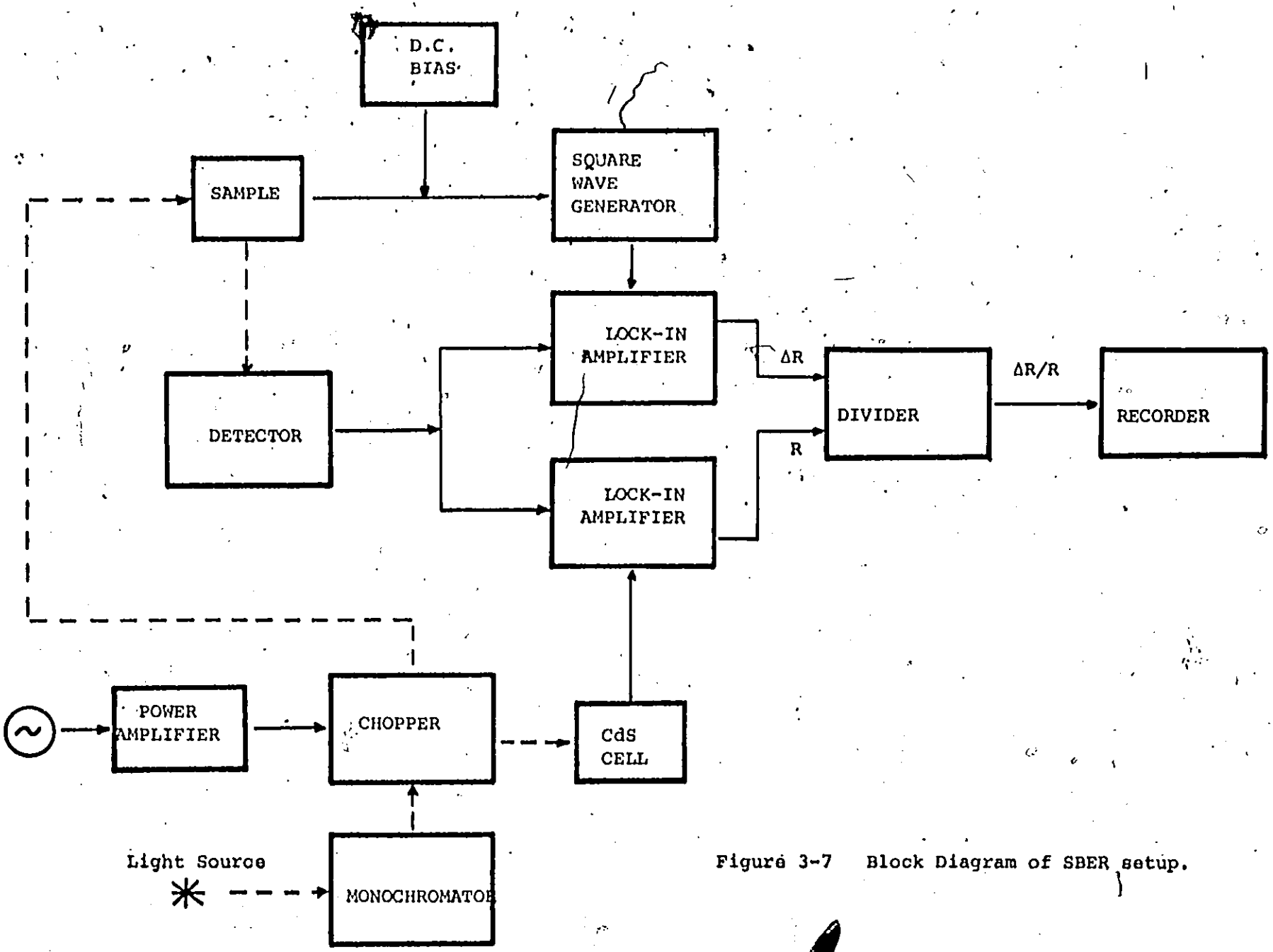

Figure 3-7 Block Diagram of SBER setup.

The light beam from the monochromator is refocussed on the sample by a short f concave mirror. The reflected light is then re-directed on the detector by another concave mirror. PbS and PbSe detectors are used from .6μ to 3.5μ and 1μ to 8μ respectively. The PbSe detector is usually functioning at liquid air temperature.

Unlike the EER setup, the light beam is chopped before entering the monochromator by a motor which is continuously tunable from 15 Hz to 120 Hz. The chopper frequency which is the motor frequency times the cuts in the chopper blade was used at ~230 Hz. The detector specifications are linear at this frequency.

The sample consists of an MOS package (see fig. 3-12 and sec. 3-8). A square wave modulating voltage is applied between the Ni film and the semiconductor from a Hewlett Packard 331A function generator with built-in $\pm$ d.c. offset usable for bias adjustments.

The signal received from the detector consists of two components, each proportional to ΔR and R at two different frequencies. R travels at the chopper frequency, ΔR at the modulating frequency. However the separation by the lock-ins, which should look at only one or the other of those frequencies, is not complete. Cross talk between the two channels is minimized by reducing the beating observed on the ΔR channel. The condition on these frequencies is then that one is not a harmonic or a fundamental of the other. The R signal is fed to a Par 120 lock-in amplifier. The ΔR signal is fed to a Par 213 pre-amplifier, through a Par 210 tunable amplifier and to a

a Par 120 lock-in amplifier. Both Par 220 and Par 210 are tuned to the modulating frequency on which ΔR travels. Both lock-in's work in the external reference mode. A CdS photocell registers the chopping frequency while the signal generator has an auxiliary output at the working frequency.

The output from each channel is then fed to a Par 230 multiplier in the dividing mode. The output proportional to $\Delta R/R$ is then recorded on a Honeywell Electronik 19 Chart recorder. The monochromator wavelength drive provides a short across the chart recorder for the purpose of marking of the wavelength reading. The time constants on the lock-in's in each channel are kept identical and in the fast response mode. The divider provides an additional time-constant adjust on the output whenever the noise level compares to the ΔR signal. This way the signals from both channels arrive simultaneously to the divider and they are both due to the same photon energy. Whenever the ΔR signal is too low then R and ΔR measurements are found separately. The ΔR signal is found smoother when the R channel is off.

Preliminary measurements were done by first locating the proper bias conditions by I.-V. measurements (sec. 3-8). Then at the appropriate biases, the structures of interest were identified for an optimum signal to noise ratio. A slow scan then followed with a good workable resolution 10 - 5 meV.

It should be pointed out that SBER measurements are equally possible to obtain up to ~8 eV, however the development of this project started with the EER and high energy measurements. SBER measurements were later done in the vicinity of the gap only.

3-5 LOW TEMPERATURE ELECTROREFLECTANCE MEASUREMENTS (SBER)

Low temperature measurements were done in order to investigate the temperature dependance of some optical interband transitions, and in particular to establish the temperature dependance of spin orbit splitting.

As it has been discussed above, EER at low temperature is limited and liquid helium temperatures are not accessible. However deviations from linearity for the E_o dependance on temperature occur at temperatures lower than those accessible by electrolytic measurements (2C69, p. 223). MOS packages solve this problem.

A Sulfrian cryostat (fig. 3-8) originally designed for transport properties has been modified for optical measurements. The cryostat is able to attain continuous temperature range from 4.2°K to 300°K. Pumping facilities would provide measurements down to 1°K. Two forms of temperature controll are available, since the cryostat tip is not in direct contact with the liquid helium tank. Thin tubes connect the He tank to the cryostat tip through which liquid helium can be pumped. The tip cools down to 4.2°K when the pumping rate is maximal. At various rates of pumping different temperatures can be obtained at the cryostat tip.

(1) to vac. 1
(2) to vac. 2
(3) Liquid N_2 in
(4) Liquid He in
(5) N_2 chamber
(6) He chamber
(7) He suction tube to cool tailpiece.
(8) N_2 shield
(9) O-sealrings
(10) He shield
(11) heater resistor to warm up tailpiece
(12) Cu wire resistance thermometer
(13) Sample
(14) LiF window
(15) Removable coldfinger, sample holder (see fig. 3-9).
(16) Removable tailpiece
(17) Liquid He entrance to tailpiece

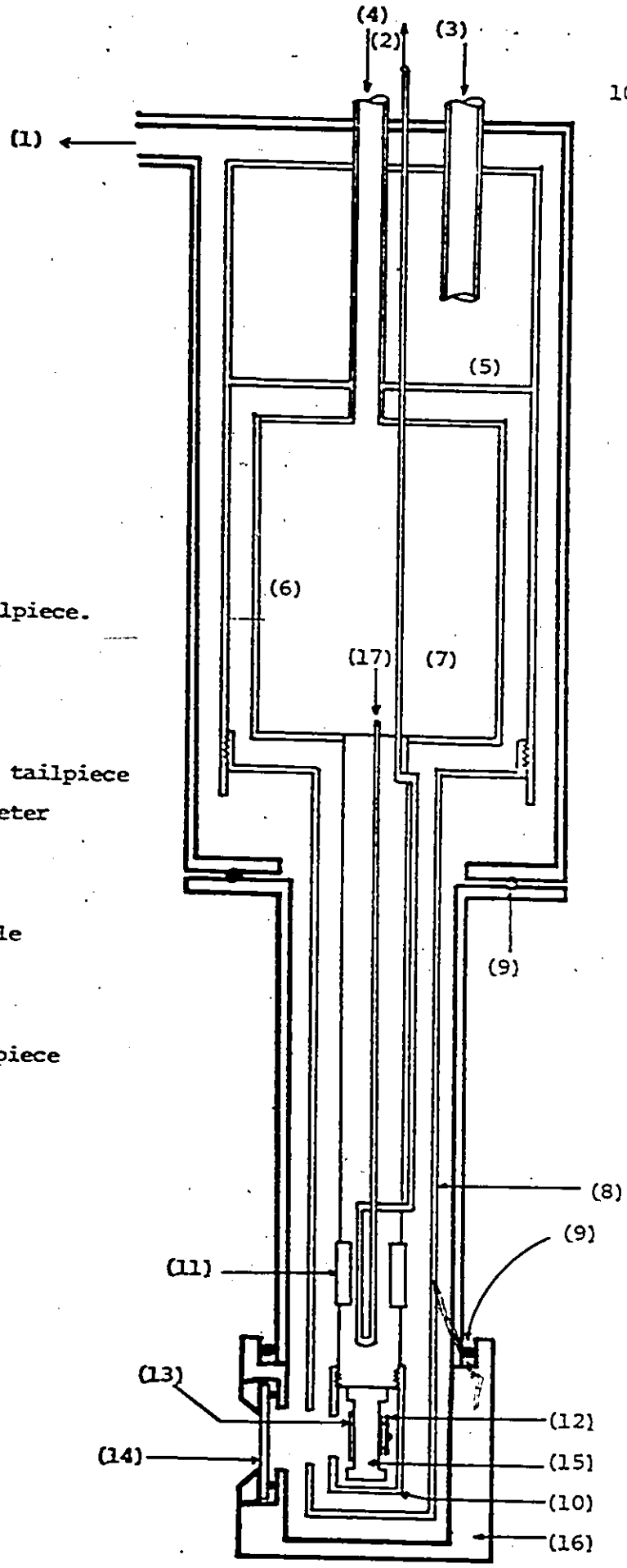

Figure 3-8. $He-N_2$ cryostat

Above the tip a small heater is mounted. By controlling the current through the heater, the tip can be brought up to room temperature. Under normal conditions 5 litres of liquid He are sufficient for an extensive run. Prior to precooling the Helium tank with liquid nitrogen, the system is evacuated to better than 10^{-5} mm Hg. Cryopumping due to liquid He will then greatly improve on the vacuum ($\sim 10^{-7}$ mm Hg).

The temperature of the tip is measured by a Cu wire resistor wound on a copper spool. The spool is fastened to the tip and it is in good thermal contact with it. The temperature at the tip is thus determined to an accuracy better than .5°K at liquid He and better than .1°K at liquid N_2. The Cu wire is of relatively pure commercial stock and it has been wound with particular care to avoid strains. To establish reliability in measurement, before calibration, the resistor was submitted to a few cooling down cycles. Care is always taken to avoid thermal shock. The advantage of this type of thermometer is its accuracy and reliability even over repeated temperature cycling, the care with which thermal contacts can be made to it and the simplicity in construction. (fig. 3.9). The thermometer was calibrated at 273°K, 77.4°K and at 4.2°K using Dauphinee's tables (1D54). His results were calibrated against two platinum resistance thermometers. These results were averaged (normalized) to his over the temperature range of interest. Disagreements between his tables and ours are less then 0.5 near4.2°K. (see table 3-1 and fig. 3-10).

Low temperature optical measurements have been a project with R. Glinski. He designed the Cu wire resistance thermometer. The author redesigned the cryostat for optical work.

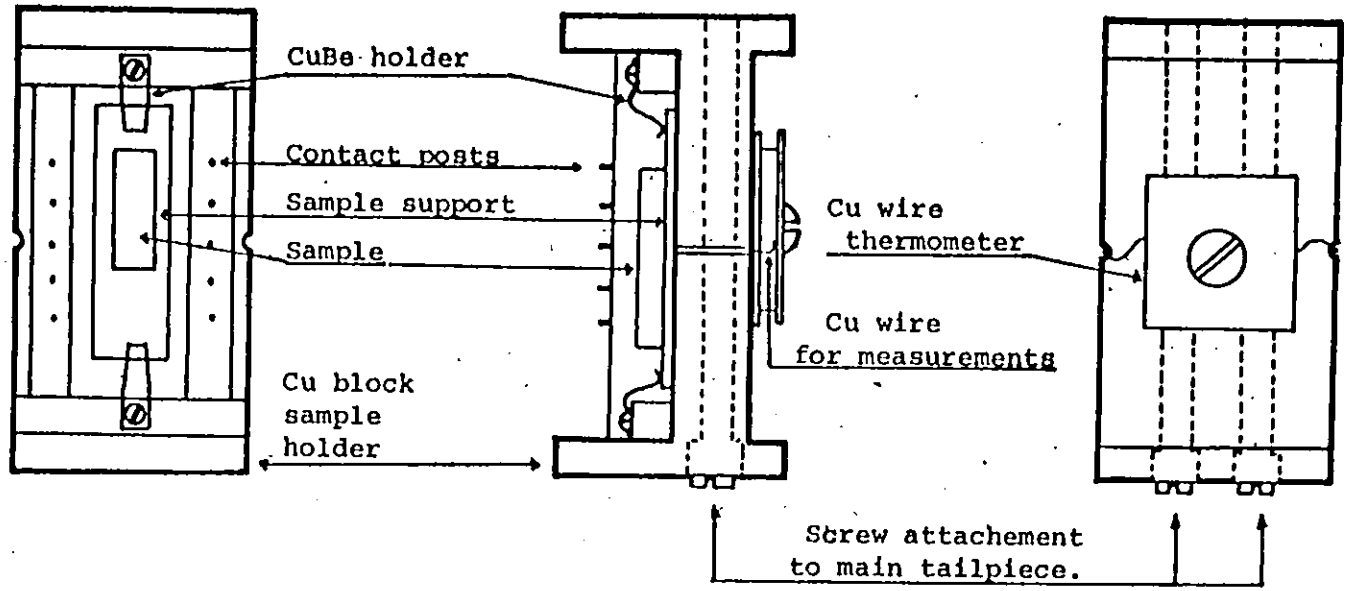

Figure 3-9 Detailed diagram of item 15 in fig. 3-8, the sample holder, Electrical contacts to the sample have not been drawn.

Figure 3-10. Showing Cu-resistor Thermometer calibration curve

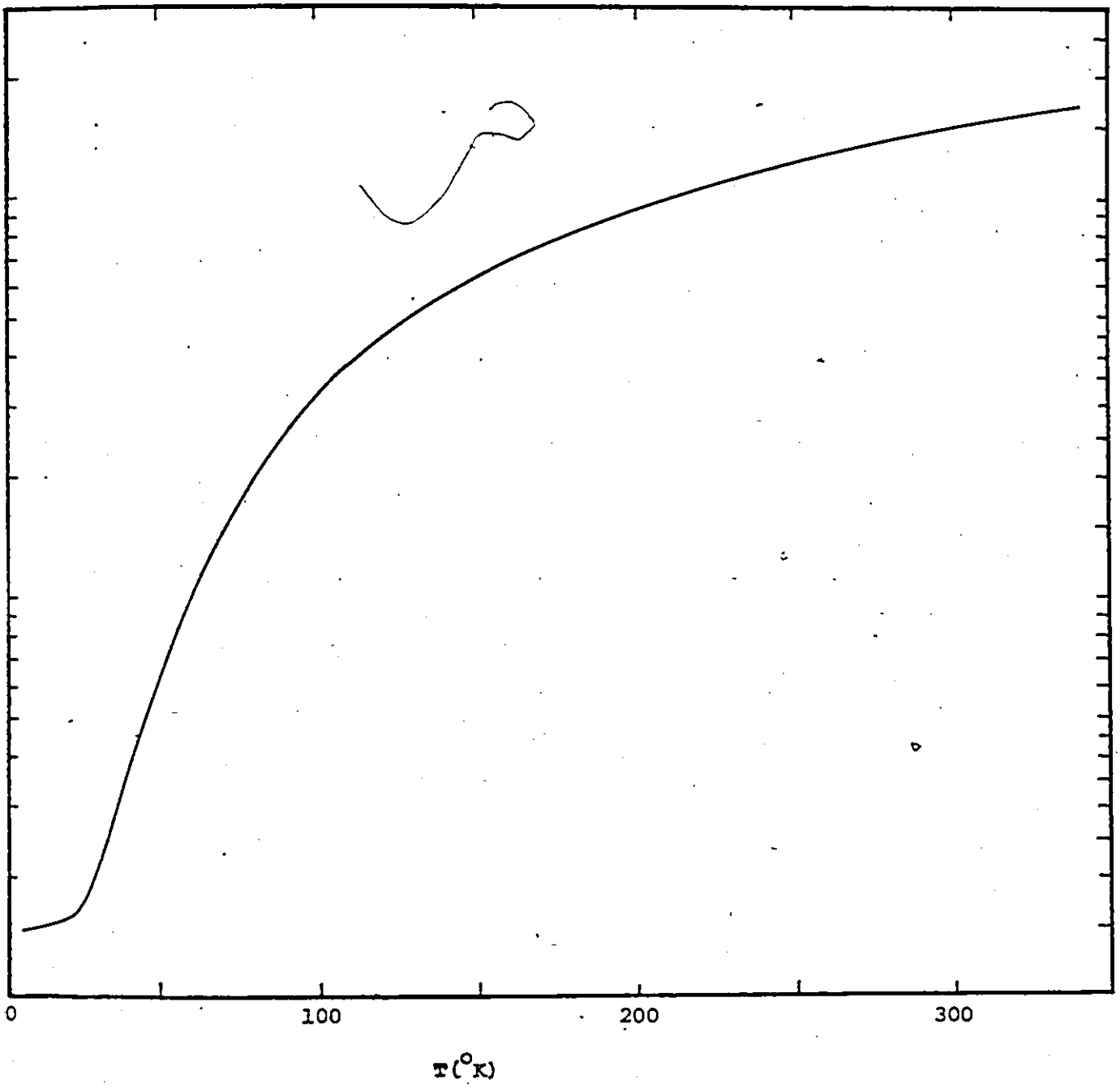

TABLE 3.1

TEMP (°K)	R(Ω)	TEMP (°K)	R(Ω)
4.2	1.48	68	13.43
19	1.56	72	15.40
20	1.58	76	17.54
21	1.605	80	19.685
22	1.64	85	22.49
23	1.67	90	25.365
24	1.71	95	28.29
25	1.76	100	31.245
26	1.81	110	37.24
27	1.87	120	43.26
28	1.94	130	49.28
29	2.01	140	55.285
30	2.10	150	61.255
31	2.19	160	67.185
32	2.29	170	73.10
33	2.40	180	78.97
34	2.52	190	84.80
35	2.65	200	90.61
36	2.795	210	96.39
38	3.12	220	102.15
40	3.47	230	107.89
42	3.88	240	113.62
44	4.335	250	119.32
46	4.865	260	125.03
48	5.42	270	130.71
50	6.025		132.50
52	6.675	280	136.38
54	7.37	290	142.06
56	8.125	300	147.74
58	8.92	310	153.15
60	9.75	320	159.075
64	11.51		

The MOS packages were mounted on the cryostat tip and the system was evacuated, precooled and then cooled near to 4.2°K. Electroreflectance measurements were done by the SBER technique with the same equipment as described in section 3-4b ii. The procedure is identical for each temperature measurement. Temperature is now an additional variable parameter.

3.6 SAMPLE PREPARATION AND MOUNTING.

The alloy systems under investigation are (GaAl)As, (In,Ga)As, In(AsP), In(As,Sb), Ga(As,P). The (InGa)As, In(AsSb) and the In(GaSb) systems were prepared by the horizontal Bridgeman technique (2W64). Ingots thus obtained display a compositional variation along their length (fig. 3-11). Slices are wire cut, cleaned and polished. The composition of these wafers is obtained from X-ray measurements (Debye-Scherner powder technique). More detailed information about the growth technique of these alloys is found in 1W68, 2W68, 1C69.

The EER sample mounting on a thin brass rod, flattened at one end. The sample is mounted on this flat portion with conducting silver point GC # 21-1. Most of the rod and the sample are covered with liquid tape GC # 176-21 to insulate the rod and the back of the sample from the electrolyte. The front reflecting surface of the sample is exposed to the electrolyte. The other end of the rod supports the unit and it acts as an electrical contact to the modulating oscillator. The electrolyte used throughout these experiments is 1:3 ≡ glycerol:H_2O. EER was done only on the (GaAl)As alloy system.

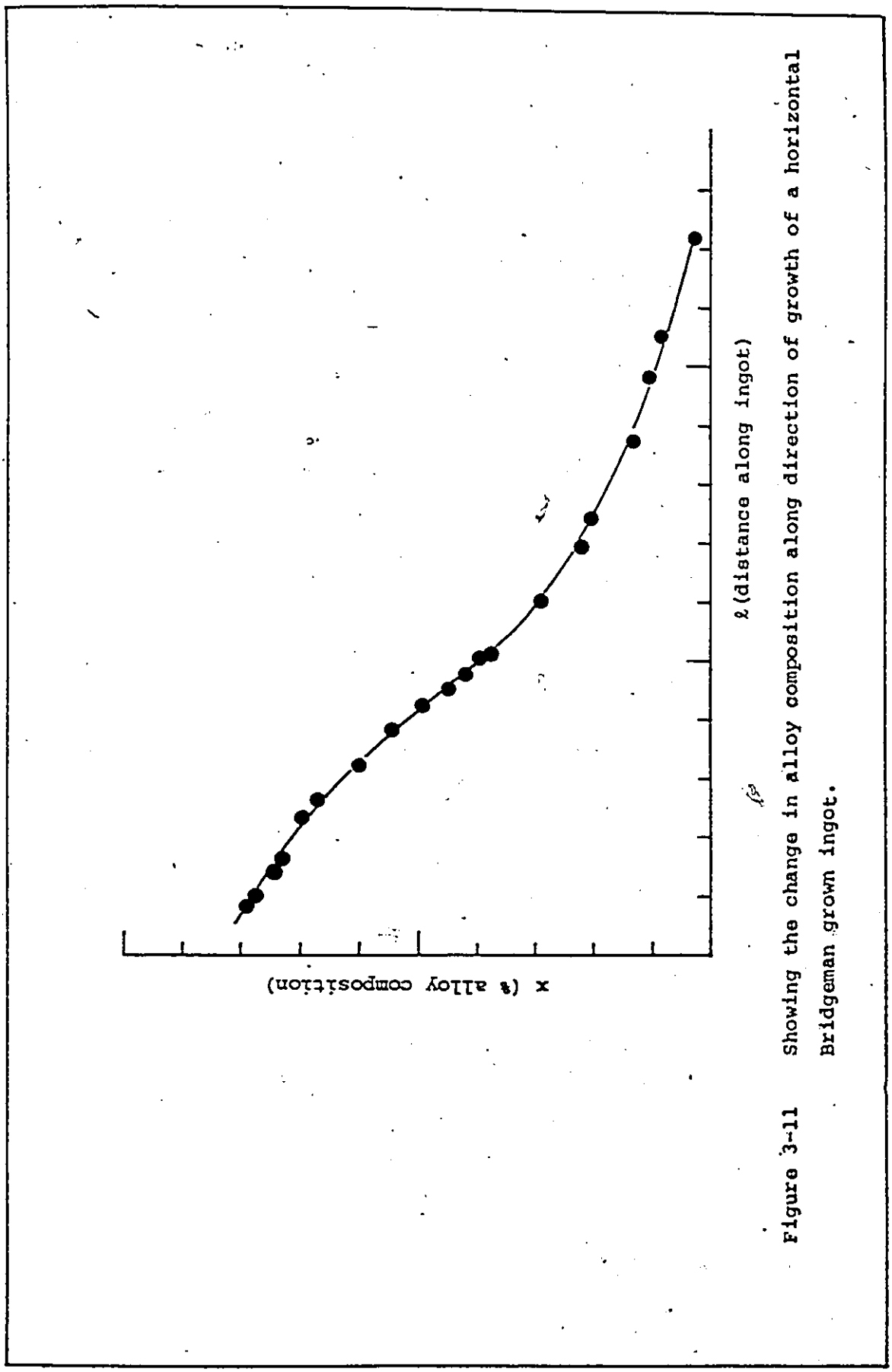

Figure 3-11 Showing the change in alloy composition along direction of growth of a horizontal Bridgeman grown ingot.

In the case of SBER measurements in the IR (300°K) and at low temperatures in the IR and visible, a metal-oxide-semiconductor configuration was used (fig. 3-12, sec. 3-8). In both cases, contact to the sample was made by annealing indium into the material. A thin gold wire is placed in the indium for electrical contact to the sample. The size of the sample permitting, two such contacts were mounted at two opposite points on the perimeter of the wafer. By measuring the resistance between contacts with the current flow in each direction, non-ohmic contacts can be rejected. The samples were then mounted on small Cu platelets with glyptol cement in the case of room temperature measurements. For low temperature the sample is mounted on a thin Ge slab with silicone white adhesive (Ge-DC29-8109S) and then the unit is again mounted with the same adhesive to the tail piece of the cryostat By running a temperature trial on a dummy specimen, with a differential thermocouple arrangement between the Cu-thermometer and the front surface of the sample, no detectable temperature gradient could be found between the sample and the thermometer. This indicates that for SBER, the temperature of the specimen is near to that measured with the Cu resistor thermometer.

Room temperature measurements of SBER were done with SiO as the transparent insulating oxide, while for low temperature measurements Al_2O_3 was used. The reason being that the linear coefficient of expansion of Al_2O_3 is considerably less than that of SiO. The thickness of the oxide, therefore the intensity of the field for the same applied voltage will not depend on temperature. Chronologically SiO layers were available

earlier and with better facilities, however as it will be discussed in the next sections, the superiority of Al_2O_3 layers eventually become of consequence and an equipment for the preparation of these layers was designed. (fig. 3-13).

Measurements with SiO were done with thicknesses of $\lambda/4$ $\lambda/2$ $3\lambda/4$ and λ ($\lambda \approx 5498\text{Å}$) as deposited by evaporation in a vacuum of better than 10^{-7} mm Hg. During the evaporation, the sample is rotated to assume a uniform film thickness. The consistency required within one alloy system meant that the same evaporation run should be done on all the samples of the same system. The accuracy in the film thickness is better than 7%. Some of the properties of these films will be discussed in the next section. The usual oxide thickness for the experimental runs was $\lambda/2$.

The SiO films are coated with a ~120Å thick 70% transmitting metal electrode (Inconel:76% Ni, 15% Cr, 9% Fe). The oxide and the electrode are evaporated in the same vacuum. The accuracy on the transmission of the film is 2%. The SiO and Ni film depositions were done in the Optical Lab section of the Applied Physics division of the National Research Center under the supervision of Mr. E. Cairns. A silver dot contact is then made with GC # 12-1 silver paint with a thin gauge gold wire. The two electrodes are then connected to the modulating voltage source.

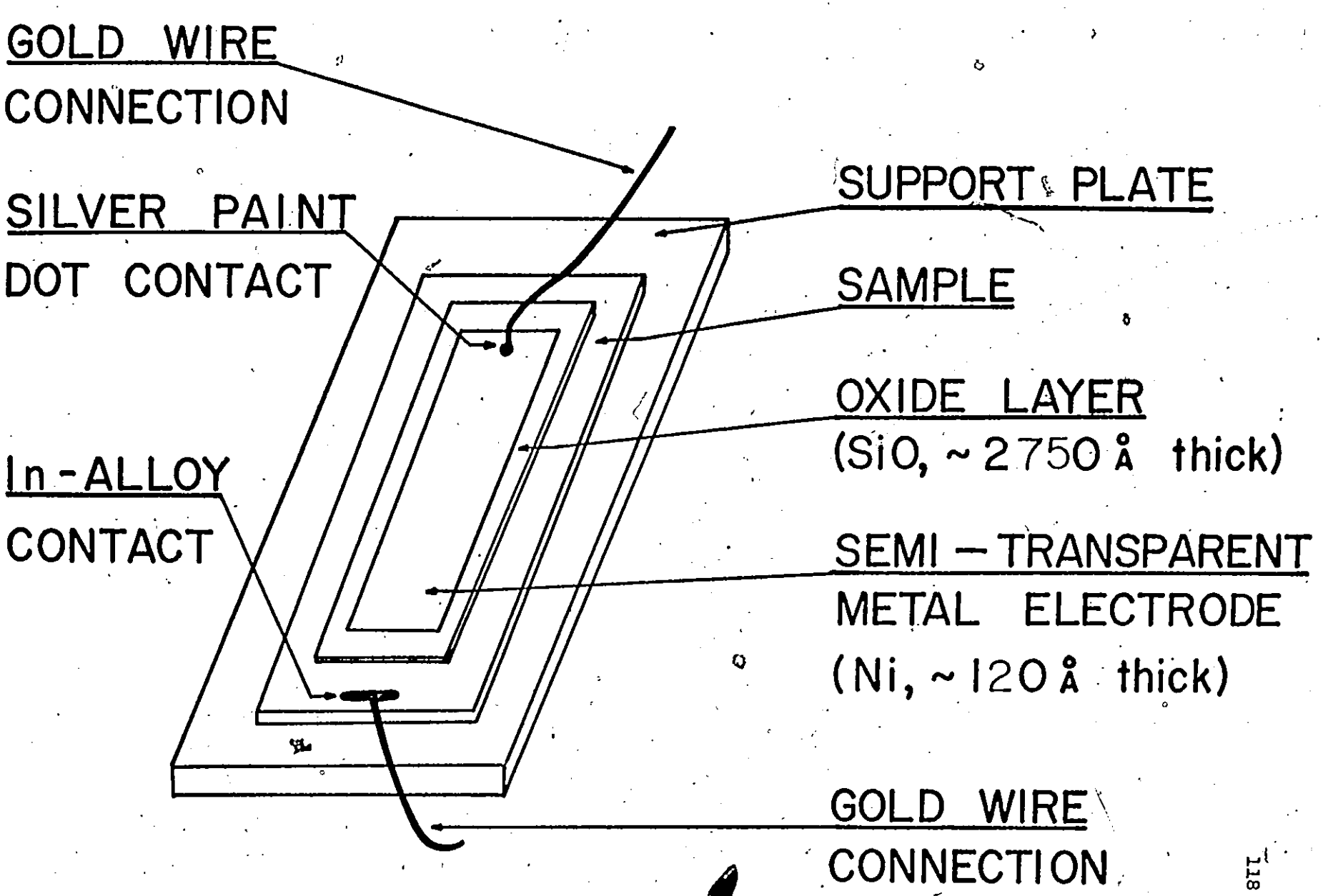

Figure 3-12 The M.O.S. Configuration

In the case of low temperature measurements Al_2O_3 was deposited by pyrolysis of aluminum propoxide. (4A67). The experimental setup is shown in fig. 3-17. Aluminum propoxide is fired at 160°C and it is carried by a dry N_2 stream to a region in the furnace at 420°C. At this temperature the propoxide dissociates and Al_2O_3 deposits on the surfaces exposed. By products of the chemical are carried out at the other end of the furnace. By controlling the nitrogen rate and the temperature of pyrolysis, Al_2O_3 oxide layers of different thicknesses and purity can be obtained. These properties will also be discussed in the next section. The problem at this stage is that no accurate control on the thickness of the deposited electrode is possible without a strenuous calibration of the influencing factors, and the use of a colour code for interference fringes. It is estimated that films vary between a thickness of 500Å to 2000Å. Ni film is then evaporated (50% transmittance) in a vacuum of $\sim 10^{-6}$ mm Hg. Contacts to the transmitting metal electrode are done by a silver dot on a small area where deposition of Ni was repeated. At low temperatures, a small amount of epoxy reinforced the contact or a conducting epoxy was used for the contact itself.

Prior to the deposition of oxide and electrode, each sample is etched and cleaned (see ch. 4 sec. 2). The desirability of clean optical surfaces by various methods of etching is discussed in the next section.

3.7 SEMICONDUCTOR SURFACES

In any reflectance measurement, the preparation of the semiconductor plays an important role when a subsequent interpretation of the measurements is needed. If the sample surface is to be representative of the material in question, the surface must be atomically clean. If proper measurements are to be obtained, the surface must be smooth and flat, so as to represent an air-semiconductor-interface which reflects all the radiation into the detector at a measureable angle of incidence.

The width of the interacting layer with the photon radiation depends on restrictive physical properties of the material such as a carrier concentration and absorption coefficient, as well as on the wavelength of the radiation.

Experimentally the closest to ideal conditions are cleaved surfaces prepared and measured under high vacuum. The formation of an oxide layer can alter the surface properties and the absolute reflecting power of the surface*. Unfortunately the materials dealt with here are usually polycrystalline and therefore they must be cut from ingots and polished. The abrasives and the oxide are then chemically removed. Often the mechanical stress created on the surface by polishing is also chemically removed when several atomic layers are etched away. However if the main interest is, as is the case in this work, to measure relative changes in energy as a function of composition, a systematic and consistent method of preparation is equally important.

* See appendix A2

As mentioned above, samples for electroreflectance are usually cut from lab. prepared materials (alloy ingots). The samples vary in size, depending on their origin. Usually both sides are mechanically flattened with SiC abrassive down to 5μ size. Subsequently one side is polished at high speed with alumina powders down to grid size 0.05μ . In(As,P) and Ga(AsP) samples (which were not cut from ingots but were obtained by a transport technique, (1R65) were prepared in oil based abrassives rather than water suspended abrassives to prevent phosphorus loss from the material. The (AlGa)As alloy system is not polished for the reasons given in (4.2)

Surfaces thus obtained are now chemically cleaned i.e. etched. Each type of material will respond with different effectiveness to the chemical solvent used. The ideal conditions are to avoid thermal shock on thin samples, to have a good etch rate control and to obtain oxide and deposit free surfaces. It is essential not to damage the optical surface (ie creation of etch pits and deformation of flat surfaces).

Etchants used for GaAs and GaAs rich alloys were usually $1H_2O_2:2H_2SO_4:3H_2O$ and for InAs and InAs rich alloys as well as for InSb rich alloys 1Br:10 Methyl Alcohol. The bromine etch was also used on phosphorus rich samples and InP, GaP. The washing of samples after the etch for the GaAs etch was done with water, the bromine etch is washed off by methyl and then ethyl alcohol. Particular exceptions to etching procedures or solvents will be discussed in Ch 4.

3.8 SOME PROPERTIES OF MOS DEVICES

Thin film techniques for electroreflectance have been first reported by R. Ludecke (2L68). As discussed before, many of the temperature and spectral range restrictions are removed and in principle can simplify the determination of the actual electric field applied. Measurements at 4.2°K have been reported on a CdTe - SiO_2 - SnO_2 configuration (1L67). The SnO_2 field electrode was chemically formed at 400°C on top of a 5000Å thick vacuum deposited dielectric (SiO_2). The suitability of materials for MOS devices is limited by the electrode and the oxide optical properties, adhesive capacity and on the etching procedure of the semiconducting material. Quantitative SBER measurements usually require the adjustment of the d.c. bias and a reasonable modulating frequency so that the effect of slow surface states can be eliminated.

The purpose of this section is to discuss the methods of preparation of MOS sandwiches and their properties.

There are several choices in technique and material to obtain a dielectric space between the sample and the Ni film electrodes: cementing a film of Myler or Saran Wrap to the surface (8S65 , 1F70); by centrifuging a dilute organic liquid photoresist (1P67) or polyesterene (1F71) dissolved in methyl-ethyl ; or a vacuum or otherwise deposited oxide (1W68, 2L68, this work). The disadvantages of the first method have already been discussed (8S65), and the coating of the semiconductor surfaces

with thin organic layers usually exhibits a spectral limitation at 4.5 eV.

At the time this project was started, several methods for the preparation of MOS devices had been attempted. Most of these involved technical difficulties which eventually affected the quality of the devices obtained.

The deposition of a dilute KPR film has been attempted by rotating the sample at a high speed. The lack of a dust free environment and low speed motors produced insulating layers of non-uniform thickness. Impurities on the surface produced discontinuities in the thickness of the layers at the contamination points. At such ultrathin points an eventual unrecoverable breakdown would occur when the electric field is applied.

The anodization of a semiconductor surface (2P67) in a 0.1N KOH solution produces oxide layers with breakdown voltages below appropriate electroreflectance fields ($10^5 \rightarrow 10^6$ Vcm^{-1}). The photovoltaic property of this type of device have been found very inappropriate for electroreflectance measurements.

Ludecke's work as well as some initial work by Williams and Rehn suggested that MOS sandwiches prepared with SiO_2 oxide layers with a semi-transparent Ni field electrode would be successful in giving reliable electroreflectance measurements.

SiO layers were evaporated on freshly etched semiconductor surfaces at the Applied Physics Division of the National Research Council. The Ni-alloy film field electrode was evaporated in the same vacuum at better than

10^{-7} mm Hg. The thickness of the oxides varied from $\lambda/4$, $\lambda/2$, $\lambda 3/4$, λ and the electrode film (~ 120Å thick) was ~70% transmitting. (λ = 5498Å).

When SiO is evaporated, the resulting vapor is comprised chiefly of single SiO molecules. Upon condensation, however, additional oxygen can be taken up if it is available, with the result that the condensed film can have any state of oxydation between SiO and SiO_2. It can be more generally expressed as SiO_x, where x can take values from 1 to 2. This variable has a greater influence on the optical properties of silicon oxide films than any other single factor. It can be controlled to some extent by the speed of evaporation since oxygen is present in any vacuum chamber. However if the partial pressure of oxygen is low in comparison to other residual gases, the greater absorption of these contaminants with very slow evaporations can cause undesirable characteristics such as sodium contamination and poor adherence (2K71).

A good film of SiO is obtained by fast evaporation at pressures below 10^{-5} mm Hg. Such films are recognized by their brownish colour (see table 3-2). The high U.V. absorption which is characteristic of SiO is shown in fig. (3-13). This absorption extends into the blue and accounts for the brown colour. An increased admixture of the SiO_x has been found to decrease the absorption in the U.V. If however the evaporation is done at an excessive temperature (above 1350°C) at low pressures, free silicon will be suspended into the glass and the small concentration of silicon in SiO will cause a greater absorption in the U.V.

The infrared transmittance and reflectance for a typical SiO film is shown in fig. 3-14. The strong absorption of energy $\sim 10\mu$ is characteristic of SiO layers. As x increases in the SiO_x admixture, this edge increases in energy, i.e. to $\sim 9\mu$.

The index of refraction n of SiO is ~ 2.0 as shown in fig. 3-13. However as the oxygen content of the film increases, this value decreases to that of SiO_2, (~ 1.5)

The evaporations at the NRC laboratories were done carefully, keeping these characteristics in mind. It is believed that in greater part SiO was deposited on the semiconductors we have done work with. However some slow oxidation through the thin metal electrode is unavoidable upon long-time exposure to the atmosphere. Indications are (4C71) that this process would be slow, if any at all.

The electrical contacts to the sample are made prior to etching and evaporation, by annealing indium with a 0.05 mm dia. wire contact on the edge of the sample (fig. 3-12). Non-ohmic contacts are rejected. Electrical contact to the Ni film is made with a small silver dot paint on the film surface and a thin (0.05 mm dia.) gold wire is immersed into it. A second Ni evaporation has often been found useful in the area where this contact is made. This protects the field electrode from the chemical solvents in the silver point. For low temperature work a 1:1 mixture of GE varnish and ethyl alcohol is applied over the silver point spot.

The Ni field electrode (70% transmittance) has a surface resistance

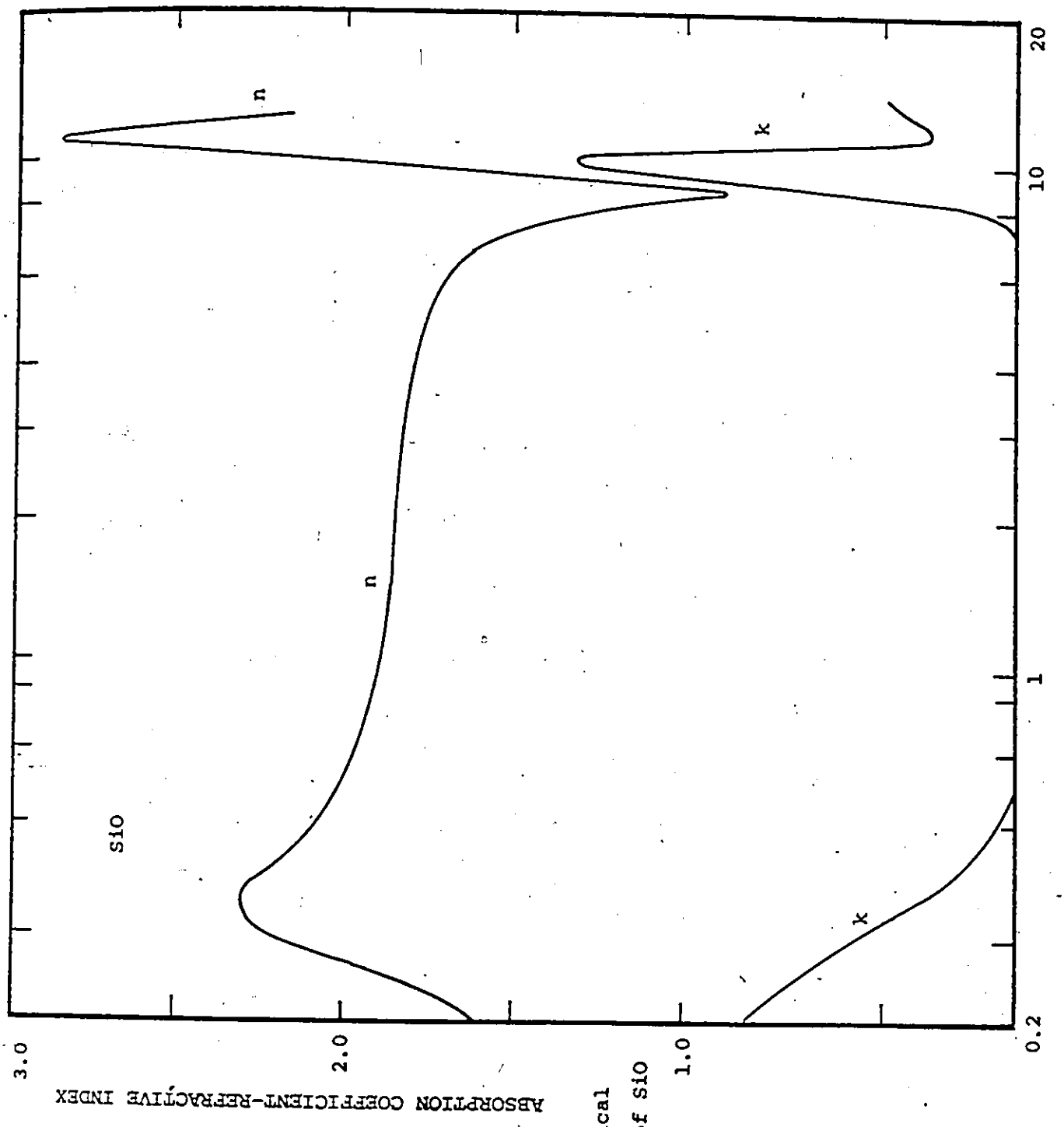

Figure 3-13 Optical constants of SiO

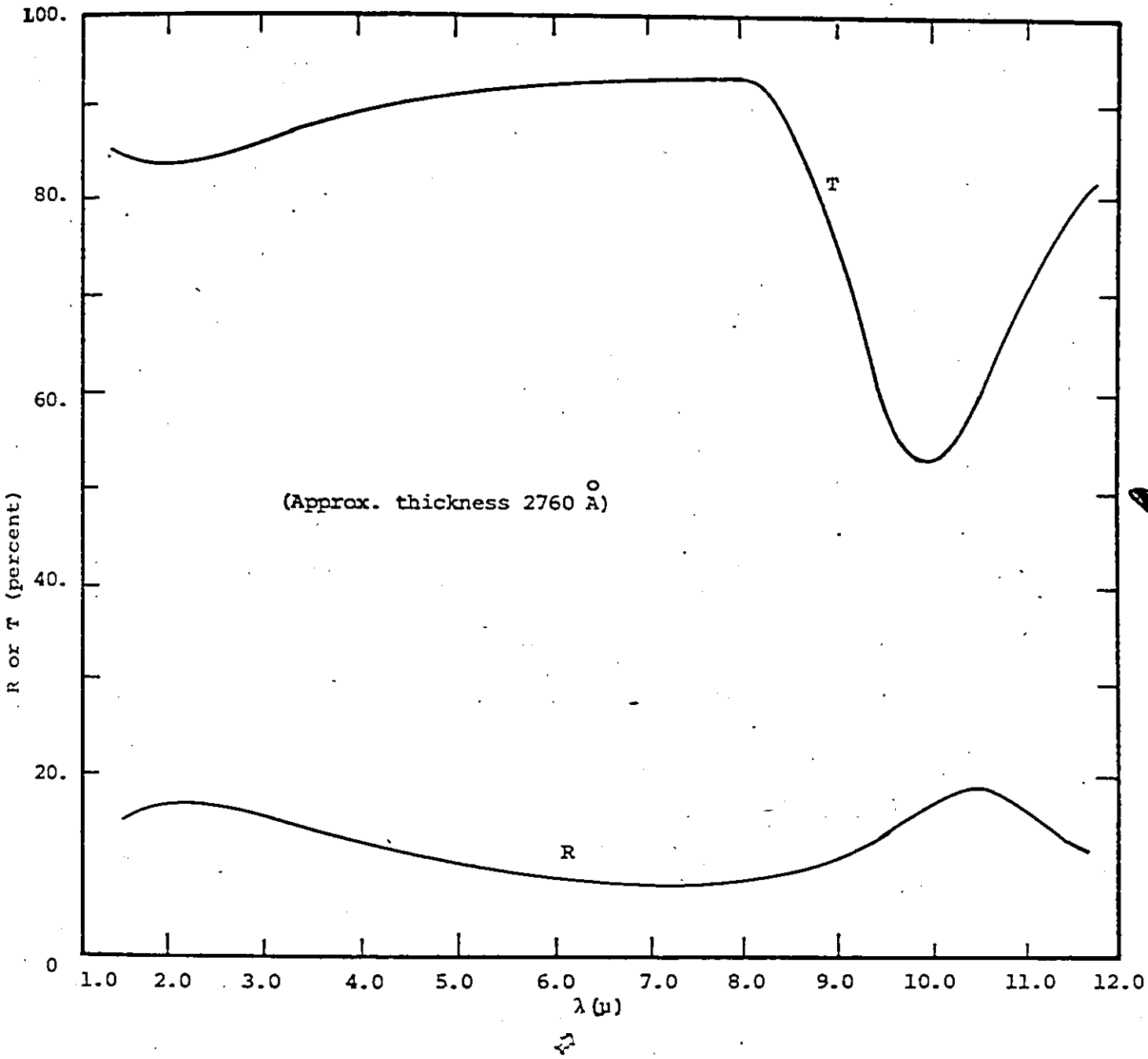

Figure 3-14 Infrared transmittance and reflectance for a typical SiO film.

of 10^3 to 2×10^3 Ω/cm^2 to insure an adequately uniform field over the oxide. The transmission of such a film is flat from $\sim.18\mu$ to 10μ. The optical properties of the field electrode lead to two effects which must be considered in SBER measurements. a) the non-zero absorption reduces the sensitivity by a factor of $(1-\text{absorb})^2$. Clearly with a 70% transmitting film we obtain a sensitivity loss of ~50%. b) The reflection of the incident beam by the nickel is also detected, so that $\Delta R/R$ is essentially smaller than the actual value. Since $R_{nickel} \sim .2 \rightarrow .3$, the reduction in $\Delta R/R$ can be significant when the semiconductor reflectance is small, (see appendix A-2).

The d.c. electrical behaviour of SiO dielectric films have been studied at 300^oK in a Ni - SiO - semiconductor capacitance configuration of varying surface area. The current voltage (I-V) characteristics were found to be reasonably symmetrical all the way to breakdown for oxides of $\lambda/2$ and λ thicknesses. Ohmic behaviour is observed over $-1. < v < +3.$ for λ and $\lambda/2$

This region of linearity and breakdown conditions, as well as noise at higher bias voltages are a function of oxide thickness (fig. 3-15). The low field resistance of the $\lambda/2$ layers is usually a few $M\Omega$ or more, at least five orders of magnitude above the resistance of the sample. Cooling to liquid nitrogen temperatures changes the thickness of the oxide layer, as the interference colour of the surface is seen to go through colour bands toward the violet. After breakdown the MOS is not recoverable,

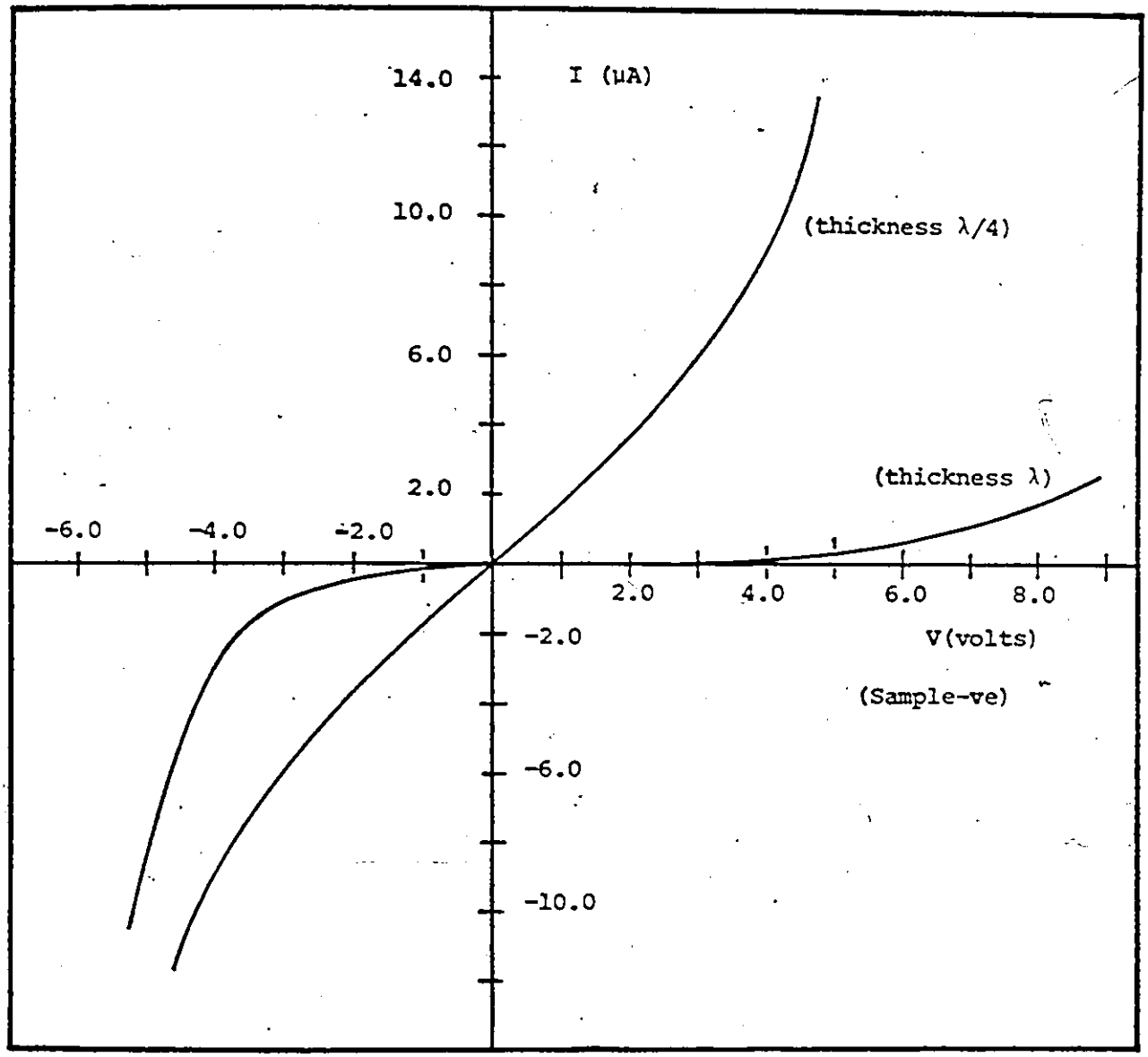

Figure 3-15. Diagram illustrating the effect of oxide thickness on the I-V characteristic of otherwise identical MOS sandwiches.

The change in I-V characteristics as a function of oxide thickness (fig. 3-15) may be attributed to contaminated surfaces as well as electrically active impurities (2K71, 1N71, 3K71, 3S72, 1F72). The effect of these impurities can be seen in fig. 3-16 where the I-V characteristics are seen to undergo a hysteresis type of behaviour (1K71, 3K71). It has been suggested by Nagosima (1N71) and others that Na^+ contamination results in ion implantation in the dielectric. The applied electric field results in a force on the ions creating a migratory effect and therefore the hysteresis. The time constant, ie. the ac response of these ions to the modulating voltage is considerably dampened at the working frequencies. Therefore it is believed that they have little effect on the ΔR signal. However, as it has been seen, it is important to achieve flat band conditions in electroreflectance measurements (2H68). Such slow states affecting the field at the oxide-semiconductor interface will screen the bias and clamp the average surface potential (8S67). It is therefore difficult to establish exactly flat band conditions for the MOS sandwiches in question. It is possible to study the I-V characteristics and to place the bias on the flat linear part of the curve. A proper combination of etching technique and bulk resistivity can give zero field at a semiconductor surface at near zero bias conditions (8S67). With most of the samples studied, although their I-V characteristics are not reproduced here, it was possible to achieve the above requirements.

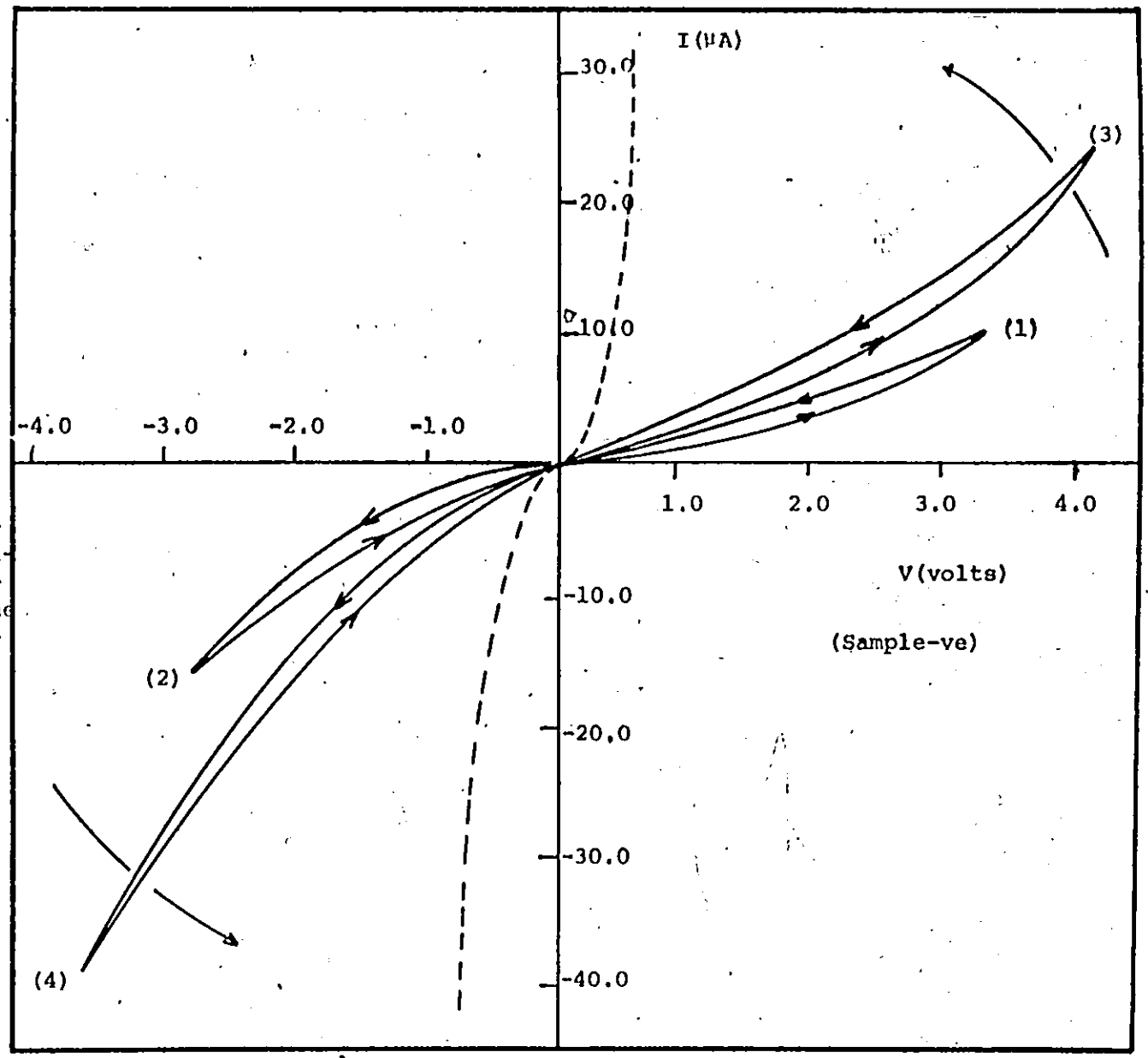

Figure 3-16.

Illustrating the hysteresis type phenomenon due to migratory implanted ionized impurities in the oxide during deposition.

It has been demonstrated by J.E. Fisher (1F71) that Al_2O_3 dielectric layers are superior to SiO_2 films for the following reasons: a) layers of Al_2O_3 exhibit greater breakdown field strength, with self healing properties, b) the oxide layer can be kept thin enough that accurate capacitance measurements are possible, c) a 200 Å Al_2O_3 film has good transmission properties, well above the 7 eV threshold of SiO_2; d) Al_2O_3 films exhibit a thermally dependent change in thickness far smaller than that for SiO_2.

However the preparation of Al_2O_3 layers represents various technical difficulties. They may be prepared by anodization of aluminium, plasma oxidation of aluminum films, by direct evaporation etc. Most of these techniques present drawbacks from one aspect or another. The pyrolysis of aluminum propoxide resulting in a thin Al_2O_3 layer was first suggested by Robinson (US Pat. 2,805, 965) and Deutcher (US Pat 2,972,555), and it is the most adequate method for III-V compounds promising no surface damages.

Initially aluminum propoxide is fired into a vapor form at 160°C from the melt by a gas of dry N_2 or O_2 gas. The carrying medium will later affect the breakdown properties and the optical properties of the oxide. The vapors are transported to a hot zone (420°C) where the propoxide is pyrolized and Al_2O_3 deposits on the exposed surfaces (fig. 3-17).

The parameters involved in the deposition of Al_2O_3 are the vapor pressure of aluminium propoxide, the deposition temperature, the total flow

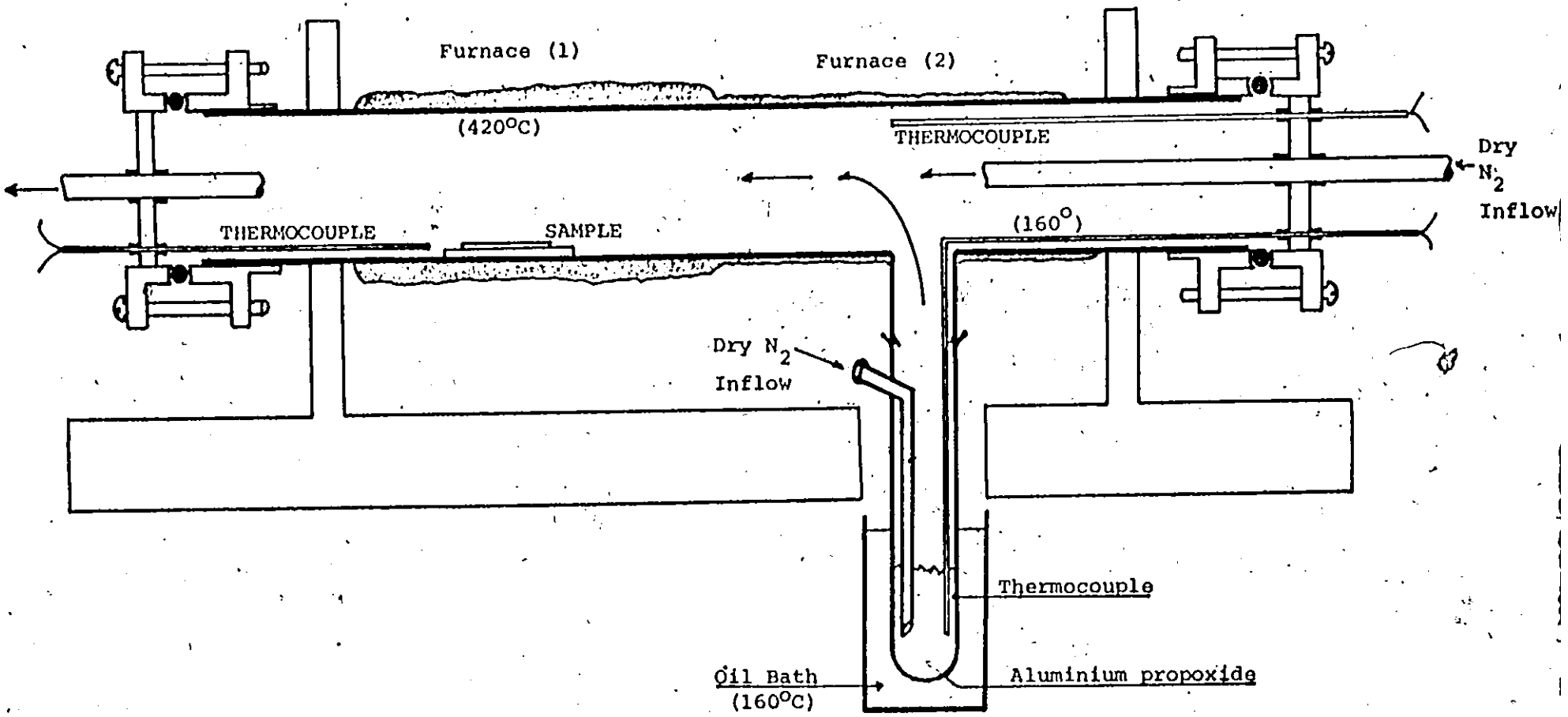

Figure 3-17: Aluminium propoxide pyrolysis equipment for the deposition of Al_2O_3 layers.

rate of the gas and the geometry of the sample position. The actual chemical process of pyrolysis is adequately dealt with by Aboaf (4A67) as well as J.E. Carnes et al (5C71) and D.A. Metha (1M72). Uniform coatings at intermediate gas rates and temperatures ($\sim 420^{\circ}C$) result in Al_2O_3 layers varying between 500Å to 2000Å. The I-V characteristics have been studied and ohmic behaviour was noted up to $\pm$ 5 V d.c.

The variation of the thickness across the surface of the sample depends on the pressure front of N_2 gas carrying the propoxide. The fringe characteristics and uniformity of colour indicate a fairly well controlled film thickness. (Table 3-2) shows the colour code of SiO_2 determining approximately the film thicknesses. The refractive index of Al_2O_3 is reported as being $1.600 \pm .004$ at $420^{\circ}C$. The dielectric constant is 7.7 (1F71). The growth rate at $420^{\circ}C$ and $\sim$10 ℓ/min N_2 gas rate gives an estimated oxide rate deposition between 50Å/min to 100Å/min. It has also been reported (1F71) that Al_2O_3 oxides enhance p-type surfaces for the semiconductors as opposed to n-type surfaces for SiO_2. The transmission properties of Al_2O_3 studied by Kyser et al. (1K69) show no structures from 7 eV to ~0.15 eV which may introduce SBER signals not due to the semiconductor.

Analogous hysteresis effects to the one observed in SiO have been reported for Al_2O_3 layers, indicating the presence of electron trapping in the case of vapor deposited dielectrics. (1M72). The films prepared in these laboratories have not shown any evidence of hysteresis in their I-V curves.

(4C71)

TABLE 3.2 Color chart for thermally grown SiO_2 films observed perpendicularly under daylight fluorescent lighting.

FILM THICKNESS (microns)	Order	COLOR AND COMMENTS
0.05		Tan
0.07		Brown
0.10		Dark violet to red-violet
0.12		Royal Blue
0.15		Light blue to metallic blue
0.17	I	Metallic to very light yellow-green
0.20		Light gold or yellow-slightly metallic
0.22		Gold with slight yellow-orange
0.25		Orange to melon
0.27		Red-violet
0.30		Blue to violet-blue
0.31		Blue
0.32		Blue to blue-green
0.34		Light green
0.35		Green to yellow-green
0.36	II	Yellow-green
0.37		Green-yellow
0.39		Yellow
0.41		Light orange
0.42		Carnation pink
0.44		Violet-red
0.46		Red-violet
0.47		Violet
0.48		Blue-violet
0.49		Blue
0.50		Blue-green
0.52		Green (broad)
0.54		Yellow-green
0.56	III	Green-yellow
0.57		Yellow to "yellowish." (Not yellow but is in the position where yellow is to be expected. At times it appears to be light creamy grey or metallic)
0.58		Light-orange or yellow to pink borderline
0.60		Carnation pink
0.63		Violet-red
0.68		"Bluish". (Not blue but borderline between violet and blue green. It appears more like a mixture between violet-red and blue green and over-all looks greyish).

CHAPTER IV RESULTS

4.1 INTRODUCTION

This chapter is concerned with the presentation of the experimental results obtained in this work. The results are obtained from some III-V compounds and their alloys by either EER or SBER in the vicinity of the fundamental gap at room temperature. Only one of these, (Ga,Al)As, has been investigated for high energy optical transistions above the gap. The behaviour for each transition as a function of alloy composition is illustrated graphically and a solid line is drawn through these representing a least-squares fit to the experimental points (eq 4-1). The coefficients of the quadratic eq (4-1) are given in Table 4-2 (page 184) and the quadratic coefficients are compared to the predicted values due to Van Vechten and Bergestresser whenever possible.

The second part of the results consists of some preliminary studies on IV-VI compounds and their alloys. The phase diagram of the (Pb,Sn)Se alloy system is investigated. It is shown that solid solubility over this alloy range only goes to some percentage of the rock-salt constituent.

Since no conclusive study of the metallurgical properties of (Pb,Sn)Se alloys and of the optical properties of the (Pb,Sn)Te alloys can be made at this time, a final analysis of the results presented is postponed to a later project. It was therefore found more appropriate to give these results as an appendix so as not to break the continuity between the results and the analysis.

4.2 NOMENCLATURE CONVENTION

In this section it is proposed to present room temperature results obtained on a number of alloy systems by either an electrolytic or a surface barrier electroreflectance technique. In order of presentation, the alloy systems studied are (Ga,Al)As, In(As,P), Ga(As,P), (In,Ga)As and In(As,Sb). The surface preparation and the procedure for measurement have been discussed in detail in the previous chapter.

Some of these systems are studied in detail over the majority of the available spectral region (7μ to 0.23μ). It might be simpler to indicate now the labelling convention adopted for the observable structures. This convention is the one due to Cardona (1C64). In fig. 2-2, a typical band structure for a III-V semiconductor is shown. The direct optical transitions E_o, $E_o + \Delta_o$, E_o', $E_o' + \Delta_o'$ around k = 0 involve transitions from the valence band to various conduction bands: E_1, $E_1 + \Delta_1$, E_1', $E_1' + \Delta_1'$ involve transitions from the valence band in the Λ direction to the conduction band. E_2, $E_2 + \Delta_2$ are in turn transitions from the valence band at the X point (100) and at the Σ point (110) direction (3W67, p. 132).

Table 4-1 shows the experimental conditions for the alloy systems studied. Table 4-2, at the end of sec. 4-7, shows the coefficient of the quadratic equation, where the observed data is least square fitted to it as a function of energy and alloy composition (see eq. 4-1, p.142). Whenever possible, results from other sources are given for comparison.

Table 4-1

System or Compound	Temp (^{o}K)	Method	Oxide electrolytic (oxide thickness)	n, carrier conc.	Bias (d.c.)	Mod. frequency and pk-pk volt	Etch
(GaAl)As	300	EER	3:10= Glyc:H_2O	$\sim 10^{16}$	-1.V	70Hz, 6 - 10V	-
In(AsP)	300	SBER	SiO ($\lambda/2$)	10^{16}-10^{17}	-1.V	80Hz, 1V	Br:CH_3OH
In(AsSb)	300	SBER	SiO ($\lambda/2$)	10^{16}-10^{17}	-1.V	80Hz, 2V	CP_6,Br:CH_3OH
(GaIn)As	300	SBER	SiO ($\lambda/2$, $\lambda/4$)	10^{16}-10^{17}	-1.V	80Hz, 1V	H_2O:H_2O_2:H_2SO_4
Ga(AsP)	300	SBER	SiO ($\lambda/2$)	10^{16}-10^{17}	-1.V	80Hz, 2V	CP_6,H_2O:H_2O_2:H_2SO_4
GaAs	4.2	SBER	Al_2O_3 ($\lambda/2$)	10^{15}	+.05	80Hz, 1V	H_2O:H_2O_2:H_2SO_4

4.3 (Ga,Al)As:

The samples used in this work were provided by Dr. M. B. Panish and Dr. H. C. Casey Jr. A detailed description of the preparation and growth is given elsewhere (1P69, 2P69). The samples were grown on n-type GaAs single crystal substrates by liquid epitaxy, and the composition of the epitaxial layers were determined by electron beam microprobe analysis.

The electroreflectance specimen were in the shape of small discs about 5 to 7 mm in diameter. It was found possible to carry out EER measurements without etching the specimen used. Etching was avoided for three reasons, viz., a) with the epitaxial layers any composition gradient along the direction of crystal growth ($\perp$ to the reflecting surface) would result in a change of surface composition; b) the complete alloy sample could be removed in case of thin epitaxy samples; c) etching solutions are usually water based and AlAs is hygroscopic: etching would result in damage to the sample. The homogeneity of the unetched surfaces was checked by comparison of data obtained at various points on the surface.

Measurements were made on a bulk sample of GaAs (fig. 4-1) and the alloys (epitaxy samples) with composition ranging up to 75% AlAs. In fig. 4-1, Onton's (1O70) EER results on AlAs are also shown. The curves of $\Delta R/R$ against photon energy in the vicinity of the gap are shown on fig. 4-2 and 4-3 for a number of alloy samples. The lineshape of the GaAs spectrum, which is in good agreement with results by

Thompson (2T66) for the values of E_o and $E_o + \Delta_o$, is used to identify the peaks above the fundamental gap over the whole alloy range.

The dependance of these structures on alloy composition is shown in fig. 4-4. A detailed representation of this dependance for E_o and Δ_o are seen in figs. 4-5 and 4-6. In fig. 4-5 the dependance of E_o on x is shown together with results from various other workers (2B66, 1K66, 1P69, 1O70). It is seen that the present data is in reasonably good agreement with those of Casey and Panish (1P69) obtained on the same samples. Results from absorption and diode emission (2B66, 1K66) fall consistently below the present results. Combining results from Casey and Panish with the present data, the values of E_o and x corresponding to the direct-indirect transition are found to be at 1.90eV and $x = 0.35$ respectively (as compared with 1.92 eV and $x = 0.37$ found by 1P69).

In figs. 4-5,4-6 the typical quadratic dependance on alloy composition of the E_o, $E_o + \Delta_o$ and Δ_o parameters is seen.

The optical structures observed above the fundamental gap are seen in fig. 4-7, 4-8 and are labelled as peak #3 for $E_1(1)$, #4 for $E_1(2)$, #5 for $(E_1 + \Delta_1)(1)$ #6 for $(E_1 + \Delta_1)(2)$, #7 for E_o', #8 for $E_o' + \Delta_o'$ and #9 for E_2. In other words, with the use of results on GaAs shown in fig. 4-7 the most obvious high energy transitions are identified over the alloy range (fig. 4-9).

Since no AlAs sample was available for the present work, the values observed by Onton (1O70) for AlAs (fig. 4-1) are plotted in fig. 4-9. In the case of the E_1 complex (peaks 3-6) it is not as clear

as with the E_o and $E_o + \Delta_o$ which peaks correspond exactly to the band gap at the Λ transition. Since we are mainly interested in the relative variation of transition energy with x, the whole E_1, $E_1 + \Delta_1$ complex has been considered. Peaks 7, 8 and 9 are identified from the GaAs results as the E_o', $E_o' + \Delta_o'$ and the E_2 transitions. Curves 3 to 6 are also seen to exhibit the parabolic dependance on composition (3V70) and can be fitted together with the experimental results for E_o, Δ_o and $E_o + \Delta_o$ to a parabolic relation of the form

$$E = a + bx + cx^2 \qquad (4\text{-}1)$$

where x is the alloy composition, E the energy. The value of the bowing parameter c can be found from experimental points and used to least-squares fit (eq 4-1). The solid lines in the diagrams of energy vs x throughout this chapter represent the results from the last squares fit to the experimental values. The value of the bowing parameter c can be compared with the predicted values by Van Vechten and Bergestresser (3V70). These, with the experimental values are plotted in Table 4-2 (page 184). Fig. 4-10 shows the dependance of $\Delta_1 = (E_1 + \Delta_1)(1) - E(1)$ with alloy composition. Its alloy behaviour is seen to resemble that of previously studied alloy systems (fig. 5-1) as the only band structure parameter so far, whose c value is -ve.

In the case of the E_o' and $E_o' + \Delta_o'$ peaks (7, 8) the structures are seen to be small in size (fig. 4-8, 4-9) as well as considerably wide. There is a subsequent inaccuracy in the determination of the transition energies. In addition, there is some uncertainty in

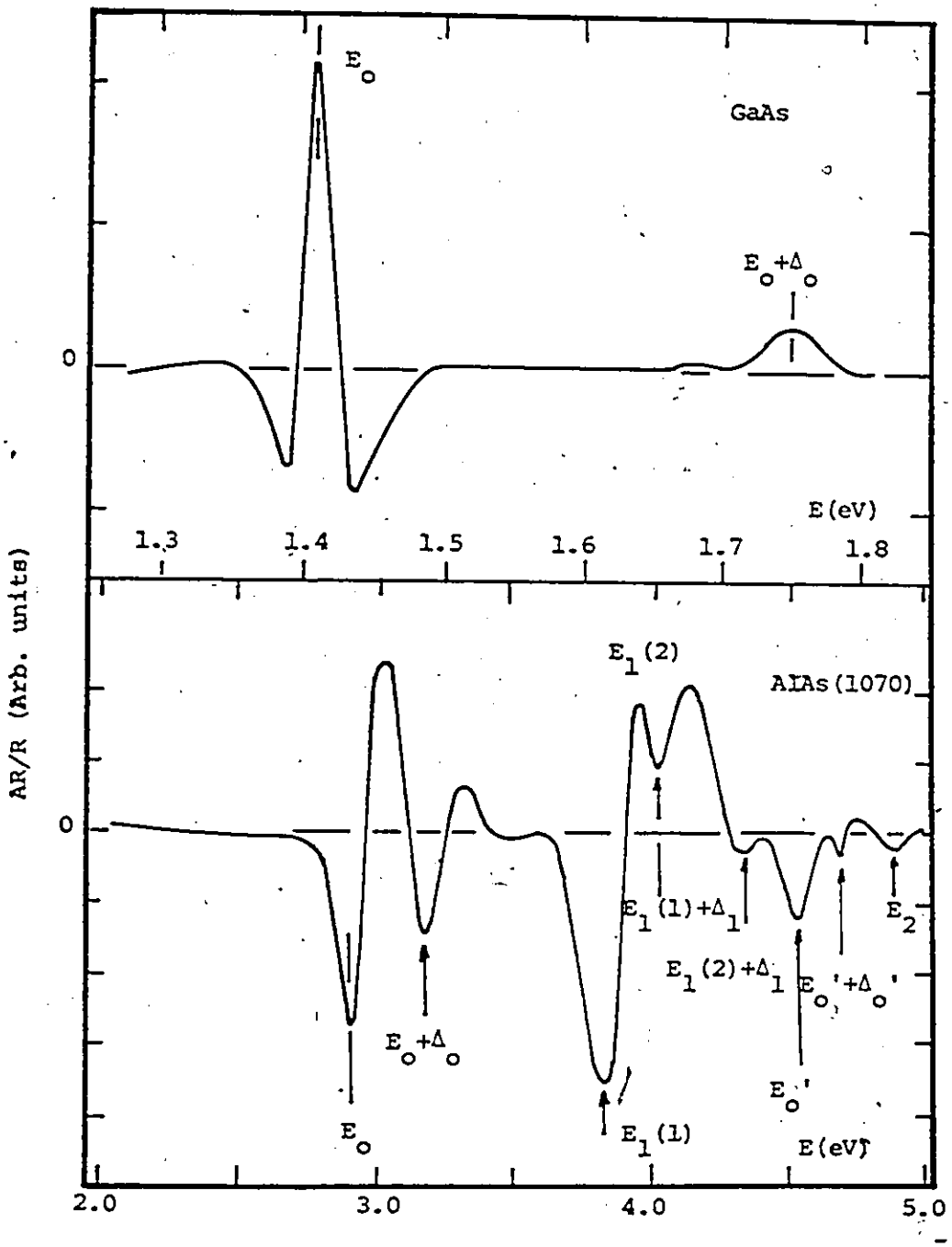

Figure 4-1 The electroreflectance spectra for GaAs (this work) and Onton results on AlAs (1070).

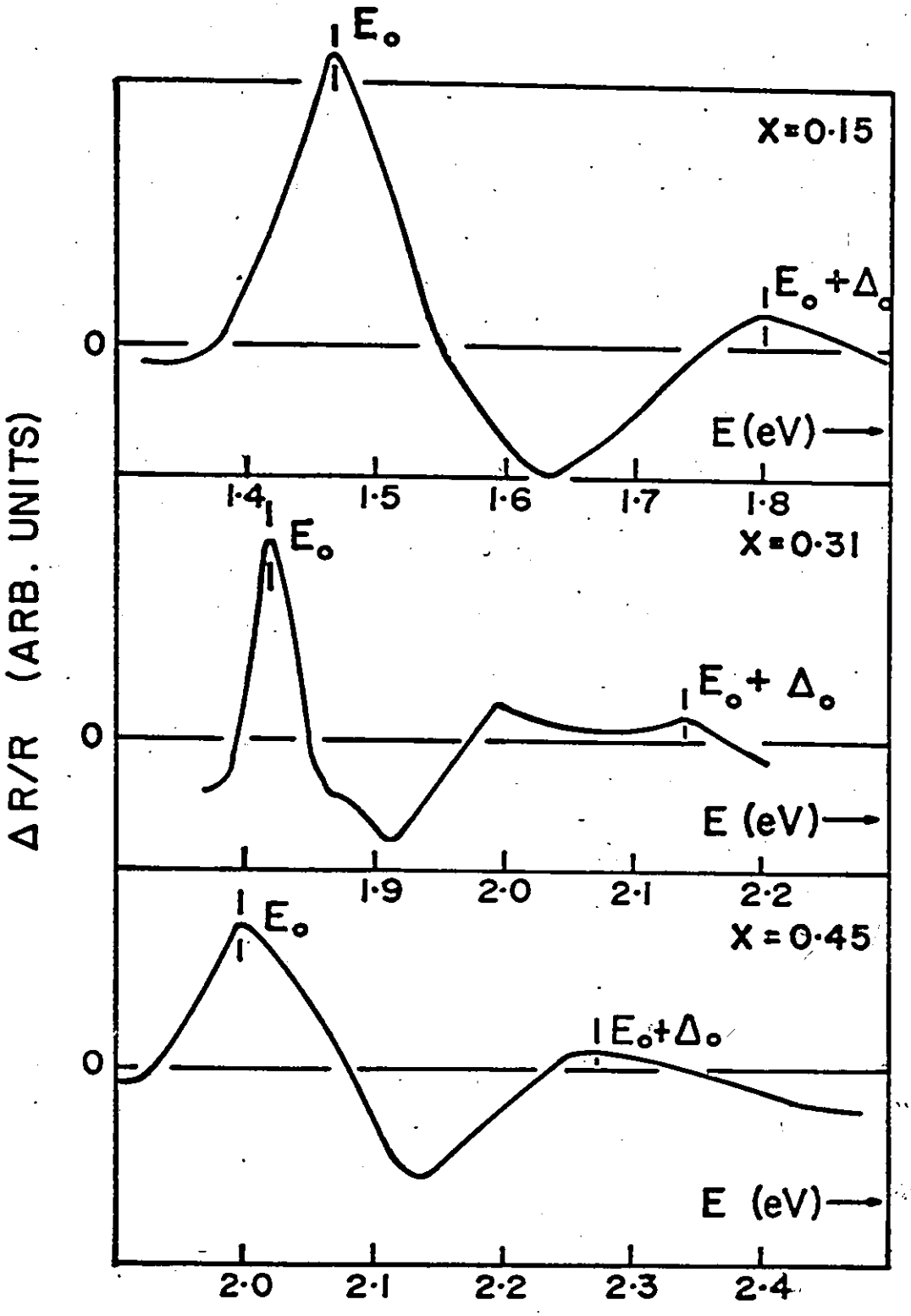

Figure 4-2. The electroreflectance results on the (GaAl)As alloys.

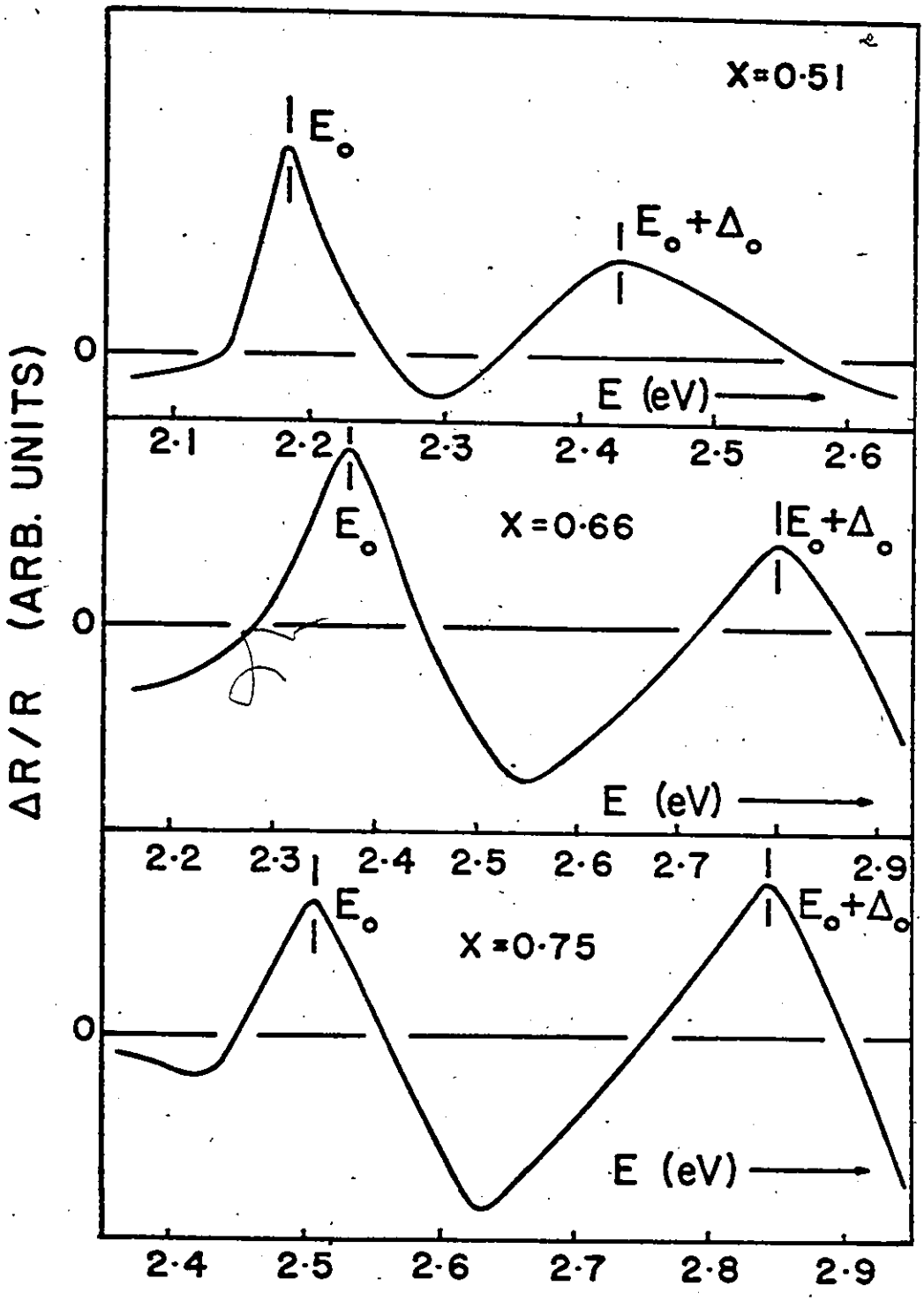

Figure 4-3 The electroreflectance results on the (GaAl)As alloys.

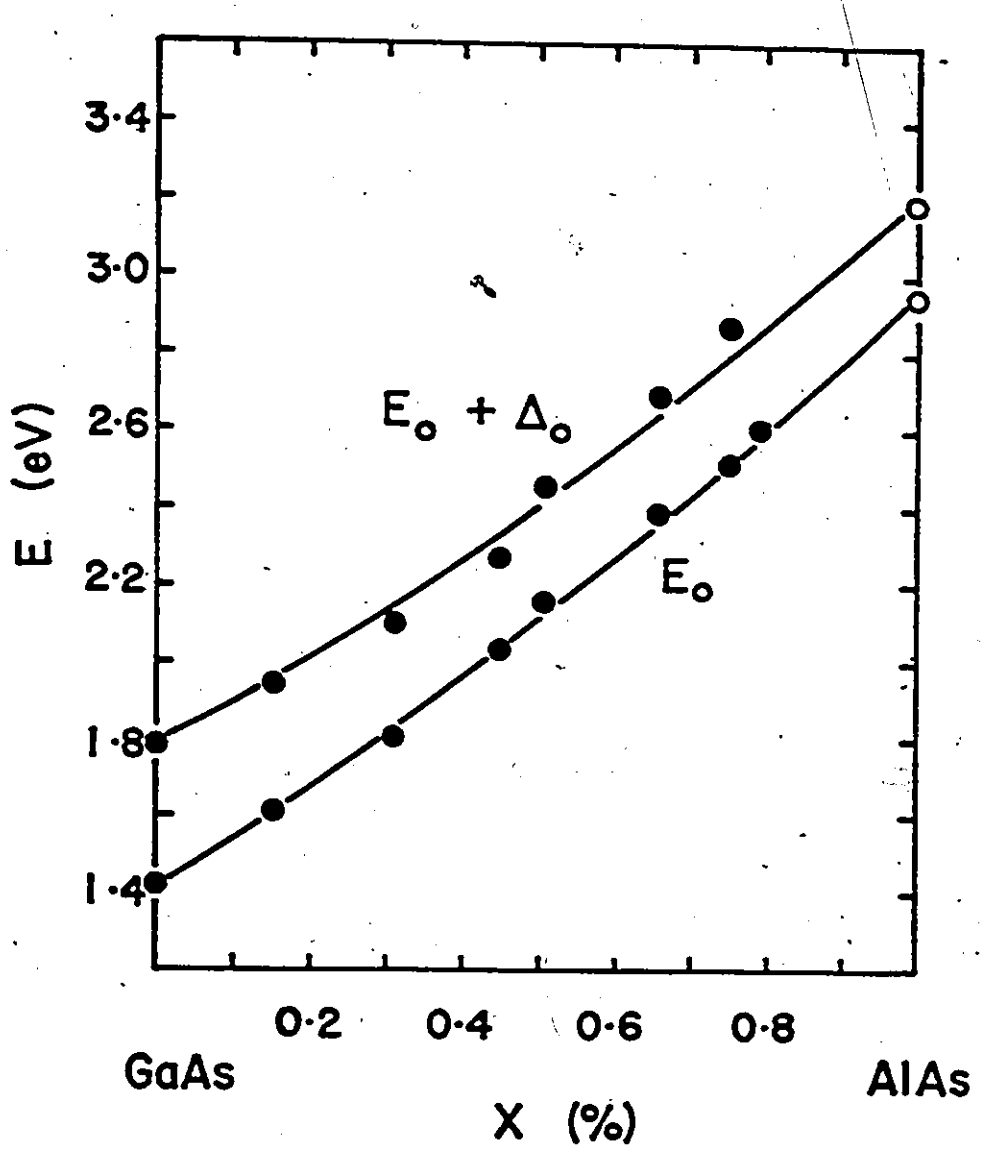

Figure 4-4. The dependence of E_o and $E_o + \Delta_o$ on alloy composition, (o) are from (1070).

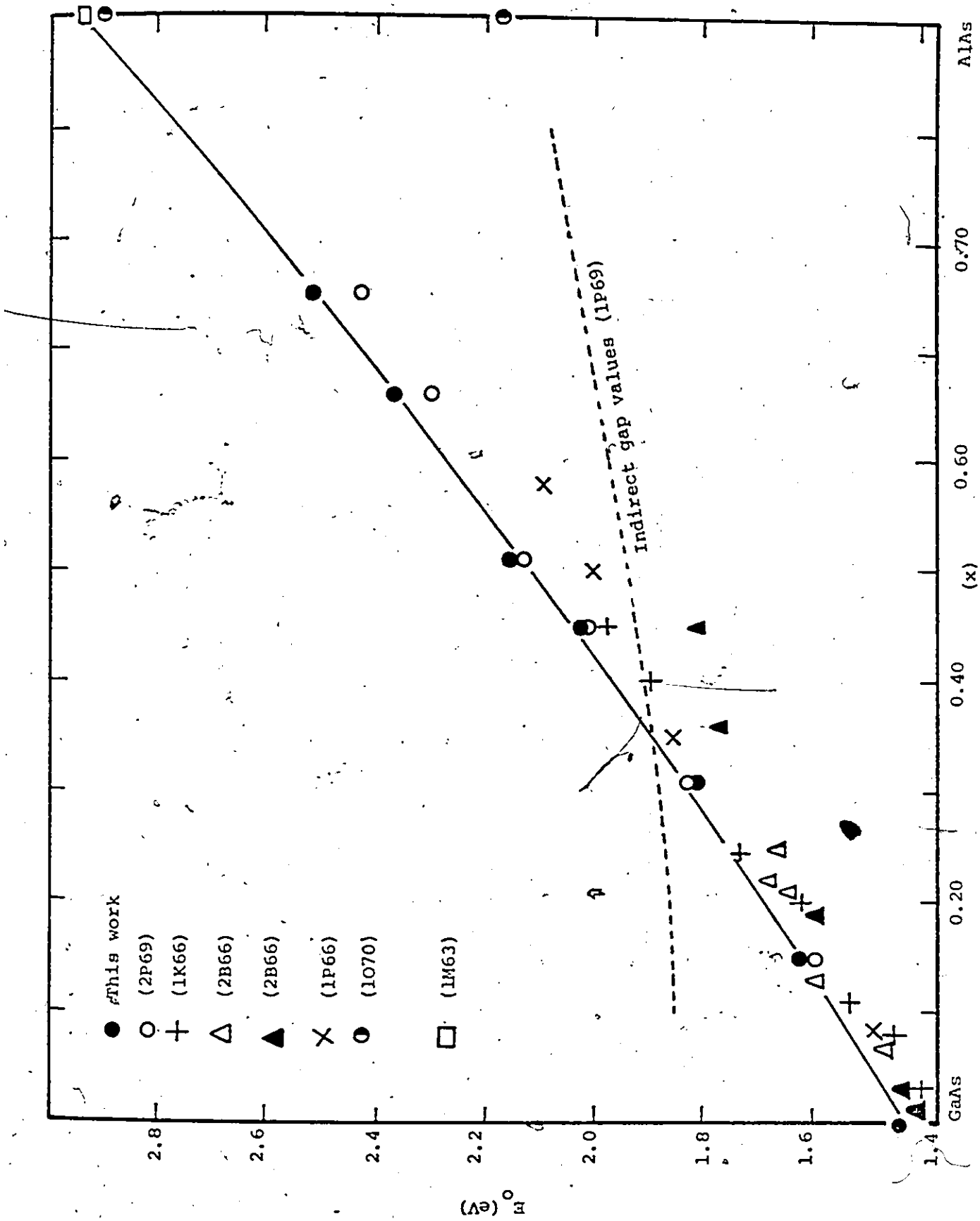

Figure 4-5. Alloy dependence of E_o as compared to results by other workers

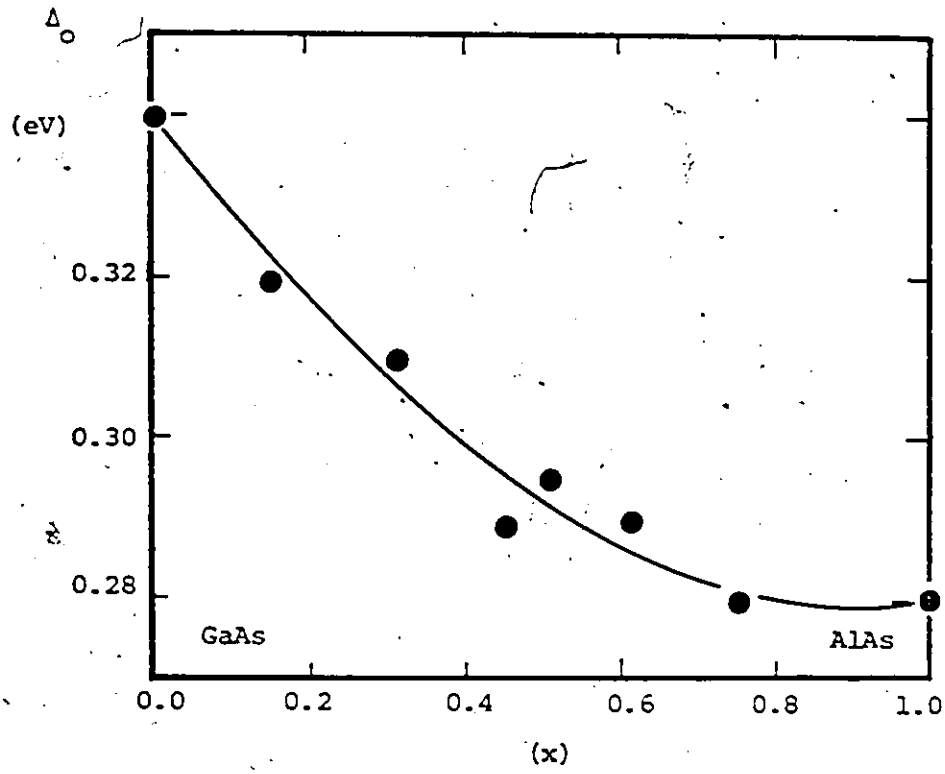

Figure 4-6. Δ_o dependence on alloy composition.

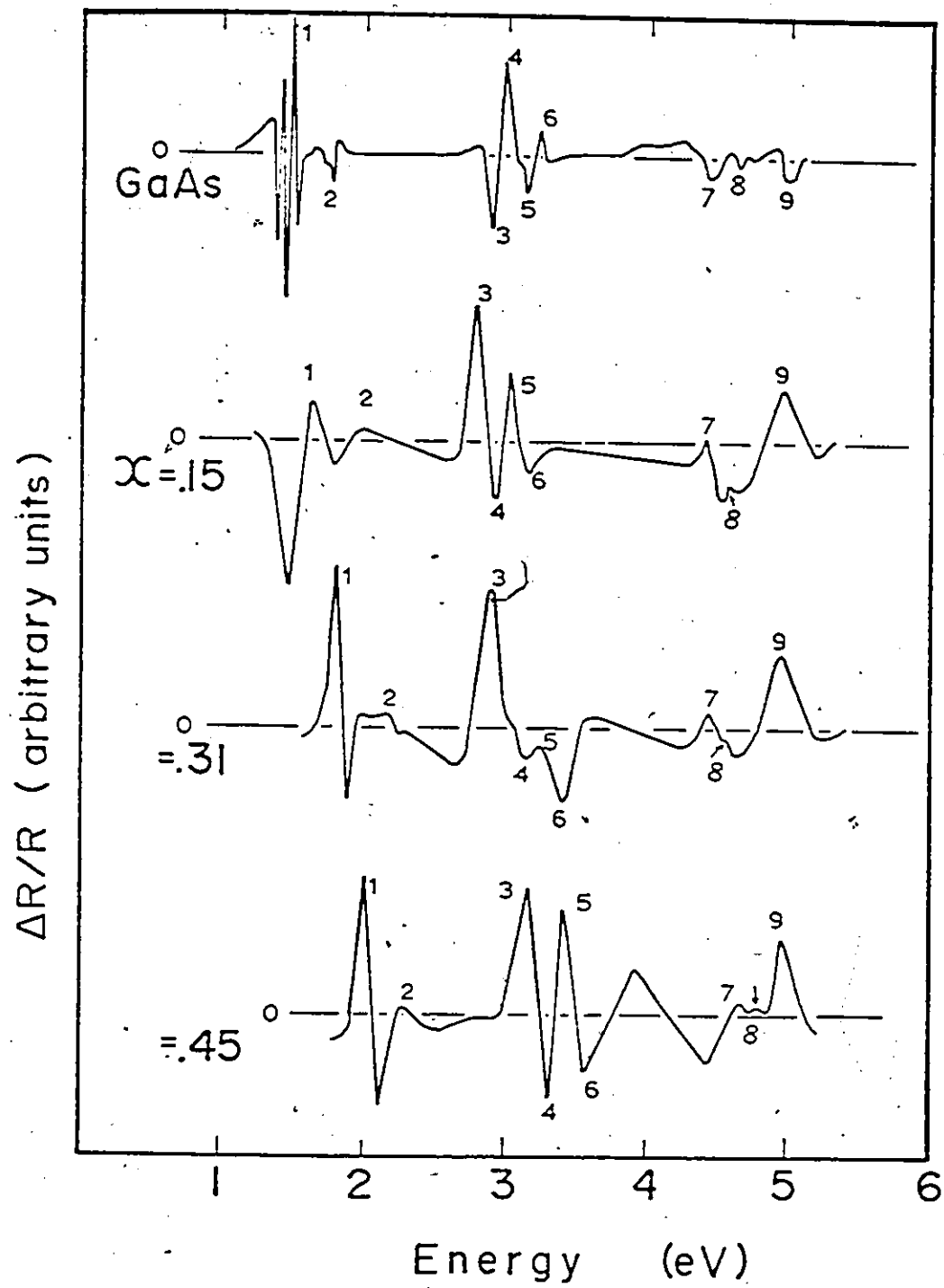

Figure 4-7. The electroreflectance results on the (GaAl)As alloys.

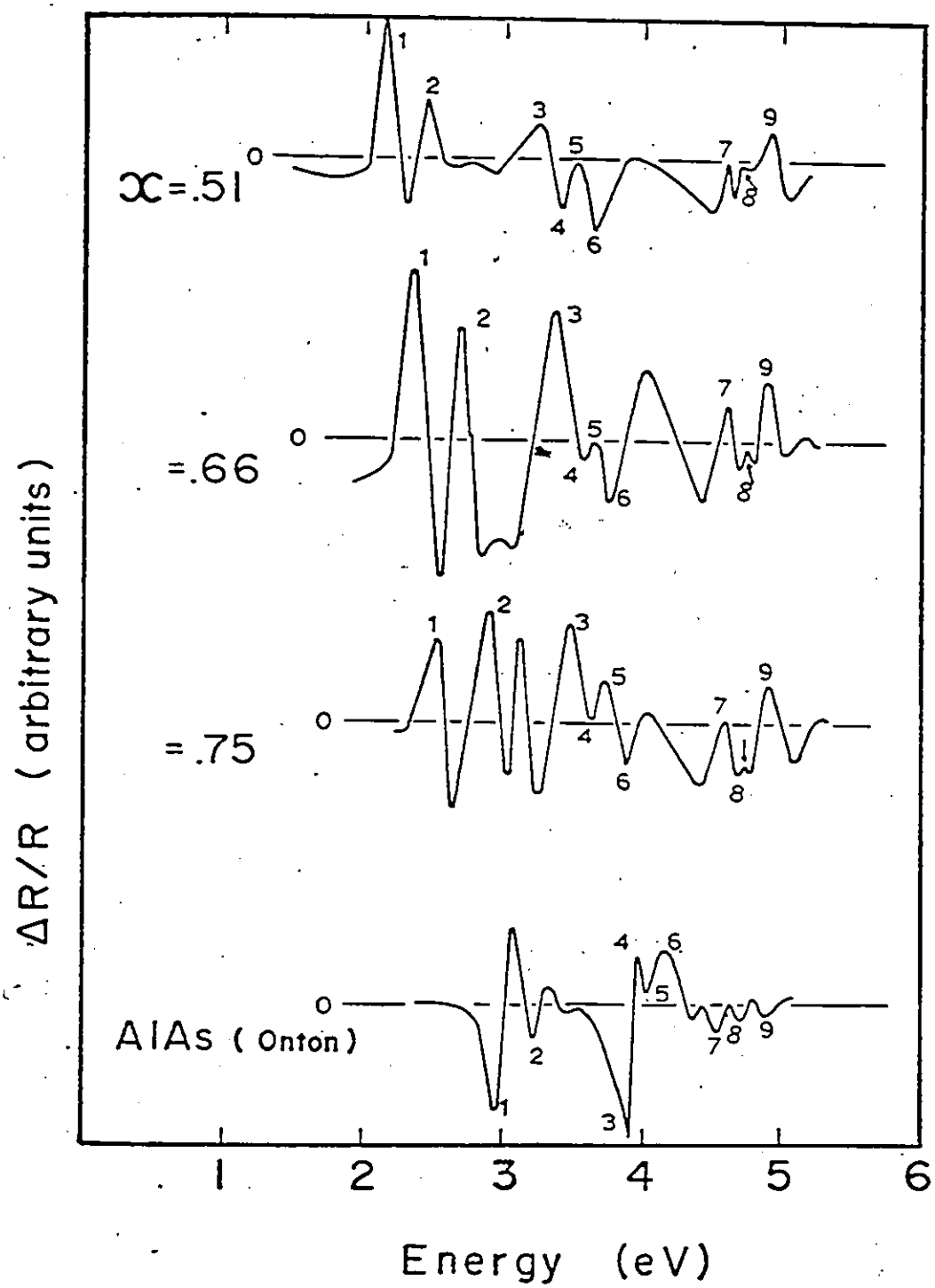

Figure 4-8. The electroreflectance results on the (GaAl)As alloys.

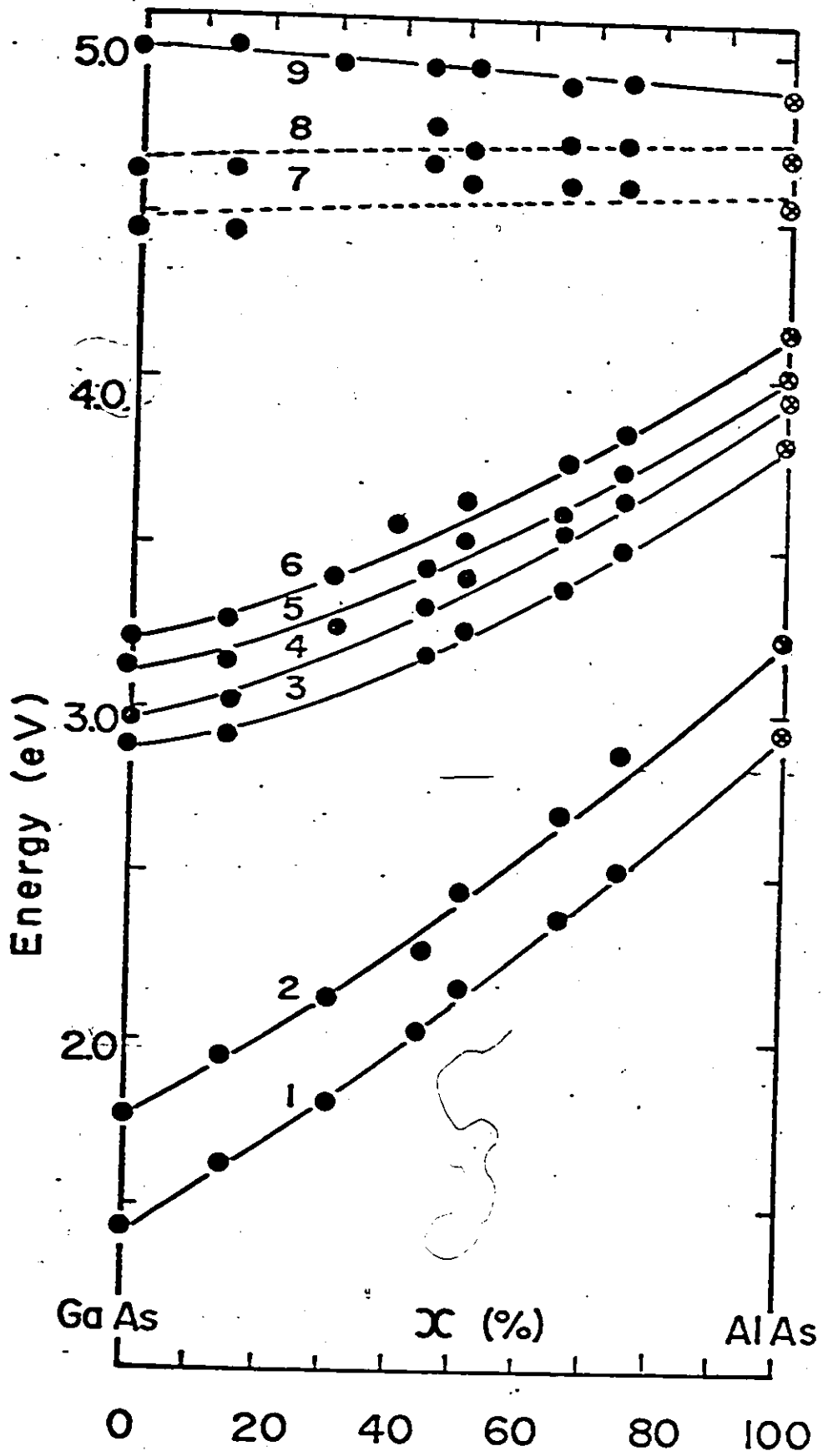

Figure 4-9. The variation of various energy transitions as a function of alloy composition (for the identification code # 1 to # 9 see text).

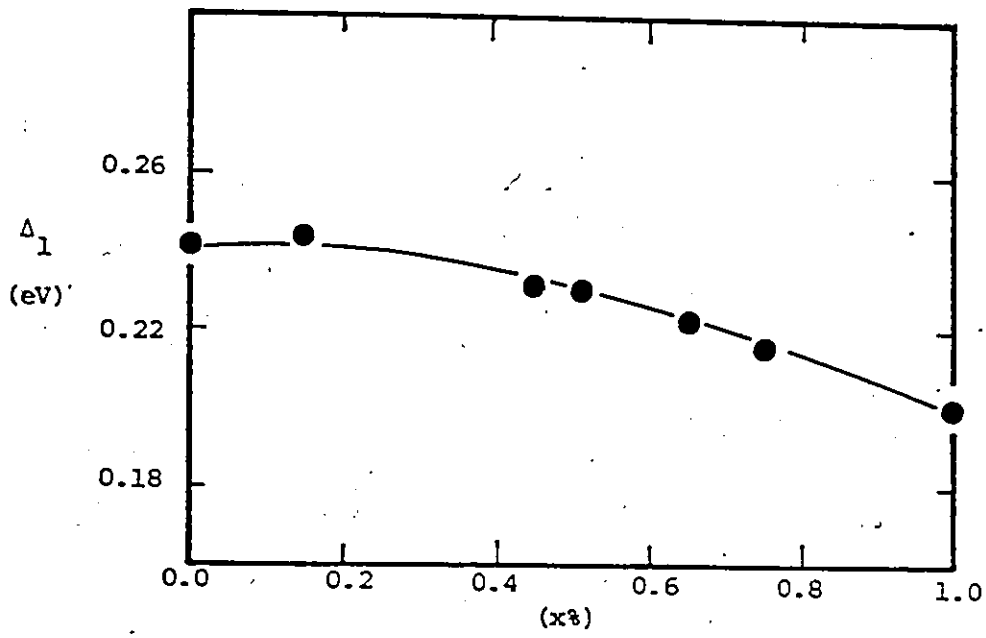

Figure 4-10. Alloys dependence of Δ_1, the s-o splitting of the top two v.b. in the (111)- See fig. 5-1.

correlating this energy region with Onton's results on AlAs. In fig. 4-9 this effect is illustrated by the considerable scatter that exists between the experimental points. Hence no attempt has been made to determine a bowing parameter for peaks 7 and 8. With E_2, a larger peak (#9) is obtained in most cases. Accuracy in the energy determination for the transition is therefore improved. As seen in fig. 4-9, the E_2 with x variation is almost linear and the experimental points are fitted to the standard parabolic form, a very small value of $c \sim 0.02$ eV is obtained, (see table 4-2).

4.4 In(As,P):

is like (Ga,Al)As an alloy system exhibiting a change from direct to indirect gap somewhere along the composition range (from the InAs end).

The samples used were prepared by Dr. M. Rubenstein of Westinghouse Laboratories. The detailed description of the preparation is given in (1T69) and consists in the growth of polycrystalline alloys be a halogen vapor-transport closed-tube technique over the entire range of composition (see also 1T71).

The electroreflectance specimen varied from surfaces of 5×5 mm^2 to 7×5 mm^2. These samples and their surfaces are prepared and treated as described in the previous chapter. X-ray measurements were made to verify the quoted composition. The results indicate homogeneity of composition of better than 2% in x. It has been reported

previously from EER that the spectrum of InAs is different from that of the other compounds and its own alloys with regard to the sign of the various electroreflectance peaks. In the observed III-V compounds the phase of the $\Delta R/R$ signal is such that all peaks are oriented in the same direction. However Kwan et al (2K68) have shown that for the E_1 complex there is a reversal in sign of the peak depending upon the carrier concentration, the d.c. bias and the type of electrolyte used. Although this investigation has not been carried out for the E_o peak as well as for the $E_o + \Delta_o$ peak, as a function of bias in any detail, analogous behaviour to that of the E_1 complex is likely. Not only because such a behaviour has also been reported by Vishnubhatla (1V70), but also because Seraphin (2S67) has found that by changing the electric field at the reflecting surface, the phase of the $\Delta R/R$ signal and therefore the sign of the peak would change. Transitions in the high energy region of the spectrum have not been seen to suffer such phase changes.

Because of this anomaly and since the carrier concentration over the alloy range and for InAs itself are about the same, the samples have all been measured consistently at -1.0 V bias.

Electroreflectance measurements were done on twelve samples covering the alloy range and involving photon energies from 0.35 eV to $\sim$ 1.35 eV. The modulating voltage was 1V pk - pk.

Measurements were initially made on InAs (fig. 4-12). A PbSe detector, cooled to liquid N_2 temperature, was used for the determination of the E_o structure. The PbS cell which was of good use thoughout this work has a poor sensitivity at photon energies below 0.35 eV. The value

of E_o of 0.34 eV for InAs and a Δ_o value of 0.39 are in good agreement with absorption measurements of Williams and Rehn (1W68) and electroreflectance measurements of Pidgeon et al (1P67).

From fig. 4-12 to fig. 4-13 the $\Delta R/R$ spectra are shown as a function of photon energy for some of the measured alloys. The E_o and $E_o + \Delta_o$ spectra are seen, with the typically smaller Δ_o structure having often a lineshape reminiscent of the E_o transition.

In InP, the value of Δ_o is expected to be quite small. Under several bias conditions, it was not possible to obtain a reliable $E_o + \Delta_o$ structure. This may be attributed to the relative sizes of the two structures, poor surface conditions and possible field inhomogeneities. The value of 1.27 eV for InP compare reasonably to the $E_o = 1.34$ eV value measured by Cardona (2C67).

In fig. 4-15, the energies at E_o and $E_o + \Delta_o$ transitions are followed through as a function of alloy composition. They both exhibit the familiar quadratic dependance. However in the case of E_o this is almost a linear dependance. This behaviour has been reported before by Dubrowskii (1D63), Oswalds (1O59) and Krioturu (3K66). The comparison with the present results is seen in fig. 4-14.

In Table 4-2 (page 184) are tabulated the coefficients for E_o, $E_o + \Delta_o$ transitions as a function of composition. They can be compared with other results by Alexander (1A64) and the other workers. The theoretical values of Van Vechten disagree for the values of c.

Fig. 4-16 shows the spin-orbit splitting dependance on alloy

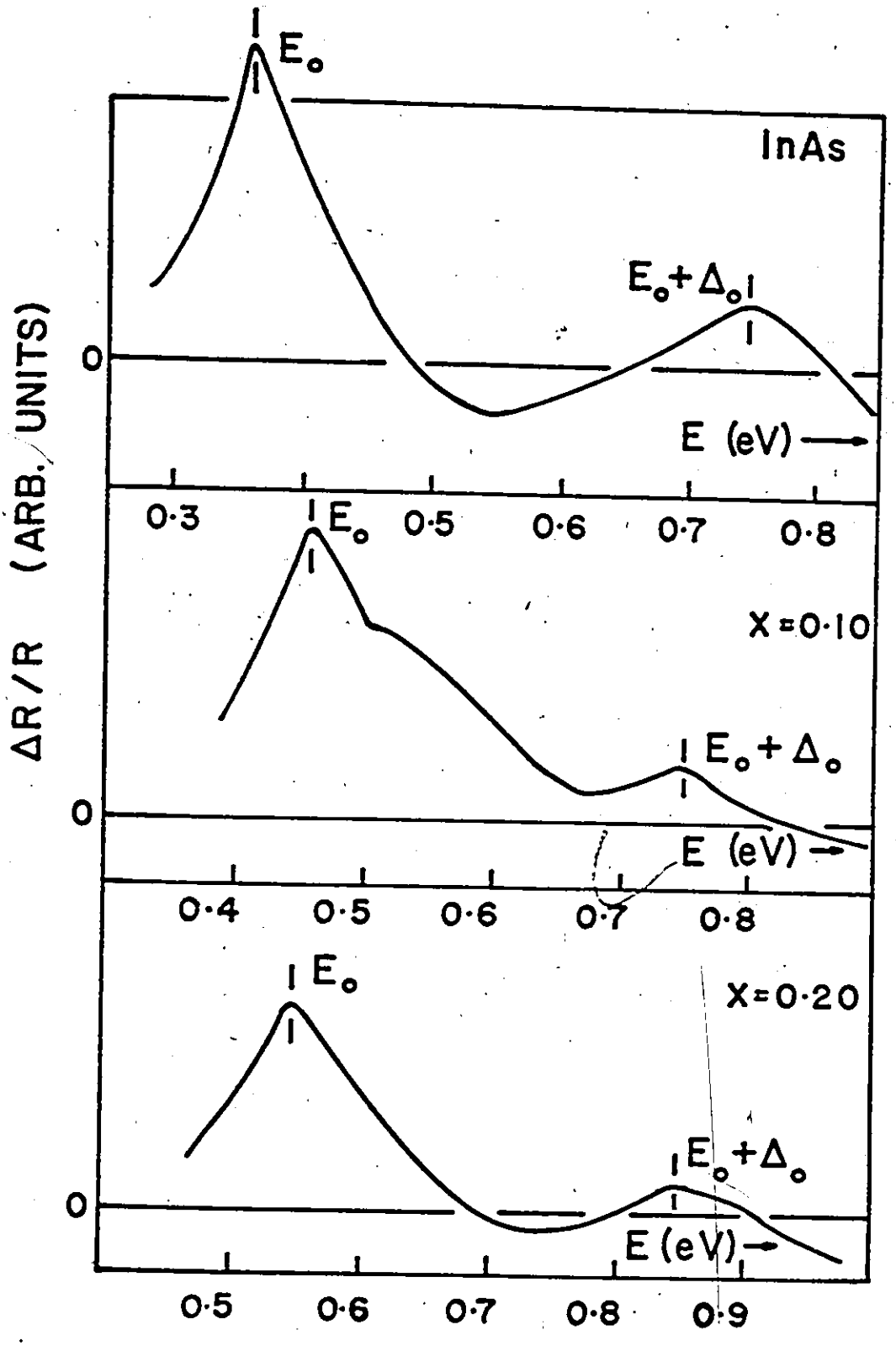

Figure 4-11. Electroreflectance results on the In(AsP) alloy systems.

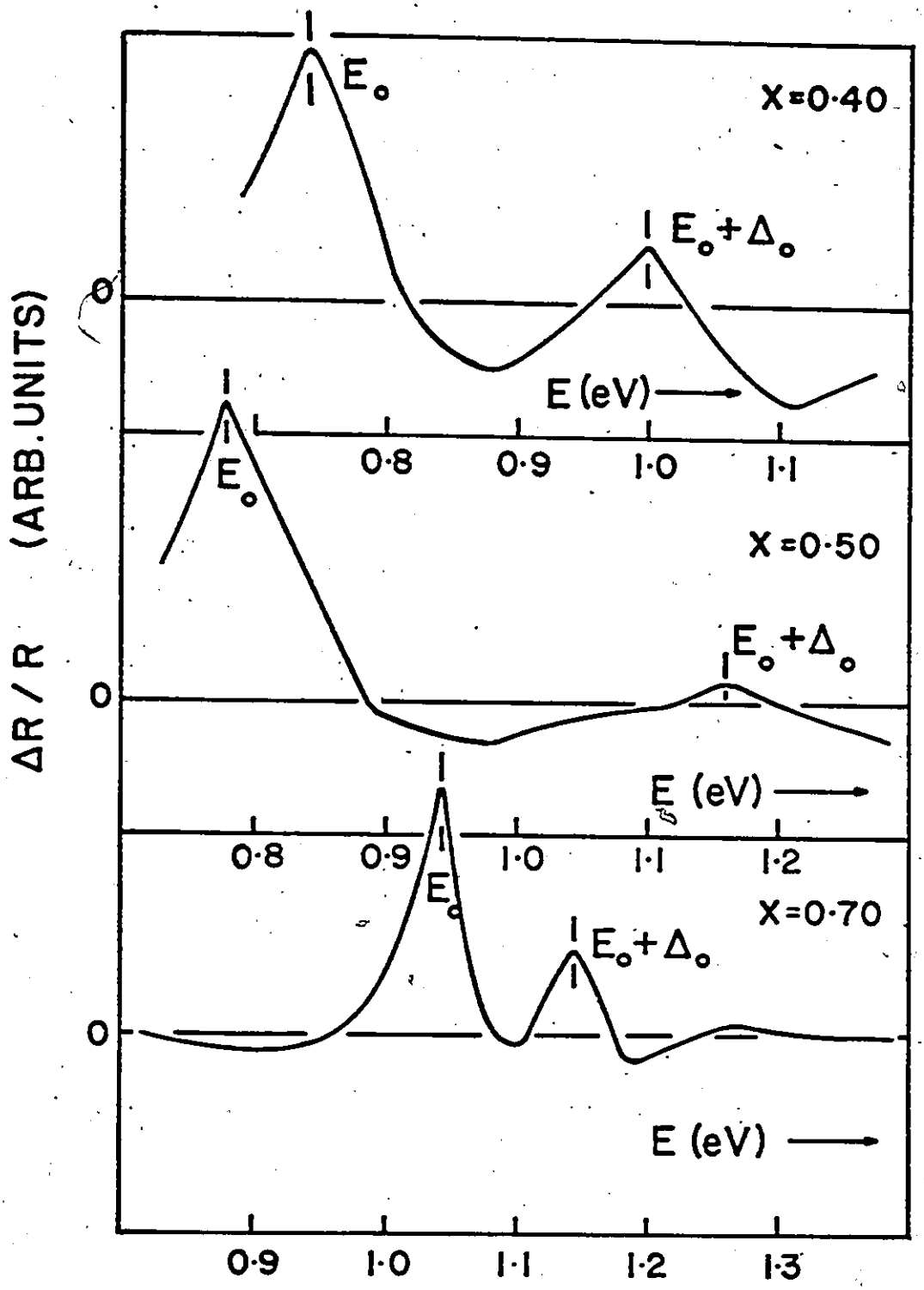

Figure 4-12. Electroreflectance results on the In(AsP) alloy systems.

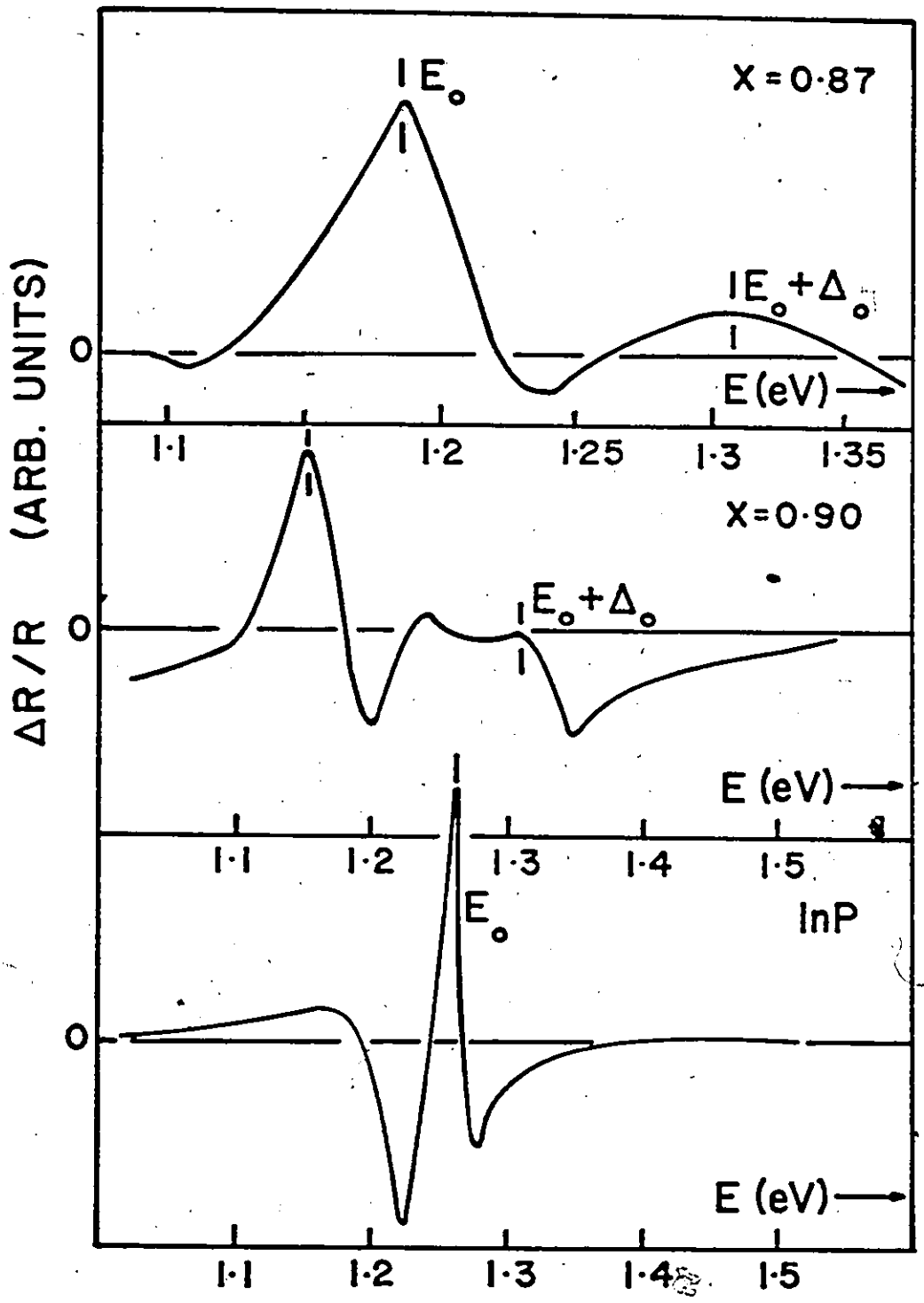

Figure 4-13. Electroreflectance results on the In(AsP) alloy systems.

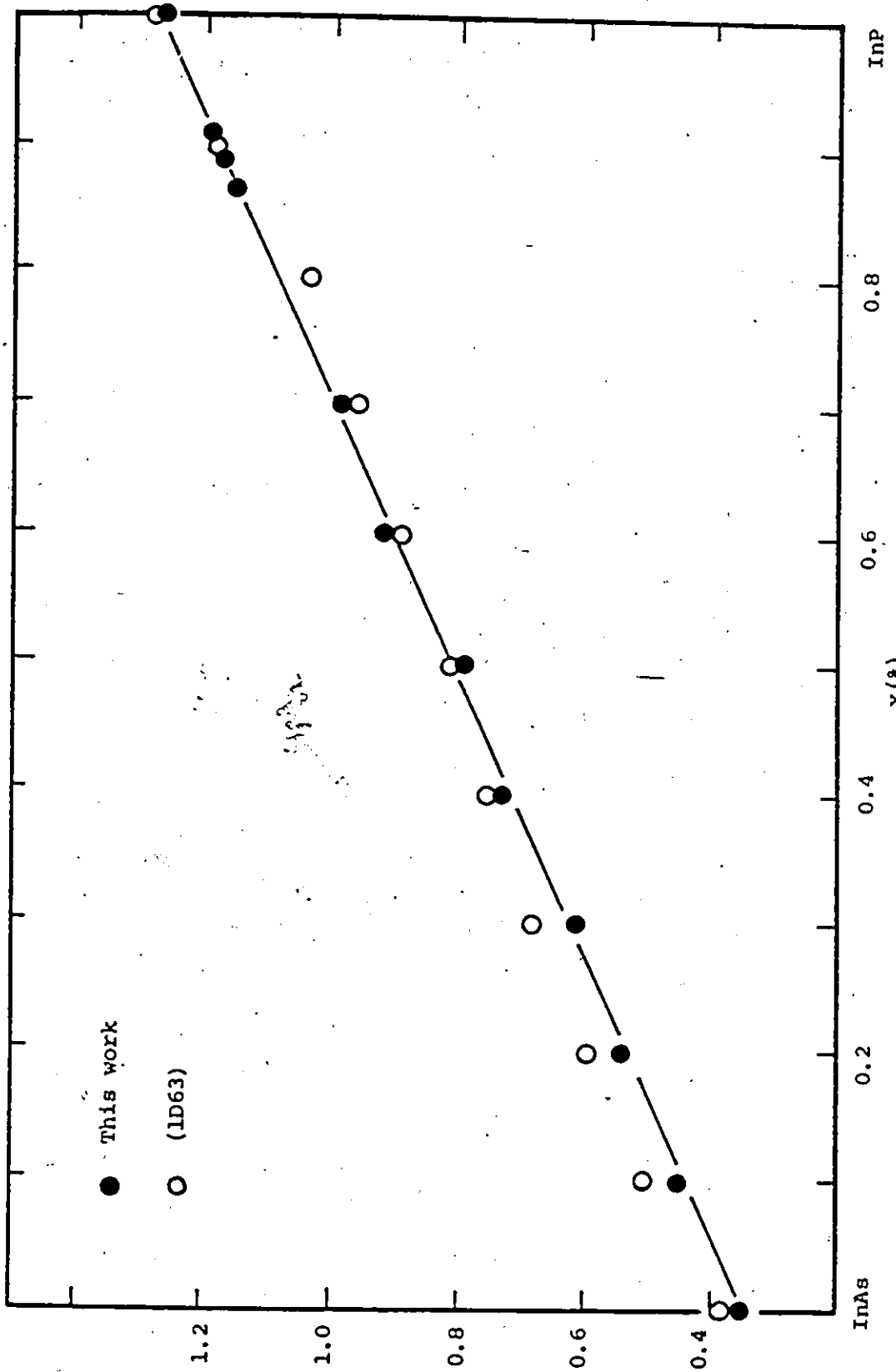

Figure 4-14. The dependence of E_o on x for the In(AsP) alloy system. The results are compared to those obtained previously by absorption (1D63).

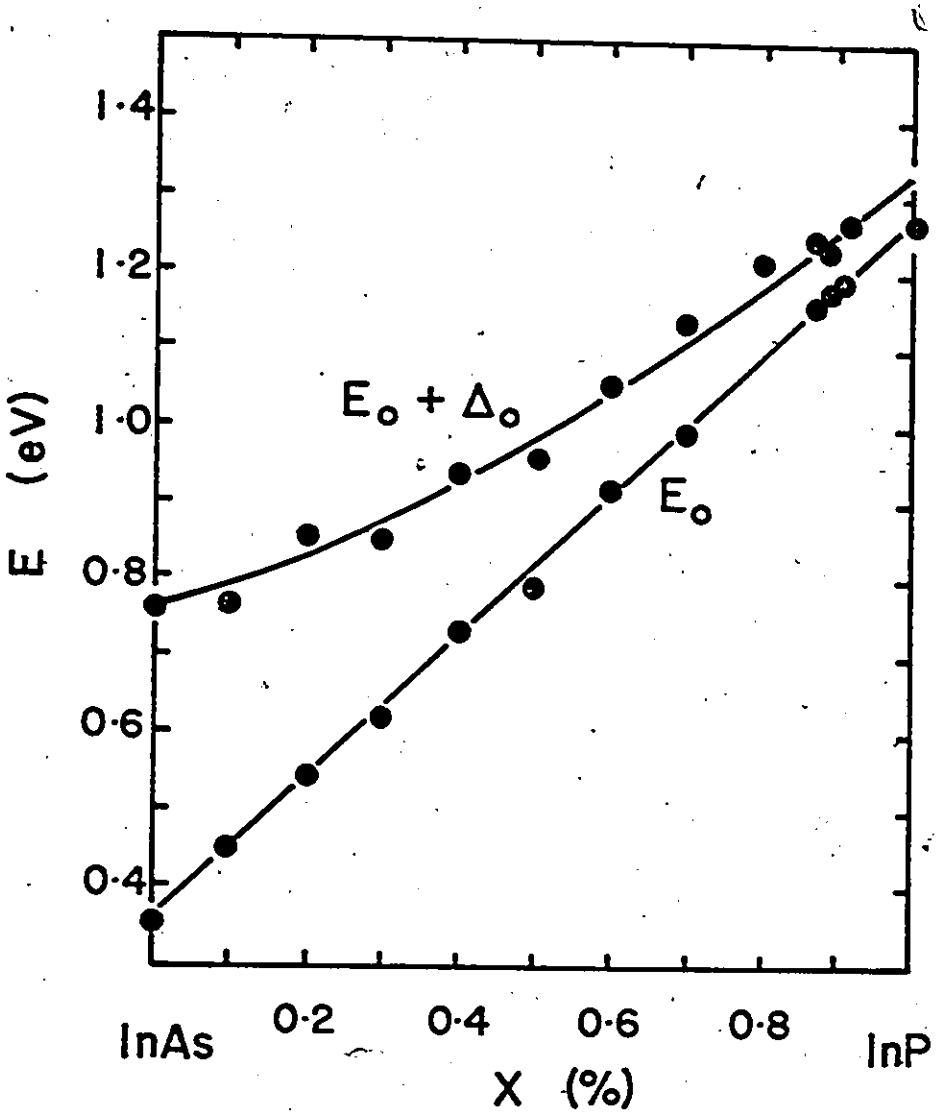

Figure 4-15. The dependence of E_o and $E_o + \Delta_o$ on alloy composition for the In(AsP) system.

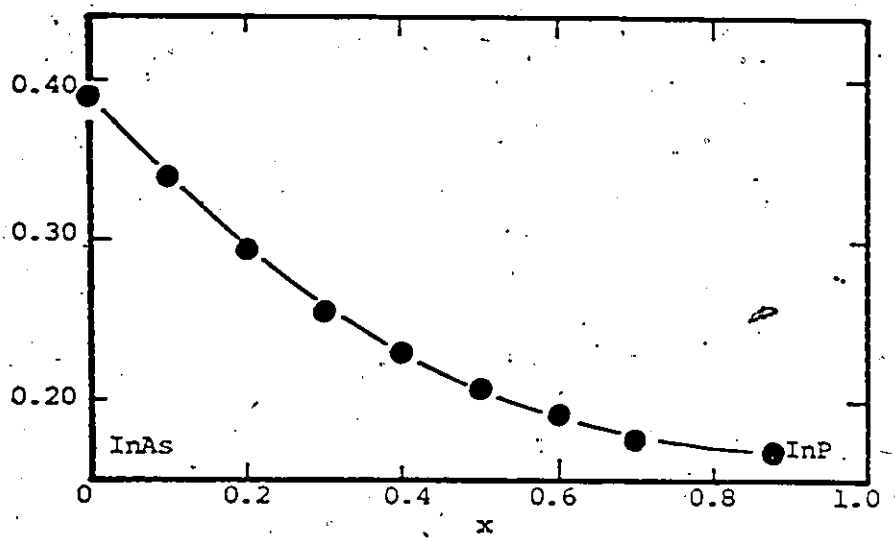

Figure 4-16. The alloy dependence of s-o splitting at k = (000).

composition. The form of alloy dependance of Δ_o confirms the measurements obtained on (Ga,Al)As.

4.5 Ga(As,P):

is another of the high gap semiconductors which exhibit fundamental transitions which change from direct to indirect over the alloy composition range. The cross over point has been determined by absorption measurements of M. Rubenstein at 46% of GaP in GaAs at an energy of 1.94 eV (1R65).

In the present work, Ga(As,P) measurements were repeated on samples measured previously (2T66) by EER. In part, the purpose of the measurement is to establish the reproductibility of electrolytic electroreflectance structure by the MOS surface barrier electroreflectance technique. We find the peaks and the general lineshapes in fig. 4-17 to 4-19 in good overall agreement with the ones found by Thompson.

The electroreflectance material for the Ga(As,P) alloy system was prepared by Dr. M. Rubenstein and the description of the halogen sealed tube transport technique analogous to the In(As,P) alloy preparation is found in (1R65). The homogeneity indicated by Rubenstein is good. Some of the polycrystalline samples contained large grains. Most of the specimens were of roughly elliptical shape. The samples were polished in the usual manner, however GaP rich alloys and GaP were polished, as in the case of InP and InP rich alloys of In(P,As) in abrasives suspended in oil. GaP rich samples, unlike the other alloy systems, were etched with CP6. The GaAs rich alloys as well as GaAs are

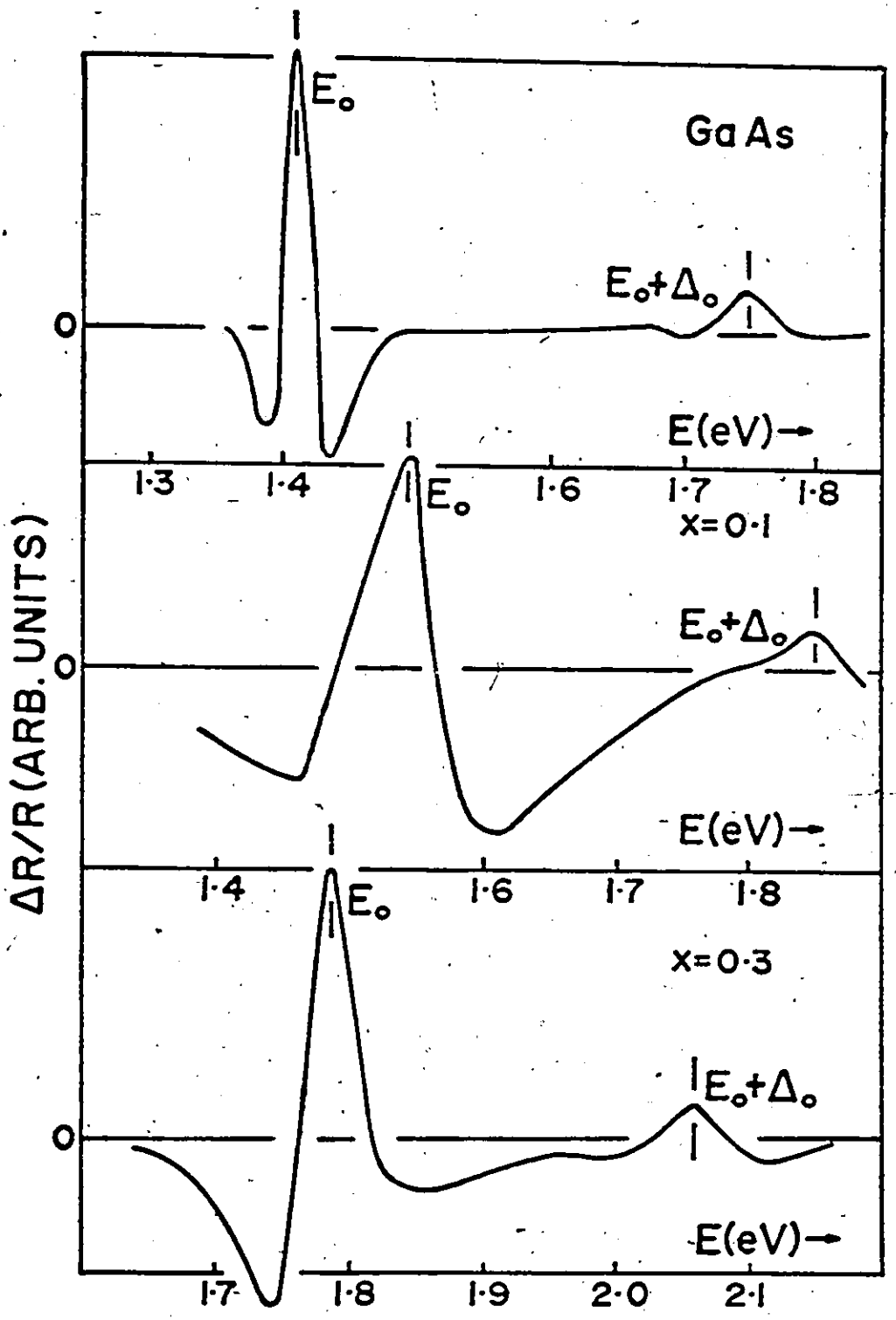

Figure 4-17. Electoreflectance spectra for the Ga(AsP) alloy system.

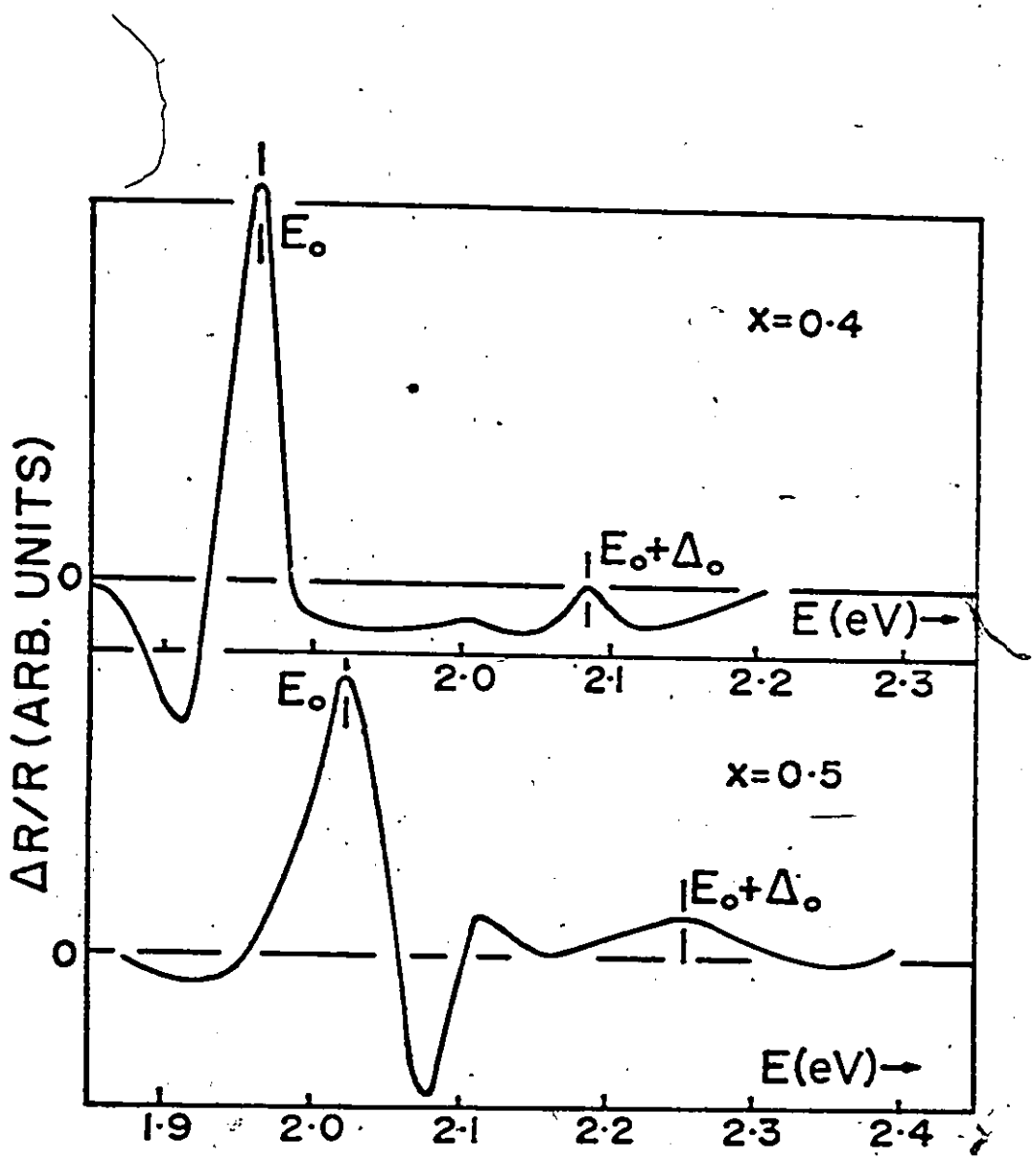

Figure 4-18. Electroreflectance spectra for the Ga(AsP) alloy system.

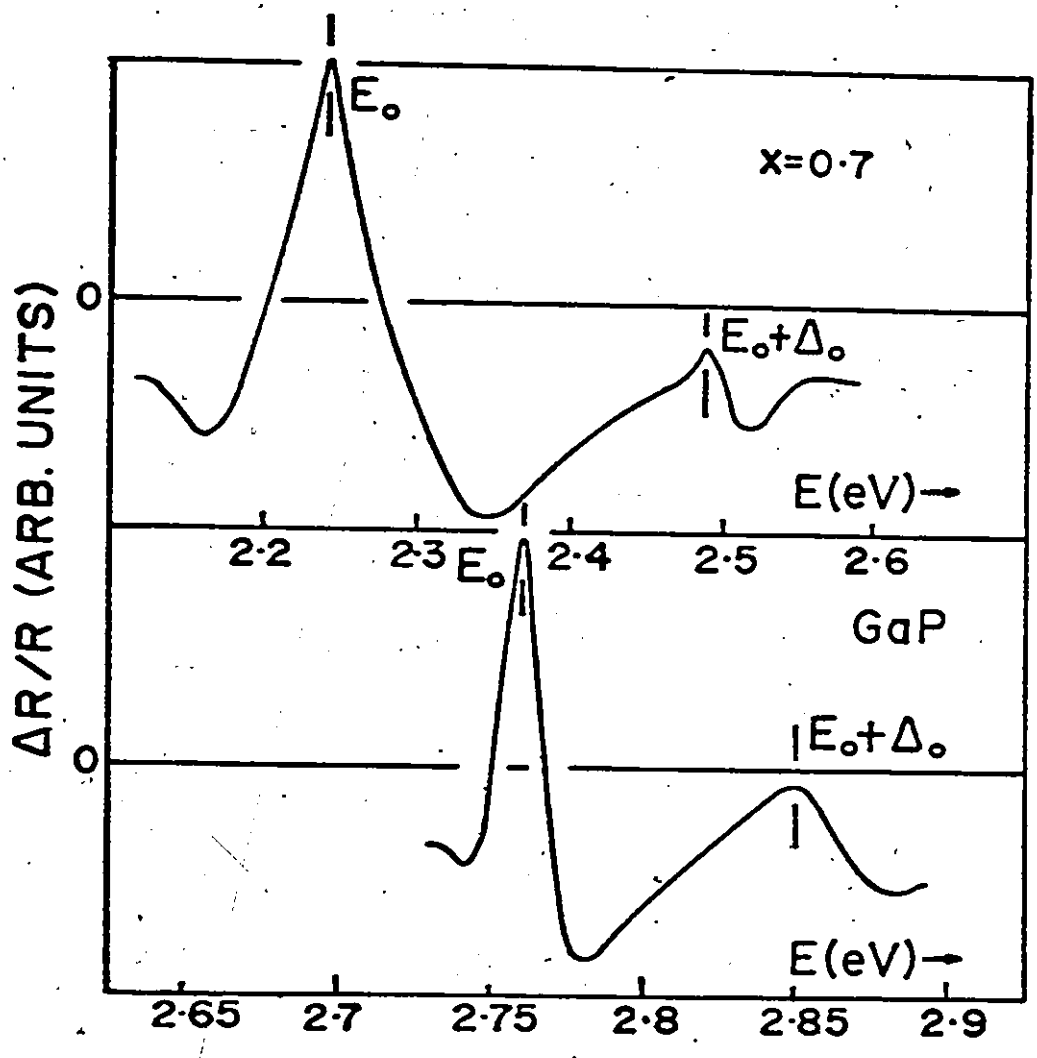

Figure 4-19. Electroreflectance spectra for the Ga(AsP) alloy system.

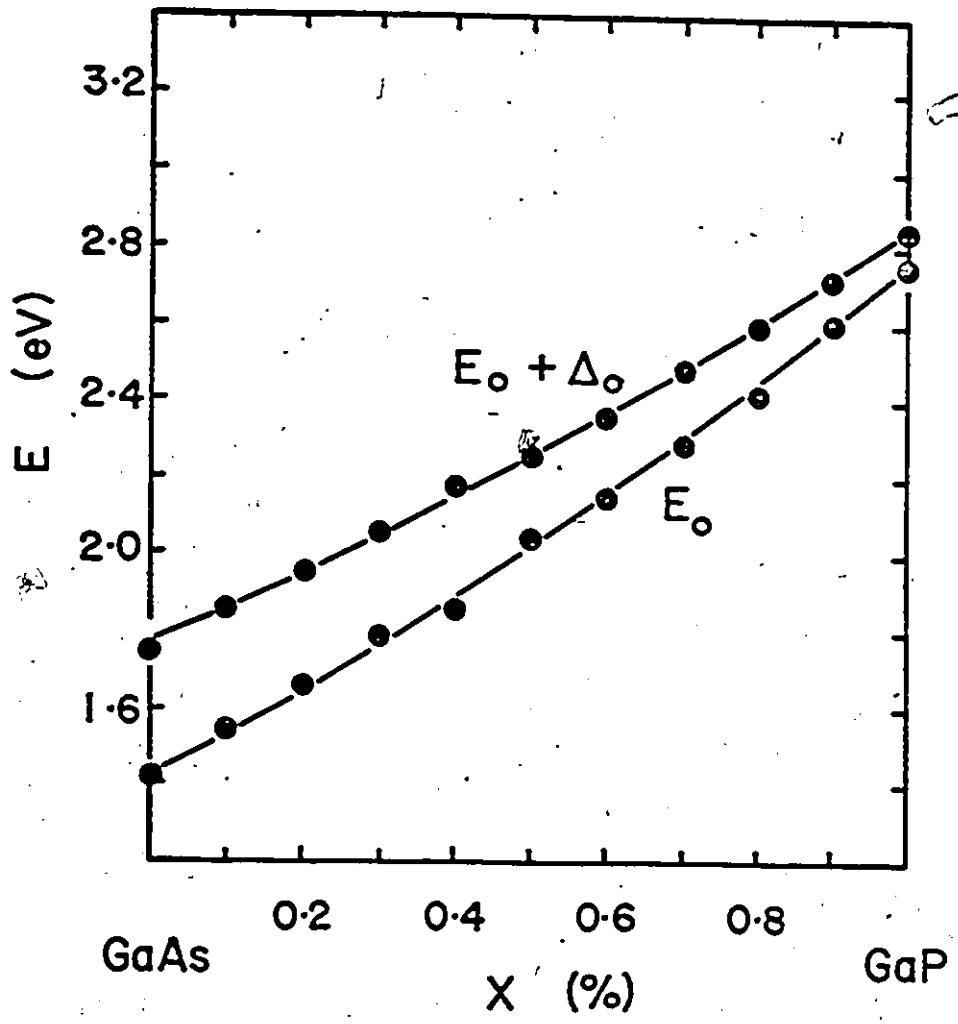

Figure 4-20. Showing the dependence of the E_o and $E_o + \Delta_o$ structures with alloy composition.

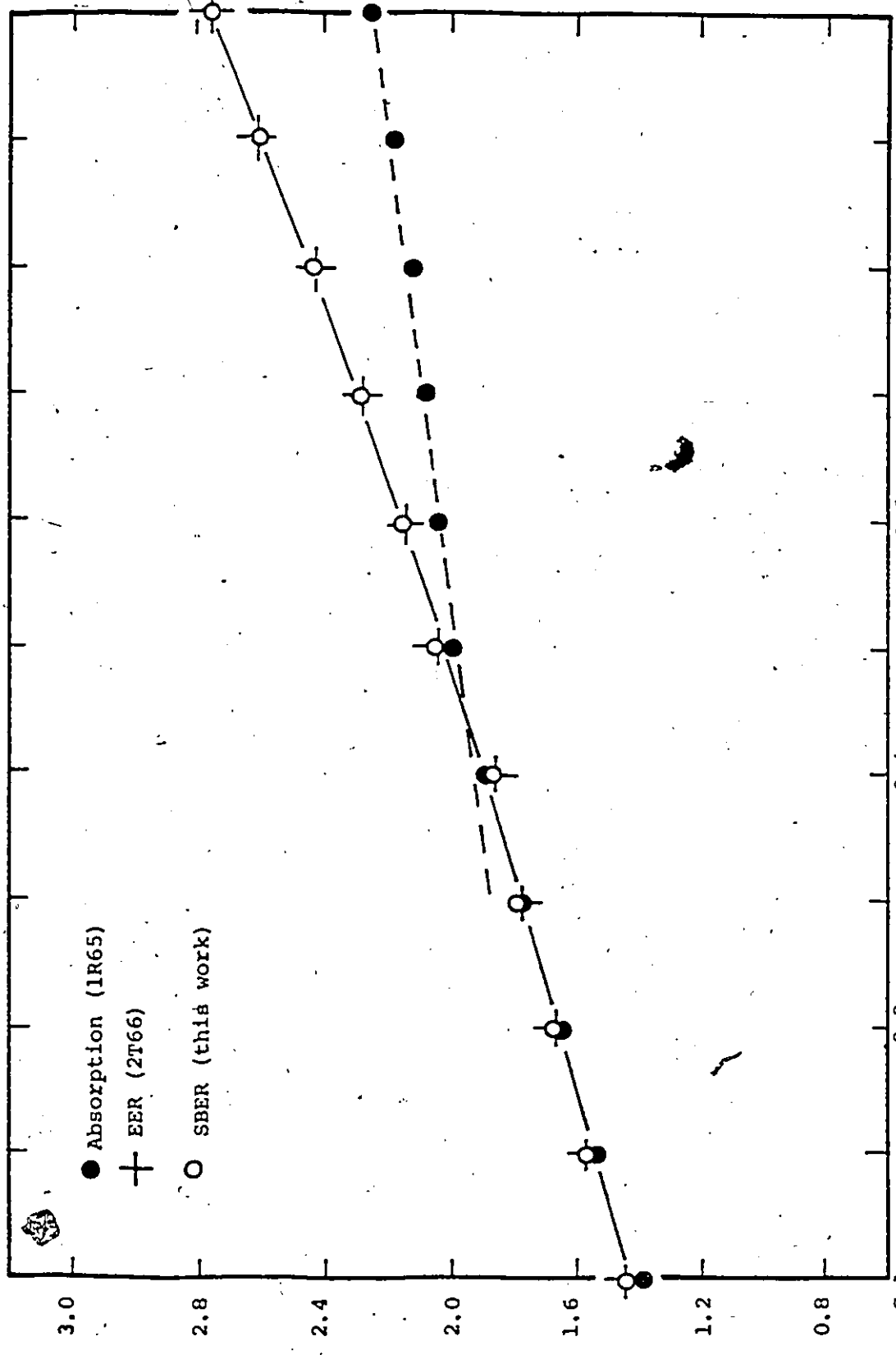

Figure 4-21. Showing the E_o direct and indirect alloy dependence . The SBER results (o) are compared to EER results (+)(2T66)) and absorption measurements. (1R65)

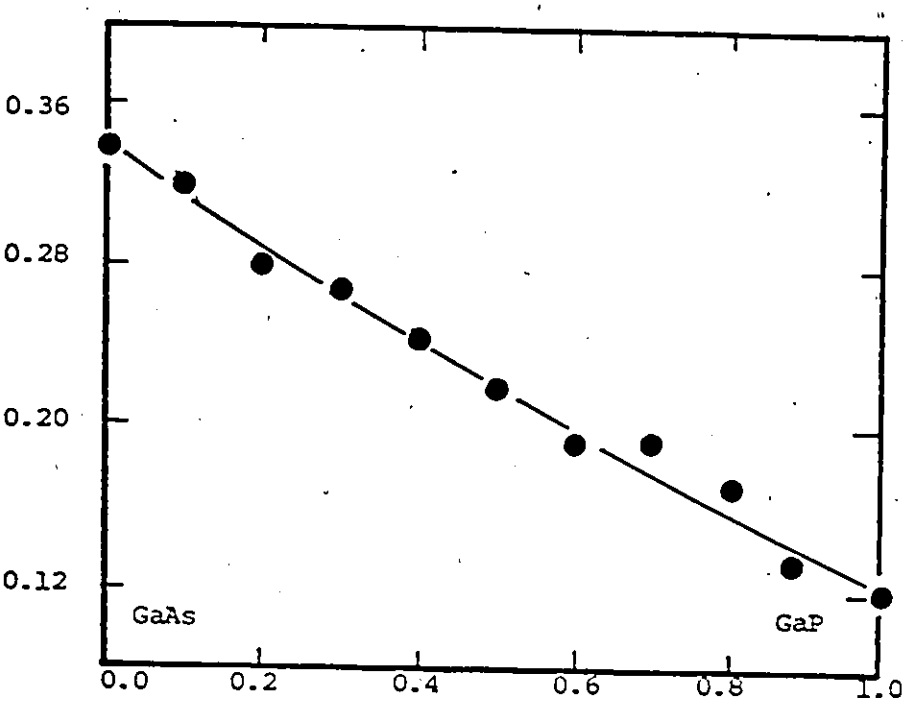

Figure 4-22. The dependence on alloy composition of Δ_o, s-o splitting at k = 000.

etched in the sulfuric acid etch described in Chapter 3.

The measurements on GaAs obtained for the (Ga,Al)As alloy system are used here to identify and follow the alloy compositions the structures due to E_o and $E_o + \Delta_o$. Fig. 4-17 to fig. 4-19 show the ER spectra for these alloys. In alloy samples, although the signal size is lower than for the compounds, the peaks are well defined for both transitions. In fig. 4-20 their dependance on alloy composition is shown. The usual smooth bowed dependance is noticed, differing from the In(As,P) system where the E_o dependance is quasilinear.

In fig. 4-21 the present SBER (O) results are compared with the EER results of Thompson (+) and the absorption measurements by Rubenstein (•). The agreement between the two electroreflectance results is good. The absorption measurements give a critical cross over from direct (GaAs) to indirect (GaP) gap at the alloy composition of 74% of GaP at 1.96 eV. In fig. 4-22 the almost linear alloy dependance of Δ_o with x is confirmed with Thompson's results (2T66).

4.6 In(As,Sb):

This alloy system is prepared by the travelling freeze horizontal Bridgeman technique referred to in Chapter 3. The preparation of homogeneous solid specimen of these alloys by the zone recystallization and directional freeze method has been first considered by Woolley and Warner (2W64, 3W64). These growth methods give alloys with 1% homogeneity, up to 20% alloy composition from either constituent. A somewhat less homogeneous material (2 to 3%) was obtained in the middle

range of the alloy. The samples were cut from the ingots, portions X-rayed for composition and then polished. The bromine based etch was used throughout the alloy composition. On some of the InSb rich alloys, CP6 was used to compare the effectiveness of the etch. No measureable difference was observed between the spectra thus obtained. The range of photon energies covered from 0.4 eV to 1.0 eV to obtain transitions of $E_o + \Delta_o$. The $\Delta R/R$ spectra as a function of photon energy are seen for a number of alloys in fig. 4-23 to fig. 4-25. Fundamental absorption measurements made by other workers (2W64, 2S71) indicated that any E_o measurements for the alloys, i.e. the measurement of E_o below the value for InAs, would be out of the working range of the equipment. Absorption results were therefore used in the subsequent calculation of Δ_o over all of this alloy range.

In the previous work described above, the spectral determination of the fundamental gap was a good indication of the reliability of measurement and running conditions. Only when a good E_o structure was established experimentally would the investigation for the $E_o + \Delta_o$ transition follow. However in this case, when no E_o measurements are available, spin-orbit splitting measurements could only be obtained after repeated measurements under different experimental conditions. The measurements of Pidgeon et al (1P67) were used as a reliable guideline from the InSb and InAs ends. The structures due to the E_1 complex and their comparison with already established data (1V70) were also an important guide in the determination of ideal experimental conditions.

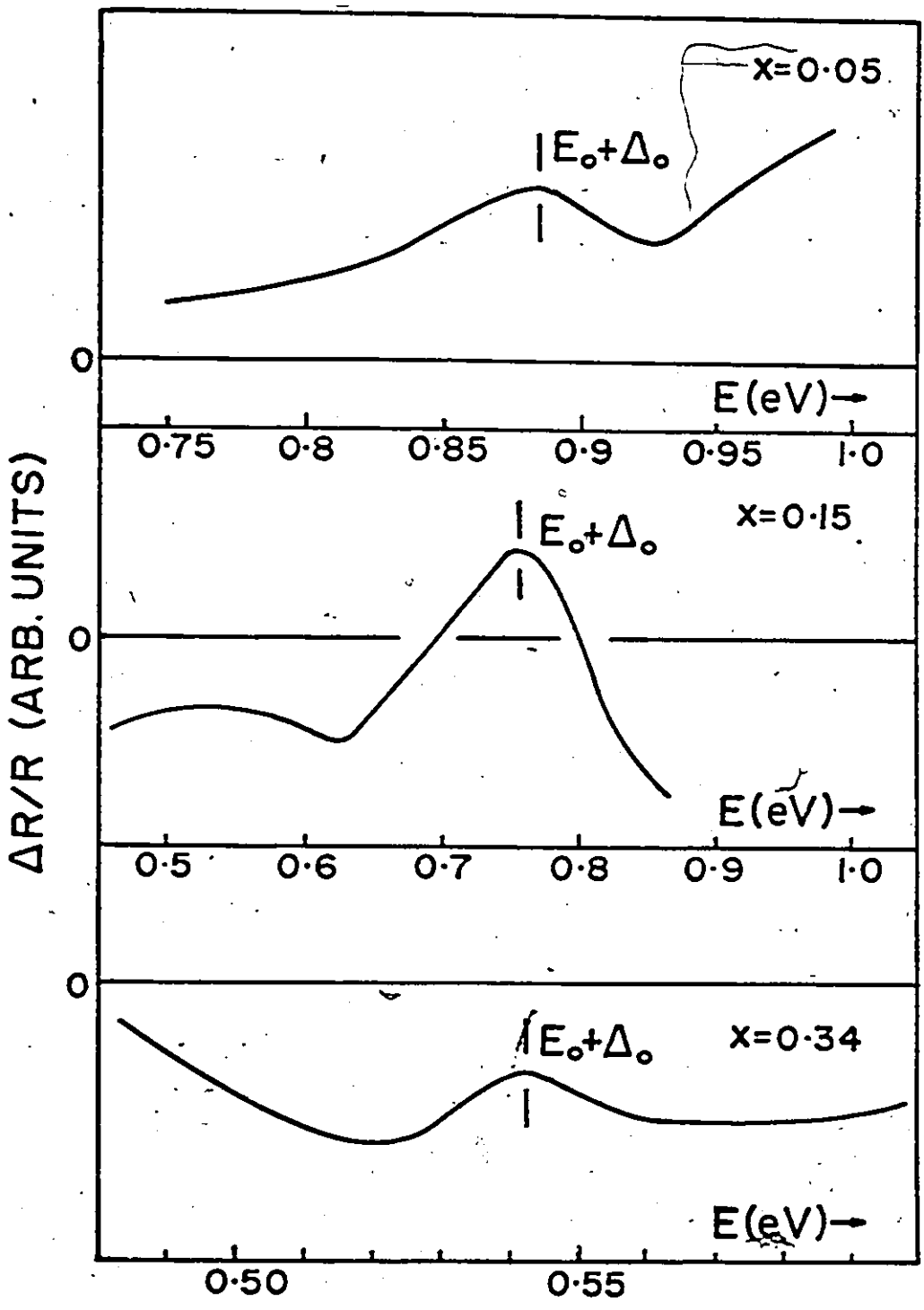

Figure 4-23. Showing the Δ_o structure for various In(AsSb) alloy samples.

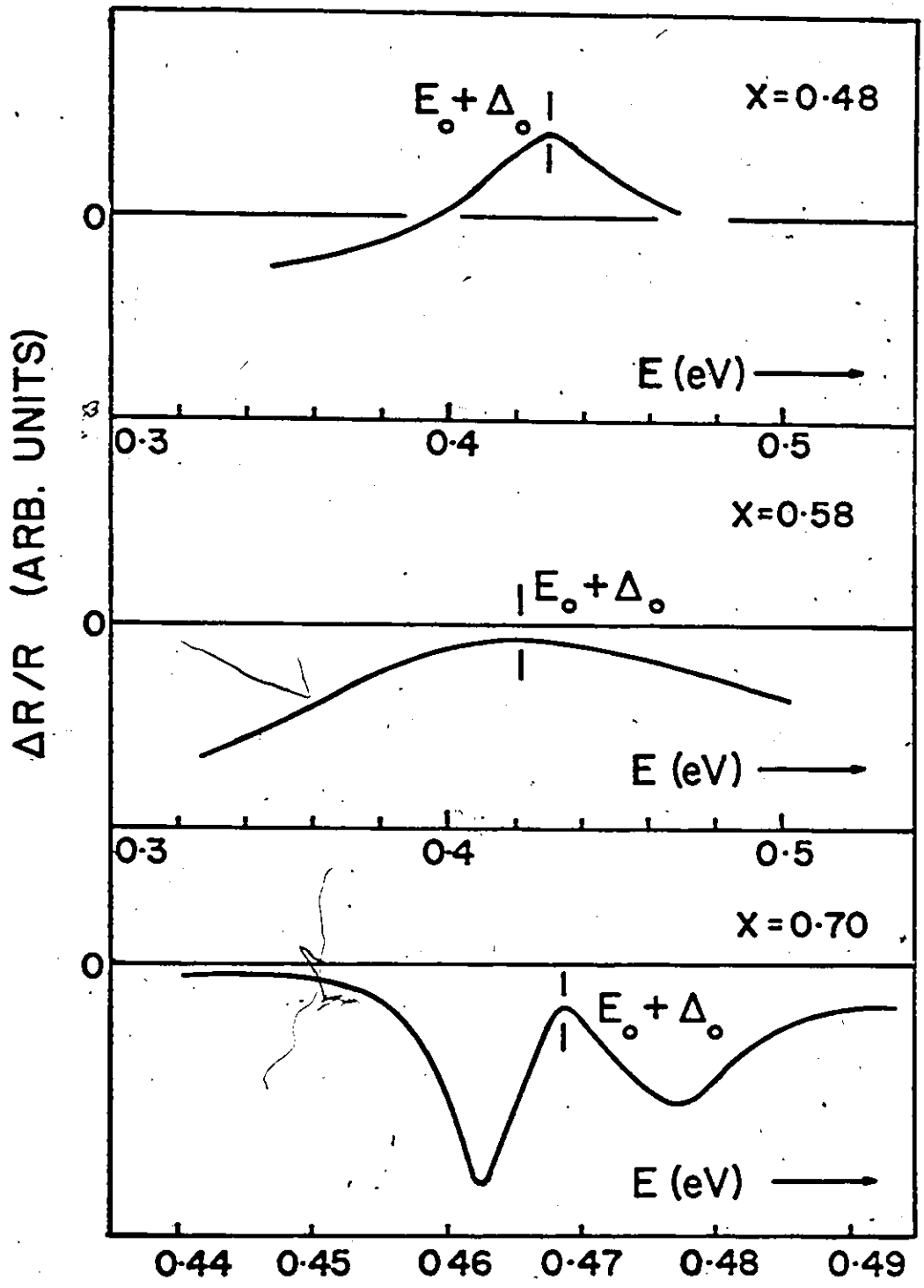

Figure 4-24. Showing the Δ_o structure for various In(AsSb) alloy samples.

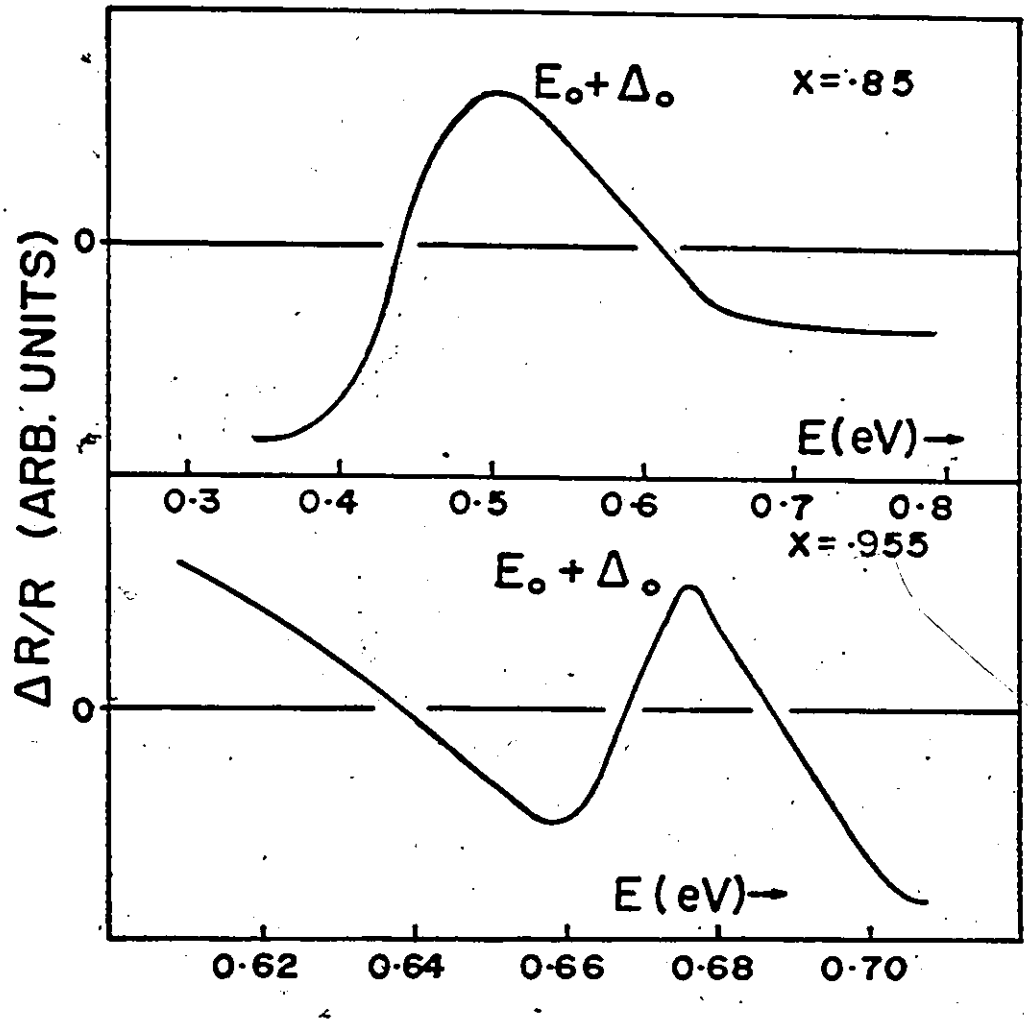

Figure 4-25. Showing the Δ_o structure for various In(AsSb) alloy samples.

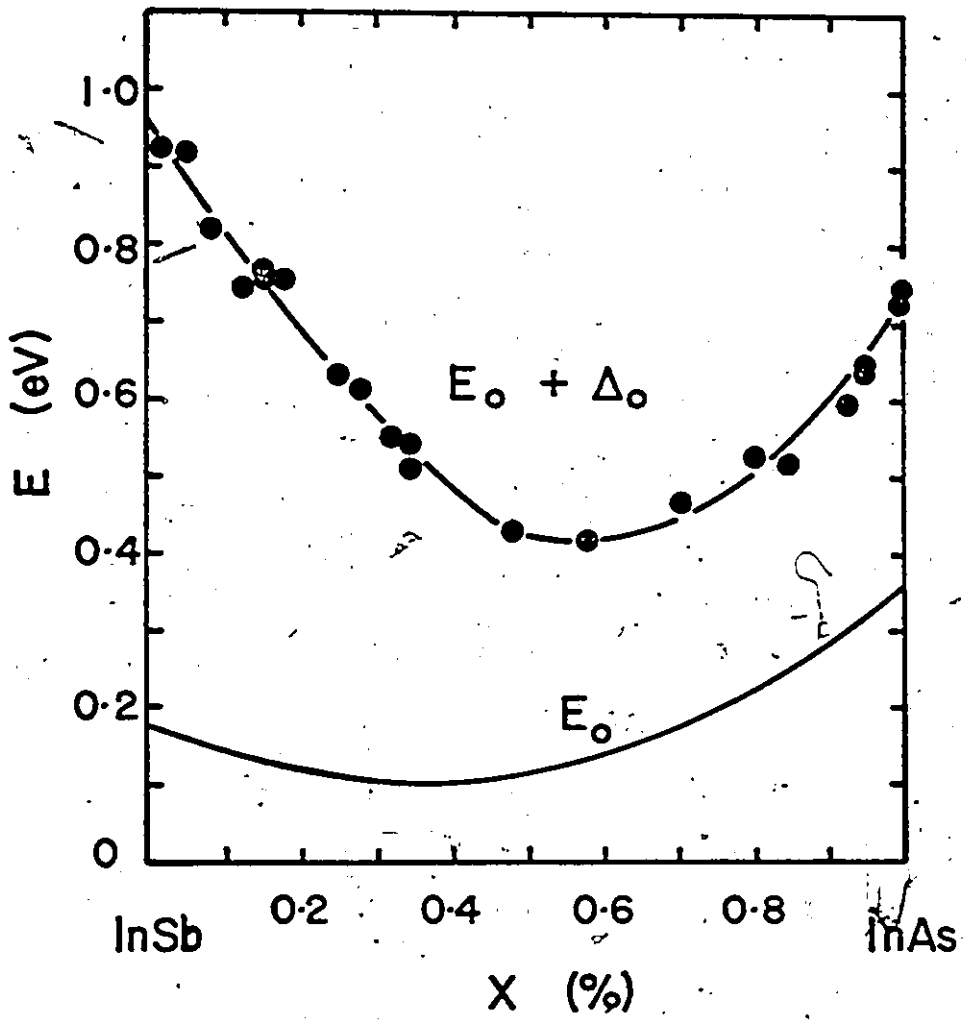

Figure 4-26. Showing the dependence of E_o and $E_o + \Delta_o$ transitions as a function of alloy composition. The E_o results are from absorption (2W64) and are not part of the results of this work.

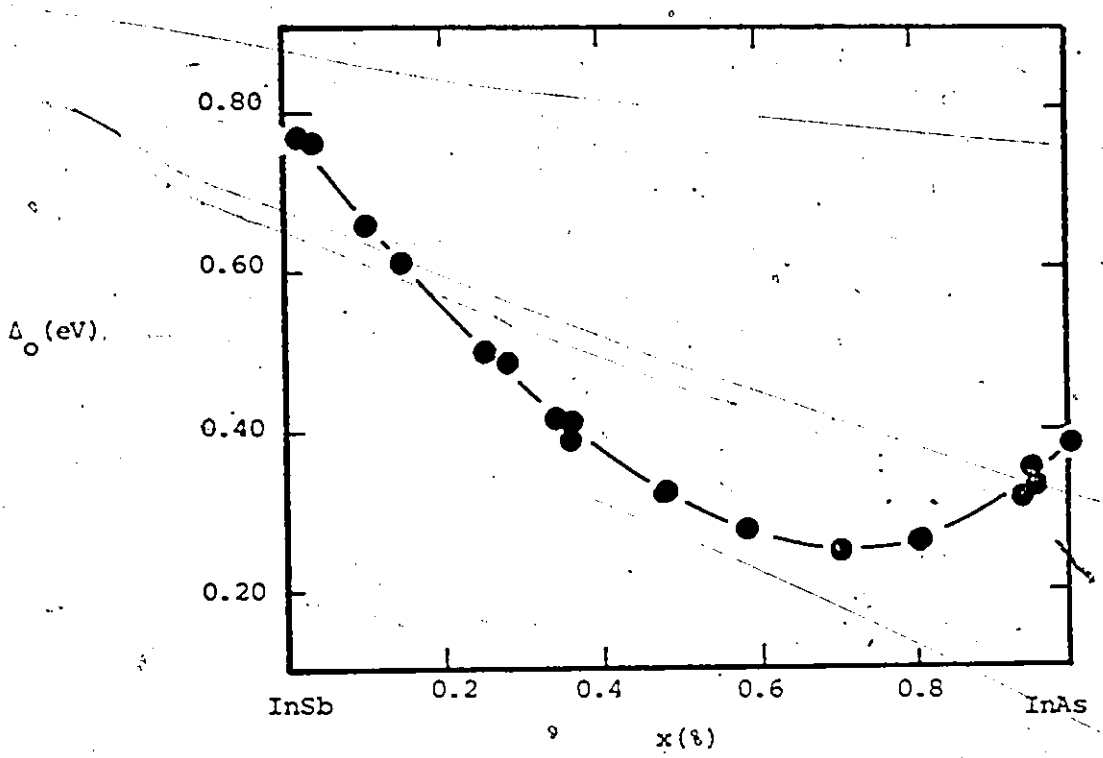

Figure 4-27. Showing the dependence of Δ_o, the spin orbit splitting at Γ as a function of alloy composition.

Therefore the investigations for the $E_o + \Delta_o$ structure were then started from the E_1 structure towards the lower energy end of the spectrum. No other structure should be present between the E_1 and the E_o transitions but the one due to the $E_o + \Delta_o$ one. Repeated runs of the weak structure give the averaged $\Delta R/R$ spectra shown from fig. 4-23 and 4-25. The structure decreases in signal at the InSb end of the alloy system. No structure could be observed for InSb. Various etchants and oxide thicknesses did not improve the signal.

In fig. 4-26 the behaviour of $E_o + \Delta_o$ with x is shown. The absorption results for E_o of Woolley and Warner (2W64) are also included and in fact they are used to calculate Δ_o (fig. 4-27). The extrapolated value of $E_o + \Delta_o$ at the InSb end gives for Δ_o = 0.78 eV, which is in good agreement with the value of other workers (1P69). Similarly, at the InAs end, 0.39 eV for Δ_o is in good agreement with previous results.

4.7 (Ga,In)As:

This alloy system was prepared in these laboratories by a travelling freeze horizontal Bridgeman technique. The grown ingots were cut and the wafers polished in the usual manner. Their composition was found by X-ray measurement with an accuracy of ±1.0 % in x. The samples were bromine etched from the InAs end and sulfuric acid etched from the GaAs end.

The fundamental gap of this alloy system has been extensively studied (1A59, 1W61, 1H66, 1W67, 1C70, 1W68) all concluding that the

fundamental gap varies non-linearly with composition. Most disagree on the extent to which the deviations from linearity occur (Table 4-2). Williams and Rehn (1W68) were the first to obtain spin-orbit splitting throughout an alloy range for any III-V alloy system. However, only a few samples were used, often the gap was measured by absorption. The samples involved in the present work have a carrier concentration comparable with that in (1W68). In fig. 4-28 to 4-30, the E_o and $E_o + \Delta_o$ SBER spectra are shown as a function of energy.

The SBER results on the compounds are those from previous measurements in this work. Fig. 4-31 shows these results as a function of alloy composition compared with those from Williams and Rehn (x, +) and Hocking (o). Hocking's (1H66) results show little scatter from a quadratic dependance for the gap, however it would seem to predict a c value for E_o which is somewhat higher than that from other results and theory (Table 4-2, page 184).

An exact reason for this behaviour is not clear at this stage. Williams and Rehn's results are in good agreement with this work. The experimental scatter involved with this work and that of Williams and Rehn for $E_o + \Delta_o$ results is a fair indication of how the smaller size of the $E_o + \Delta_o$ signal affects the error in the energy determination.

In fig. 4-32 the alloy dependance of Δ_o is shown. The shape of the bowing of the alloy dependance of Δ_o is by now of an experimentally established consistency and is in an intersting contrast with the Δ_1 behaviour (1V70, fig. 5-1, Table 4-3).

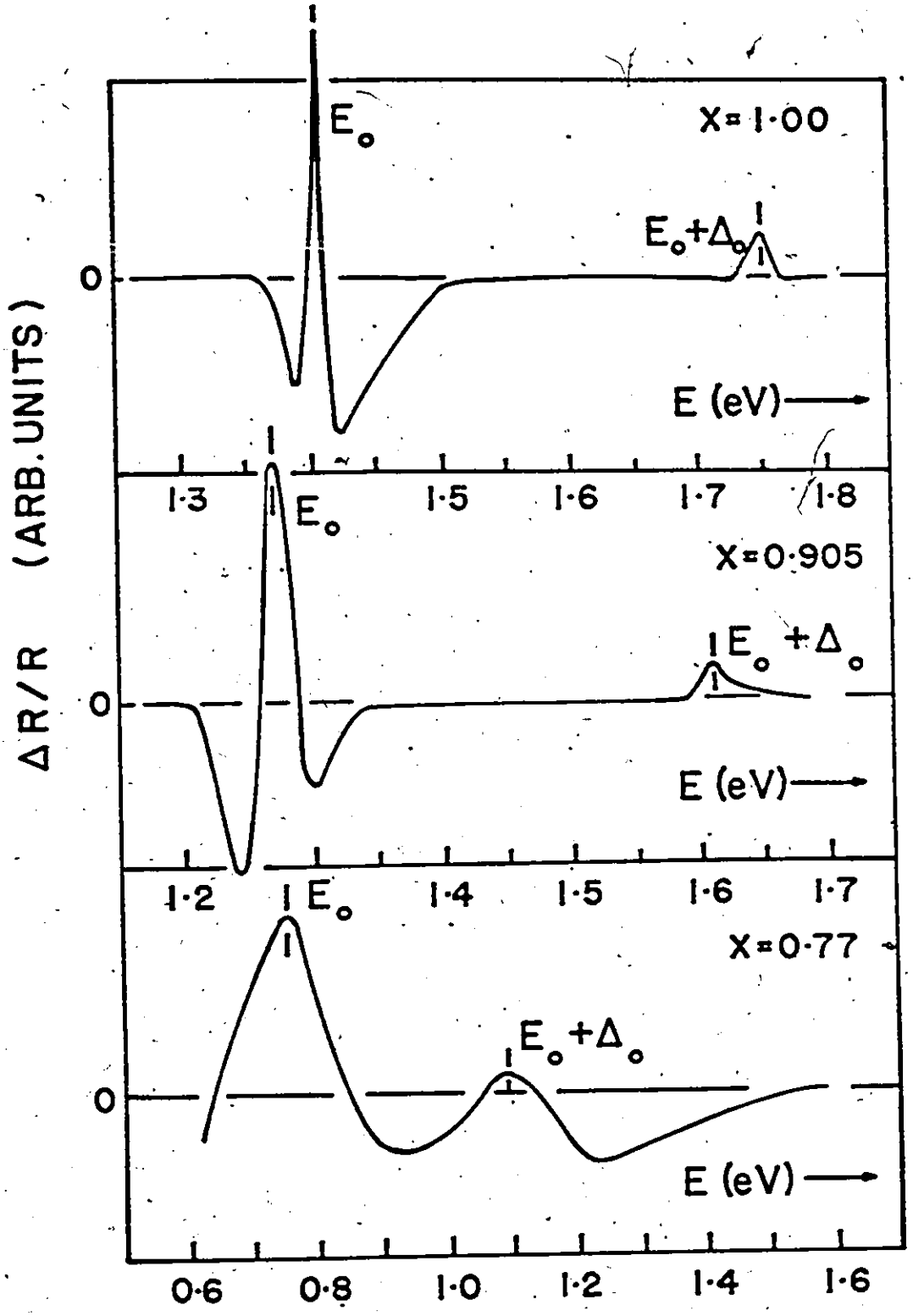

Figure 4-28. Showing the electroreflectance spectra of (GaIn)As alloys.

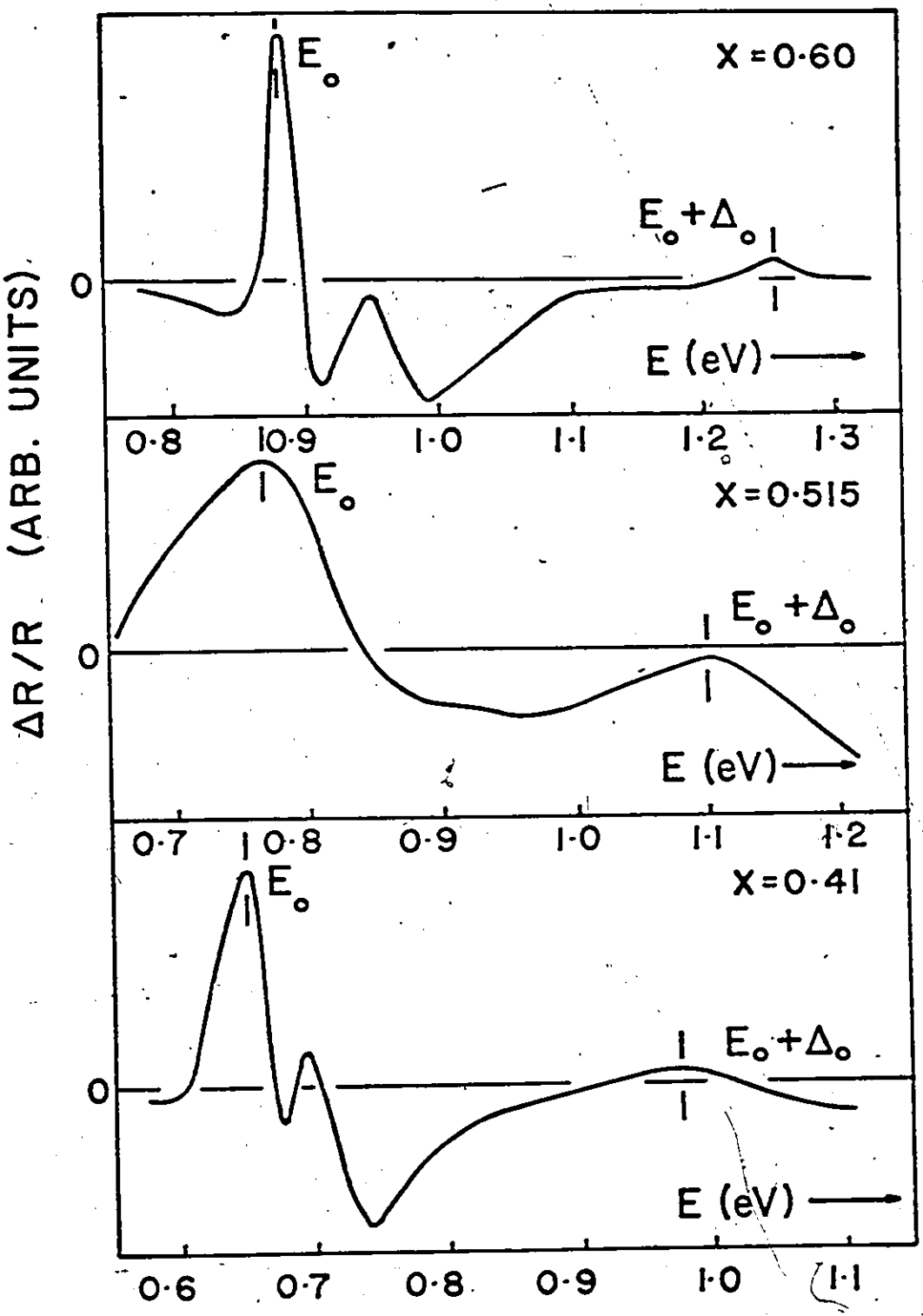

Figure 4-29. Showing the electroreflectance spectra of (GaIn)As alloys.

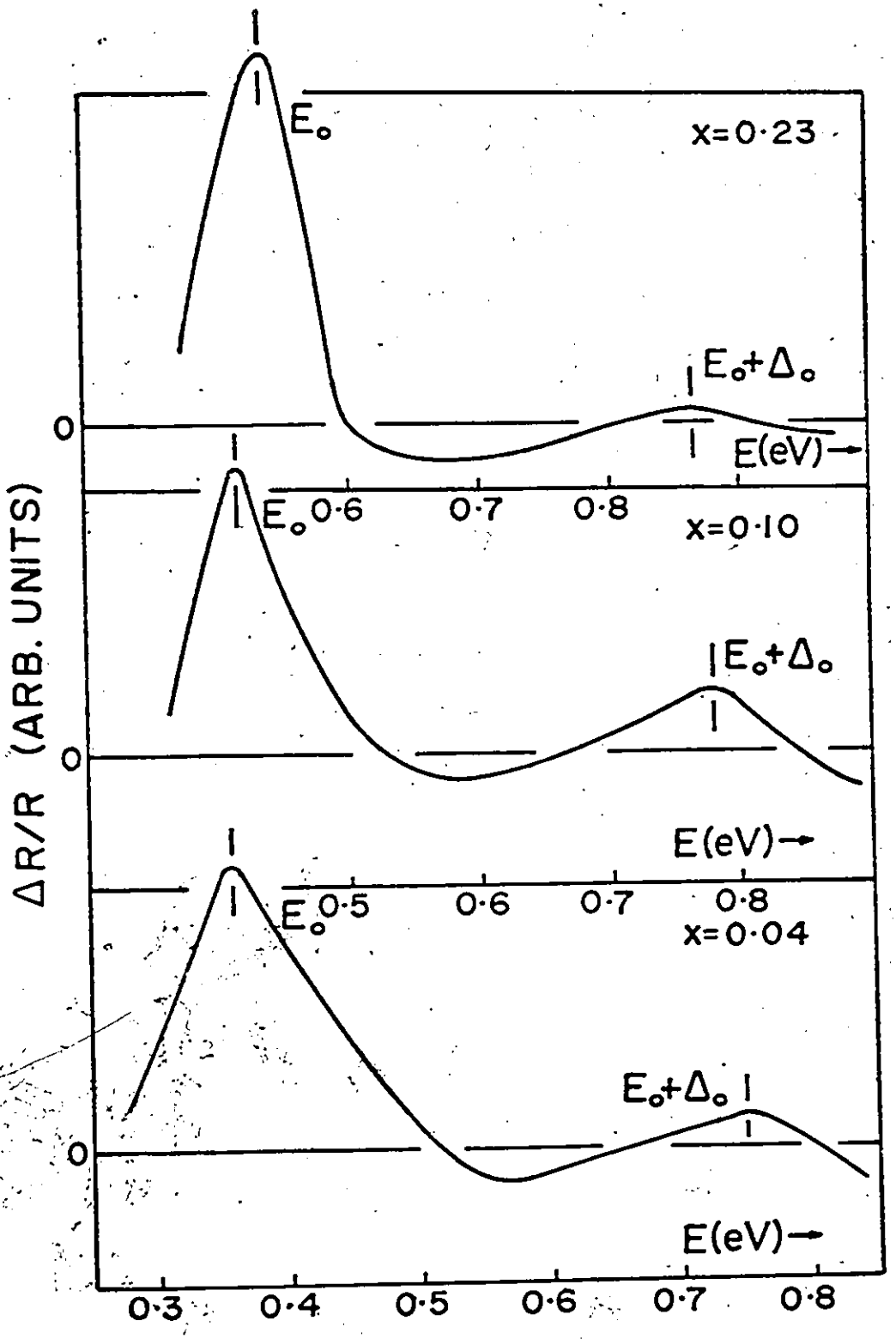

Figure 4-30. Showing the electroreflectance spectra of (GaIn)As alloys.

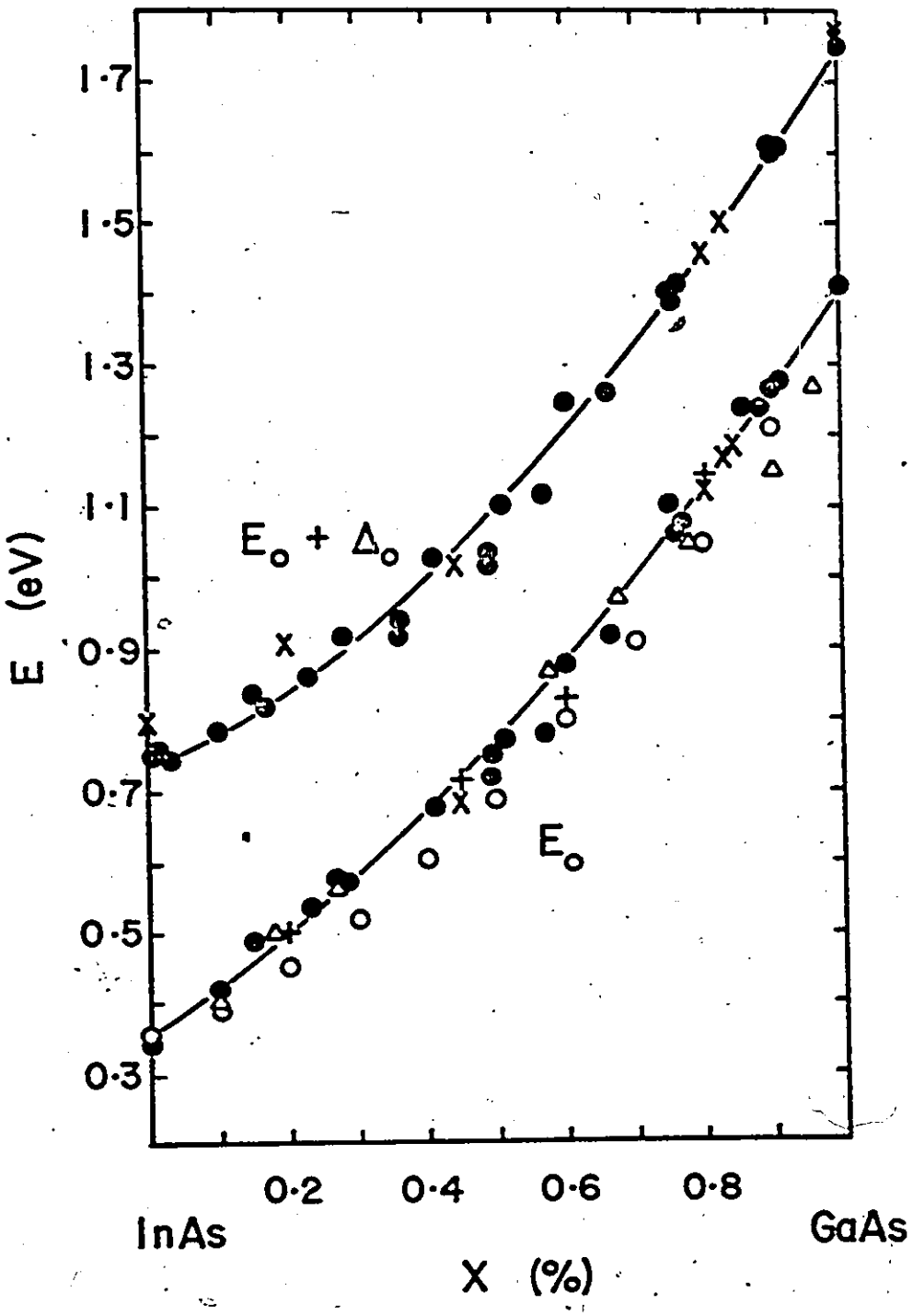

Figure 4-31. Showing the dependence of E_o and $E_o + \Delta_o$ structures with alloy composition. Results from (1W68) (x,+), 1H66 (o), (1W67) (Δ)are compared to this work (•).

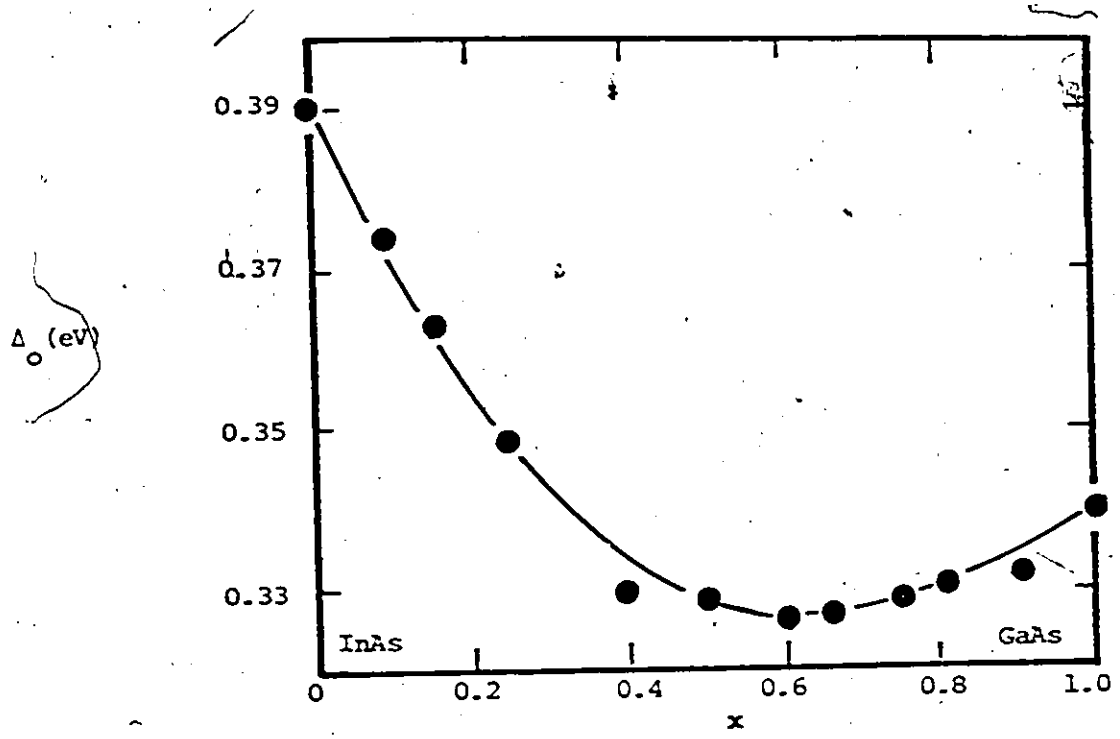

Figure 4-32. Showing the alloy dependence of Δ_o, with alloy composition for the (GaIn)As alloy system.

Table 4-2 Showing the coefficients of eq. 4-1 for the various transitions observed. The values are found by a least-squares fit to the experimental data.

	Structure	a	b	c	Reference
Ga(Al,As)	E_o	1.427	1.252	0.262	t.w.
	$E_o + \Delta_o$	1.765	1.135	0.337	t.w.
	E_o	1.430	1.311	0.20	(1P69)
	E_o	-	-	0.03	(3V70)
	$E_1(1)$	2.886	0.373	0.572	t.w.
	$E_1(1) + \Delta_1$	3.111	0.474	0.447	t.w.
	$E_2(2)$	2.956	0.642	0.362	t.w.
	$E_1(2) + \Delta_1$	3.204	0.5955	0.3611	t.w.
	E_1	-	-	-	(3V70)
	E'_o	4.456	0.500	-0.412	t.w.
	$E'_o + \Delta'_o$	4.626	0.311	-0.247	t.w.
	E_2	4.99	-0.122	-0.0178	t.w.
	E_2	-	-	-	(3V70)
In(As,P)	E_o	0.350	0.891	0.0210	t.w.
	$E_o + \Delta_o$	0.739	0.458	0.1322	t.w.
	E_o	0.34	0.71	0.27	(1A64)
	E_o	0.40	0.965	0.015	(1D63)
	E_o	-	-	0.23	(3V70)
Ga(As,P)	E_o	1.427	1.10	0.211	t.w.
	$E_o + \Delta_o$	1.765	0.892	0.182	t.w.
	E_o	1.44	1.09	0.21	(2T66)
	$E_o + \Delta_o$	1.78	0.88	0.18	(2T66)
	E_o	-	-	0.3	(3V70)

	Structure	a	b	c	Reference
Ga(In,As)	E_o	0.35	0.56	0.486	t.w.
	$E_o + \Delta_o$	0.743	0.344	0.676	t.w.
	E_o	0.35	0.687	0.388	(1W68)
	$E_o + \Delta_o$	0.80	0.328	0.712	(1W68)
	E_o	0.33	0.46	0.56	(1H66)
	E_o	0.35	0.71	0.28	(1W61)
	E_o	0.34	0.75	0.33	(1W67)
	E_o	-	-	0.57	(3V70)
In(As,Sb)	E_o	0.18	-0.41	0.58	(2W64)
	$E_o + \Delta_o$	0.979	-1.892	1.621	t.w.
	E_o	-	-	0.70	(3V70)

Table 4-3

System	$\Delta_o = a_o + b_o x + c_o x^2$			$\Delta_1 = a_1 + b_1 x + c_1 x^2$		
	a_o	b_o	c_o	a_1	b_1	c_1
(Ga,Al)As	0.34	-.113	.053	.24	-.007	-.033
In(As,P)	0.39	-.88	.64	.28	-.024	-.106†
Ga(As,P)	0.34	-.268	.048	.24	.032	-.142†
Ga(In,As)	0.39	-.202	0.152	.286	.0357	-.0337†
In(As,Sb)	0.80	-1.45	1.04	0.50	0.029	-0.249†
Ga(In,P)*	0.112	0.002	-0.033	0.0532	0.232	-0.1936
(GaIn)Sb	-	-	-	.5029	.0372	-.0577†

* (lA72)

† (lV70)

4.8 GaAs, ELECTROREFLECTANCE (SBER) NEAR 4.2°K

The low temperature measurement of E_o and $E_o + \Delta_o$ for GaAs was done on a sample $n \simeq 10^{15}$ (at 300°K). Originally it was of interest to measure these parameters as a function of temperature from 4.2°K to 300°K. However, here only one measurement is discussed. The relevant point here is to demonstrate that SBER measurements can be consistently obtained by the procedure described in Ch. 3.

Al_2O_3 was used as an insulating layer by the propoxide pyrolysis technique described before. Several runs were done until a uniform oxide layer could be obtained. The refractive index of Al_2O_3 at λ^* is ~ 1.768 (at 300°K). This is a little different from that of SiO (see Table A2-1). Therefore to obtain a film of approx. $\sim \lambda/2$ thickness it is suggested that since n(SiO) = gold colour ($\sim$ 2750Å) where d is the geometric thickness of the film. To have the same geometric thickness d with a layer of Al_2O_3 one must have

$$d = \frac{2750\text{Å}}{n(SiO)} \quad \text{and therefore}$$

$$n(Al_2O_3)\ \frac{2750\text{Å}}{n(SiO)} =$$

$$\frac{1.76}{2.0} \times 2750\text{Å} = 2421\ \text{Å}$$

which corresponds to a light blue color. An Al_2O_3 film was therefore prepared on a GaAs sample corresponding to this color. A Ni film was evaporated with a 50% transmittance.

* $\lambda = 5498$ Å

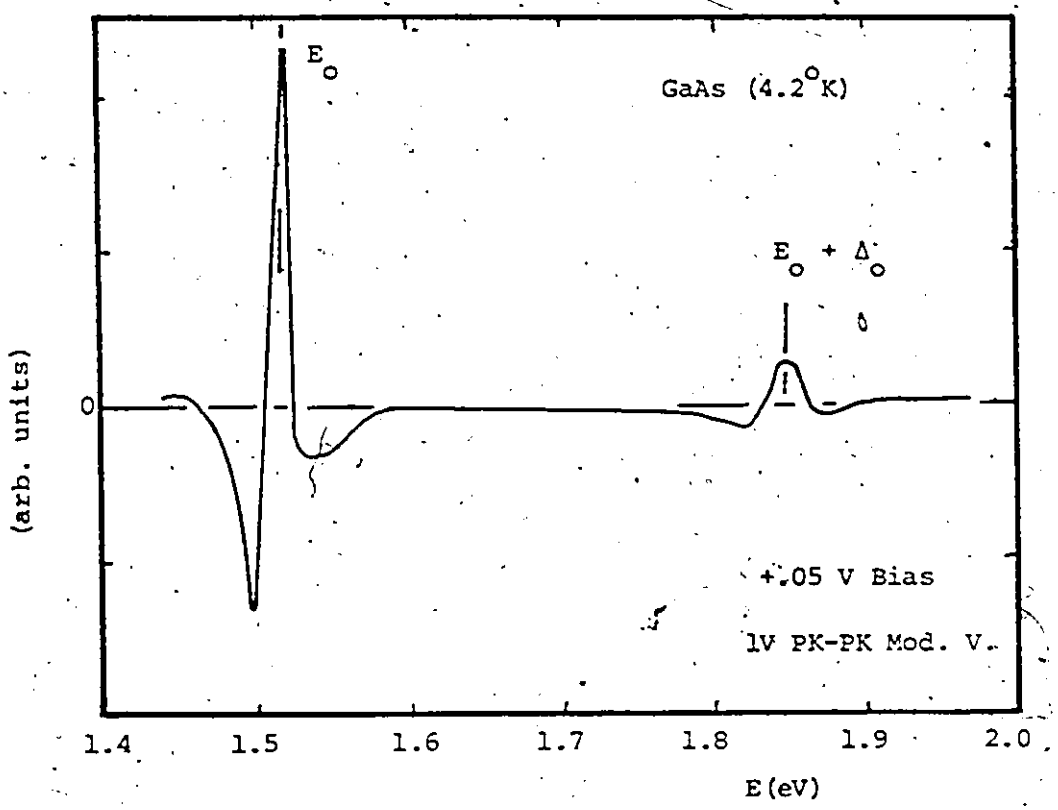

Figure 4-33. Showing the electroreflectance spectrum of GaAs at liquid He temperature in the energy region covering the E_o and $E_o + \Delta_o$ transitions.

Fig. 4-33 shows the electroreflectance of the GaAs - Al_2O_3-Ni configuration. Preparation and mounting were done as described in Ch. 3. Both E_o and $E_o + \Delta_o$ are measured. $E_o \sim 1.517 \pm 0.005$ eV and Δ_o is found to be $\sim 0.34 \pm 0.01$.

The first conclusion to be drawn from this is that the temperature dependence of Δ_o is if any, considerably smaller than that of the fundamental gap. Pressure measurements (1M71) give a dependence of Δ_o two orders of magnitude smaller than the dependence of E_o. A similar difference in the order of magnitude for the thermal dependence is likely.

1.517 eV compares well with 1.52 eV of (2S62). The colour of the Al_2O_3 film does not seem to change upon cooling suggesting little change in oxide thickness. This is the reason why Al_2O_3 was used rather than SiO as insulator.

CHAPTER V ANALYSIS AND DISCUSSION OF THE RESULTS

5.1 INTRODUCTION

It is the purpose of this chapter to use the data obtained by EER and SBER measurements to explain alloy processes in III-V pseudo binary systems. The measured quantitites such as E_o and Δ_o, conjointly with results obtained elsewhere (1V70, 1B73), are analysed to explain the effects that a non-periodic potential has on the band structure of the crystal.

After a brief review of the implications of the results obtained in ch. 4, the Δ_1 results obtained by Vishnubathla, 1V70 and those on Δ_o obtained in this work are shown to depend on the difference of the atomic splittings of the mixed atoms in the alloy.

The effect of the aperiodic potential on the alloyed crystal is then considered in terms of effects such as intraband and interband mixing. Each is shown to affect the final band structure of the alloy in an order of importance determined by the band structure in the VCA condition.

This concept is then further used to explain the experimental results obtained previously on the bottom of the conduction band effective mass. A satisfactory correlation with the experimental data is obtained.

5:2 SUMMARY OF THE RESULTS ON III-V ALLOYS (Ch. 4)

For the five alloy systems investigated [(Ga,In)As, In(As,P), Ga(As,P), In(AsSb) and (Ga,Al)As], the variation of E_o and $E_o + \Delta_o$ at Γ

has been found to vary non linearly as a function of composition (table 4-2). This is in good agreement with previous results (see other, results quoted in table 4-2) as well as some theoretical prediction (3V70). However, to date there is no theoretical prediction as to the alloy behaviour of Δ_o, the spin-orbit splitting of the valence band at Γ. Here we have found Δ_o to depend quadratically on alloy composition with a positive bowing parameter (see eq. 4-1, table 4-2, fig. 4-6, 4-10, 4-22, 4-27 and 4-32). These results show a different type of behaviour from that observed for Δ_1 (1V70, fig. 5-1), where the bowing parameter has been found to be negative.

With reference to the 2/3 approximation relating Δ_o to Δ_1 (section 1-6) for the III-V compounds, clearly alloying effects are in validating this approximation. The results suggest that the effect of the aperiodic part of the potential has a different effect on the alloy band structure at different points in the B.Z. Such effects have been thought constant throughout the B.Z. (3V70).

The experimental values of Δ_o can now be used in the Kane expression for effective mass (eq. 1-15) to calculate $m_o(\Gamma_{1c})$, when a linearly interpolated P^2 term is used over the alloy range. This is an improvement on previous calculations (1V68, 1V70) where Δ_o had been assumed to depend linearly on composition. It is clear from our results that narrow gap semiconductor alloys show a Δ_o dependence far from linear. However when the effective mass values obtained from experiment are compared with the predicted ones, even with accurate Δ_o values, these underestimate the

experimental results by a considerable amount ($\sim$ 10→ 12% in (GaIn)As at 50% alloy composition).

5.3 SPIN-ORBIT SPLITTING AT Γ AND Λ (Δ_o, Δ_1 RESPECTIVELY).

It has been discussed in Ch. 1 how information about spin-orbit splitting of the valence band at the Γ point (Δ_o) and in the Λ direction (Δ_1) are parameters of considerable interest. Their experimental values can be used to verify the accuracy of theoretical models (1M71, 1W71, 1C62, 1B69) as well as the calculation of other band parameters (1B62, 1C63, 1W64, 1C71).

In Kane's theory (1K56), the k.p method of band calculation, the spin-orbit splitting Δ_o of the valence band at Γ_{15} is given as

$$\Delta_o = \frac{3\hbar i}{4\, mc^2} \langle \Gamma_{15}^{(x)} \left| \frac{\partial V}{\partial x} p_y - \frac{\partial V}{\partial y} p_x \right| \Gamma_{15}^{(y)} \rangle \qquad (5.1)$$

where $\Gamma_{15}^{(i)}$ $(i = x,y)$ are the p type w.f. in the degenerate Γ_{15v} representation. V is the self consistent crystal potential and p is the linear momentum operator. This energy Δ_o results from the perturbation calculation when spin orbit coupling is used in the Hamiltonian (eq. 1-10).

It is interesting to note at this point that Δ_o is related to the gradient of the potential and therefore it should be particularly sensitive to aperiodic terms in the potential. It is additionally obvious that the greater part of the contribution to the above matrix element will

be near the atomic cores where the gradient of the potential and the electron momenta are largest. In the case of III-V compounds this contribution may be seperated out in terms of the individual atoms, (1B62). It would seem then that if the atomic core wavefunctions are considered similar to free atomic wavefunctions, the proper atomic splittings can be used in an expression for Δ_o (eq. 5-2). The electron affinity of various elements constituting the compound i.e., their ionicity, will modify the probability of an electron being centered around each atom. In the case of III-V compounds, the probability that the electron is associated with each atoms is viewed as if the electron were concentrated a fraction of the time around the III atom (t), and (1-t) around atom V. This involves a modification of the radial part of the wavefunction. There is also a renormalization which takes into account the changes between free atomic states and those defined within the unit cell of the solid. This last renormalizing parameter, N_o, has been taken to be the same for all III-V compounds and it is defined as the ratio of the spin-orbit splitting in Ge to the atomic splitting of the Ge atom, ($N_o \sim 29/20$). Thus from such considerations, if Δ_{III} and Δ_V are atomic splittings (1B62, table 5-1) of the elements constituting the compound, then the S-O splitting in the solid is given by

$$\Delta_o = N_o \, (t \, \Delta_{III} + (1-t) \, \Delta_V) \qquad (5.2)$$

Cardona and Greenaway (1C62) show that there is an analogous expression for Δ_1, the splitting in the Λ direction of the top two valence bands:

$$\Delta_1 = \frac{2}{3} \frac{3\hbar i}{4mc^2} < \Lambda_3^{(x)} \mid \frac{\partial V}{\partial x} P_y - \frac{\partial V}{\partial y} P_x \mid \Lambda_3^{(y)} > \qquad (5.3)$$

For analogous reasons to the case above, the matrix element in eq. (5-3) is taken to be roughly the same as that in eq. (5-1).

In view of the 2/3 approximation,(*) expression 5-2 for Δ_o may be rewritten for Δ_1 as

$$\Delta_1 = N_1 \, (t \, \Delta_{III} + (1-t) \, \Delta_V) \qquad (5.4)$$

where $N_1 = 2/3 \, N_o$

The quantity t, which is looked upon as the fraction of time the electron passes with the atom in question has been taken in the past to be 3/8 for a group III atom and 5/8 for a group V atom, as if the III-V compound were totally homopolar. t is an average value which in fact is not be the same for all III-V compounds. Hilsum (2W67) defined $t = (3-e^*)/8$, $1-t = \frac{(5-e^*)}{8}$. This definition includes a polarization of the bonds and assumes a certain localization of the electronic charge, whereby reducing the time-sharing of the electrons by the atoms. Using these values for the evaluation of Δ_o and Δ_1 might be more accurate as it does not use an average value of t for all compounds, however it requires a value of e* for each compound (2W67).

(*) (See page 31).

TABLE 5-1 Atomic spin orbit splittings (in eV) of column IIIA, IVA and VA elements as determined from atomic spectra.

Al	Si	P
0.016	0.028	0.046
Ga	Ge	As
0.12	0.20	0.29
In	Sn	Sb
0.27	0.60	0.80

If one considers Phillip's arguments (1P70), a different, perhaps a more reliable calculation of t is possible. Phillip's representation of the valence states by atomic orbitals (see eq. 1-1) in a bonding orbital configuration is;

$$\psi = \frac{1}{\sqrt{N}} (\phi_A + \lambda\phi_C) \tag{5.5}$$

for one of the tetrahedral bonds between the $A_{III} - C_V$ atoms. N is a normalizing parameter equal to $1 + \lambda^2$, and λ is a parameter sensitive to the difference in electron affinity between atoms of type A and C (1P60).

The electron density can now be found as

$$e|\psi|^2 = \frac{1}{N} e |\phi_A|^2 + \frac{\lambda^2}{N} e |\phi_C|^2 \tag{5.6}$$

TABLE 5.2

MATERIAL	Δ_o(1) k.p	Δ_o(1) (atomic sp) theory	Δ_o ionicity	Δ_o(2) expt.	Δ_1(1) k.p	Δ_1(1) (atomic sp) theory	Δ_1 ionicity	Δ_1 expt.
AlP		.099	.05			0.33	.03	
AlAs		.27	.265	.28 (4)		.180	.176	.20 (4)
AlSb	.75	.60	.83	.7	.41	.40	.55	.40 (3)
GaP	.10	.10	.104	.10	.073	.06	.06	.10 (3)
GaAs	.34	.33	.335	.34	.22	.22	.223	.22 (3)
GaSb	.80	.66	.860	.73	.46	.44	.573	.47 (3)
InP	.11	.17	.160	.11	.11	.113	.106	.15 (3)
InAs	.43	.40	.411	.39	.28	.267	.274	.28 (3)
InSb	.82	.72	.89	.81	.48	.48	.59	.50 (3)

(1) Willardson & Beer Vol. 3 ch. 1 (2W67) (2) (2C69) (3) (1V70) (4) (1070)

where any interaction between ϕ_A and ϕ_C state has been neglected. If one now uses the definition of ionicity as the difference in electron density per unit charge between two elements and one keeps in mind that in (5-6) $\frac{1}{N}$ and $\frac{\lambda^2}{N}$ are essentially the fraction of time the electron spends with atom A and atom C respectively, then the ionicity

$$f_i = \frac{\lambda^2}{N} - \frac{1}{N} \tag{5.7}$$

and

$$t_{III} = \frac{1-f_i}{2}, \quad t_V = \frac{1+f_i}{2} \tag{5.8}$$

By using ionicity values found by Phillips (1P70) we can calculate the t_{III} fraction for each III-V compound. Table 5-3 shows the values calculated and they can be compared to the value of 3/8. Some interesting deviations from this value can be observed. The general trend with the exception of AlSb is that heavier ie. with more metallic compounds, have a larger value of t_{III}. All these values are furthermore lower in value than 3/8 or 0.375. The more ionic, ie. lighter compounds have smaller values of t_{III}.

Where spectroscopic values for the atomic splittings are used together with the experimental values for Δ_o and Δ_1 in the case of the compounds one can calculate the normalizing parameters N_o and N_1

$$N_o = \frac{\Delta_o \text{ (expt.)}}{Q_o}$$

$$N_1 = \frac{\Delta_1 \text{ (expt)}}{Q_o}$$

where with t_{III} and with the values of atomic splittings Δ_{III} and Δ_V one finds

$$Q_o = t_{III}\Delta_{III} + (1 - t_{III})\,\Delta_V$$

The values of N_o and N_1 are also shown in table 5-3 and can be compared with the value of 29/20 = 1.45 for N_o and 2/3 (1.45)= 0.967 for N_1.

5.4 THE SPIN ORBIT SPLITTING IN THE VCA WITH APERIODIC EFFECTS

When two compounds are alloyed together [viz., $(AC)_x(BC)_{1-x}$] with the zinc-blende structure, it has been shown how atoms of the same valency freeze out on the same f.c.c. sublattice. The sublattice associated with the atoms that are common to both constituents will contribute an atomic splitting Δ_C to eqns. 5-2 and 5-4. However, by virtue of the V.C.A. where the potentials in the crystal are compositionally averaged, the contribution to the s-o splitting in the VCA will be equally averaged compositionally $x\Delta_A + (1-x)\Delta_B$. This is clear when one remembers that the splitting is proportional to the gradient of the potentials. Therefore if for example one associates atoms A and B with column III of the periodic table ($t_{III} = t$) then a generalized expression for spin orbit splitting ($i = 0$ for Δ_o, $i = 1$ for Δ_1)

$$\Delta_i = N_i[\, t\,(x\Delta_A + (1-x)\Delta_B) + (1-t)\Delta_C] \qquad (5.9)$$

results.

TABLE 5.3 Showing a survey of parameters for most III-V compounds.

COMPOUND	f_i	t	Q_o	Δ_o	Δ_1	N_o	N_1
AlP	.307	.346	.03562	-	-	-	-
AlAs	.274	.303	.1905	.028 (1)	0.20 (1)	1.47	1.05
AlSb	.426	.287	.5749	(.7)	(.4)	(1.30)	(0.696)
GaP	.374	.313	.0692	0.12*	0.10 (2)	1.74	1.45
GaAs	.310	.345	.2313	0.34	0.24 (2) 0.22 (3)	1.47	1.06 0.96
GaSb	.261	.369	.5491	0.80	0.47 (2)	1.49	0.88
InP	.421	.289	.1107	0.16* 0.11(3)	0.15 (2) 0.10 (3)	1.44 0.99	1.35 0.86
InAs	.357	.321	.283	0.39	0.28 (2)	1.35	0.99
InSb	.321	.339	.6203	0.81	0.50 (2)	1.34	0.83
RATIO VALUE		0.375				1.45	0.9667

(1) (1070), (2) (1V70) (3) (2T66) *Extrapolated from alloy data.

This expression is linear in composition and follows the initial 2/3 approximation for the compounds. One must note that this expression does not take into account the changes of N_i and t that occur from one constituent to the other. As seen in table 5-3 in some alloy systems such differences can be significant. Invoking the VCA where parameters can be linearly interpolated between the compounds, (5-9) may be re-written as

$$\Delta_i = N_{iB}(1+\delta_i x)\{ [t_B(1+\tau x)(x\Delta_A+(1-x)\Delta_B] + [1-t_B(1+\tau x)\Delta_C]\} \qquad (5.10)$$

where $\delta_i = (N_{iA}-N_{iB})/N_{iB}$ and $\tau = (t_A-t_B)/t_B$ allow the N_i and t terms to be varied linearly between the values found for the two compounds. N_{iA}, t_A are associated with compound AC, $N_{iB} t_B$ with compound type BC Therefore now the Δ_i dependence on alloy composition is no longer lineraly dependent on x.

The effect of disorder in the alloy lattice is considered by way of the aperiodic part of the potential (eq. 1-20). It has been treated by second order perturbation by Parmenter (1, 2P55) eq. (1-22) and the effect on any energy term which is due to the non-periodic part of the potential has been found proportional to x(1-x). This term therefore disappears at either of the terminal materials and has greatest effect at x = 0.50. The interpretation given by Cardona (2C62) to the proportionality constant is that it depends on the mean square deviation of the potential from its VCA value. It is proposed here

to investigate further the results obtained on Δ_o (Ch. 4) and Δ_1 (fig. 5-1), (IV70), in the light of the above arguments and possibly to arrive at a more quantitative meaning of γ_i, the proportionality constant which takes into account the non-periodic effects in the potential.

Therefore when we want to consider disorder effects, eq. 5-10 is rewritten with the additional term $\gamma x\,(1-x)$ ie.

$$\Delta_i = N_{iB}(1+\delta_i x)\{\,[t_B(1+\tau x)(x\Delta_A+(1-x)\Delta_B)] + [1-t_B(1+\tau x)\Delta_C]\}+\gamma_i x(1-x) \tag{5.11}$$

which would therefore by the proper adjustment of the γ_i term predict either the Δ_o and/or Δ_1 alloy behaviour.

It is clear from eq. 5-11 that if γ_i is not the same for Δ_o and Δ_1 (ie. $\gamma_o \neq \gamma_1$) then the 2/3 approximation is invalidated by alloying effects. When we compare results obtained for Δ_o and Δ_1 (fig. 5.1) it is implied by the results that $\gamma_o \neq \gamma_1$ and furthermore that they carry opposite signs.

Vishnubathla and Woolley used eq. 5-9 as the VCA component in their initial analysis. The effect of the aperiodic potential was then, as with the arguments for eq. 5-11, to add on a term proportional to x(1-x) ie.

$$\Delta_1 = N_1\,[t(x\Delta_A + (1-x)\Delta_B) + (1-t)\Delta_C] + \gamma_1(x)(1-x)$$

When expanded in x they showed that it reduces to

$$\Delta_1 = a_1 + b_1 x - c_1 x^2 \tag{5.12}$$

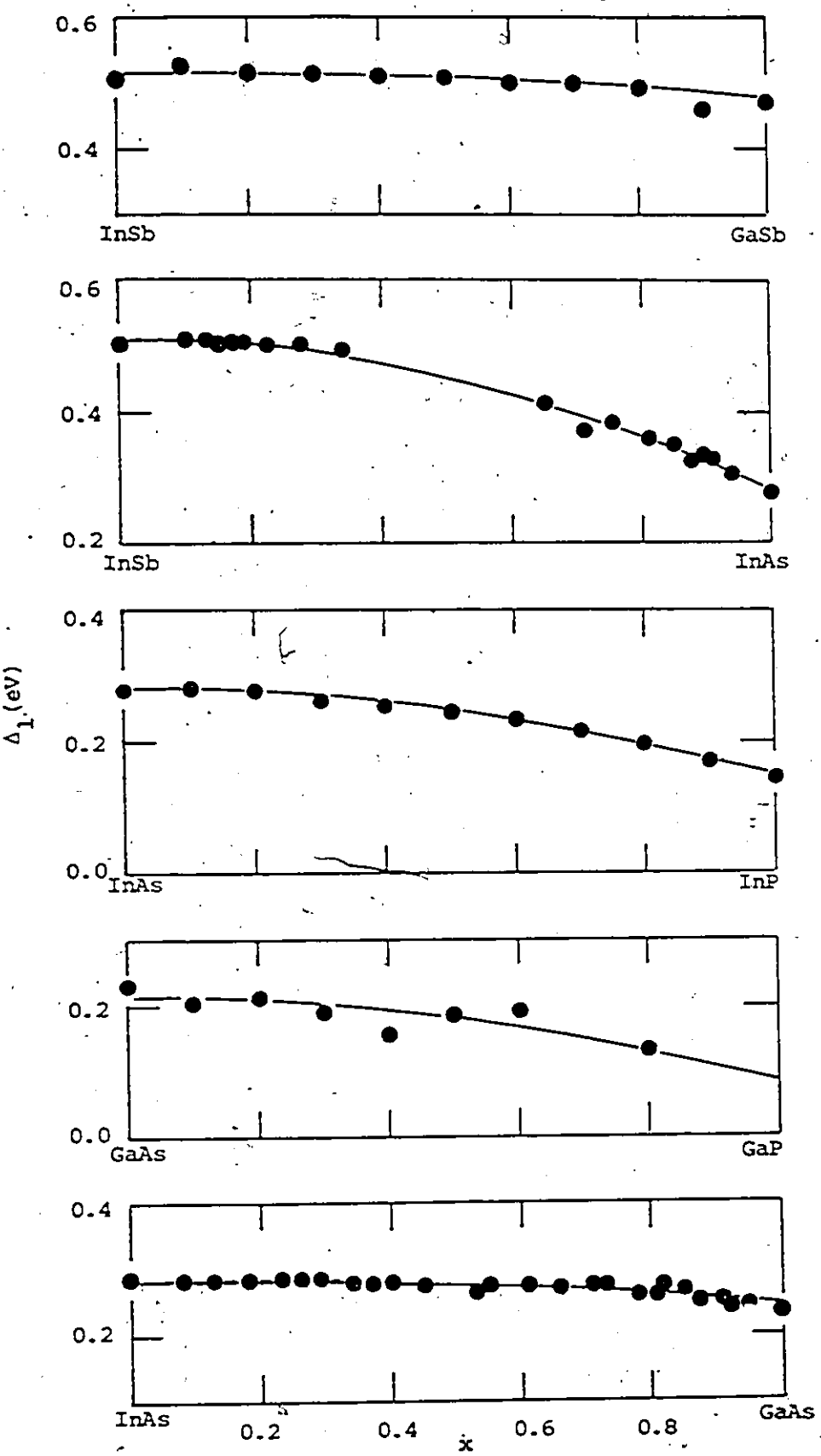

Figure 5-1 Showing the results on Δ_1 obtained by Vishnubathla (1V70).

where

$$a_1 = N_1 \left[t\, \Delta^B_{III} + (1-t)\, \Delta^C_V \right]$$

$$b_1 = N_1 (1-t) \left(\Delta^A_{III} - \Delta^B_{III} \right) + \gamma_1 \qquad (5.13)$$

$$c_1 = \gamma_1$$

A least square fit of Δ_1 and x in the form of eq. 5.12 gave values of b which were very small if not zero, and it was found that an equally good fit could be obtained when b was chosen as zero. Their fits were always done from the higher Δ_1 compound side.

It has been noted in the least squares fit to Δ_o and a further analysis of Δ_1 results that when the fit is done from the high energy value $b(\Delta_o) \sim -2\gamma_o$ and $b(\Delta_1) \sim 0$ within the experimental error associated with the coefficients of the least squares fit. When the analysis is done from the lower energy end ie. Δ_o, Δ_1 are smaller for the constituent present at x = 0, then $b(\Delta_o) \sim 0$ and $b(\Delta_1) \sim 2\gamma_1$ (see table 4-3). Further

$$-b_i \cong 2\gamma_i \cong 2c_i \qquad (5.14)$$

In view of the terms involved in 5.13 for the expression for b_1, it would appear that γ_i should depend somehow on $\Delta^A_{III} - \Delta^B_{III}$ in the case of mixed III alloys and $\Delta^A_V - \Delta^B_V$ in the case of mixed V alloys.

Eq. 5-11 shows an expression where all terms are determined by the terminal materials of the alloys. The only quantity which may take on parametric values is γ_i. It is therefore possible to fit the experi-

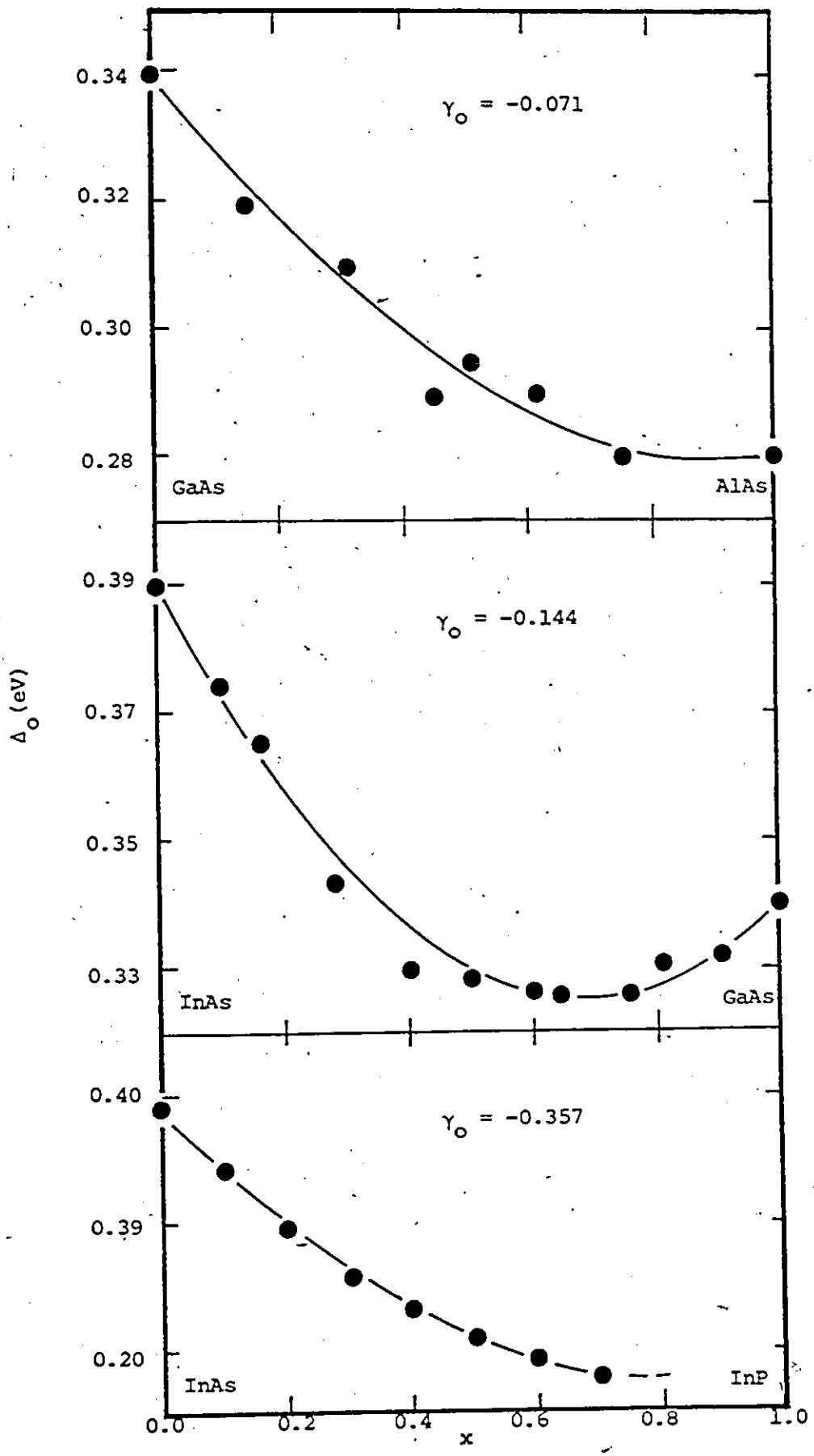

Figure 5-2. Diagram showing the experimental points for Δ_o and the fit (solid line) according to eq. (5.11) as a function of alloy composition x for some alloy systems.

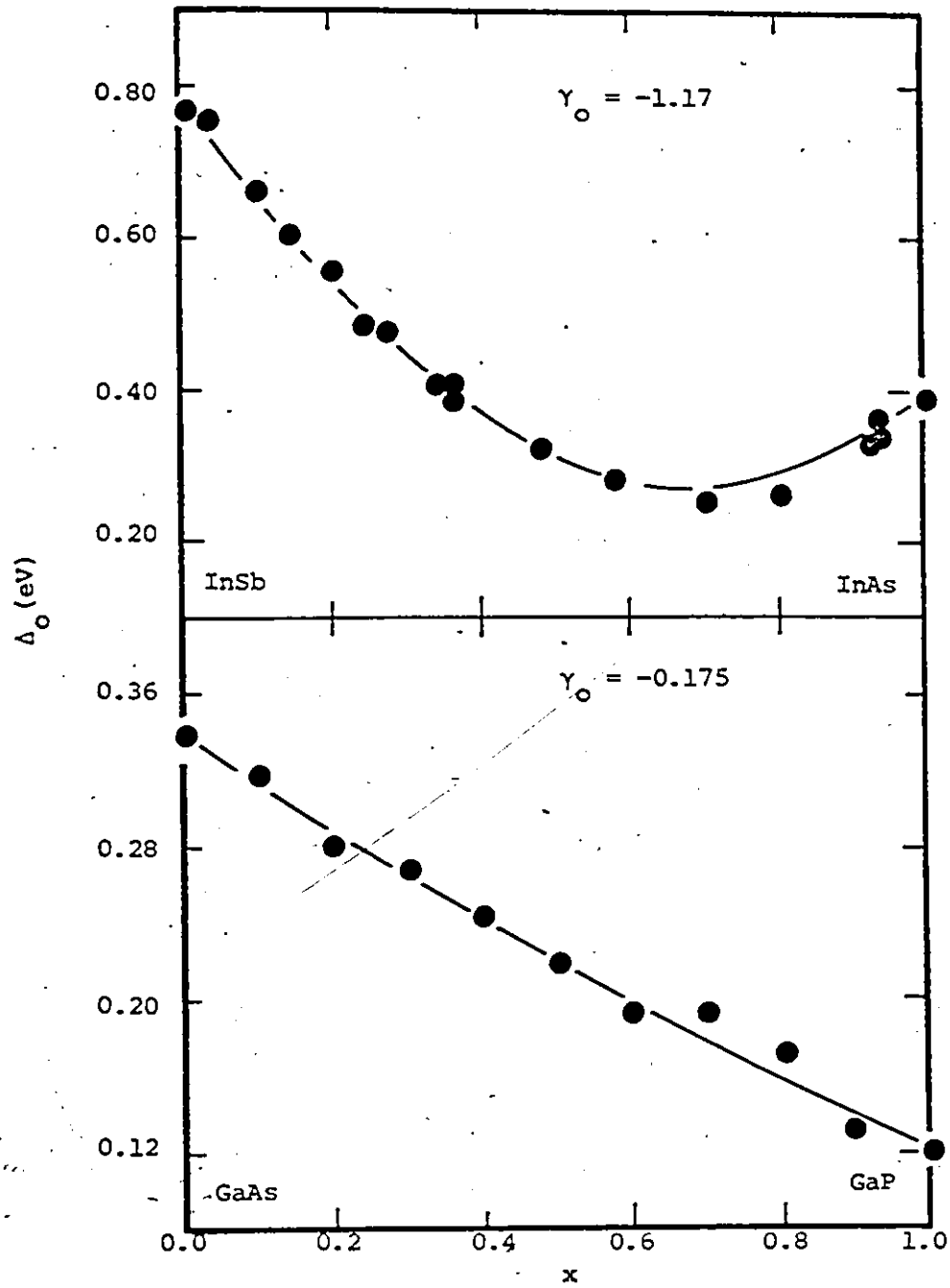

Figure 5-3. Diagram showing the experimental points for Δ_o and the fit (solid line) according to eq. (5.11) as a function of alloy composition x for some alloy systems.

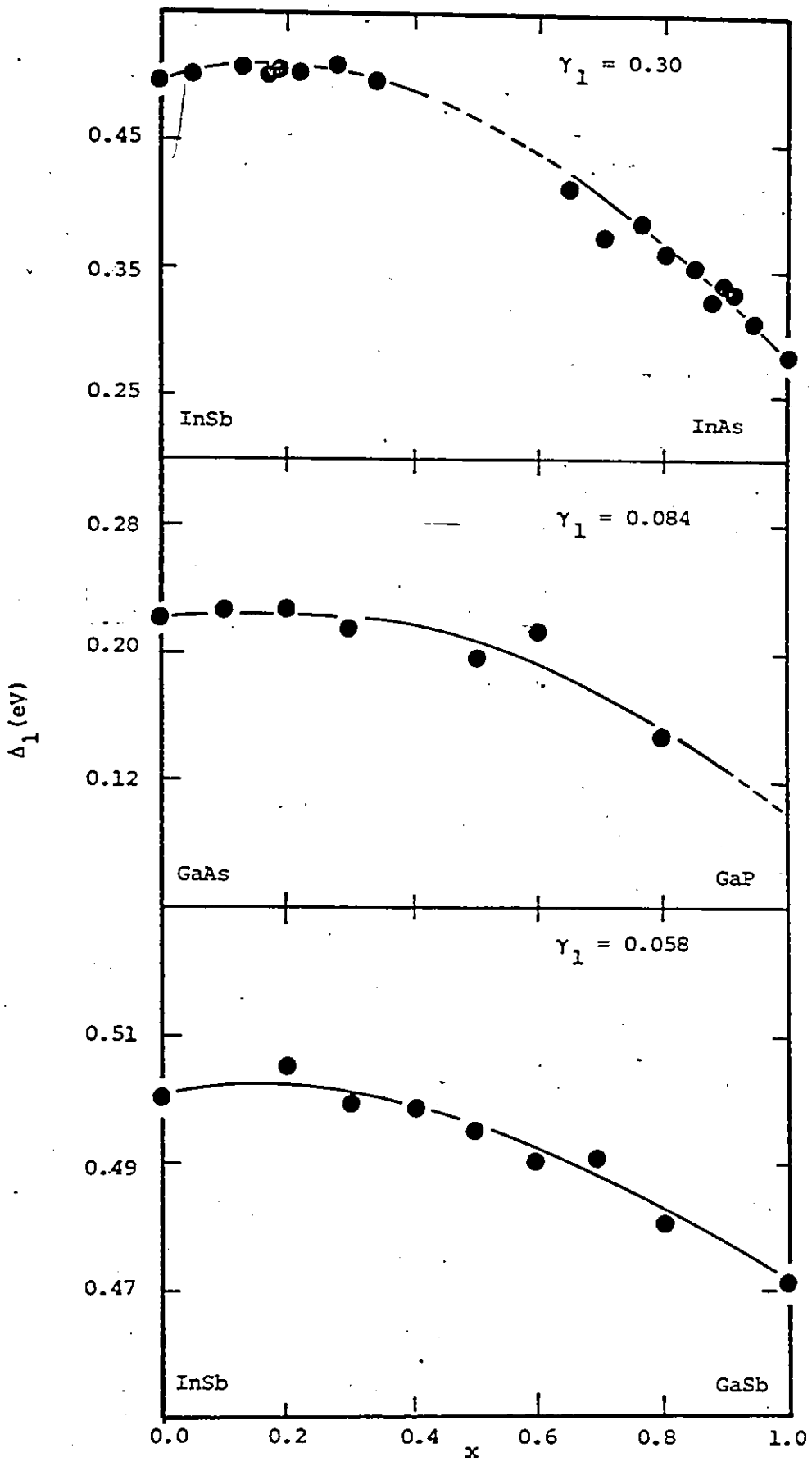

Figure 5-4. Diagram showing the experimental points for Δ_1 and the fit (solid line) according to eq. (5.11) as a function of alloy composition x for some alloy systems.

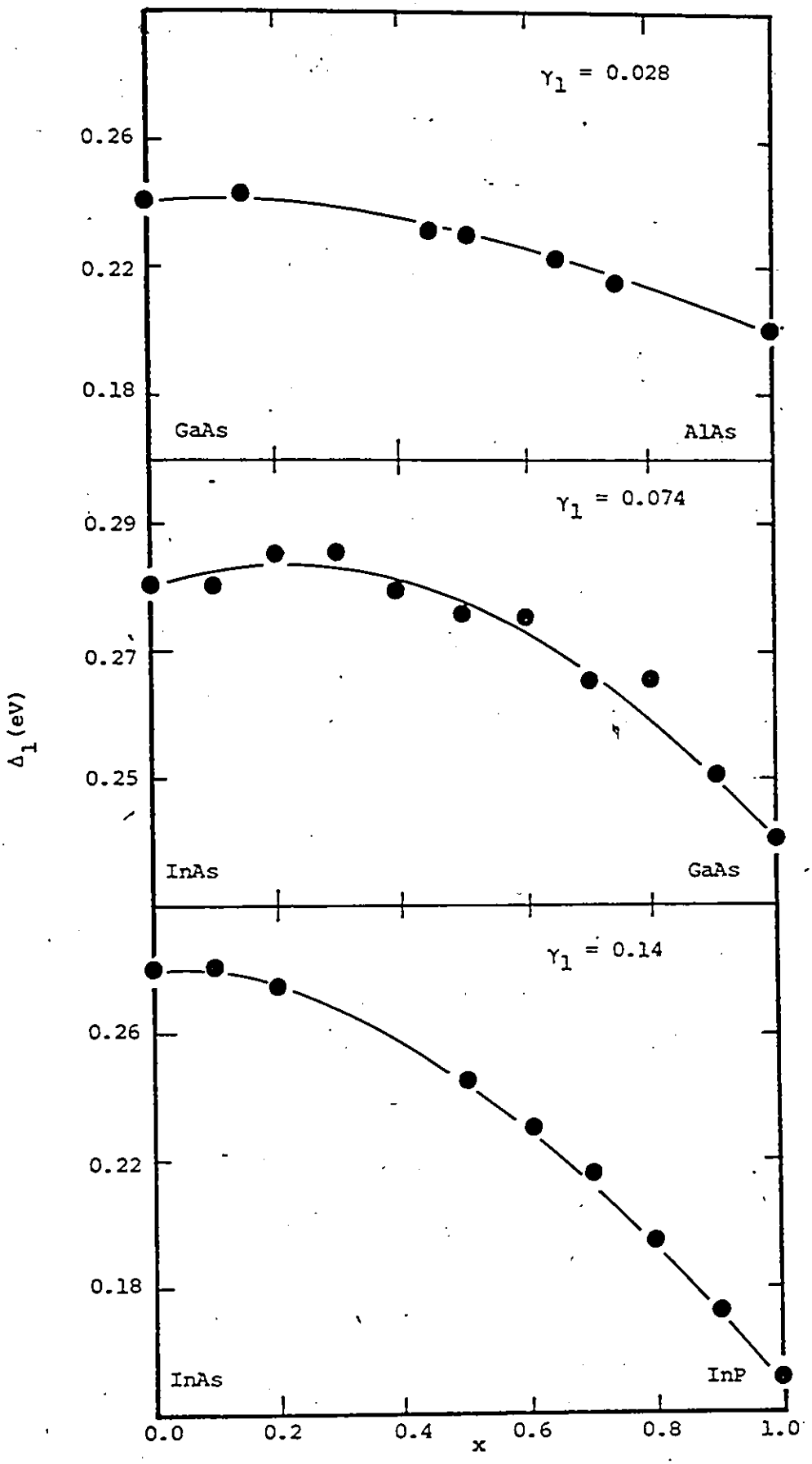

Figure 5-5. Diagram showing the experimental points for Δ_1 and the fit (solid line) according to eq. (5.11) as a function of alloy composition x for some alloy systems.

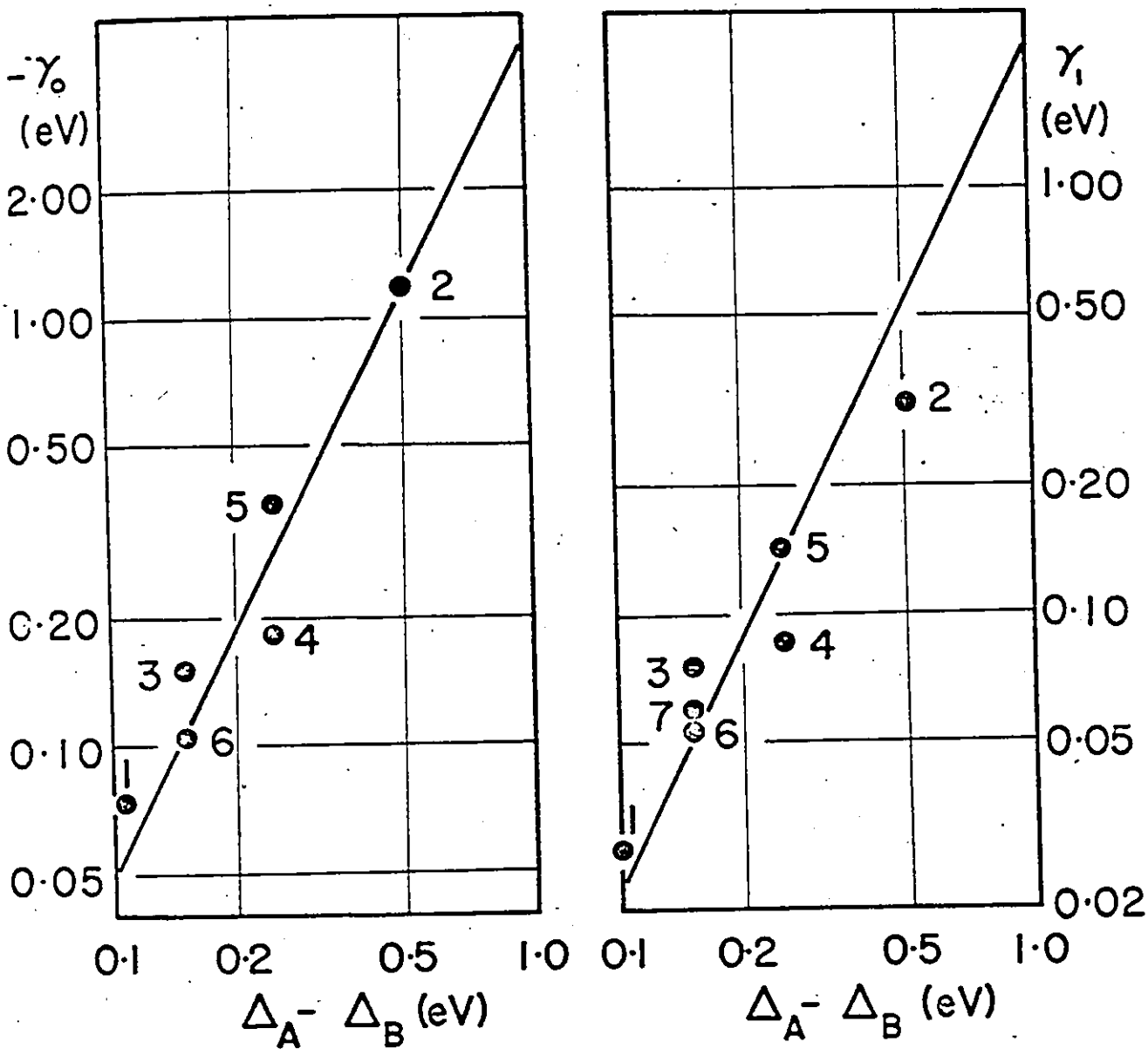

Figure 5-6. Showing the relationship of γ_o and γ_1, the one free parameter in equation (5.11), to the difference between the atomic splittings of the mixed constituents, $\Delta_A - \Delta_B$. The straight line represents a quadratic dependence of γ_i with $\Delta_A - \Delta_B$. The agreement between this line and the points are close to the quadratic dependence

Alloy systems are: 1. $Al_xGa_{1-x}As$ 2. $InAs_xSb_{1-x}$ 3. $Ga_xIn_{1-x}As$ 4. GaP_xAs_{1-x}
5. InP_xAs_{1-x} 6. $In_xGa_{1-x}P$ 7. $Ga_xIn_{1-x}Sb$.

mental information for all the alloy systems investigated by changing γ_i. One then minimises the least squares deviation between the theoretical values predicted with the parameter γ_i to the experimental values. The fitted curves and the experimental points obtained for Δ_o in Chapter 4 and for Δ_1 in (1V70) are shown in fig. 5-2 to 5-5 for the various alloy systems studied.

The values of γ_o for Δ_o and $-\gamma_1$ for Δ_1 thus obtained were inspected for all the alloy systems. The remarkable trend observed was that the values of the γ_i were very close in value for alloy systems where the mixed elements are the same (eg. (In,Ga)As, (In,Ga)P, (In,Ga)Sb). This suggested, in addition to the conclusions drawn from eq. 5-13 and 5-14, that γ_i might be a function of $\Delta_A - \Delta_B$ where Δ_A, Δ_B are atomic splittings. This dependance would be also logical since when $\Delta_A = \Delta_B$ for all intents and purposes, no effects due to the aperiodic potential should be present.

To investigate this dependance, log-log plots of γ_o and $-\gamma_1$ vs $\Delta_A - \Delta_B$ are drawn (fig 5-6). The second order perturbation approach to the treatment of the aperiodic potential suggests that $\gamma_i \alpha (\Delta_A \approx \Delta_B)^2$, (1A55, 2P55, 2C62). Lines satisfying this condition are drawn through the experimental points comparison to the straight line indicates that a square law dependance is observed.

Therefore to a good approximation γ_i may be written as

$$\gamma_i = k_i (\overline{N_i t})^2 (\Delta_A - \Delta_B)^2 \qquad (5.-15)$$

where $k_i (\overline{N_i t})^2$ is a normalizing parameter for all compounds considered.

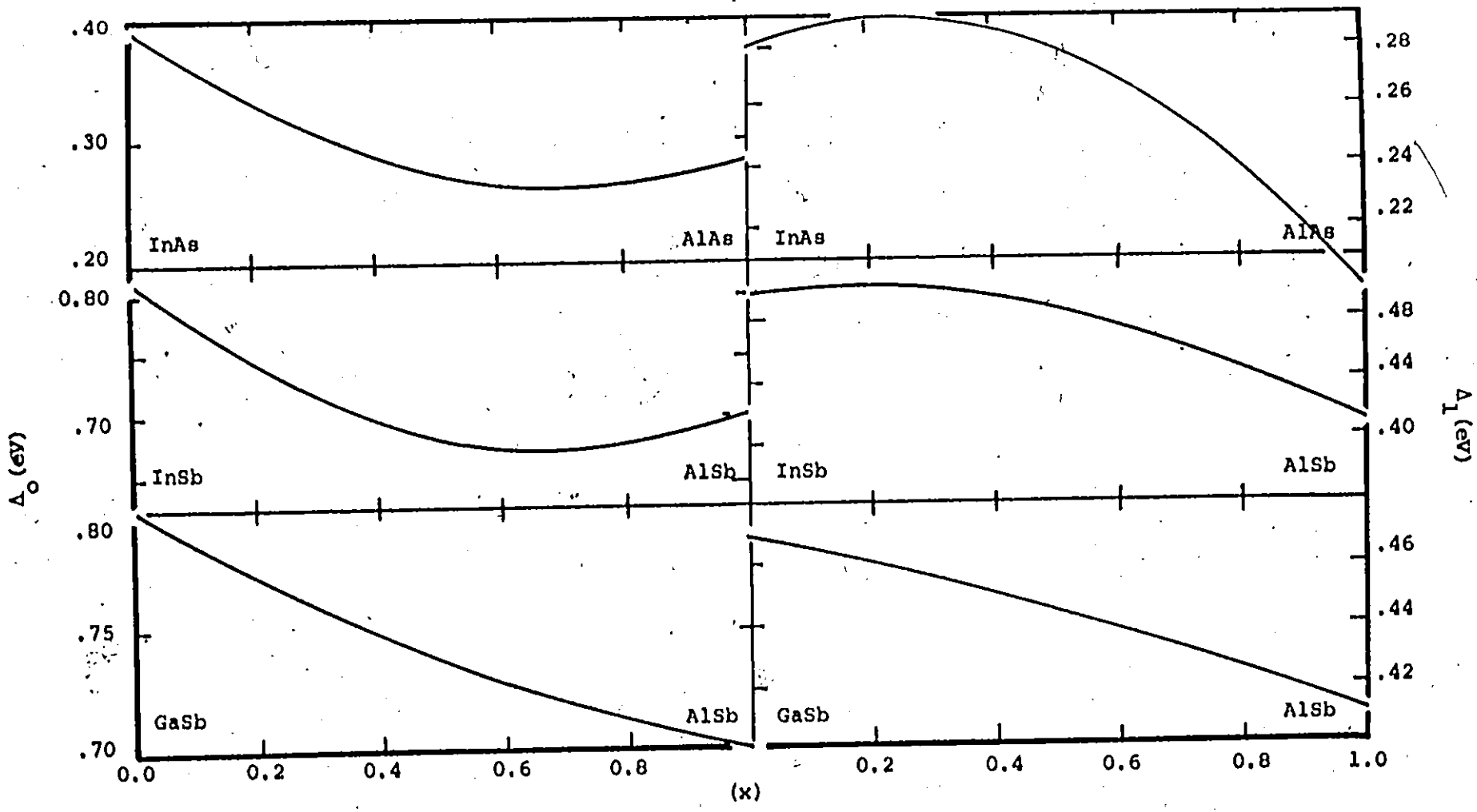

Figure 5-7. Predictions for Δ_o and Δ_1 for a number of alloy systems as a function of composition using γ_o and γ_1 from equation (5.15).

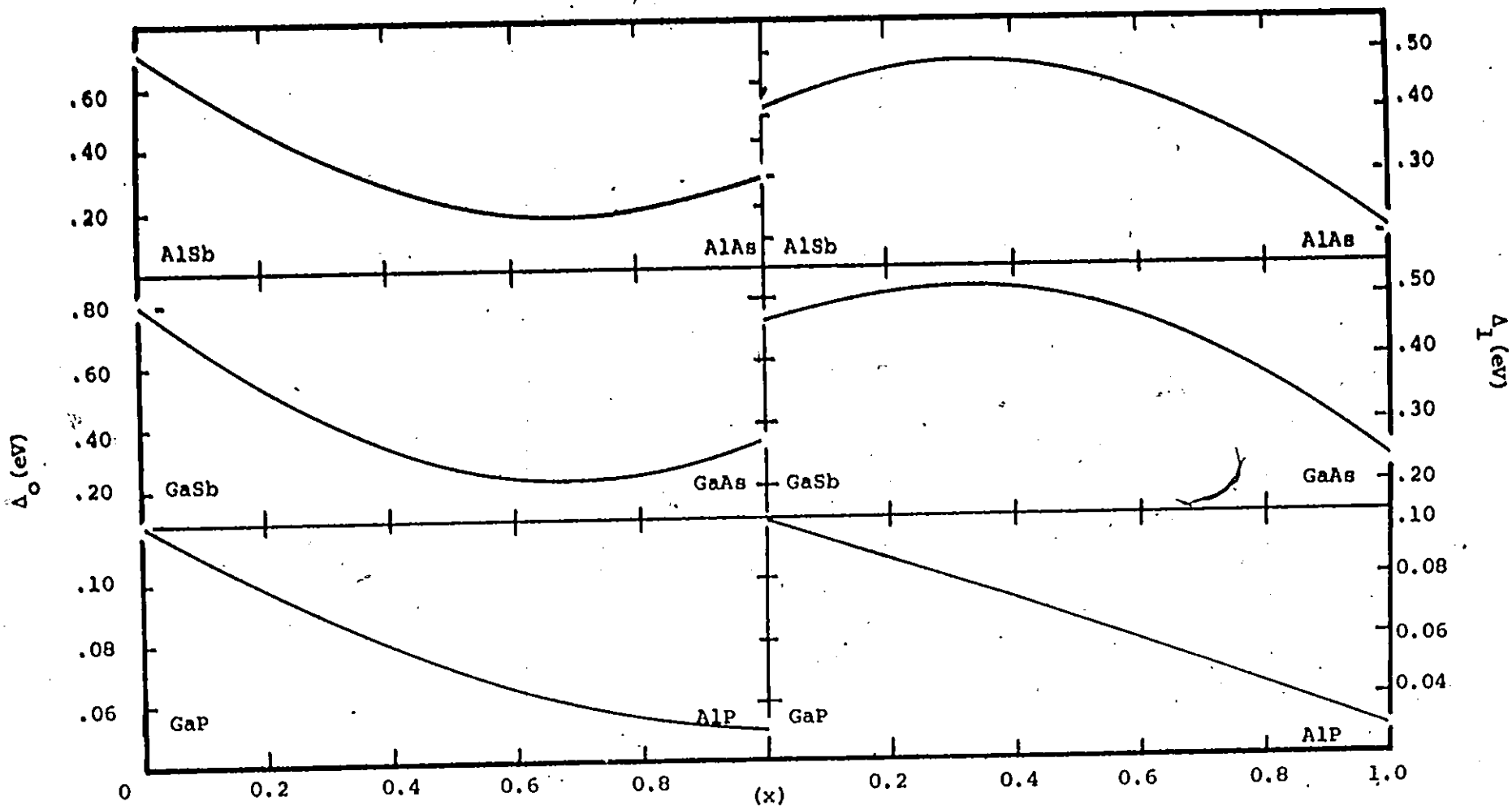

Figure 5-8. Predictions for Δ_o and Δ_1 for a number of alloy systems as a function of composition using γ_o and γ_1 from equation (5.15).

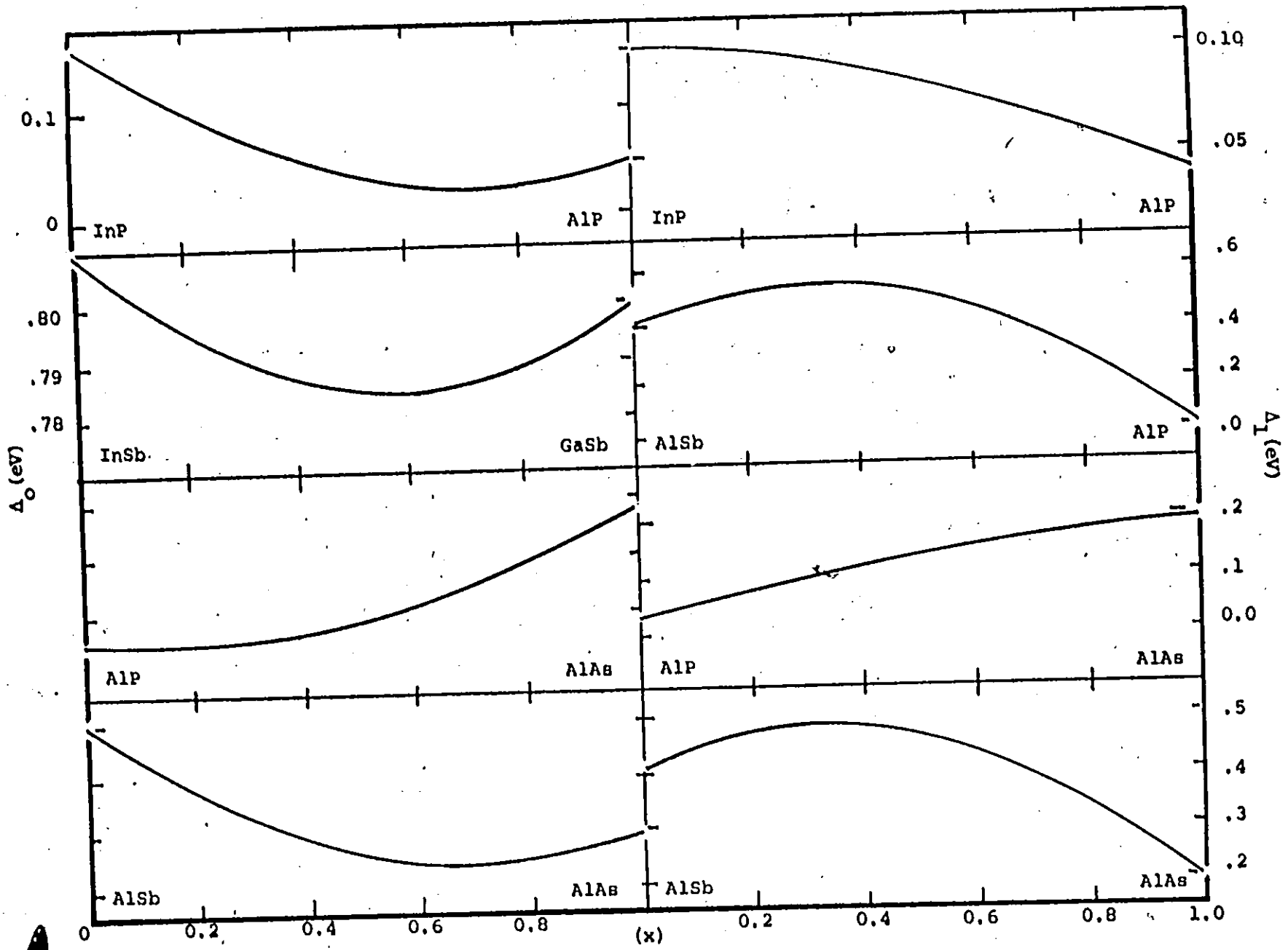

Figure 5-9 Predictions for Δ_o and Δ_1 for a number of alloy systems as a function of composition using γ_o and γ_1 from equation (5.15).

While the above analysis clarifies how the γ_i term is related to characteristic parameters of the constituents, it does not explain why the values of Δ_o are less and Δ_1 are larger from their values in the VCA. Disorder effects have been reported to be independent of k throughout the Brillouin zone (1V70). The result from eq. 5-16 implies that k_o and k_1 are of opposite sign.

In fact, the above analysis is not sensitive to changes in band-structure and its purpose was to establish that a disorder parameter can be related to a semi-empirical formula.

The expression in 5-15 has been used to predict Δ_o and Δ_1 behaviour with alloy composition for a number of alloy systems. These can be seen in fig. 5-7 to 5-9.

5.5 EFFECTS OF THE APERIODIC POTENTIAL ON THE VCA BAND STRUCTURE.

The usual way to describe an alloy is as if it were ordered and to invoke the VCA (1N31) which assumes a perfect lattice with compositionally averaged atomic potentials at each site. The resulting band structure is exactly analogous to that of the pure compounds forming the alloy, because it is assumed that the crystal potential has no disorder.

The effect of the aperiodic term on the band structure due to disorder in the lattice has then to be included (1, 2P55, 1M36 etc). In some work it has been suggested that the effect of the aperiodic term is small (2J69, 2R71, 2R72), and can thus be ignored.

However the experimental data presented here on E_o and Δ_o in addition with results on E_o, E_1, Δ_1 represent a collection of information on alloy behaviour that provide a good test for any proposed theoretical calculation of band structure. Any such analysis should be capable of making predictions concerning all these parameters. It is the contention of the present analysis that the disorder effects are of importance and must be included in to any prediction of alloy band parameters.

It is clear from the type of band structure analysis discussed in the previous chapters that a rigorous derivation from standard theory will be extremely difficult because large energy corrections are needed to the results of the VCA to explain the experimental data. In fact, in those alloy systems with narrow band gap, the aperiodic term would have to be so large that normal perturbation theory is not valid when the behaviour of the Γ point is being considered. Therefore, some different approach must be used.

It has been widely supported from experimental data that the variation of the fundamental gap as well as optical transitions, will depend quadratically on alloy composition

$$E(x) = a + bx + cx^2 \qquad (5\text{-}16)$$

where c is the bowing parameter and it is usually positive (Δ_1 (fig. 5-1) clearly exhibits a negative c).

The aperiodic potential in an alloy has been treated by Nordheim and Muto. They showed that the treatment of the aperiodic terms by

perturbation theory does not affect the alloy band gaps in the first order approximation. Parmenter and others (1, 2P55, 3W68, 1068) showed that the effect of higher order perturbation on the band structure is similar to that of the effect of an applied electric field (Chapter 2). The presence of the aperiodic term breaks the symmetry of the crystal upon alloying and the adjacent states within the same band (intra-band) interact. The second order perturbation term

$$\delta E_2 = \sum_{i \neq j} \frac{|\langle c_i|\delta V|c_j\rangle|^2}{E_c(i) - E_c(j)} \qquad (5\text{-}17)$$

has two effects. One, it lowers the energy at a band minimum (increase the band energy at a maximum) and second, it may diffuse the states of the extremum into the forbidden gap region. This last effect has been demonstrated as the tailing of the density of states function into the forbidden region near a van Hove singularity. The experimental evidence for this would result as broadened optical spectra, which to present date may be attributed to alloy inhomogeneities. However this analysis considers effects only on one band and for adjacent states within that band.

The result of this treatment is to reduce the band edge itself as a function of composition. This effect is well illustrated by the results shown in the previous chapter as well as several of the references in it.

As mentioned above, in the case of narrow gap alloys (viz. In(Sb,As)) the correction term δE_2 (eq 5-17) represents energy terms exceeding the

justification of perturbation theory. Therefore the validity of the above approach may be questionable.

It is the conjecture of the present analysis that the additional effect of the aperiodic term between two bands (say the lowest c.b. and the highest v.b. at Γ) must be considered if the alloy behaviour of such parameters as E_o, Δ_o, Δ_1 and $m^*(\Gamma_{1c})$ is to be understood. The breaking of the crystal symmetry upon substitutional alloying would therefore result in the interaction between the valence and the conduction band states:

$$\delta E_2' = \sum_{c_f \neq v_i} \frac{|\langle c_f|\delta v|v_i\rangle|^2}{(E_{c_f} - E_{v_i})} \qquad (5\text{-}18)$$

The effect of the $\delta E_2'$ term is to mix the symmetry of states between the conduction and the valence band thereby transferring some character from each band to the other, (interband). It is the purpose of this analysis to demonstrate on the basis of the results obtained here and elsewhere that this is an important effect predominant particularly in the case of narrow gap semiconductors.

It is possible to illustrate the importance of these interactions by way of studying some trends observed already in some III-V compound semiconductors.

There is a loss of symmetry from a IV elemental semiconductor to a III-V compound which is viewed as the effect of a perturbing assymmetric potential (1, 2P55, 1V72). It is stronger in the case of larger

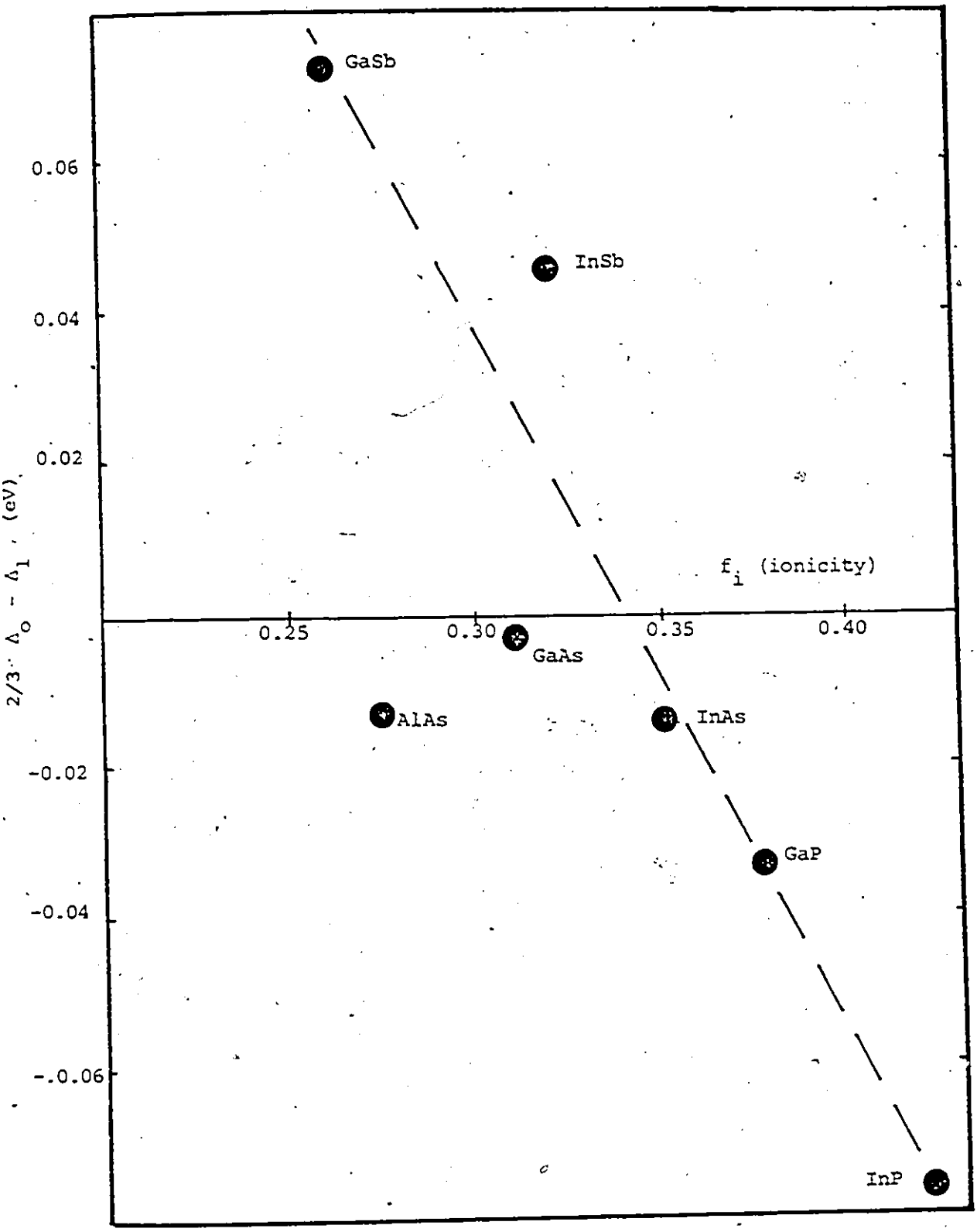

Figure 5-10 Showing the deviation from the 2/3 rule as a function of ionicity.

ionic compounds. A larger ionicity implies an increase in the direct gap and a decrease in the spin orbit splitting (eq. 5-8 and 5-2) at Γ. Larger band gaps (and smaller spin orbit splittings) indicate a stronger interaction between the s and p states of the two bands. Since this type of interaction is considerably smaller at Γ than in the Λ direction (viz., $E_o < E_1$), the spin orbit splitting Δ_1 will be less affected than Δ_o. The deviations from the 2/3 rule as a function of ionicity illustrates this effect and can be seen in fig. 5-10. The deviation decreases and it is negative as the ionicity increases. This interband interaction via the assymmetric potential in the compound semiconductor and the reduction of Δ_o accompanied by it shows an interesting trend which may be a guideline in the study of alloy processes.

The overall situation for alloy band structure is more complicated and less obvious than the above picture. The effects of the aperiodic potential on the band structure of the alloy are usually treated separately but the experimental information is obviously a combination of all these.

5-6 THE EFFECT OF THE APERIODIC TERMS ON E_o

In an attempt to calculate the variation of E_o with x, Van Vechten and Bergestresser (3V70) used the dielectric model (1P70, 4V72) in the VCA to give values of E_{ov} (E_o in the VCA). The curves of E_{ov} vs x were obtained showing a quadratic dependance (bowing para-

meter c_i) such that $c_i < c$ always. The difference $E_{ov} - E_o = \delta E(x)$ was attributed to the aperiodic potential terms due to disorder. Van Vechten and Bergestresser showed that to a good approximation, for all the alloy systems $\delta E(x)$ can be related to the heteropolar part of the average gap. (3V70)

$$\delta E(x) = x(1 - x) \frac{C_{FG}^2}{A} \qquad (5\text{-}19)$$

where C_{FG} is defined as the screened Phillips electronegativity difference between the mixed elements (1P70) and A in a band parameter, found by comparison with experiment to be $\sim$1.0 eV, (3V70).

In this analysis the first striking result is that, contrary to what has been predicted by the initial calculation of Nordheim, Muto and Parmenter, the fundamental gap in the VCA is not linear in x but has a quadratic dependance. This is a plausible result since the VCA determines a linear dependance on x for the potential in the crystal. The renormalization of the wf's alone due to a change in lattice parameter already implies that when the Schrodinger equation is solved, the eigenvalue clearly will not have a linear dependance on the alloy composition. However, eq. 5-19 represents a combination of the interband and intraband interactions and their separate effect cannot be estimated. The intraband interaction will further narrow the energy gap, the interband interaction widens it, (fig. 5-19). The former is larger in effect than the latter since the over all bowing $c_e = \delta E(x)$ is positive. The total c is then $c_i + c_e$. Fig. 5-12 shows a collection of experi-

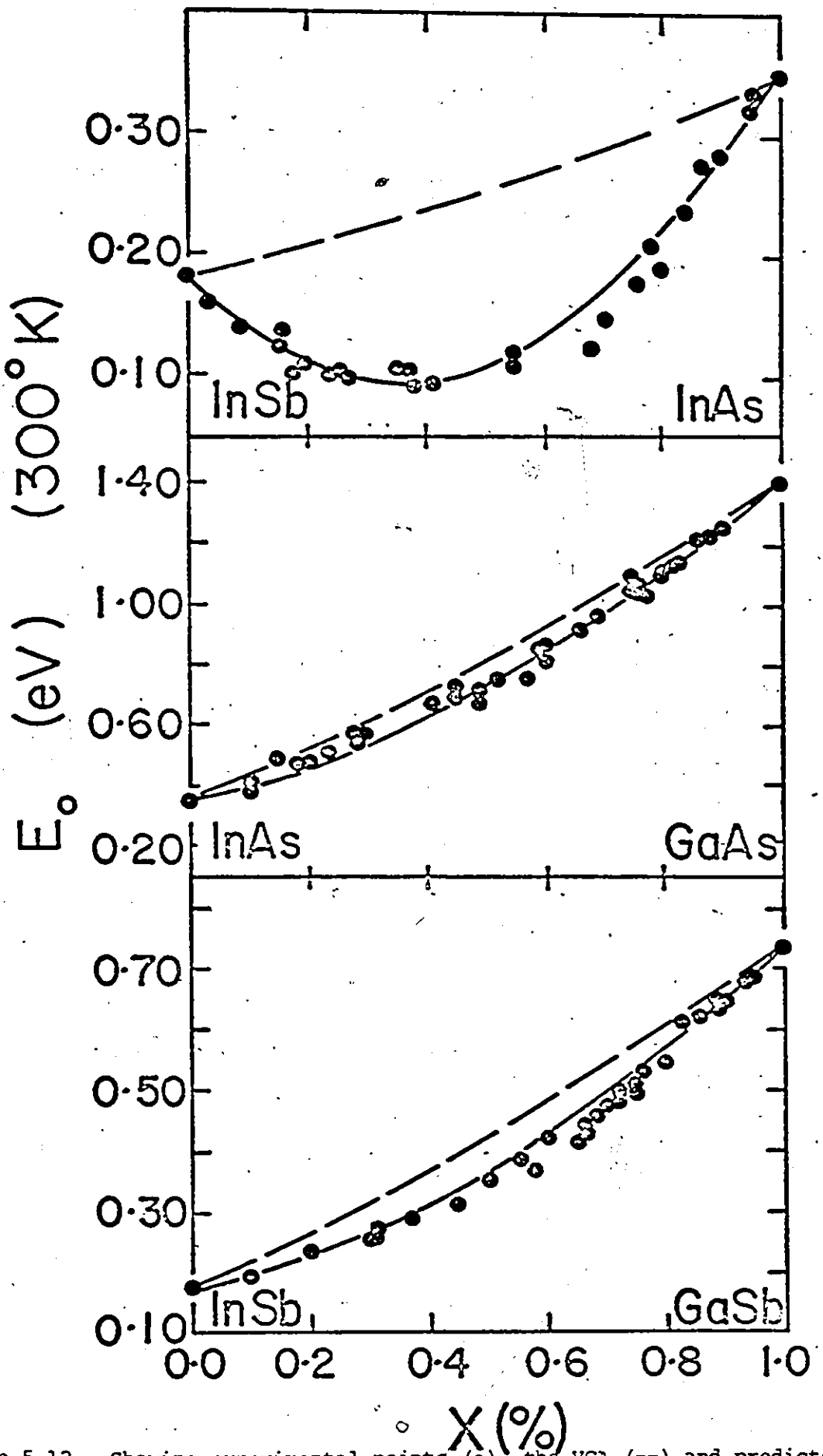

Figure 5-12. Showing experimental points (•), the VCA (--) and predicted (___) dependence of the fundamental gap E_o.

mental results with the theoretical solid line. The agreement is usually within experimental error (3V70).

5-7. THE EFFECT OF THE APERIODIC TERMS ON Δ_o AND Δ_1

Turning to the values of spin-orbit splitting, experimental data on Δ_o, the top valence band splitting at the Γ point and Δ_1, the splitting in the Λ direction as a function of composition are shown in fig. 5-1 and (4-6, 10, 16, 22, 27, 32). It is found that in all cases the $\Delta_1(x)$ curve is bowing upwards (negative) while $\Delta_o(x)$ curves downwards (positive c) In the VCA, $\Delta_o(x)$ and $\Delta_1(x)$ may be interpolated linearly between the constituent compounds as cross terms in eq. 5-1 between wf's of the different material is negligible (1V72, 1P70, 1V70). Thus the sign and the magnitude of the bowing of $\Delta_o(x)$ and $\Delta_1(x)$ can be justified mainly in terms of aperiodic effects.

To explain the general decrease of $\Delta_o(x)$ below the approximately linear VCA ($\Delta_{ov}(x)$) prediction (fig. 5-2, 5-3) one must argue that the state corresponding to the split off Γ_7 state is pushed up in energy more than the light and heavy hole states in Γ_8, (fig. 5-19). The second order perturbation theory (intraband effect, Parmenter) says that the Γ_8 states are pushed up by the interaction with all the other states in the same valence band as well as the Γ_7 states are pushed up by the adjacent states in that valence band. Therefore by intraband effects, Δ_o is either increased or decreased by such interactions, depending on the distribution of valence band density of states relative to the Γ_8

and Γ_7 bands as well as the strengths of the corresponding matrix elements. This effect is likely of similar magnitude and it will not alter the VCA value of Δ_o too significantly.

If, as suggested above, the mixing of the valence and conduction band states occurs at Γ, and we denote by $y(x)$ the fraction of conduction band s character mixed into the valence band at Γ, then this s character will not contribute to the spin orbit splitting Δ_o and only the p states can be split by the s-o interaction. The net effect is to reduce Δ_o by a factor of $1 - y(x)$.

From comparison with the effect of disorder on E_o (eq. 5-19), y is assumed to have the form

$$y = \frac{x(1 - x)\, C_{FG}^2}{\tilde{E}_{ov}\quad A}$$

where $\tilde{E}_{ov}$ is an average energy separation for the interaction and it is

$$\frac{1}{\tilde{E}_{ov}} = \frac{1}{3}\left[\frac{2}{E_{ov}} + \frac{1}{(E_{ov} + \Delta_{ov})}\right] \qquad (5\text{-}20)$$

where $E_{ov}(x)$ and $\Delta_{ov}(x)$ are calculated according to the VCA.

If, as the results of (VV + B) indicate, the VCA model gives an approximately linear variation of Δ_{ov} and Δ_{lv} with x, the intraband effects are considered negligible, Δ_o may be rewritten as

$$\Delta_o = (1 - y(x))\Delta_{ov} \qquad (5\text{-}21)$$

where Δ_{ov} is as of (eq. 5-9).

When such interband mixing occurs, the spin-orbit splitting

decreases in value as $(x)(1 - x)$ in eq. 5-21. There is the additional effect of inter-valence band interaction which will be demonstrated as considerably smaller than the inter-band effect.

In the case of $\Delta_1(x)$, the inter-valence-conduction band effects which are inversely proportional to the energy gap E_1 (eq. 5-20) are considerably weaker in the Λ direction. ($E_1 >> E_o$). Therefore intra-band and inter-valence band effects influence the curving up behaviour of $\Delta_1(x)$ with alloy composition. The result is to increase the value of $\Delta_1(x)$ over the VCA value.

The Parmenter type of intraband interaction in the Λ direction depends on the distribution of the valence band density of states relative to the Λ_6 and $\Lambda_{5,4}$ bands (fig. 1.7) as well as to the strength of the corresponding matrix elements (5-17,18).However it is predicted for most III-V compounds that the density of states and therefore the effective masses of these two bands do not differ greatly (1R73) at Λ. The intraband contribution to the Λ_6 band and the $\Lambda_{5,4}$ band are about the same and thus the intraband effects in this case will have a very small effect on $\Delta_1(x)$.

It is therefore more likely that the intervalence band interaction be the dominant contributor to the $\Delta_1(x)$ deviation from $\Delta_{1v}(x)$. It is logical to assume that this interaction will take a form similar to that of eq. 5-20. The energy separation between the two bands in the VCA is $\Delta_{1v}(x)$, therefore the correction term takes the form

$$\delta E \sim \frac{k\, x(1 - x)}{\Delta_{1v}(x)} \quad \frac{C_{FG}^2}{A} \qquad (5\text{-}22)$$

where k is a constant taking into account a modification in the strength of the interband interaction as it is changed from that between a conduction and a valence band at k = 0 to one between two valence bands in the Λ direction.

It is found (IV72) that a reasonable fit is obtained by

$$\Delta_1(x) = \Delta_{1v}(x) + \frac{k\, C_{FG}^2}{A\, \Delta_{1v}(x)}\, x(1-x) \qquad (5\text{-}23)$$

where k is found to be ∿ 0.14 for all alloy systems and Δ_{1v} is as of eq. 5-9.

In the theoretical calculation of Δ_o and Δ_1, eq. 5-21 and 5-23 are used to test the experimental results. The assumptions in these calculations (which were justified in the above arguments) are: 1) the VCA values for Δ_{ov} and Δ_{1v} are assumed to vary linearly with alloy composition x and are therefore interpolated linearly between the values for the constituents; 2) C_{FG} is assumed constant for one alloy system; 3) interband effects are considered to be the main contribution to Δ_o and intervalence band effects to be the main contribution for Δ_1; 4) Y is calculated (eq.5-20) by using E_{ov} found with c_i, the intrinsic VCA bowing parameter, and Δ_{ov}.

The intervalence interaction given by eq. 5-22 should also be present at the Γ point. This interaction, will be reduced approximately by a factor of 2/3, since the separation between the bands at Γ is 3/2 times larger than in the Λ direction. From fig. 5-1, if the Δ_1's deviation from linearity is mainly due to the 5-22 term, it is seen as

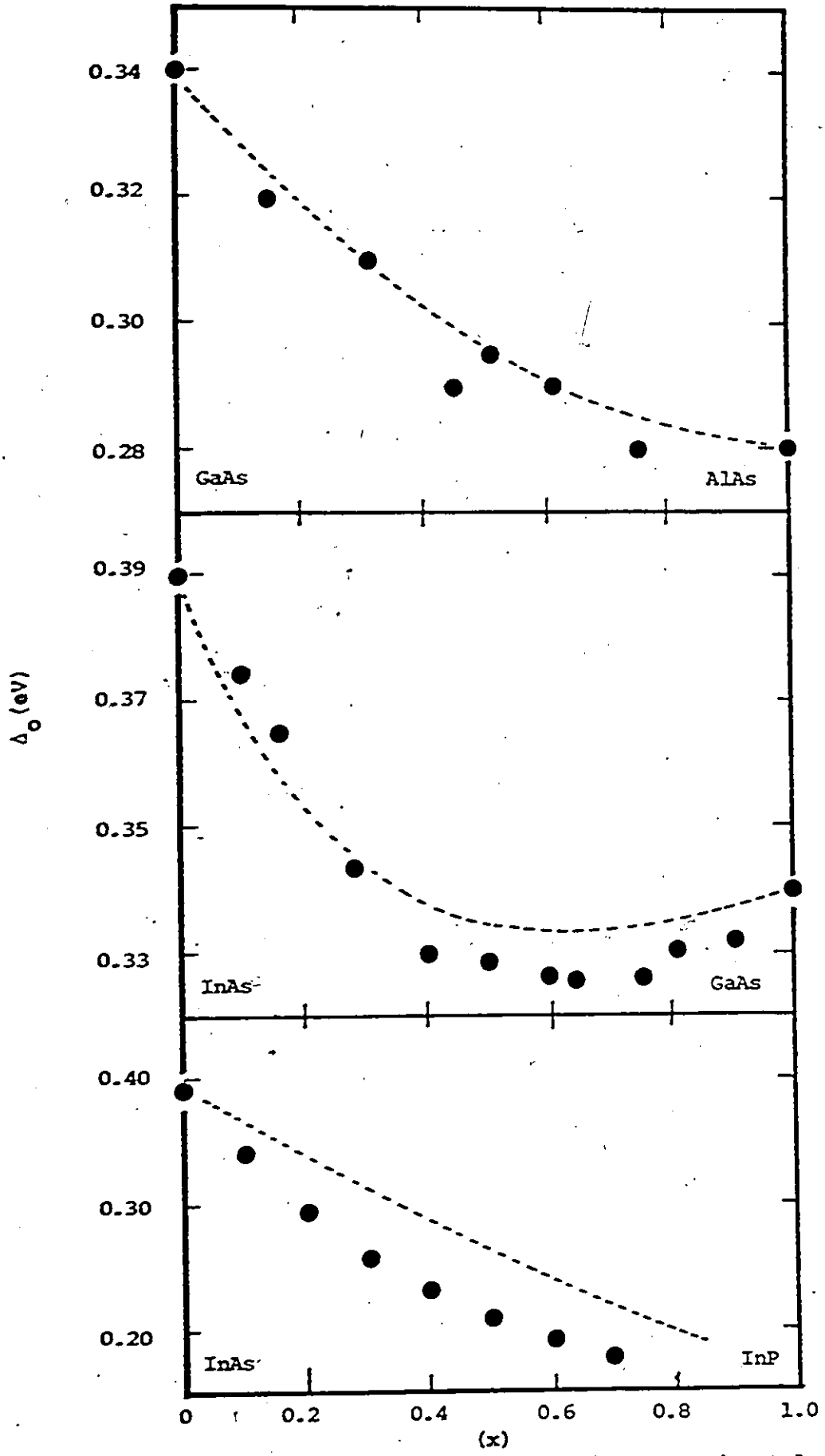

Figure 5-13. Dependence of Δ_o on alloy composition, experimental points and predicted curves from eqn. 5.21.

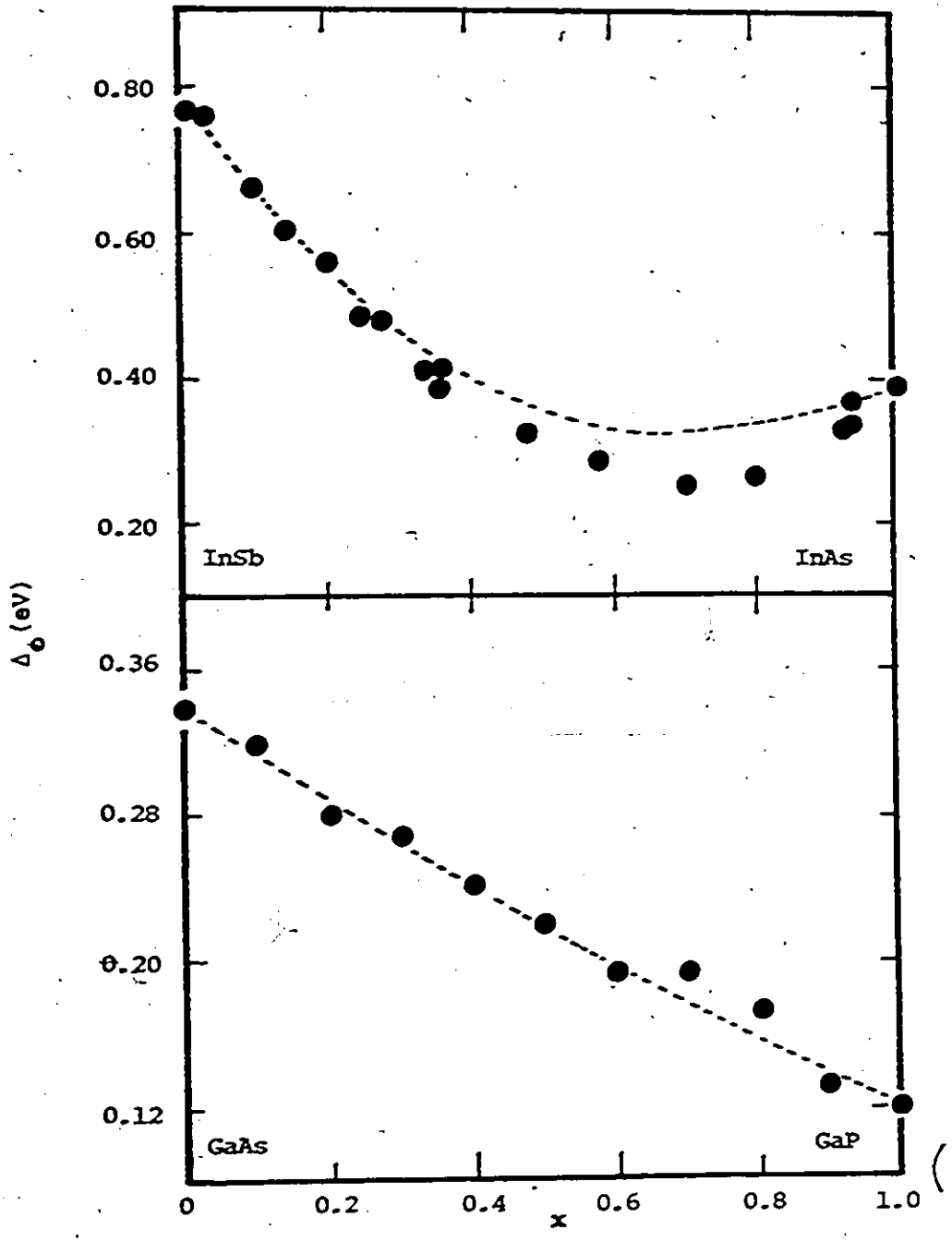

Figure 5-14. Dependence of Δ_o on alloy composition, experimental points and predicted curves from eqn. 5.21.

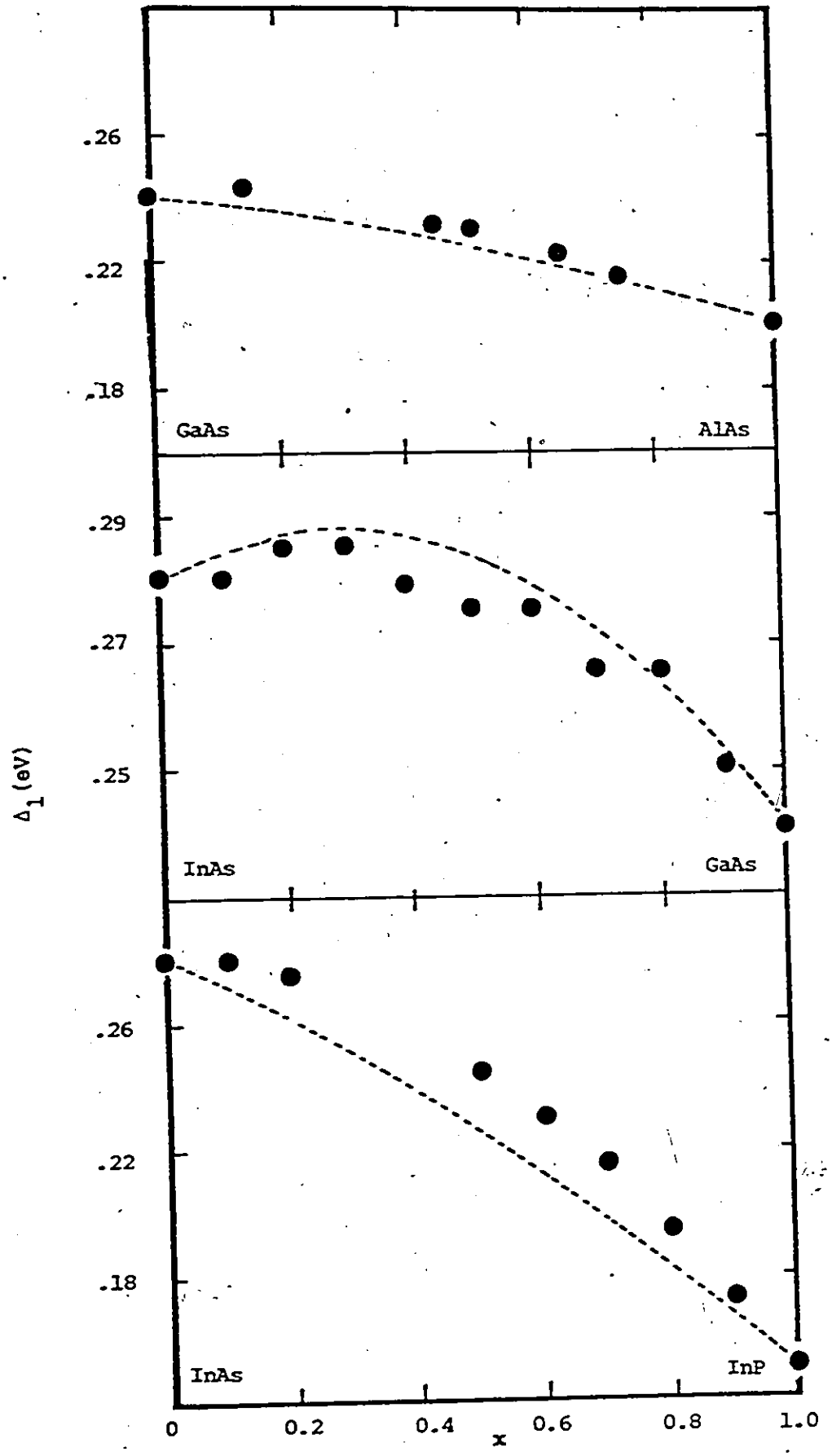

Figure 5-15. Dependence of Δ_1 on alloy composition, experimental points and predicted curves from eq. 5.23.

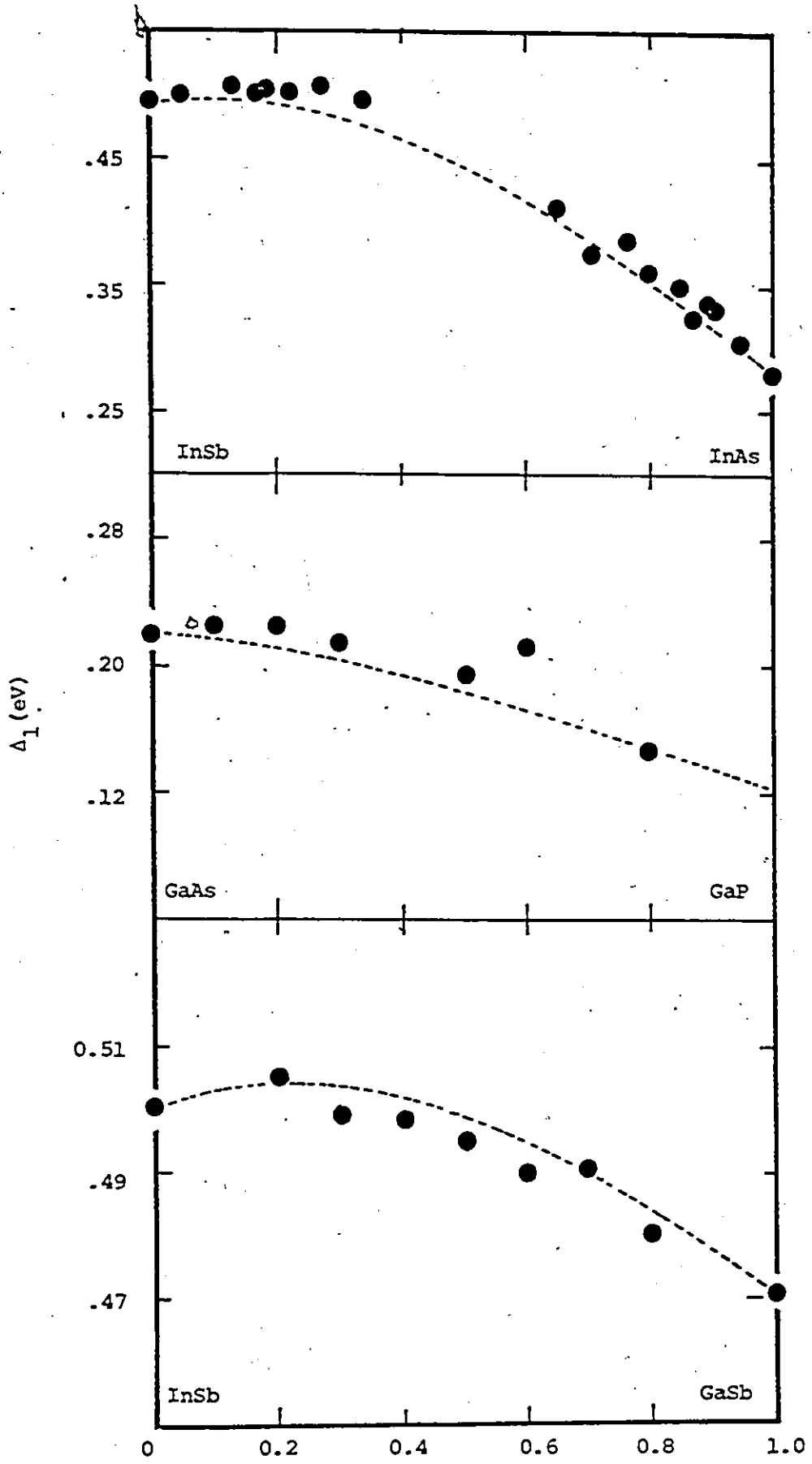

Figure 5-16 Dependence of Δ_1 on alloy composition, experimental points and predicted curves from eqn. 5.23.

TABLE 5-4 Calculated and observed deviations from linearity for several 50% - 50% alloys. Estimates of experimental uncertainty are shown in the table.

Alloy	$\Delta_{ov} - \Delta_o$ Calc (meV)	$\Delta_{ov} - \Delta_o$ Expt (meV)	$\Delta_1 - \Delta_{1v}$ Calc (meV)	$\Delta_1 - \Delta_{1v}$ Expt (meV)
InAs-Sb	295	285 ± 10	58	58 ± 5
Ga-InSb	92	.....	17	13 ± 5
Ga-InAs	29	37 ± 10	38	18 ± 5
InAs-P	4	20 ± 10	11	32 ± 10
GaAs-P	3	5 ± 10	18	32 ± 10
Ga-InP	4	0 ± 10	92	70 ± 20
Ga-AlAs	1	5 ± 10	4	8 ± 5
Si-Ge	1	7 ± 10	19	.....

not too strong, and therefore even weaker at Γ. Thus in the calculation for Δ_o (eq. 5-21) this contribution has been neglected.

Figs. 5-13 to 5-16 show the experimental points and the predicted curves according to the above theory. In table 5-4 the calculated and observed deviations from the VCA values for both Δ_o and Δ_1 are tabulated at x = 0.5. The predicted values are clearly in best agreement for narrow gap alloy systems. Here interband effects are expected to be large and therefore the approximations discussed above are reasonable.

The approximation in the above analysis, that of considering C_{FG} independent of alloy composition, is particularly visible in the case of Δ_o for (In,Ga)As and In(As,Sb) systems. An additional dependance of C_{FG} on x may correct the deviations observed between theory and experiment. This dependance arises possibly through the screening term be^{-Rk_s} (3V70) which may be modified with composition x.

5-8 THE EFFECT OF THE APERIODIC POTENTIAL ON m^* (Γ_{1c}) THE BOTTOM OF THE CONDUCTION BAND EFFECTIVE MASS

Introduction

The properties of electrons in semiconductors are largely determined by their effective mass. This quantity has been a key parameter in the understanding of compound semiconductors and their alloys (1B62, 1L71, 2W68, 7D71).

Predictions of the effective mass (1C63, 2M67, 1W68) for alloys has

been only of partial reliability since some assumption about the alloy dependance of P^2 and Δ_o was necessary (1W68, 1C63).

From eq. 1-14 in the Kane model, the expression for various effective masses has been used: the conduction band effective mass (eq. 1-15): (2M67, 1C63)

$$\frac{m}{m^*_c} = 1 + \frac{2}{3}\frac{P^2}{\hbar^2}\left[\frac{2}{E_o} + \frac{1}{E_o + \Delta_o}\right]$$

the light hole valence band mass:

$$\frac{m}{m^*_{\ell h}} = 1 + \frac{4}{3}\frac{P^2}{\hbar^2}\frac{1}{E_o}$$

and the spin-orbit valence band effective mass:

$$\frac{m}{m_{so}} = 1 + \frac{2}{3}\frac{P^2}{\hbar^2}\left[\frac{1}{E_o + \Delta_o}\right]$$

where E_o is the direct energy gap, Δ_o the spin orbit splitting and P^2 is as defined in eq. 1-15.

Later, Cardona (1C63) modified the expression (1-15) to take into account the loss in inversion symmetry in the III-V compounds (which should increase the value of P^2). When it was assumed that P^2 was a constant (23 eV) for all the III-V compounds the final expression for $m^*(\Gamma_{1c})$ was

$$\frac{m}{m^*(\Gamma_{1c})} = 1 + \frac{P^2}{E_o'}\left[\frac{E_o' + E_o'(IV)}{3}\left(\frac{2}{E_o} + \frac{1}{E_o+\Delta_o}\right) - \frac{E_o'-E_o'(IV)}{E_o' - E_o}\right] \quad (5.24)$$

where E_o' is the optical transition between the Γ_{15v} and Γ_{15c} bands and $E_o'(IV)$ is the equivalent transition for the homopolar analog for the III-V compound.

Experimental

When room temperature values of m_o, the bottom of the conduction band effective mass, were determined for (Ga,In)As (1D71, 2F72), $InAs_xSb_{1-x}$ (2W68) and for $Ga_xIn_{1-x}Sb$ ((1A69), alloy systems, it was assumed) that a Kane model (1, 2K56) applied in these cases and values of the square of the matrix element, P^2, were calculated. It was found that although the values of P^2 varied little from one compound to another, the values determined in this way for the alloys showed a minimum at the center of the alloy range (2W68). Recently, Fetterman et al. (2F72) determined m_o for a limited range of $Ga_xIn_{1-x}As$ alloys. Assuming that P^2 varied linearly between the values for the compounds, they showed that the values calculated from a simple Kane model did not agree with the experimental values. This is essentially the same conclusion as found above for $InAs_xSb_{1-x}$ and $Ga_xIn_{1-x}Sb$. It is suggested in this work that this deviation from a simple Kane model form is due to the same conduction-valence band mixing which is required to explain $\Delta_o(x)$.

Values of m_o have been obtained by four types of experiment: Faraday rotation, magneto-thermoelectric power, infrared reflectance and cyclotron resonance. There is no detectable difference among the

values obtained by these different types of experiment (1A69). Therefore, it is unlikely that any discrepancy between experiment and the simple Kane model be due to any systematic experimental error.

Band Mixing and the Effective Mass at Γ_{1c}

When such band mixing occurs, the fraction of valence band states transferred to the conduction band equals the fraction of conduction band states transferred to the valence band. Hence, the resultant conduction band effective mass will be determined to some extent by valence band characteristics. Let y_1, y_2 and y_3 be the fractions of heavy hole, light hole and split-off valence band states mixed into the conduction band. To be consistent with eq. (5-20) it is assumed that

$$y_1 = y_2 = \frac{x(1-x)\,C_{FG}^2}{3A\;E_{ov}} \quad ; \quad y_3 = \frac{x(1-x)\,C_{FG}^2}{3A\;(E_{ov}+\Delta_{ov})} \qquad (5\text{-}25)$$

The resultant conduction effective mass can be written

$$\frac{1}{m_o} = \frac{(1-2y_1-y_3)}{m_{co}} + \frac{y_1}{m_{hh}} + \frac{y_1}{m_{1h}} + \frac{y_3}{m_{so}} \;, \qquad (5\text{-}26)$$

where m_{co}, m_{hh}, m_{1h} m_{so} are the values the various effective masses would have in the absence of conduction-valence band mixing:

$$\frac{1}{m_o} = \frac{1}{m_{co}} + \frac{x(1-x)C_{FG}^2}{3A}\left(\frac{1}{m_{hh}E_{ov}} + \frac{1}{m_{lh}E_{ov}} + \frac{1}{m_{so}(E_{ov}+\Delta_{ov})}\right)$$

$$- \frac{1}{m_{co}}\left(\frac{2}{E_{ov}} + \frac{1}{(E_{ov}+\Delta_{ov})}\right) \qquad (5\text{-}27)$$

In order to determine $m_o(x)$ for any system, the parameters in eq. 5-27 need to be known. Here, the following assumptions have been made. E_{ov} and Δ_{ov} are the VCA values and are obtained from the Van Vechten and Bergestresser analysis, i.e. E_{ov} is calculated from the values of c_i given by Van Vechten and Bergestresser and Δ_{ov} is assumed linear with x. Similarly, m_{hh} and m_{so} are assumed to vary linearly between the values for the compounds. The light-hole mass m_{lh} has been assumed to have the same value as m_{co}, which is a good approximation in the Kane model. Finally, m_{co} is the effective mass for the conduction band in the absence of conduction-valence band mixing but with all other effects, in particular the true $E_o(x)$, included. Thus, it has been assumed that m_{co} is given by the simple Kane type, eq. (5-24), where P^2 is linearly interpolated between the values for the compounds and E_o and Δ_o take the experimentally observed values.

The experimentally observed $m_o(x)$ for the three alloy systems $InAs_xSb_{1-x}$, $Ga_xIn_{1-x}As$, (2T71) and $Ga_xIn_{1-x}Sb$ (1A69) are shown in Fig. 5-17 (curve (a)). Also shown in each case are the following curves: (b) the VCA

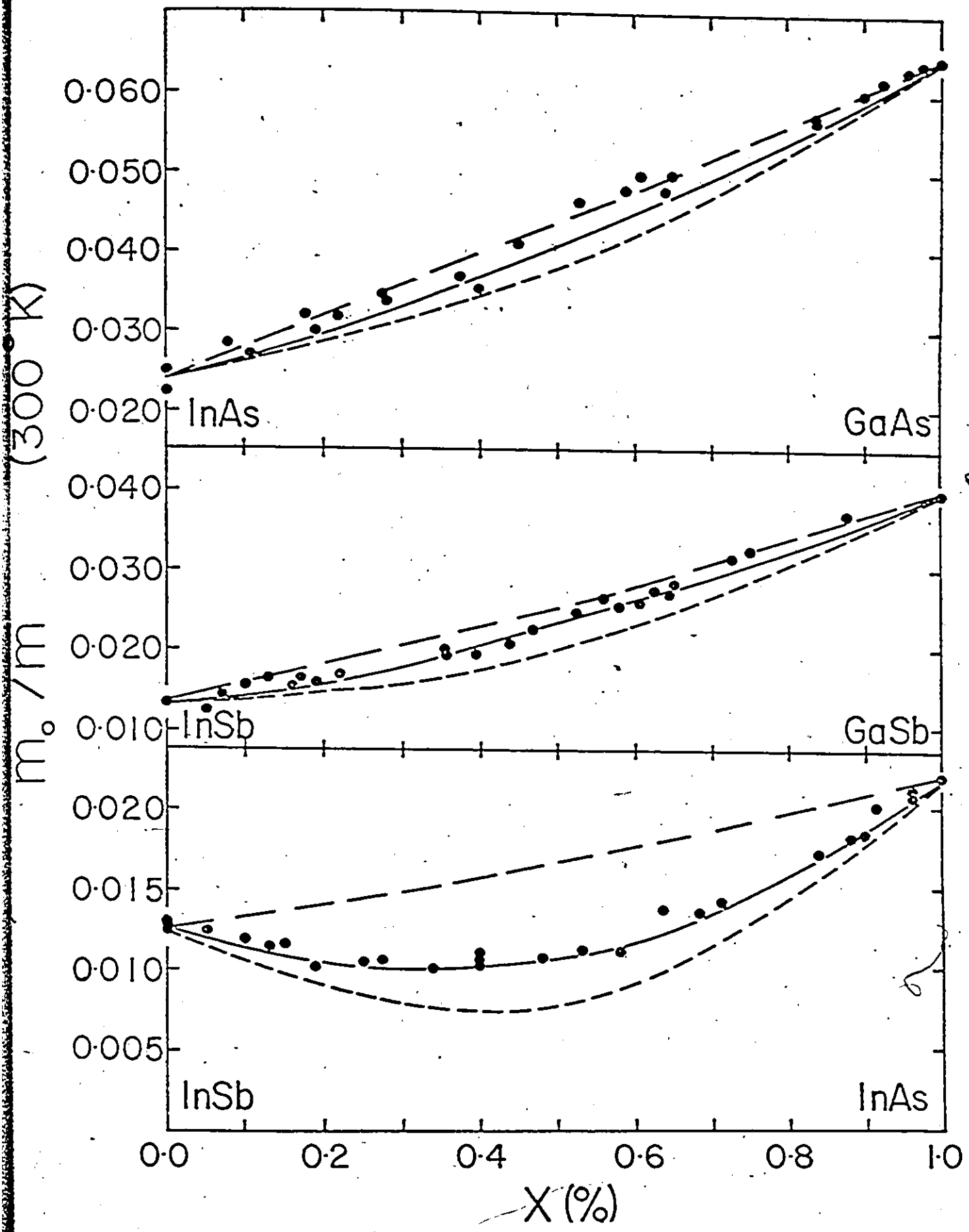

Figure 5-17. Showing the $m(\Gamma_{1c})$ alloy dependence (o) experimental (a), ---Kane model, (eq. 5-24) (c), —— —— VCA Prediction using values of E_{ov} and Δ_o in eq. 5-24 (b), —— eq. 5-27, this theory (d).

prediction, m_{vc}, obtained by using the values E_{ov} and Δ_{ov} in eq. (5-24); (c) the simple Kane model prediction, m_{co}, obtained by substituting the measured values of E_o and Δ_o into eq. (5-24) and assuming P^2 varies linearly; (d) this prediction, m_o, obtained from eq. (5-26).

Although the agreement is not perfect, it is seen that the values obtained by assuming conduction-valence band mixing give the best fit to the experimental values. Thus, it may be concluded that conduction-valence band mixing is present and must be taken into account in calculating effective mass values and other band parameters. The conduction band in alloy semiconductors will not be accurately represented by a Kane type equation if the VCA is assumed.

This latter conclusion raises the question of the accuracy of the experimentally determined values of m_o. In almost all cases, the experimental observations have been made on n-type material and the results then computed to give a bottom of the band value. This correction has been made using a Kane model. However, in the majority of the results quoted here, the doping of the samples was not large, so that the Fermi level was normally within one or two k_BT (at room temperature) of the band edge and hence the correction term was relatively small. Thus, the error in assuming a simple Kane model is an error in this correction term only and should not be too large a percentage of the quoted final value. However, this effect might explain some discrepancy between experimental and predicted values of m_o.

In fig. 5-18 the predicted values (eqn. 5-27) for the (GaAs)Sb alloy system are seen. This system is presently being studied by Faraday rotation by Woolley and Devlin. This alloy system has been reported to have a miscibility gap over the alloy range $0.38 < x < 0.60$ (4S72, 1G73). Therefore no predictions for the effective mass are shown in this range of composition.

5-9 DISCUSSION

It is of interest to consider qualitatively, the effects which cause the observed changes in the values of E_o, Δ_o or m_o. The presence of disorder, which breaks the symmetry of the lattice, produces interactions between various states in the Brillouin zone. The ones of interest here can be considered under two headings: (i) intraband interactions as discussed by Parmenter (1, 2P55) and (ii) interband interactions as proposed here. Both of these will affect the band energies at the Γ point. Intraband effects in the conduction band will push the minimum of that band to lower energies and, similarly, in the valence band will increase the energy of the maximum; this leads to a reduction of E_o. According to simple perturbation theory, conduction band-valence band mixing will cause the bands to separate, leading to an increase in E_o. It seems clear that the intraband effects on E_o are larger since $E_o(x)$ is less than the VCA prediction (see fig. 5-12).

In the case of $\Delta_o(x)$, the problem is more complicated since inter-

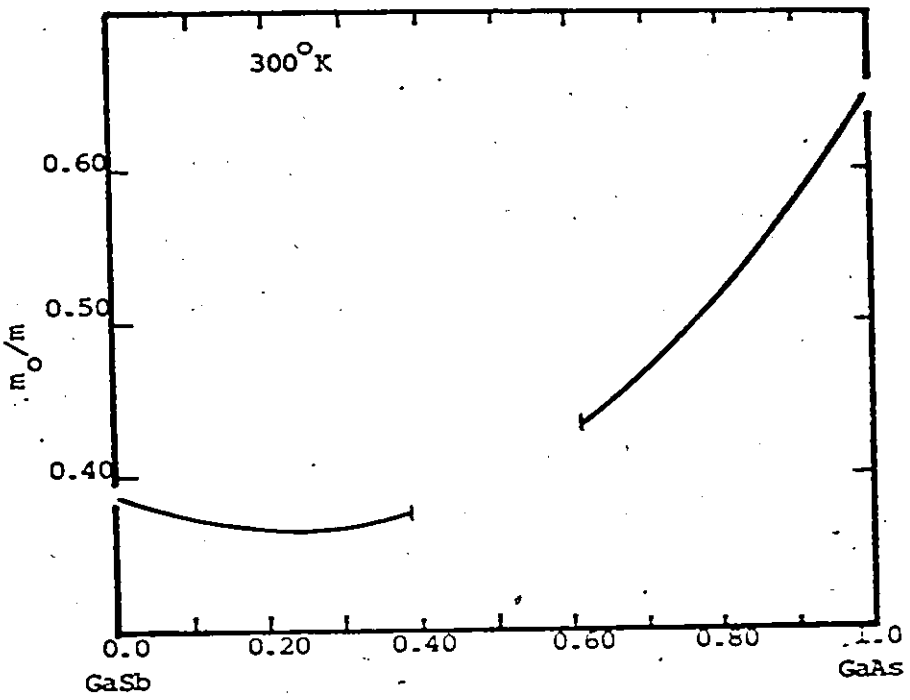

Figure 5-18. Predicted variation of the conduction band effective mass (eqn. 5-27) for the Ga(AsSb) alloy system.

actions between valence bands will occur. Intraband effects will raise the energy of both the degenerate valence bands and the split-off valence band so the effect on Δ_o may be small. Inter-valence band interaction will tend to separate the interacting bands and hence would increase Δ_o (fig. 5-19). However, this effect, which causes the observed increase in Δ_1 with disorder (giving the upward curvature of the $\Delta_1(x)$ curve), is relatively small for Δ_1 for the cases of interest here, for which both Δ_1 and Δ_o are large. As this effect is inversely proportional to the splitting and as $\Delta_o \sim 3/2\Delta_1$, it should be still smaller for Δ_o. The sum of the intraband effects and intervalence band effects at the Γ point would thus be small and in the analysis of Δ_o was treated as negligible. Hence, the major disorder effect on Δ_o is the conduction-valence band interaction which results in mixing of s-like states into the valence band. As has been shown previously, the form of the $\Delta_o(x)$ curve can be well explained on this basis.

Finally, in the case of the varation of $m_o(x)$, the effects of the various interactions can again be seen; the results for $InAs_xSb_{1-x}$ alloys show these particularly well. As indicated above, the various interactions will cause a reduction in E_o and this of itself would produce a corresponding reduction in m_o. Thus, the effects of intraband interactions can, to a good approximation, be taken into account by using a Kane equation and the experimentally observed values of E_o and Δ_o to calculate values for m_{co}. The change in effective mass due to this effect, i.e. from m_{vc} to m_{co}, is in fact, the difference between curve (b)

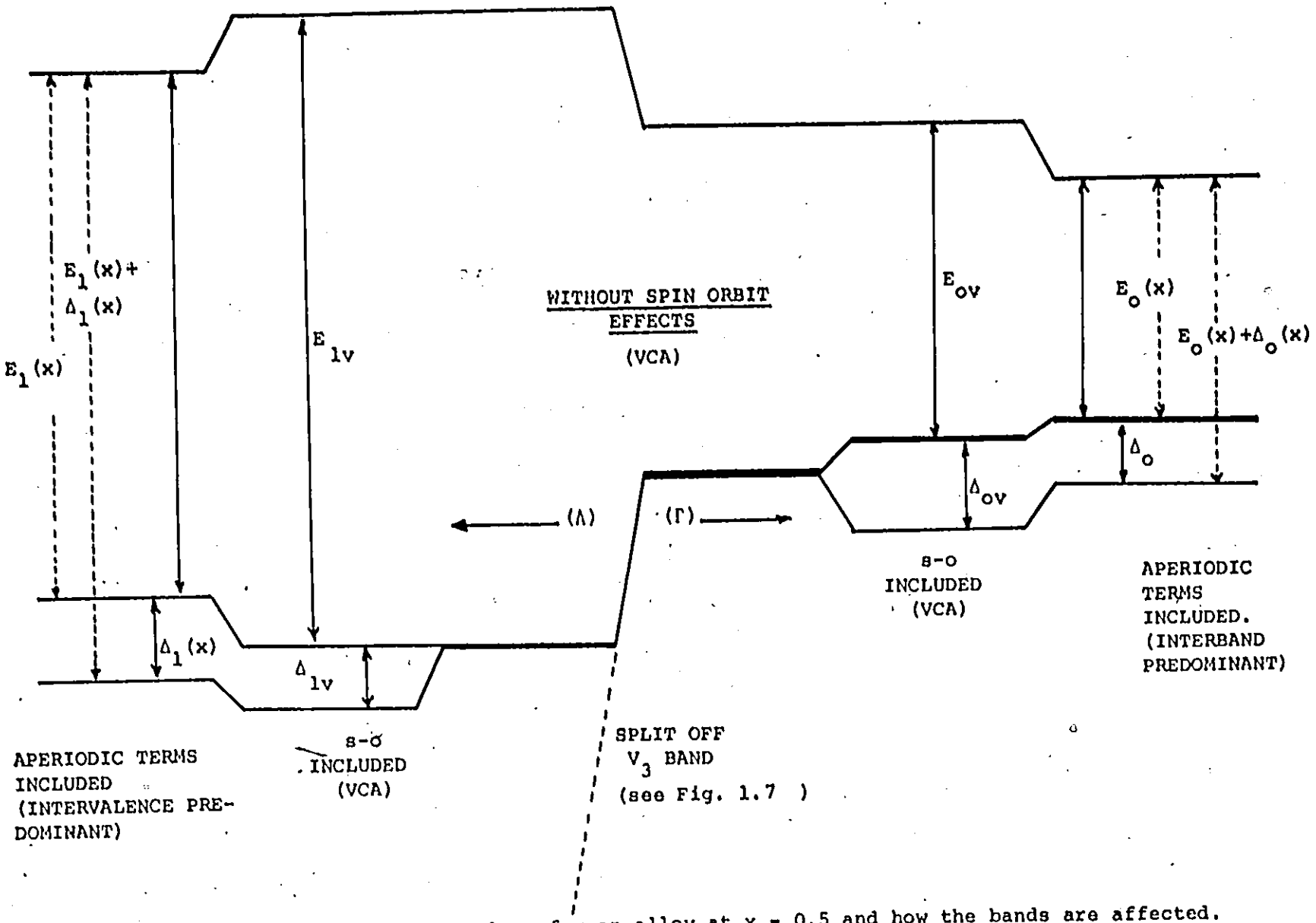

Figure 5-19. Various effects taking place for an alloy at x = 0.5 and how the bands are affected.

and curve (c) in fig. 5-17. In addition, however, the conduction-valence band mixing causes transfer of valence band states to the conduction band thus increasing the effective mass in the band. This increase is the difference between curve (c) and the final curve (d) in fig. 5-17. It is seen that the reduction from curve (b) to (c) is larger than the increase from (c) to (d), again indicating that intraband interactions have the largest effect, consistent with the results for E_o.

5-10 CONCLUSION

In this Chapter it has been shown how the results in Chapter 4 can be studied to gain some insight into the more complex problem of an alloy band structure and the various inherent alloy processes. Many problems still remain to be understood and it is still not clear how some of the initial properties of the constituents will affect alloy behaviour.

However, it is believed that the model of band mixing presented in this analysis is more than coincidental in its capacity to explain the alloy dependance of such band parameters as E_o, E_1, Δ_o, Δ_1 and $m_o(\Gamma_{1c})$. Its capacity to predict values for Δ_o and Δ_1 in the case of the (Al,In)Sb alloy system (1P73) as well as values of the effective mass (fig. 5-18) test the reliability of the model. Some important considerations have been made along the development of the theory, and in fact this explains why a better agreement between predicted and experimental values is obtained in the case of small gap alloy systems.

The next step in the evaluation of alloy data would be perhaps

to overcome the approximations by approaching the alloy problem from a more quantum-mechanical point of view. If indeed the initial assumptions in the Kane model are overridden by grosser corrections in the case of an alloy system, it might be useful to review the theory from that point.

APPENDIX I

A1-1 Introduction

A1-2 The alloying of IV-VI compounds and some of their properties.

A1-3 Phase studies of the (Pb,Sn)Se alloys.

A1-4 Review of the (Pb,Sn)Te alloy system.

A1-5 Reflectance studies of the (Pb,Sn)Te alloys.

APPENDIX I

A1-1 INTRODUCTION

As mentioned in the first section of Chapter 4, Appendix 1 is mainly concerned with the presentation of some partial results on the optical properties of the (Pb,Sn)Te alloy system and the lattice parameter and the phase diagram of the (Pb,Sn)Se alloy system. The reasons why these results are presented as an appendix have already been discussed in Section 4-1.

The principal interest in the lead salts like PbTe, PbSe and PbS was motivated by their small gap, low resitivities and high mobilities. These factors are characteristic of ideal infrared detectors.

In the sixties, electrical and optical measurements (1D66, 2D63, 2D68, 4T67, 5T67) suggested that (Pb,Sn)Te has a fundamental gap going to zero somewhere in the alloy composition range. It has been suggested (1L66, 5C64) that there is in this case a cross-over of the conduction and valence bands. In fact, by the proper choice of composition, IR detectors of (Pb,Sn)Te can be designed for virtually any photon range in the infrared.

The crystal structure of most IV-VI compounds is f.c.c. (fig. A1-1) as that of NaCl, i.e. two interpenetrating f.c.c. latticestranslated by $(\frac{1}{2}\frac{1}{2}\frac{1}{2})$ along the body diagonal. As with the III-V compounds, the like valency atoms crystallize on one of the f.c.c. sublattices. The first Brillouin zone of the rocksalt structure is a truncated octahedron, as that of the zinc-blende (Fig. 1-2b). However, the fundamental gap in the lead salts and their alloys occurs at the L point.

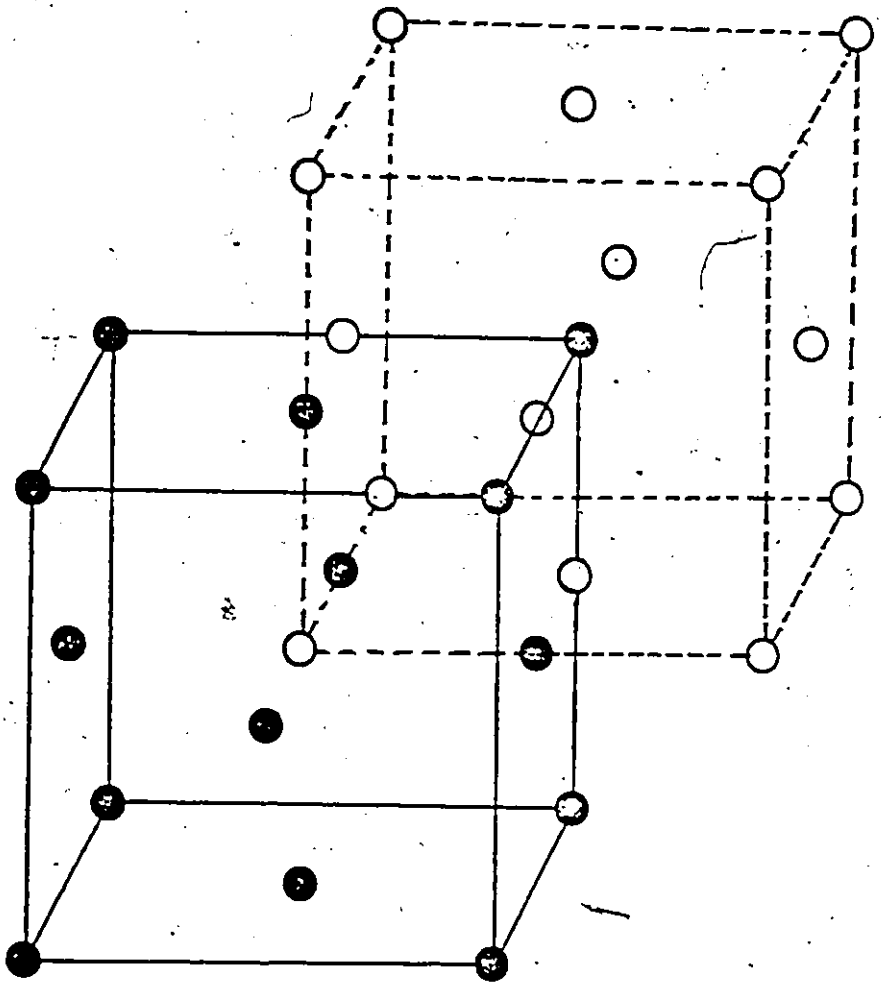

Figure A1-1 The crystal structure of a IV-VI compound (eq. Pb(o), Te(o)).

This part of the research is involved with the study of the phase diagram of the (Pb,Sn)Se alloy system and with some of the optical properties of the (Pb,Sn)Te alloy system.

A1-2 THE ALLOYING OF IV-VI COMPOUNDS AND SOME OF THEIR PROPERTIES.

The earliest work reported on lead salts was on PbS (2L51) and it was mainly concerned with the preparation of the material. Since then, there has been a large amount of work done on the preparation (1N67, 3W67, 4W68), the calculation of band structure (1L66, 2C67, 5C64) and electrical and optical properties of these compounds (1, 2D72, and references therein).

Yamamoto (1Y51) was the first to report about the preparation of solid solution of IV-VI alloy systems. Later, work on (Pb,Sn)Te (3W67) PbSe - SnTe(1N67, 1N65) has been reported. A finite range of solubility in the (Pb,Sn)Se system has been found by both Krebs (1K61) and this worker (5W68). Kreb's work also includes studies on Sn(Te,Se) and (Sn,Ge)Te alloy systems. They are found to exhibit miscibility gaps at 40% from the compound and to have rocksalt crystal structure. The (Ge,Pb)Te mixed crystal system has been studied by Woolley and Nikolic (3W65). They report a continuous range of solubility with a change from rocksalt to rombohedral structure over the alloy composition. Additional work on the Ge(Se,Te) (2M67) and Pb(Se,Te) (2B65) systems has shown differing ranges of solid solubilities.

For reliable experimental information, good homogeneous material is necessary. At the time this work was done, few if any sources of

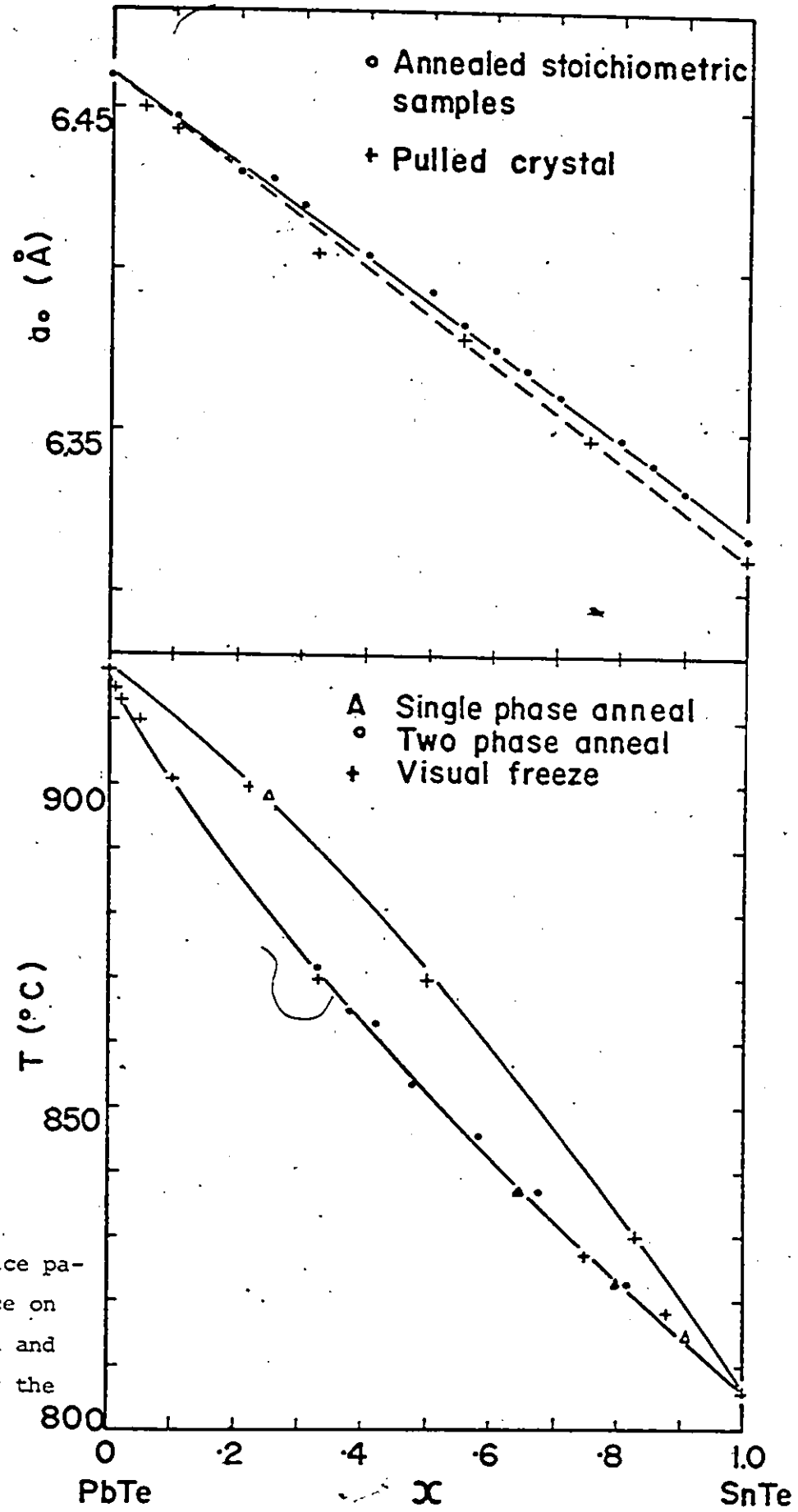

Fig. A1-2. Lattice parameter dependence on alloy composition and phase diagram for the (Pb,Sn)Te system.

pure, medium conductivity, dislocation free samples of (Pb,Sn)Te were available. Later Dionne and Woolley (1, 2 D72) investigated the metallurgical and some of the transport and optical properties of (Pb,Sn)Te alloys. They found, among other things, that non-stoichiometric growth of this system, with an excess of Te at the SnTe end of the composition doped the material to excess p-type at $\sim 10^{20}$ carriers/cm^3. By appropriate temperature-anneal times they could control the Te non-stoichiometry until acceptable samples could be obtained for optical and electrical work.

The initial requirement for the preparation of alloys over the composition is reliable information about its phase diagram. While this was available for the (Pb,Sn)Te alloy system (fig. A1-2), the (Pb,Sn)Se system had not been fully investigated at the time this work was started.

A1-3 PHASE STUDIES OF THE (Pb,Sn)Se ALLOYS (5W68).

Introduction

The interest shown (2D63, 4T67) in the lead salt and their alloys due to the properties discussed above prompted further metallurgical investigations of these systems (5W68). In order to carry out the various materials preparations such as single crystal growth from the melt etc., it is necessary that the appropriate T-x phase diagram be known with reasonable accuracy. Also accurate values of lattice parameter are of use in determining the composition of samples taken from grown crystals and ingots. In (3W67), accurate lattice parameter data and the T-x phase diagram for the $Pb_{1-x}Sn_xTe$ system was presented.

In the case of the $Pb_{1-x}Sn_xSe$ alloys, various authors (1K61, 1Y51) have shown from X-ray powder photograph data that single phase solid solution in the rock salt type PbSe phase is limited to $x < 0.4 - 0.5$, and have given lattice parameter values in this range. However, until the results of Strauss (3S70), no T-x phase diagram had been given. The data given by Strauss were determined from differential thermal analysis results and from the first-to-freeze composition values for directionally frozen samples. Here, data for the curves bounding the rock salt type phase have been determined by the same X-ray technique as was used for the $Pb_{1-x}Sn_xTe$ alloys.

Method and Results

Samples of three grams weight were weighed out from the component elements so as to be as close as possible to the stoichiometric composition required and were sealed under vacuum in small quartz ampoules. The ampoules were kept very small so that the loss of selenium from the alloy as vapour in the ampoule was practically negligible. Other samples were made in a similar way from appropriate weights of the compounds, but no noticeable difference was found between results for samples prepared by the different methods. In every case the samples were melted by holding them at 1100°C for two or three hours, to give good mixing of the components, and were then air quenched.

Samples were then held at temperatures about 20 - 50°C below the estimated solidus temperature and annealed until a good equilibrium condition was obtained, as indicated by X-ray powder photographs. Periods

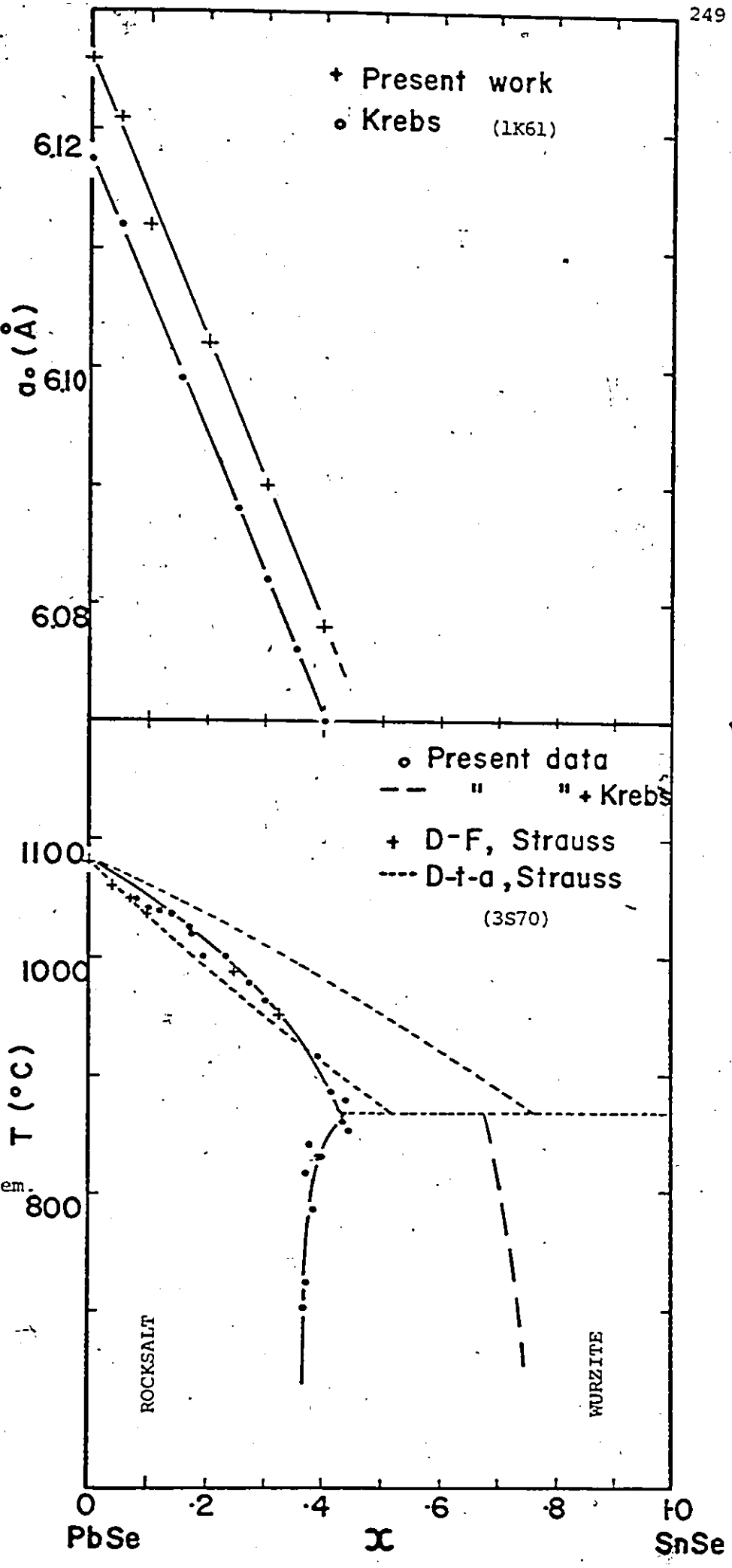

Fig. A1-3 Showing lattice parameter a_o and T-x phase diagram for (Pb,Sn)Se alloy system.

of annealing of approximately 12 hours were used in this case. The X-ray powder photographs were then analysed and the value of the corrected lattice parameter a_o for each sample was obtained from the standard extrapolation of lattice parameter a against the function $\frac{1}{2}(\frac{\cos^2\theta}{\sin\theta} + \frac{\cos^2\theta}{\theta})$ where θ is the Bragg angle (1H61). The resulting variation of a_o with x is shown in fig. A1-3, the estimated relative accuracy of these parameters being $\pm 0.001\text{Å}$.

Similar alloy samples were annealed at temperatures corresponding to points in the liquid-solid two phase field, annealing times of three hours being found sufficient in this case. At the end of the anneal, the sample was rapidly quenched in water, so that the solid phase appropriate to the annealing temperature T was quenched in. X-ray powder photographs were then used to find the lattice parameter of this solid phase and hence from the data in fig. A1-3a, the corresponding value of x for the sample. The point (x, T) then is a point on the solidus curve and the resulting curve is shown in fig. A1-3b.

Various alloy samples with x = 0.5 and 0.6 were annealed at temperatures in the range 700 - 860°C, i.e. in the two solid phase field. In this case, samples were annealed for 24 hours to give equilibrium conditions. The composition of the rock salt type phase, determined as above, then gave points on the line limiting the terminal single phase field and these also are shown in fig. A1-3.

Finally, samples with x varied by increments of 0.05 in the range 0.5 to 0.8 were annealed to equilibrium at 850°C and the phase then present in the samples observed from X-ray powder photographs.

It was found that the lines of the rock salt type phase were very faint when $x = 0.65$ and could not be observed for $x > 0.65$. This gives an approximate estimate of the limit of solid solubility to be at $x \sim 0.70$ and certainly $x < 0.75$. Krebs et al. (1K61) showed that the corresponding value at 500°C was $x = 0.76$ and hence an approximate boundary to this single phase field can be drawn as in fig. A1-3b.

Discussion

In fig. A1-3a, the lattice parameter values of Krebs et al. are given in addition to the present data. It is seen that within the limits of experimental error the variation of a_o with x is linear, but that the data of Krebs et al. lie systematically below those given here. (Present data $a_o = (6.126 - 0.123x)$ Å Krebs et al. $a_o = (6.117 - 0.120x)$ Å). The size of the discrepancy is such that it could be due to Krebs et al. not using the extrapolation method for a_o described above, but no indication is given of their method of analysis.

The solidus curve given in fig. A1-3 is in fair agreement with the curve given by Strauss. If the directional freeze data and heating curve data of Strauss are considered independently, the present curve gives very good agreement with the directional freeze data (derived from the liquidus and shown as points in fig. A1-3) as opposed to the heating curve data (dotted line in fig. A1-3).

The present data are in good agreement with a horizontal at 870°C, although the maximum solubility of SnSe in the rock salt type phase is given here as $x = 0.45$ while Strauss obtained a value of $x = 0.52$.

However the retrograde solubility of SnSe in PbSe could lead to some systematic error of this type if the quench rate used in the present work were not fast enough, particularly for observations at temperatures just below the 870°C horizontal. The solubility limit of the SnSe phase at 850°C has been estimated only approximately. However, if $x < 0.75$ for this limit as indicated above, it is possible that the diagram in fig. A1-3 has peritectic rather than eutectic form.

A1-4 REVIEW OF THE (Pb,Sn)Te ALLOY SYSTEM

As discussed above, it has been reported by Woolley and Wagner (3W57) that (Pb,Sn)Te is a pseudobinary alloy system having miscibility over the whole alloy range.

The band structure calculations due to Lin and Kleinman (1L66) and Conlin et al. (5C64) for the lead salts by the semi-empirical pseudopotential calculation indicate that the fundamental gap occurs at the L point. The band structure of SnTe is still unknown. When considering the conduction band minimum and the valence band maximum for PbTe (fig. A1-4), and 3S67, with SnTe it would seem that from one compound to the other the two gaps meet at some alloy composition and then separate with an interchange in the symmetry of the c.b. and v.b. This type of behaviour has been observed in absorption (1D66, 2D68, 2D63, 4T67, 5T67) for this alloy system. Similar effects have been noted in a number of other IV-VI alloy systems (1M73, 3S67, see Fig. A1-5).

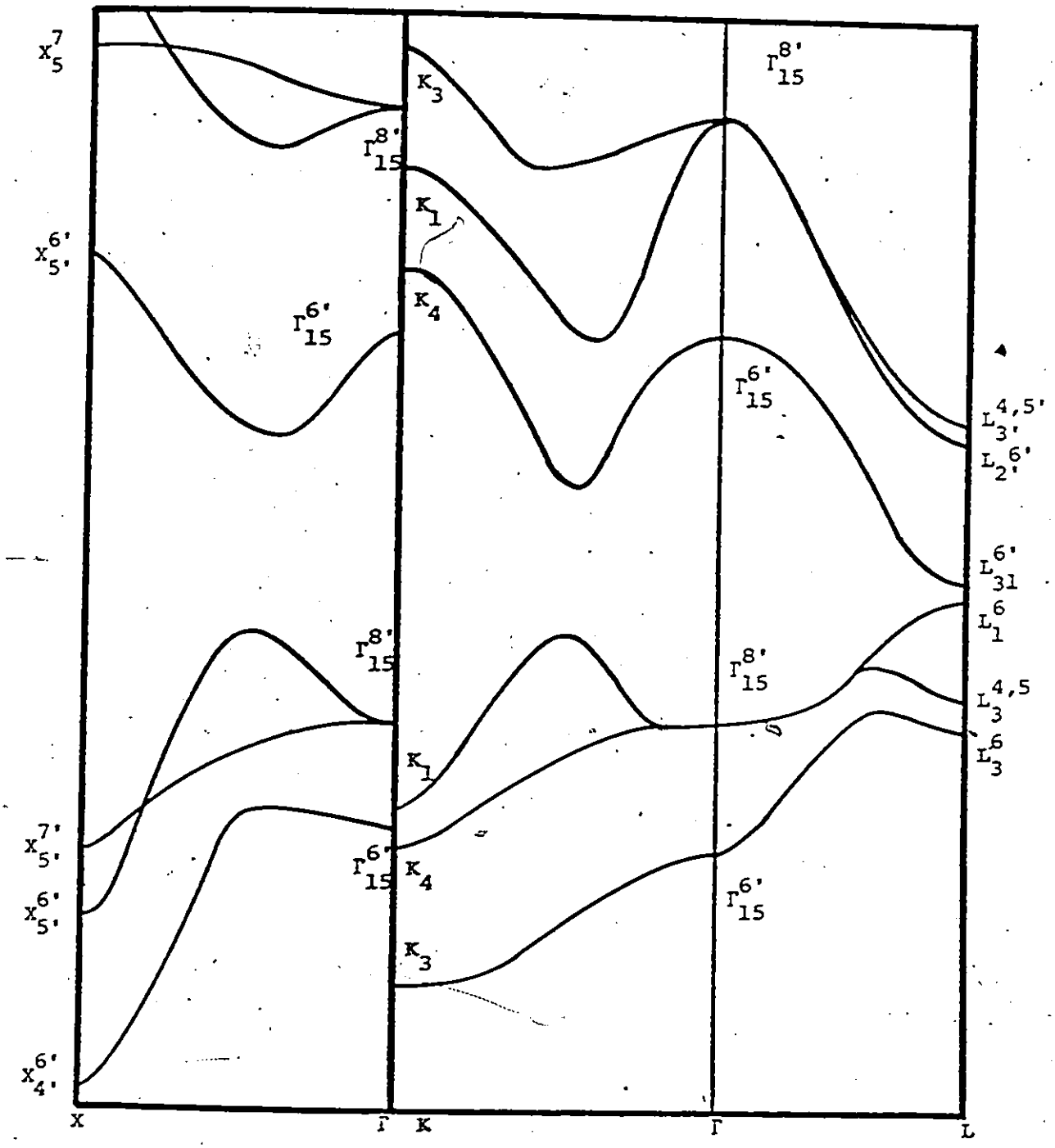

Fig. A1-4 Band structure diagram for PbTe (1L66), (subscripts: without s-o splitting, superscript: double group notation, with s-o splitting).

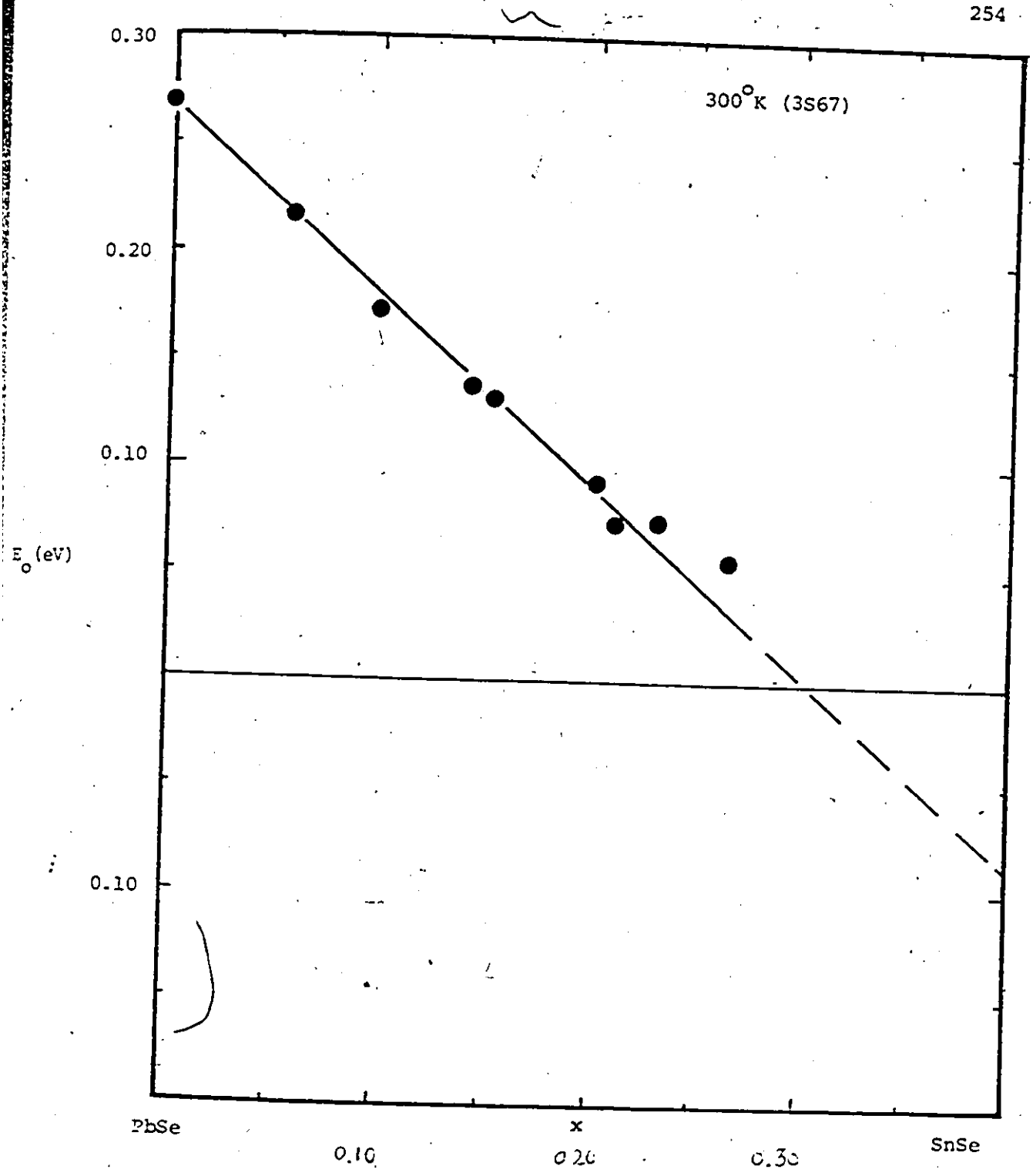

Figure A1-5. Showing the typical behaviour of E_o for the lead salts and their alloys. (3S67).

The particular difficulty in preparing alloys for this system, as mentioned before, is that there is a considerable deviation from stoichiometry in the case of pulled alloy ingots. This is graphically demonstrated by deviations of the lattice parameter seen on fig. A1-2. The deviation in a function of alloy composition and it reaches 0.94% at SnTe end (1U62, 3M63, 4,5B63). Therefore if the method of preparation is not known, the determination of lattice parameter is no indication of the correct composition of the alloy.

The effect of deviation from stoichiometry as found by a number of workers (1, 2D72) is to keep the carrier concentration at $p \gtrsim 10^{20} cm^{-3}$, as discussed before.

A1-5 REFLECTANCE STUDIES OF THE (Pb,Sn)Te ALLOYS

The samples used in this work were prepared at the Bell Howell Laboratories. The composition of slices of the ingots were obtained by X-ray powder photographs. The quoted compositions were in good agreement with these measurements. Some samples were small grain polycrystalline, but some contained larger grains. The samples were cut and polished by the same procedure as described in Chapter 3. The size of the samples varied from 5 x 10 mm^2 to 1cm^2.

Prior to reflectance measurements, the samples were etched in a solution of 25=NaOH:1 = I_2 by weight in 10 ml of distilled H_2O (1N66). After the etch, the sample is washed with distilled water, alcohol and then acetone. No appreciable improvement in the optical spectra was

observed for different etching times. The samples were extremely brittle, with a considerable risk to cleave. Being so hard, the surfaces were probably little contaminated by polishing and grinding. It is expected that the effectiveness of the etchant for SnTe-rich samples would decrease with increasing concentration of Sn. At the time this work was being completed, no alternative etchant for SnTe had been found which would guarantee undamaged optical surfaces (4K66, 5B63).

Reflectance measurements on these alloys were made on the equipment described in Chapter 3. The measurements in the near IR and the visible to u.v. were made in two separate runs. Figs. A1-6 and A1-7 show the results in the two photon regions for a number of alloy samples. The results at the end points for PbTe and SnTe are compared in Table A1-1 to results obtained by Cardona (2A68, 5C64) and Belle (2B65).

Four structures are observed in the reflectance spectra of (Pb,Sn)Te alloy system. From the assigned structures in PbTe (5C64) the observed peaks are labelled as E_1,E_2 and E_3 over the alloy composition. An additional structure which has here been labelled as E' is found at energies lower than E_1. E_2 appears generally as the dominant structure followed by E_3 as a shoulder. The prominence of this shoulder decreases with SnTe content in the alloy (fig. A1-7).

In fig. A1-8 the behaviour of the measured structures with alloy composition is shown. It is seen that in the case of these energies no clear alloy behaviour can be established. The width of the peaks and therefore their poor resolution, except for the E_2 peak, is the main cause of the considerable scatter between experimental points.

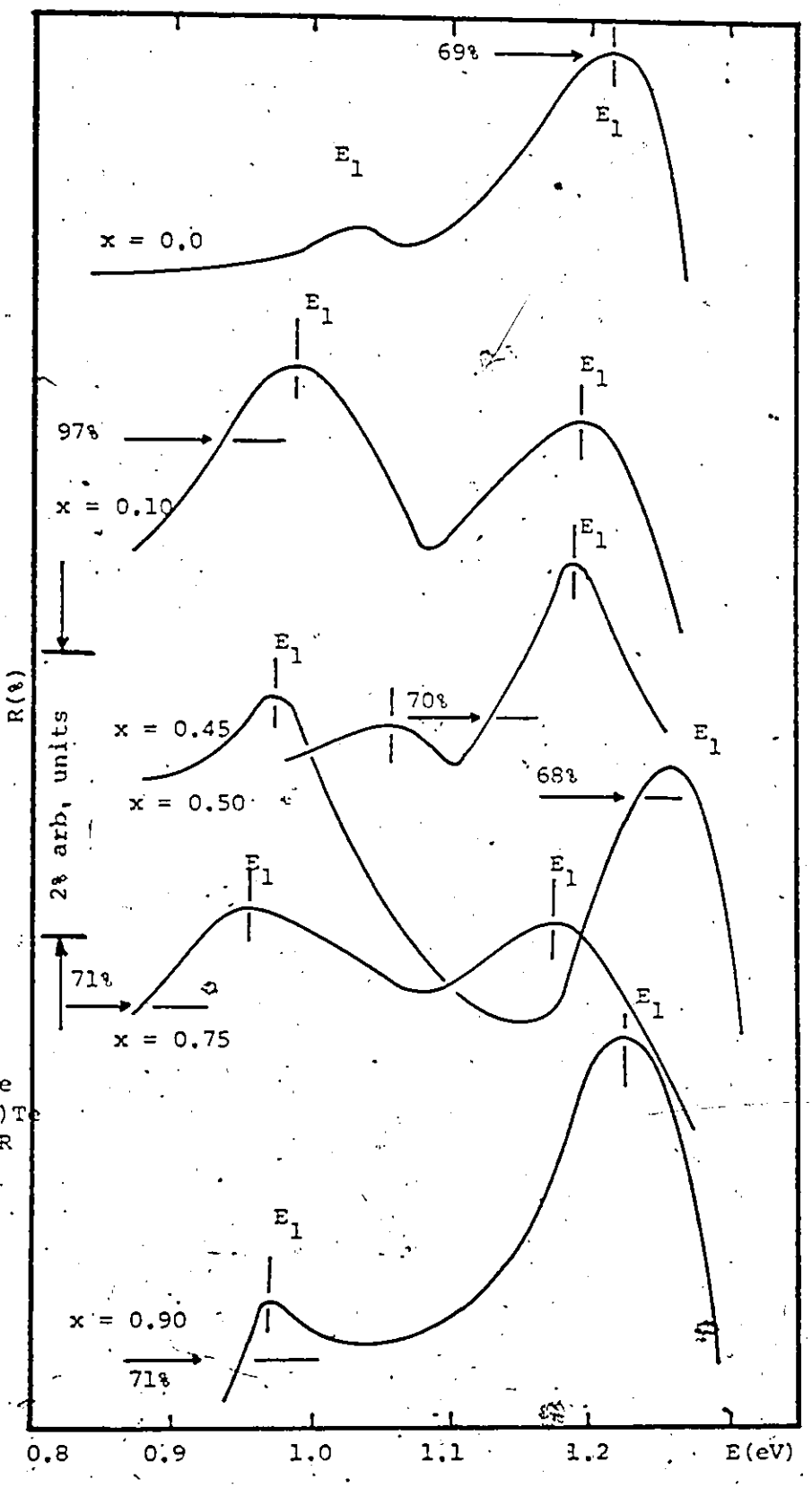

Figure A1-6. Reflectance spectra of some (PbSn)Te alloys, in the near IR region.

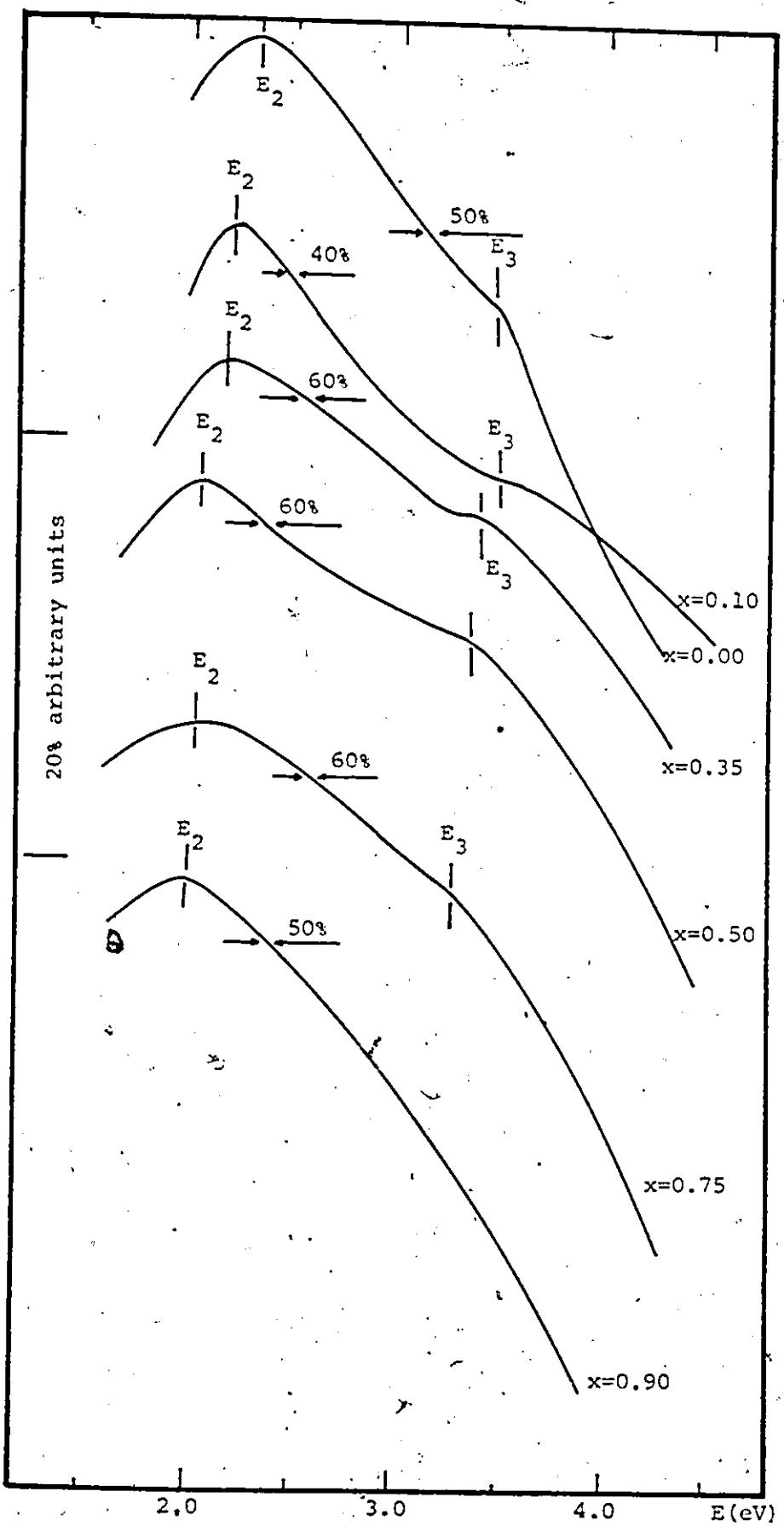

gure A1-7. Reflectance spectra of some (PbSn)Te alloys in the visible and near UV spectra.

Table A1-1 Energies in eV

PEAK	REFERENCE	PbTe	SnTe
E_1	5C64 R	1.24	
	5C64 Tr	1.26	0.97
	2B65 R	1.22	
	2A68 Tr	1.2	
	Present Work	1.22	1.30*
E_2	5C64 R	2.45	2.07
	5C64 Tr	2.2	1.96
	2B65 R	2.45	
	2A68 Tr	2.25	
	Present Work	2.22	1.98*
E_3	5C64 R	3.5	3.2
	5C64 Tr	3.36	3.06
	2B65 R	3.55	
	2A68 Tr	3.45	
	Present Work	3.48	3.2

* Extrapolated

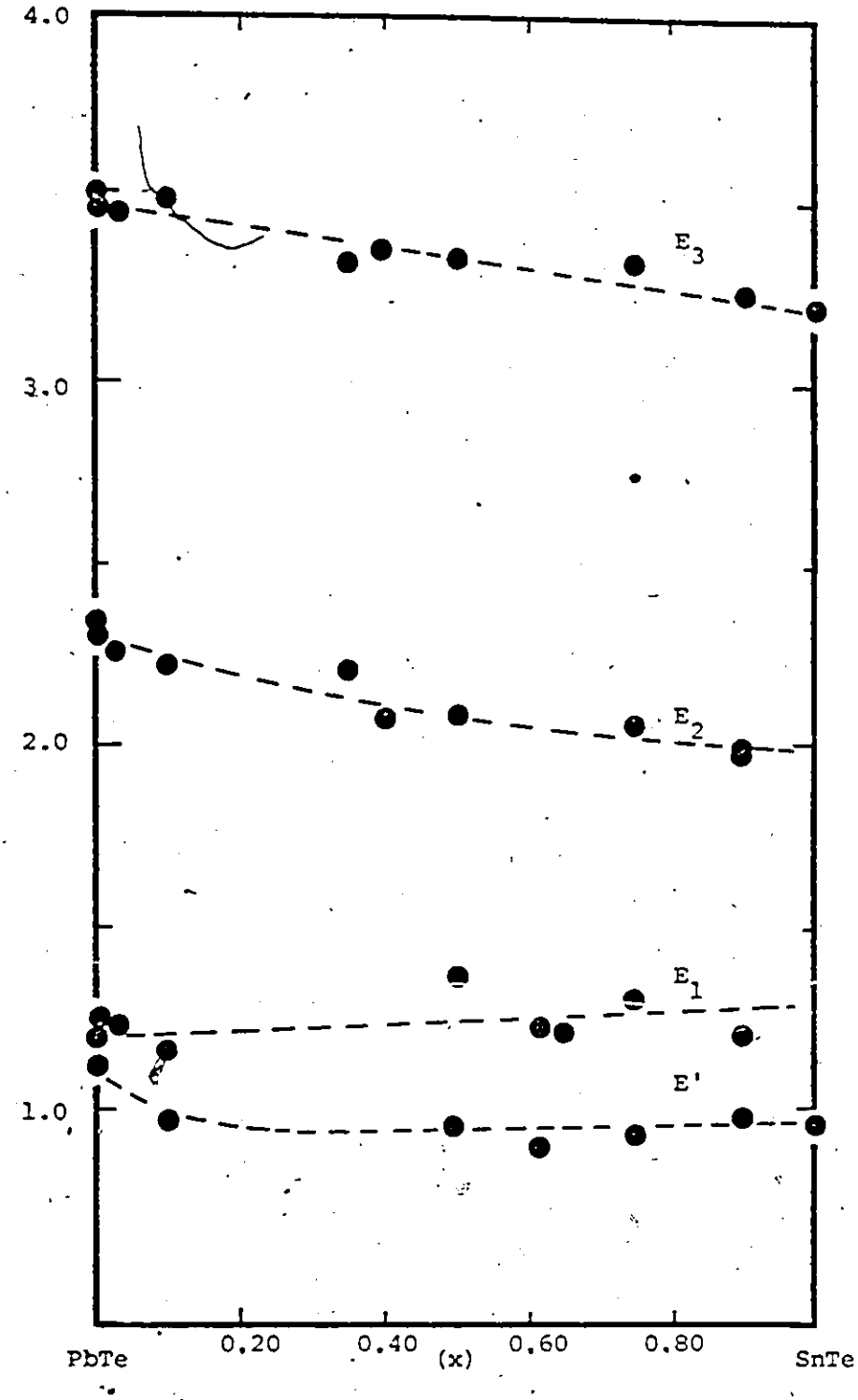

Figure A1-8. The energy variation of the reflectance peaks observed with alloy composition for the (PbSn)Te system.

Furthermore, if one considers these peaks as due to a combination of transitions at slightly differing energies at various points in the B.Z. (5C64), no relevant comment can be made on the alloy behaviour of a complex when no valid assumptions can be made on individual structure behaviour.

It would seem then that because of the poor resolution in reflectance, electroreflectance might be an experimental approach that could resolve these energies. But it was found for the alloys of (Pb,Sn)Te (but not for PbTe itself) that with carrier concentrations in the order of $10^{20} cm^{-3}$ it was difficult to establish an electric field on the surface of the samples. Already the penetration depth of the photon radiation is greatly reduced when carriers are in excess, therefore the possibility of detecting $\Delta R/R$ spectra which are reliable is difficult. In fact, with the electric field modulation technique only E_2 could be detected to any significant extent. These results are not reproduced here since they are not considered sufficiently reliable or in any sense more useful in explaining the reflectance results. There has been also an attempt to obtain thermoreflectance measurements. The quality of these results is not improved. For these reasons in part, further measurements on this alloy system have been interrupted until better material would be available. However, it has been found by Cardona that several transitions in the B.Z. can be assigned at energies close to the observed E_2 and E_3 peaks. The E_1 transition has been assigned to occur in the (110) direction, involving M_1 and M_2 critical points (5C64, 2A68). The experimental value of 1.24 eV of Cardona compares well with

the E_1 = 1.20 eV measured in this work for PbTe. Johnston et al. (1J62) predict a value of 1.23 eV for this energy transition.

The E_2 transition has been found as the absolute maximum in reflectivity. This maximum according to Brust (3B64) is due to saddle point singularities at X and Σ very close in energy for zinc-blende materials. It has been suggested by Cardona (5C64) that this transition in the case of the lead salts giving E_2 may be partly due to transitions in the (100) directions.

Cardona et al., have seen fine structures on the E_2 and E_3 peaks for PbTe indicating that it is likely that these peaks are the cumulative effect of optical transitions at various B.Z. localities. However, Johnston's band structure calculations are not complete enough that much finer structure in reflectance may be reliably correlated to band structure. The E_3 transition has been tentatively assigned to occur at the X point.

The E' peak, whose resolution is often comparable to that of the E_1 throughout the alloy range (fig. A1-6) has not been identified by Cardona and workers. The Lin, Kleinman (1L66) band structure calculations would indicate a transition at the L point of 0.98 eV. This value compares reasonably with the 1.11 eV value experimentally observed. This transition would then be an admixture of M_0 and M_1 singularities.

APPENDIX A2

A2-1 INTRODUCTION

In section 3-8 some of the properties and aspects of the preparation of MOS sandwiches has been discussed. Clearly when thin films are deposited on an optical surface, the absolute reflectance of the heterostructure will undergo a certain change.

In other words, it is important to investigate how the reflectance and the electroreflectance spectra are altered and whether the observed electroreflectance lineshape changes. This change will be affected by various parameters, such at the refractive index and the thickness of the film layers.

In practice, it has been already (cf. ch. 4) demonstrated that for layers of SiO of thickness $\lambda/2$ (λ= 5498Å and Ni-alloy (inconel), 70% transmitting films no detectable difference between the EER and the SBER spectra is seen for the Ga(As,P) alloy system.

Here it is wished to make a qualitative study of this effect in the vicinity of the fundamental gap of GaAs. This is done in terms of the optical parameters of the compound and the thin films within that energy range. This study has not been made on lower gap materials, since important parameters such as $\Delta\epsilon_1$ and $\Delta\epsilon_2$ are not available.

A2-2 ELECTROREFLECTANCE FOR AN MOS CONFIGURATION

Eq. (2-31) gives the electroreflectance signal in terms of $\alpha(\varepsilon_1,\varepsilon_2)$ and $\beta(\varepsilon_1,\varepsilon_2)$ as

$$\frac{\Delta R}{R} \quad \alpha(\varepsilon_1,\varepsilon_2)\ \Delta\varepsilon_1 + \beta(\varepsilon_1,\varepsilon_2)\quad \Delta\varepsilon_2 \qquad \text{(A2-1)}$$

where it can be shown that $\alpha(\varepsilon_1,\varepsilon_2) = \frac{1}{R}\frac{\partial R}{\partial \varepsilon_1}$ and $\beta(\varepsilon_1,\varepsilon_2) = \frac{1}{R}\frac{\partial R}{\partial \varepsilon_2}$. Seraphin (2C69) has shown how in the vicinity of the fundamental gap $\alpha >> \beta$ for most III-V semiconductors. However, $\Delta R/R$ will undergo serious changes when metal electrodes (Shockley barriers) and oxide layers (MOS) cover the optical surface under study (1G73). In the past, as recently as (1A73) these effects have been ignored.

Clearly, the total reflectance R is changed, α and β will change and they will be a function of the oxide optical constants $(\varepsilon_{1o},\varepsilon_{2o})$ and thickness, the metal optical constants $(\varepsilon_{1m}, \varepsilon_{2m})$ and thickness, as well as the optical constant of the semiconductor $(\varepsilon_{1s}, \varepsilon_{2s})$. The effect of these will also depend on the thickness of the oxide (d_o) and that of the metal layers (dm). Therefore eq. (A2-1) becomes:

$$\frac{\Delta R}{R} = \alpha(\varepsilon_{1s},\varepsilon_{1o}, \varepsilon_{1m}, \varepsilon_{2s}, \varepsilon_{2o},\varepsilon_{2m}, d_o, d_m)\ \Delta\varepsilon_{1s} + \beta(\varepsilon_{1s}, \varepsilon_{1o}, \varepsilon_{1m},\varepsilon_{2s},\varepsilon_{2o},\varepsilon_{2m},d_o,d_m)\ \Delta\varepsilon_{2s} \qquad \text{(A2-2)}$$

when it is assumed that the application of an electric field does not involve changes in the optical constants of the oxide or the metal electrode nor in the geometric thicknesses of either. (i.e., $\Delta\varepsilon_{1o} = \Delta\varepsilon_{2o} = \Delta\varepsilon_{1m} = \Delta\varepsilon_{2m} = \Delta d_o = \Delta d_m = 0$). This can be easily be verified for the optical constants by preparing a metal-oxide-metal sandwich and performing an electroreflectance run between the metal electrodes. No observable change in either the transmitted or the reflected intensities and the $\Delta R/R$ signal has been seen, indicating also that no detectable change in the thickness of the thin film layers occurs.

In the past, the fact that $\beta << \alpha$ has been a neat guideline that the electroreflectance spectra $\Delta R/R$ is characteristic of the $\Delta\varepsilon_1$ term in eqn. A2-1 i.e.

$$\left.\frac{\Delta R}{R}\right|_{d_o=d_m=0} = \alpha(\varepsilon_{1s},\varepsilon_{2s})\ \Delta\varepsilon_{1s} \qquad \text{(A2-3)}$$

But if, as is the case in MOS devices, β can be comparable to α or even be , $\Delta R/R$ will undergo serious lineshape changes whereby easily shifting the apparent peaks to different energies. If the peaks are taken as the optical energy transitions, serious errors may be made if no careful consideration is taken of the above mentioned changes. Such changes must be investigated before deciding on the appropriate configurations of layer thicknesses and their refractive indices over the photon energy range.

A2-3 REFLECTANCE OF A DOUBLE LAYER: TWO ABSORBING LAYERS ON AN ABSORBING SUBSTRATE

In (LH65) the reflected intensity due to a double layer on an absorbing substrate is given as

$$R = \frac{t_{13}^2 \quad U_{13}^2}{P_{13}^2 \quad q_{13}^2} \tag{A2-4}$$

where

$$P_{13} = P_{12}P_3 - q_{12}q_3 + r_{12}t_3 - s_{12}U_3$$
$$q_{13} = q_{12}P_3 + P_{12}q_3 + s_{12}t_3 + r_{12}U_3$$
$$t_{13} = t_{12}P_3 - U_{12}q_3 + V_{12}t_3 - W_{12}U_3$$
$$U_{13} = U_{12}P_3 + t_{12}q_3 + W_{12}t_3 + V_{12}U_3$$

$$W_{12} = W_2 + h_{12}r_2 + g_1s_2 \qquad U_{12} = U_2 + h_1P_2 + g_1q_2$$
$$V_{12} = V_2 + g_1r_2 - h_1s_2 \qquad t_{12} = t_2 + g_1P_2 - h_1q_2$$
$$s_{12} = s_2 + h_1V_2 + g_1W_2 \qquad q_{12} = q_2 + h_1t_2 + g_1U_2$$
$$r_{12} = r_2 + g_1V_2 - h_1W_2 \qquad P_{12} = P_2 + g_1t_2 - h_1U_2$$

$$V_2 = e^{-\alpha_1}\cos\gamma_1 \qquad q_2 = e^{\alpha_1}\sin\gamma_1$$
$$P_3 = e^{\alpha_2}\cos\gamma_2 \qquad P_2 = e^{\alpha_1}\cos\gamma_2$$
$$s_2 = e^{\alpha_1}(h_2\cos\gamma_1 + g_2\sin\gamma_1) \qquad t_2 = e^{-\alpha_1}(g_2\cos\gamma_1 + h_2\sin\gamma_1)$$
$$r_3 = e^{\alpha_1}(g_2\cos\gamma_1 - h_2\sin\gamma_1) \qquad U_2 = e^{-\alpha_1}(h_2\cos\gamma_1 - g_2\sin\gamma_1)$$
$$U_3 = e^{-\alpha_2}(h_3\cos\gamma_2 - g_3\sin\gamma_2) \qquad P_3 = e^{\alpha_2}(\cos\gamma_2)$$
$$t_3 = e^{-\alpha_2}(g_3\cos\gamma_2 + h_3\sin\gamma_2) \qquad q_3 = e^{\alpha_2}(\sin\gamma_2)$$

$$\alpha_1 = \frac{2\pi K_m d_m}{\lambda} \qquad \alpha_2 = \frac{2\pi K_o d_o}{\lambda}$$

$$\gamma_1 = \frac{2\pi n_m d_m}{\lambda} \qquad \gamma_2 = \frac{2\pi n_o d_o}{\lambda}$$

$$g_3 = \frac{n_o^2 - n_s^2 + k_o^2 - k_s^2}{(n_o+n_s)^2 + (k_o+k_s)^2} \qquad h_3 = \frac{2(n_o k_s - n_s k_o)}{(n_o+n_s)^2 + (k_o+k_s)^2}$$

$$g_2 = \frac{n_m^2 - n_o^2 + k_m^2 - k_o^2}{(n_m+n_o)^2 + (k_m+k_o)^2} \qquad h_2 = \frac{2(n_m k_o - n_o k_m)}{(n_m+n_o)^2 + (k_m+k_o)^2}$$

$$g_1 = \frac{n_v^2 - n_m^2 - k_m^2}{(n_v+n_m)^2 + k_m^2} \qquad h_1 = \frac{2 n_v k_m}{(n_v+n_m)^2 + k_m^2}$$

where the optical constants and the thickness are considered as

vacuo $\equiv (n_v = 1, k_v = 0, d_v = \infty)$

metal layer $\equiv (n_m, k_m, d_m)$

oxide layer $\equiv (n_o, k_o, d_o)$

semiconductor $\equiv (n_s, k_s, d_s = \infty)$

The application of thin films on the surface of a semiconductor will alter the reflectance of that surface.

Volume 3 of Willardson and Beer:" Optical Properties of Semiconductors and Semimetals" contains measured optical constants for some of the III-V compounds. Values of n, k and R are available over the energy range close to the fundamental gap.

These values are obtained by a number of different techniques which are discussed in the text (3W67). The information supplied by Sturge (1S62) and Marple (^{3}M64) are found also in table A2-1. With these, the optical constants for the oxide and the metallic film are also given. These are then used in equations A2-4. The reflectance of an MOS layer is then reproduced by increasing the oxide thickness and the metal thickness from zero to those desired values which are characteristic of the sample mountings (eq. $d_m \sim 120\text{Å}$, $d_o \sim \lambda/2$). The optical constants for the SiO layer are obtained from tables given in (fig. 3-13, 14) and the optical constants of the metallic film are those of Ni (1A57) since no Ni-alloy values are available. This is justifiable as it is wished here only to demonstrate the effect that these layers have on the electroreflectance lineshape, and no actual comparison to experiment is done. Fig. A2-1 shows how the reflectance of GaAs in the 1.2 to 1.6 eV energy range is affected by the deposition of a $\lambda/4$ thick SiO layer, (compare a) to b)) and then a layer of Ni film ($\sim 120\text{Å}$ thick, c)). The behaviour of R as a function of energy is completely changed from monotonically increasing to one with a maximum over this energy range. The SiO layer

TABLE A2-1 Showing values of (n_s, k_s), (n_o, k_o) and (n_m, k_m) in the vicinity of the GaAs fundamental gap as used to calculate R the reflectance of the MOS Sandwich.

λ (Å)	R(%)	n_s	k_s	n_o	k_o	n_m	k_m
7820	0.31710	3.82363	0.09000	1.91020	0.50901	2.32000	4.12000
7990	0.31580	3.77212	0.08400	1.90560	0.50584	2.35000	4.17000
8120	0.31450	3.73873	0.08000	1.90220	0.50316	2.75000	4.21000
8200	0.31400	3.72030	0.07800	1.90050	0.50035	2.39000	4.23000
8300	0.31350	3.69919	0.07450	1.89850	0.49690	2.42000	4.26000
8370	0.31280	3.68556	0.07210	1.89730	0.49394	2.43500	4.27500
8490	0.31200	3.66409	0.06720	1.89500	0.49035	2.47000	4.32500
8600	0.31130	3.64628	0.06200	1.89300	0.48487	2.50000	4.33000
8670	0.31250	3.63576	0.06150	1.89180	0.48135	2.52000	4.38000
8800	0.31100	3.61772	0.00455	1.88950	0.47517	2.55000	4.42000
8900	0.31000	3.60502	0.00455	1.88800	0.46994	2.57500	4.46000
9000	0.30950	3.59323	0.00455	1.88620	0.46403	2.60000	4.50000
9050	0.30930	3.58764	0.00455	1.88550	0.46079	2.62000	4.52000
9270	0.30880	3.56522	0.00455	1.88230	0.44819	2.67500	4.60000
9600	0.30820	3.53707	0.00455	1.87820	0.42722	2.76000	4.72000
10000	0.30760	3.50959	0.00455	1.87480	0.39962	2.87000	4.87000

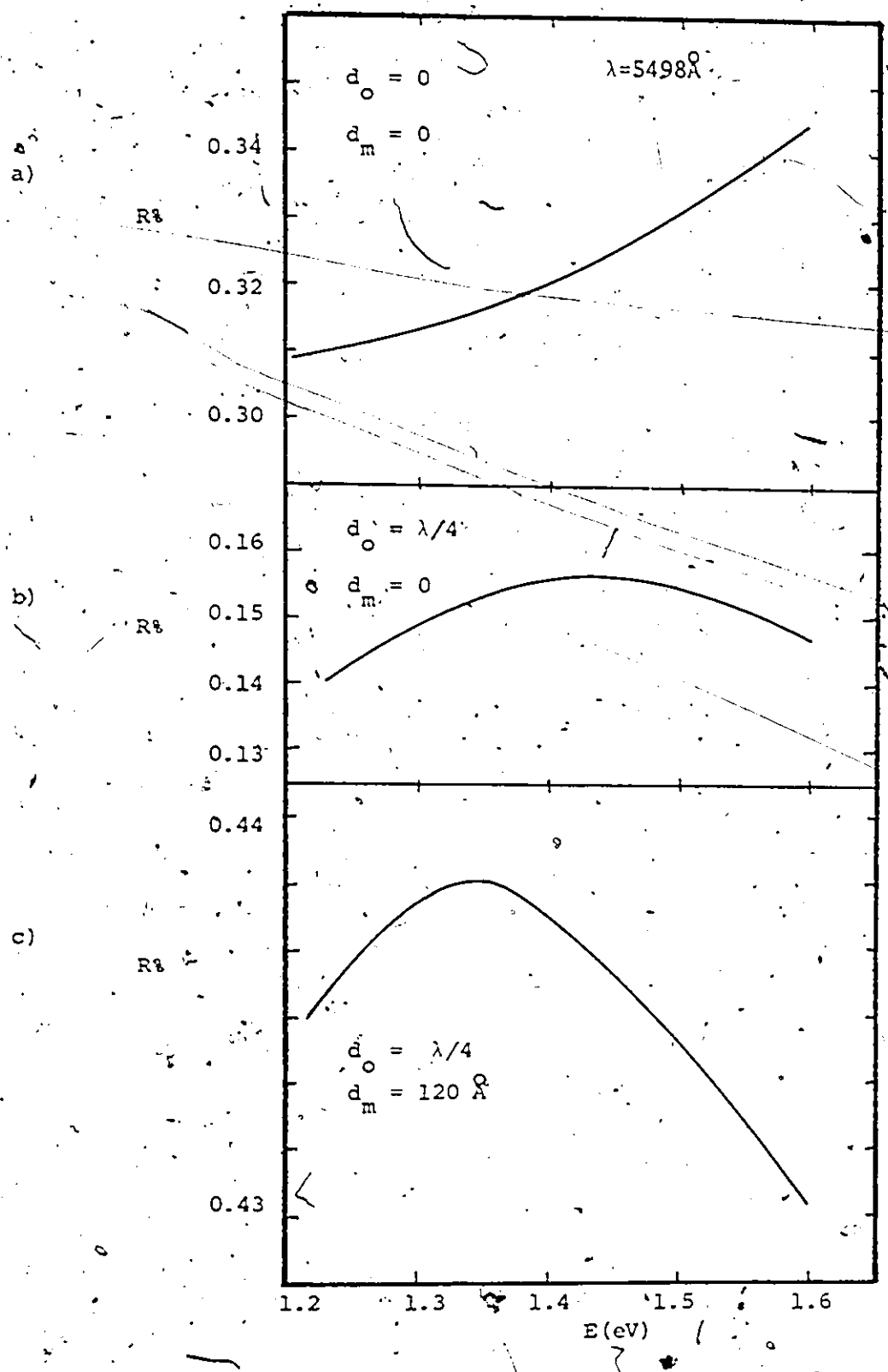

Figure A2-1 Showing the effect of an oxide (SiO) and a metal electrode (Ni) on the reflectance of GaAs in the vicinity of the gap.

decreases the reflectivity of the sample but the Ni film increases it as well as reduces the actual change in reflectance, whereby masking the structures due to the semiconductor alone.

In figs. (A2-2a,b) reflectance as a function of d_o and d_m is shown at the 1.437 eV energy point, which is taken as the gap of GaAs. The reflectance decreases at odd $\lambda/4$ oxide thicknesses and suffers a maximum at even $\lambda/4$ oxide thicknesses. For reasons shown in the next section as well as because R is the highest value at $\lambda/2$ with a reasonable oxide thickness, this thickness was used to obtain experimental information. Because in the vicinity of the gap for any semiconductor n_s and k_s will have similar behaviour and for SiO (see variation of n_o and k_o, fig. 3-13 over the energy range from $\sim$ 0.7μ to 8μ), k_o is very small and $2. < n_o < 1.7$, the systematic behaviour for R for any semiconductor will be close to that at the gap of GaAs. Therefore the investigation of the behaviour of R for GaAs will not be too different than that for other compounds having lower fundamental gaps.

In Fig. A2-3 and A2-4 the dependence of R at Eg for GaAs in an M-S and in an MOS configuration are shown respectively. The behaviour of R ($d_o = 0$, E = 1.437) in a M-S configuration resembles that of R ($d_o = \lambda/2$, E = 1.437) in an MOS configuration, they both increase with increasing d_m. The actual values of R are lower at $d_o = \lambda/2$ than at $d_o = 0$.

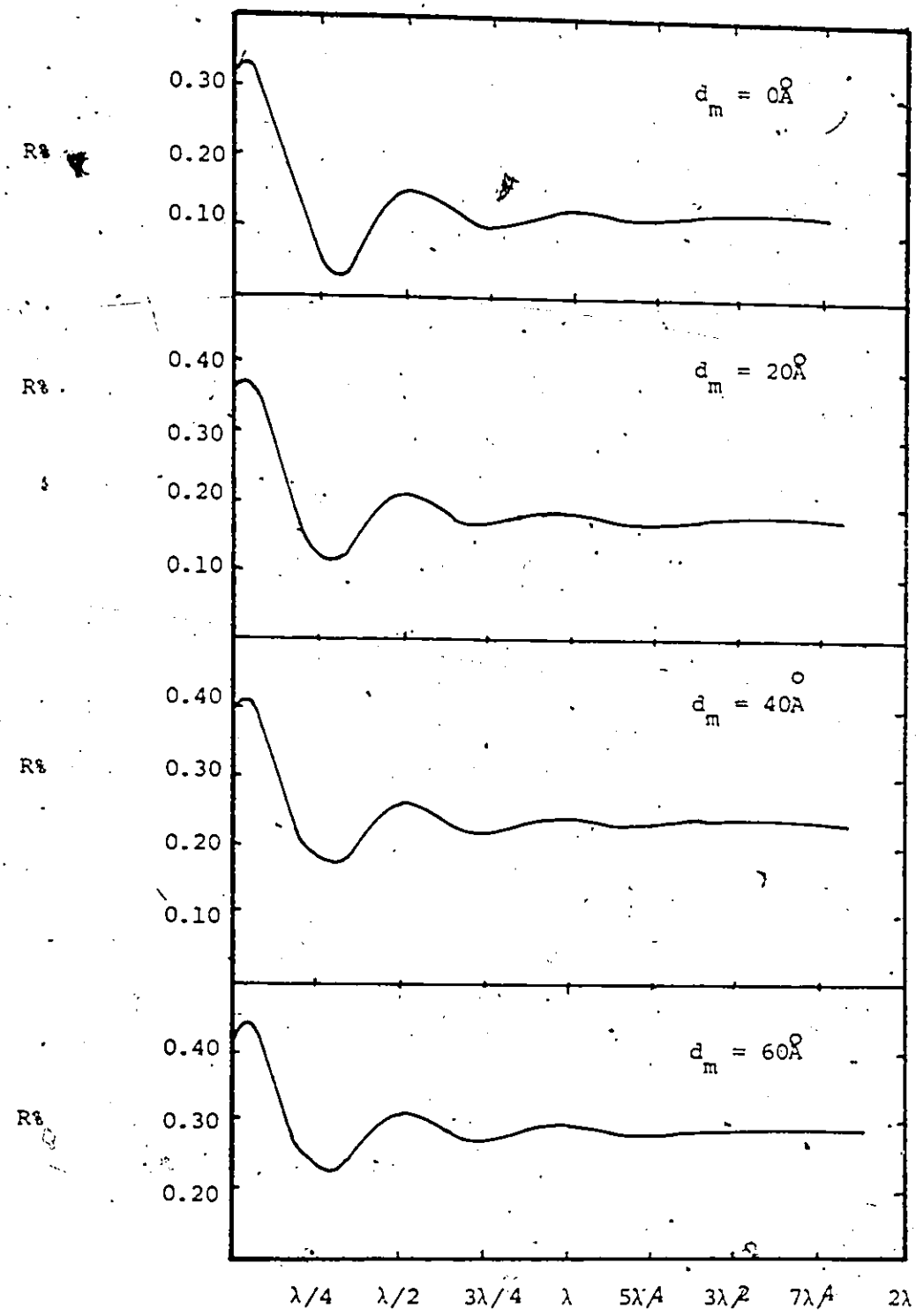

Figure A2-2a) Showing how R changes a function of d_o and d_m at 1.437 eV for GaAs.

λ=5498Å

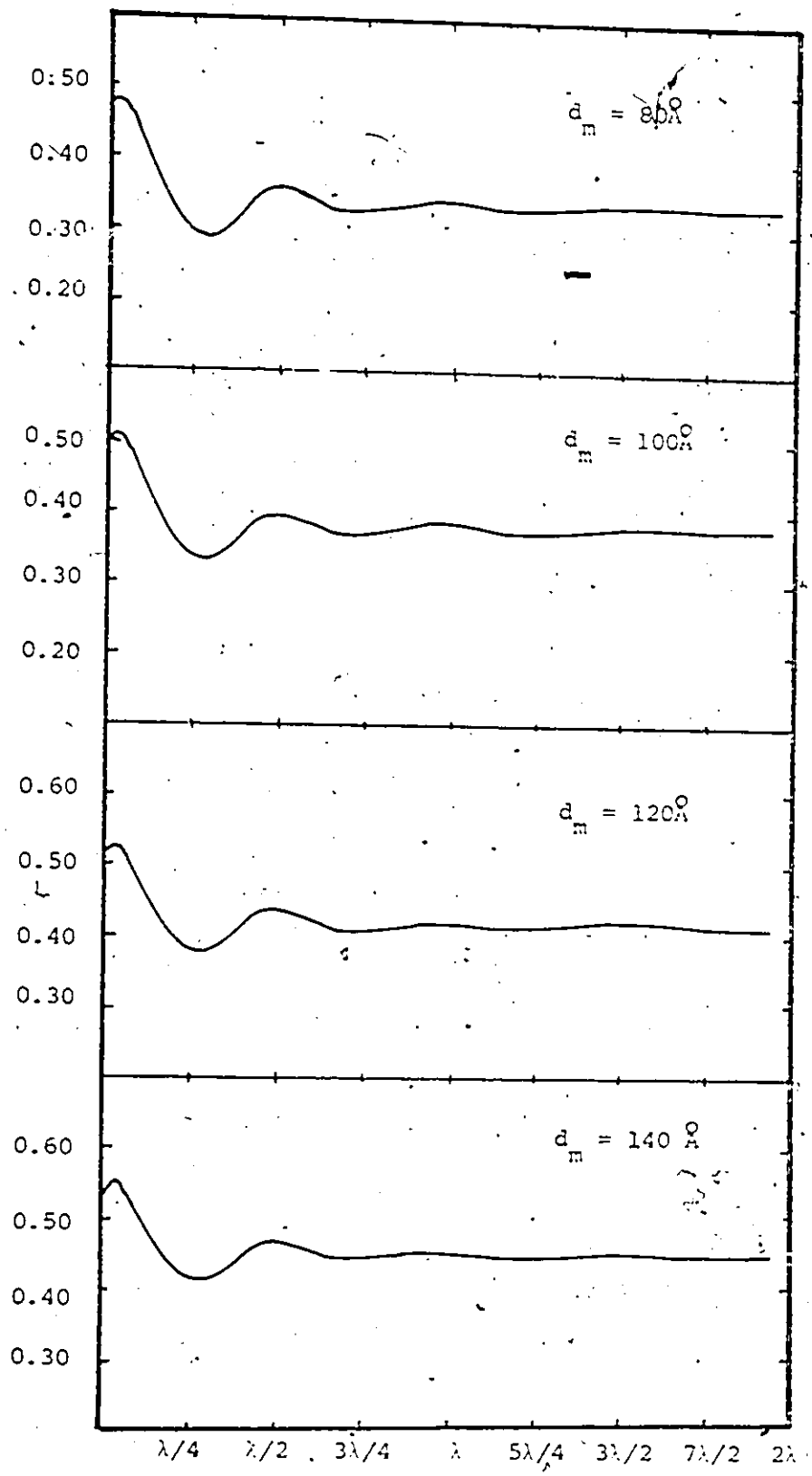

Figure A2-2b) Showing how R changes a function of d_o and d_m at 1.437 eV for GaAs.

λ=5498Å

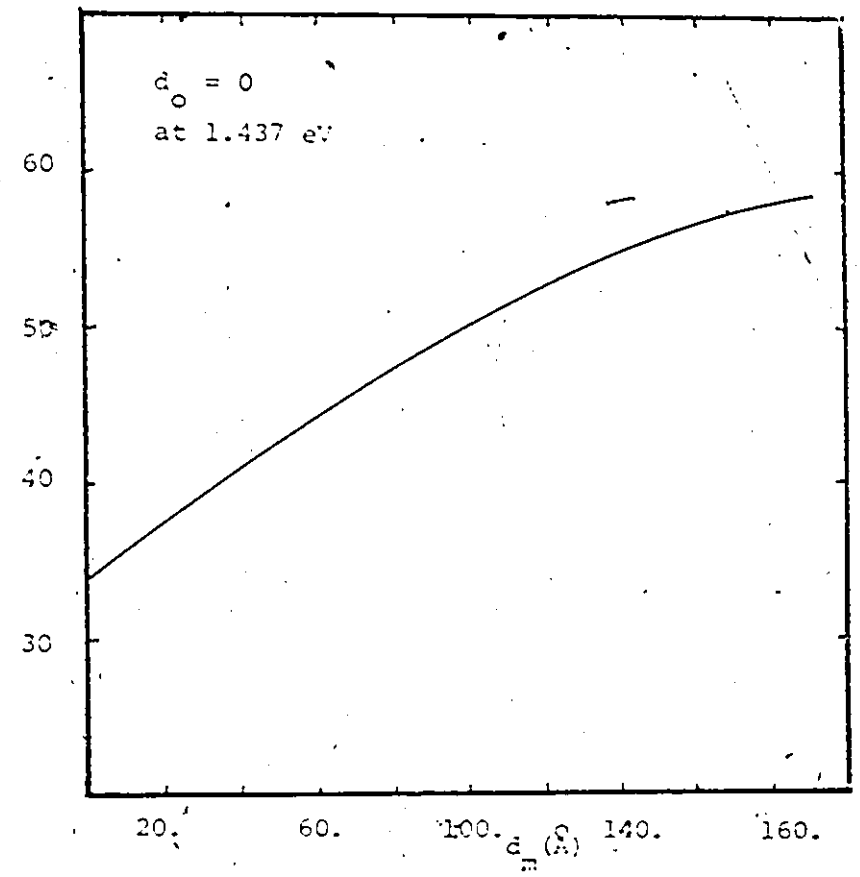

Figure A2-3. Showing the dependence of reflectance R on the metal electrode thickness in an M-S or Schottky barrier configuration at the gap of GaAs.

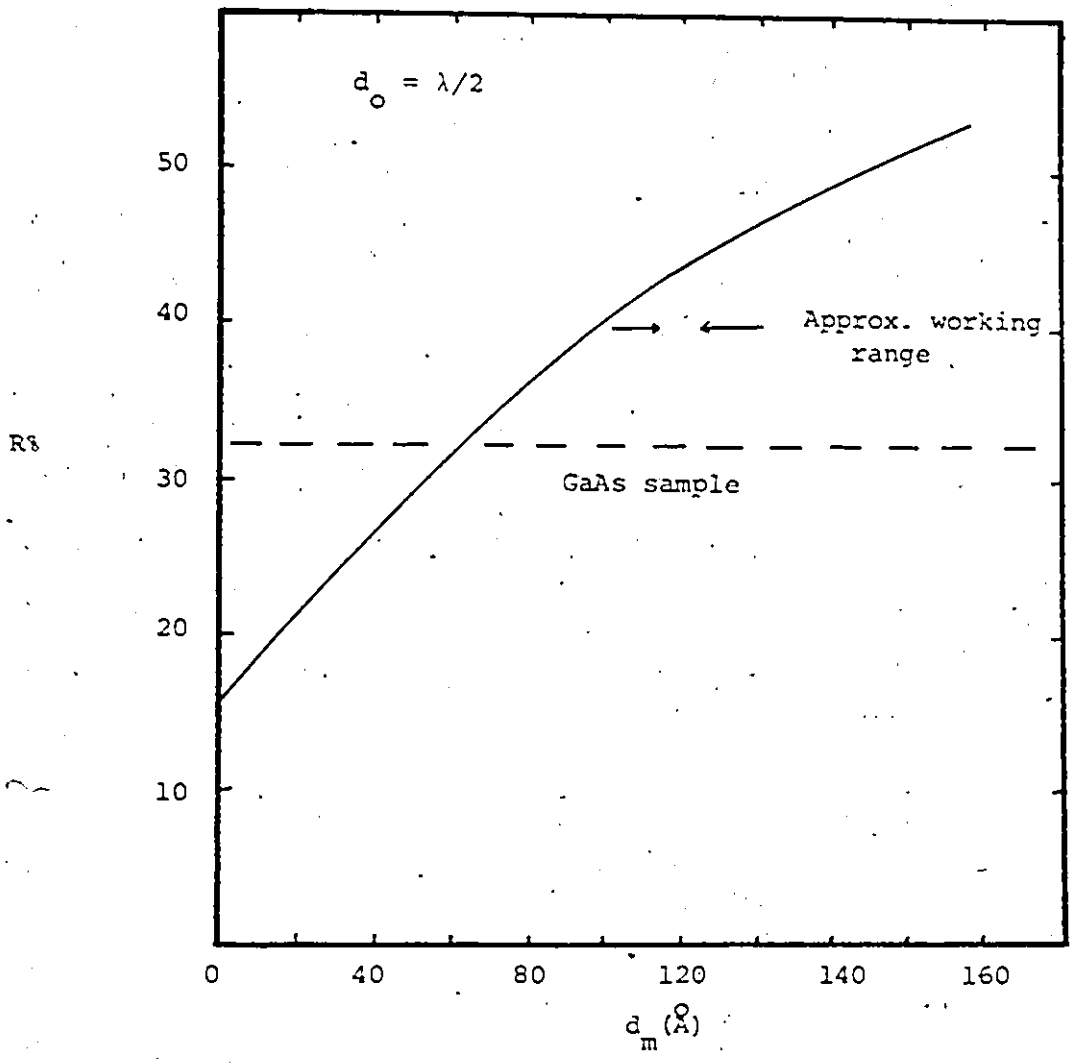

Figure A2-4. Showing the reflectance dependence of an MOS configuration on the electrode thickness for a GaAs sample at the fundamental gap.

The question now is that if R is changed by the deposition of oxide and metal layers how will the electroreflectance spectrum be affected.

A2-4. ELECTROREFLECTANCE OF A DOUBLE LAYER

The change in reflectance due to a modulating effect can be written as

$$\Delta R = \sum_i \left(\frac{\partial R}{\partial \varepsilon_{1i}} d\varepsilon_{1i} + \frac{\partial R}{\partial \varepsilon_{2i}} d\varepsilon_{2i}\right)$$

where the summation over i takes into account the contribution of the ith layer to both the ΔR signal and R as a function of the E_{1i} and E_{2i}.

Therefore eq. A2-2 can be rewritten as

$$\frac{\Delta R}{R} = \frac{1}{R}\left(\frac{\partial R}{\partial \varepsilon_{1s}} d\varepsilon_{1s} + \frac{\partial R}{\partial \varepsilon_{1o}} d\varepsilon_{1o} + \frac{\partial R}{\partial \varepsilon_{1m}} d\varepsilon_{1m}\right) +$$

$$\frac{1}{R}\left(\frac{\partial R}{\partial \varepsilon_{2s}} d\varepsilon_{2s} + \frac{\partial R}{\partial \varepsilon_{2o}} d\varepsilon_{2o} + \frac{\partial R}{\partial \varepsilon_{2m}} d\varepsilon_{2m}\right)$$

which reduces to

$$\frac{\Delta R}{R} = \frac{1}{R}\frac{\partial R}{\partial \varepsilon_{1s}} d\varepsilon_{1s} + \frac{1}{R}\frac{\partial R}{\partial \varepsilon_{2s}} d\varepsilon_{2s}$$

when it is assumed that there is no change in the optical constants of either the oxide or the electrode when an electric field is applied. As mentioned before this fact has been experimentally verified over the photon energies of interest.

The next step is to differentiate eq. A2-4 to obtain $\frac{\partial R}{\partial \varepsilon_{1s}}$ and $\frac{\partial R}{\partial \varepsilon_{2s}}$ where R is a function of $(\varepsilon_{1s}, \varepsilon_{2s}, \varepsilon_{1o}, \varepsilon_{2o}, \varepsilon_{1m}, \varepsilon_{2m}, d_m, d_o)$ or of $(n_s, k_s, n_o, k_o, n_m, k_m, d_m, d_o)$. The differentiation of R w.r.t. each optical constant and in particular the optical constants of the semiconductor is only lenghtly but not difficult. $\Delta\varepsilon_{1s}$ and $\Delta\varepsilon_{2s}$ are obtained from the work of (lP72, fig. 2-8) where the EER spectrum of GaAs has been studied extensively. The $\Delta R/R$ spectrum calculated with $d_o = d_m = 0$ should reproduce these results. (Compare fig. 2-8 and A2-5a). In fig. A2-5, the $\Delta R/R$ spectrum is showed for cases of $d_m = 0$ and the effect of an increasing oxide layer thickness. In fig. A2-6 a similar set of $\Delta R/R$ spectra is seen with the 120Å thick electrode. Considerable changes in the electroreflectance line shape are seen for the various oxide thicknesses. If the threshold is taken to be the peak in the structure, a serious error in the determination of the fundamental gap can be made. Table A2-2 lists for a number of oxide and film thicknesses the peak energies. 1.437 eV is taken as the normal threshold for GaAs. It will be shown that at oxide thicknesses of $\lambda/2$ and λ is where least errors can be made in the determination of these energies.

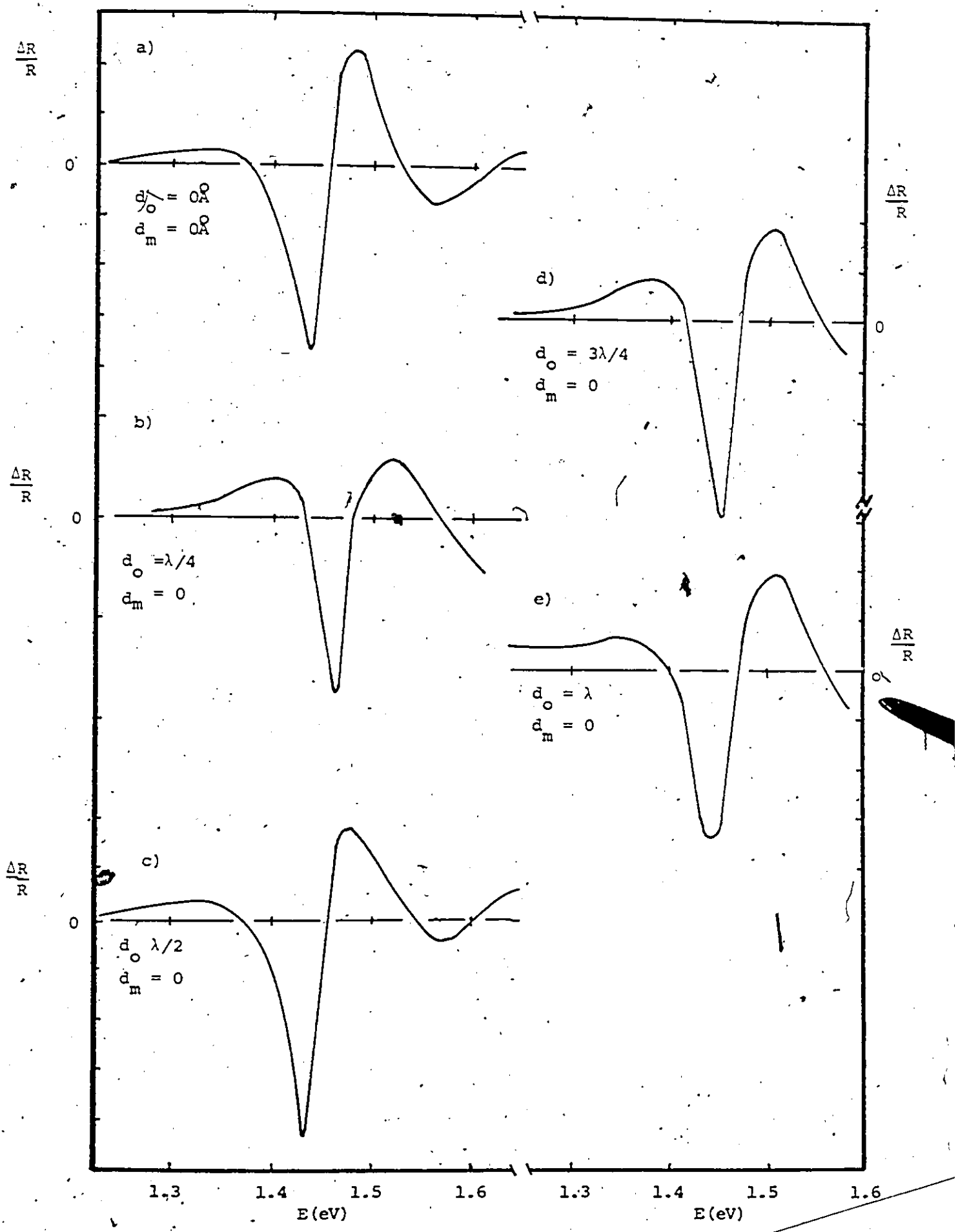

Figure A2-5. Showing electroreflectance line shape change due to a SiO deposited film in the vicinity of the GaAs gap.

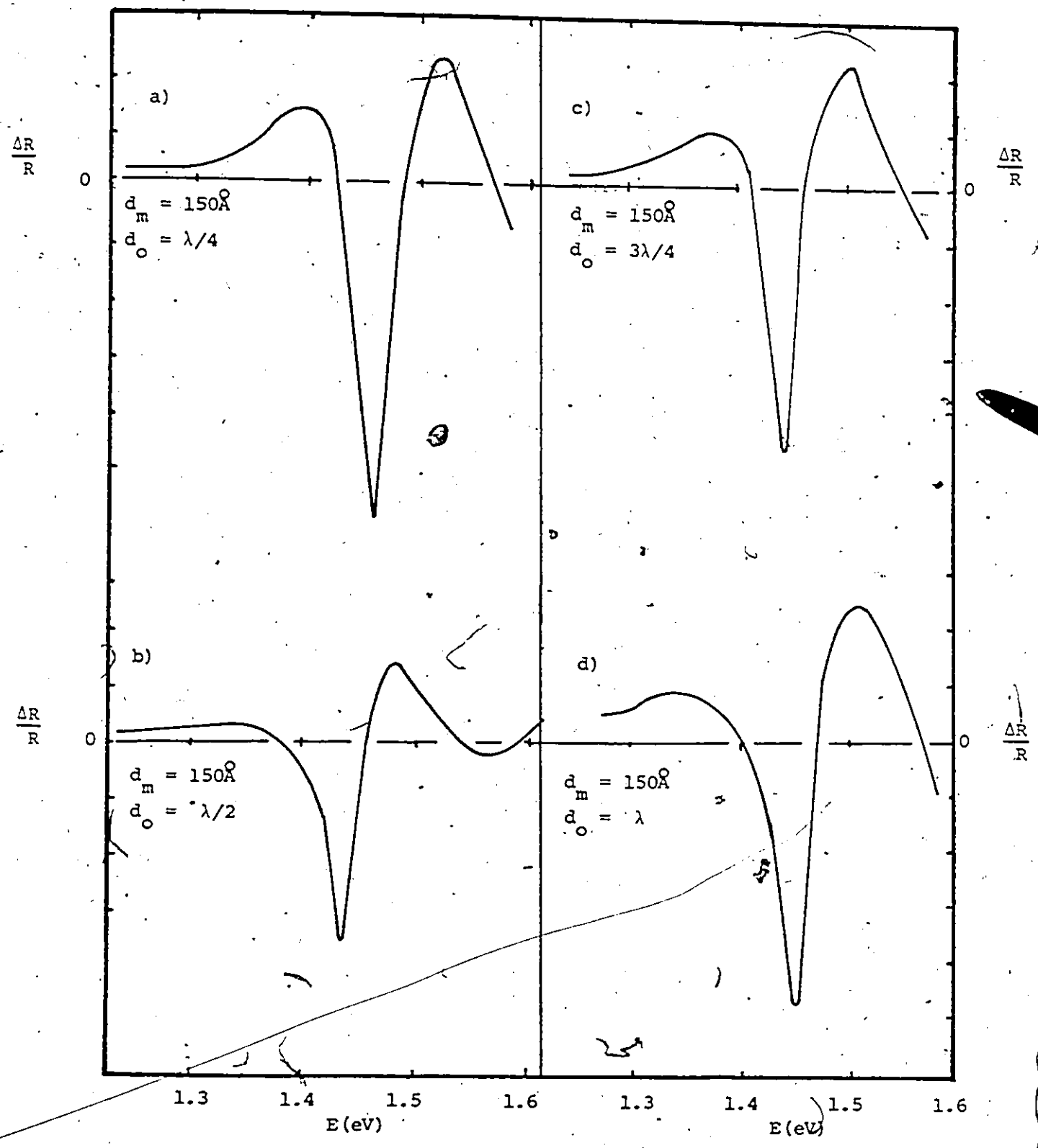

Figure A2-6. Showing the lineshape change in electroreflectance for GaAs in the E_o region as a function of oxide (SiO) thickness with a 150Å thick Ni electrode..

TABLE A2-2: In part (A) the energy values of the peaks is shown as a function of d_o and d_m. In part (B) the width at half the height of the peak is shown as a function of d_o and d_m.

(A)

d_m / d_o	0	λ/4	λ/2	3λ/4	λ
0	1.437	1.463	1.431	1.451	1.440
25		1.457	1.433	1.455	1.447
50		1.455	1.434	1.455	1.449
75		1.457	1.434	1.454	1.447
100		1.459	1.434	1.453	1.448
125		1.461	1.433	1.454	1.447

(B)

	0	λ/4	λ/2	3λ/4	λ
0	4.28	.1314	.595	.384	1.06
25		.303	1.157	.80	2.32
50		.543	1.503	1.1	3.11
75		.825	2.17		5.11
100		1.136	2.19	1.76	5.71
125		1.47	3.648	2.10	7.72

This is due to the dependence of α and β on the optical constants and the thicknesses of the oxide and electrode layers. Fig. A2-7 shows the α, β dependence on d_m for an M-S configuration ($d_o = o$) at 1.437 eV. Fig. A2-8 shows this same dependence at $d_o = \lambda/2$. The qualitative dependence of α is similar although the values of α are reduced. β's dependence is very different in these two cases: in the M-S configuration β undergoes a maximum at $d_m \sim 30\text{Å}$. The magnitude of β is also drastically reduced.

In fig. A2-9, always at the gap of GaAs, the behaviour of α and β are seen for $d_m \sim 120\text{Å}$ as a function of oxide thickness. The dependence of α and β at the gap (and similarly over the energy range of interest) are seen to be similar but with some interesting features. As pointed out in (2G73) the oscillating behaviour is out of phase in such a way that it is possible to choose oxide thicknesses where either $\alpha >> \beta$ (eg. $d_o = \lambda/2$) or $\alpha << \beta$ ($d_o = \lambda/10,\ \lambda/4,\ 3\lambda/5$). Clearly therefore, by the proper choice of oxide thickness it is possible to get a $\Delta R/R$ spectrum characteristic of the $\Delta\varepsilon_1(\alpha > \beta)$ or the $\Delta\varepsilon_2(\alpha << \beta)$ spectrum. The working conditions ($d_o \sim \lambda/2$) during these experiments is such that over most of the energy range studied, little if any difference in line shape should be present between MOS and EER measurements.

In fact this is the relevant point in this appendix. As argued before, the changes in n_o, k_o n_m k_m over the photon transition energies studied in this work by SBER do not change to the extent that the qualitative conclusions

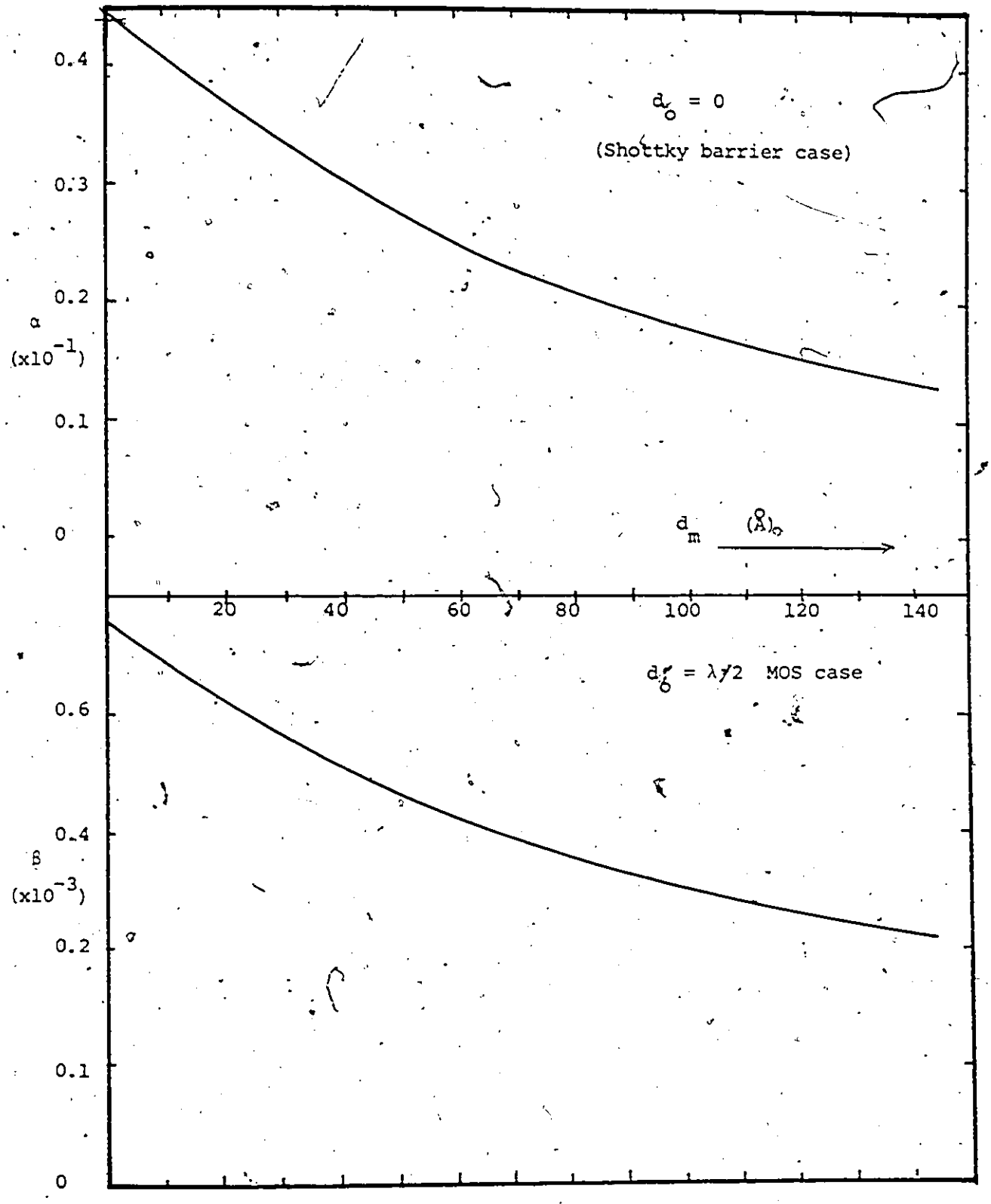

Figure A2-7. α,β dependence on d_m, d_o = 0 at the gap value of GaAs.

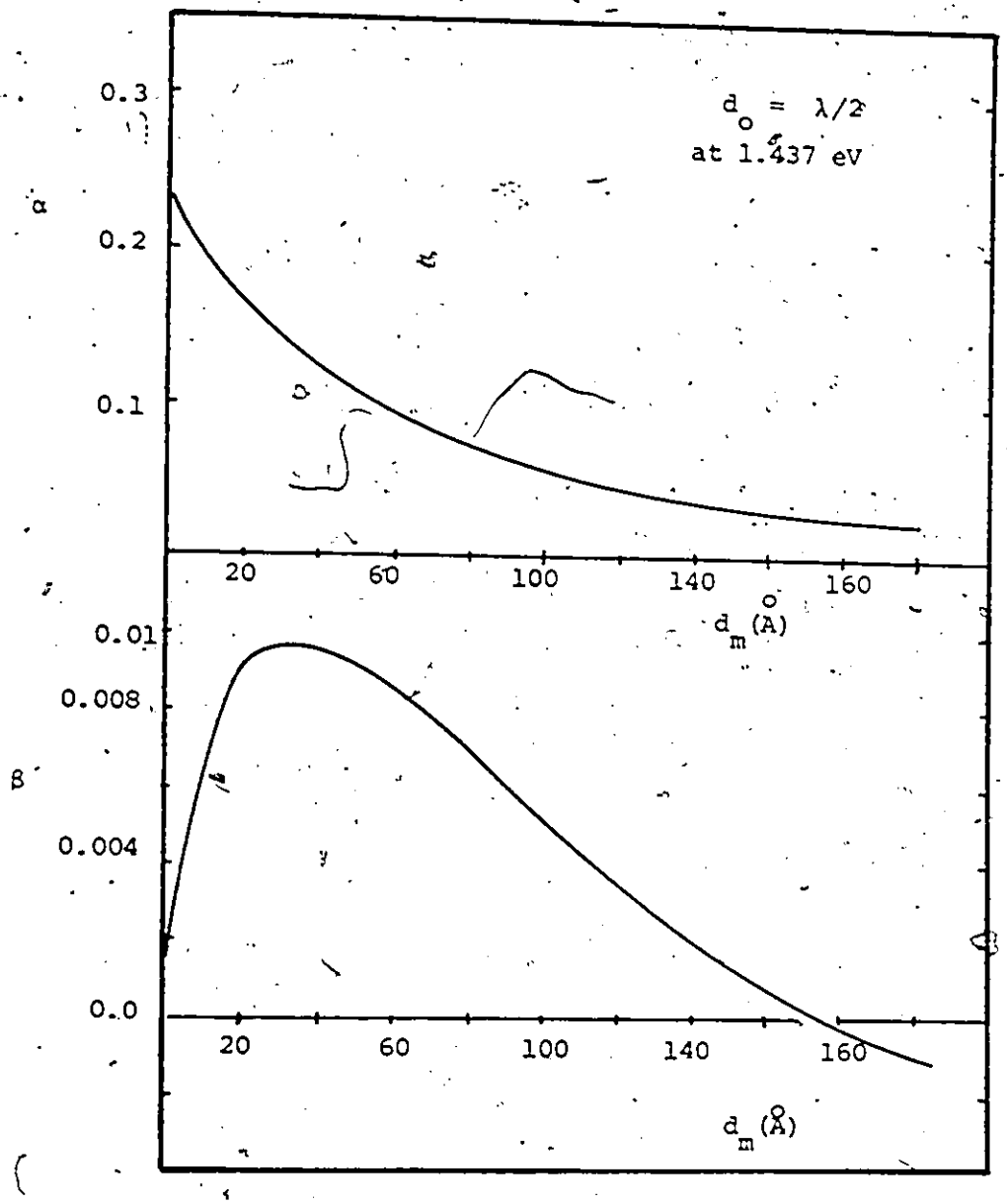

Figure A2-8 Showing the dependence of α, β on the electrode (Ni) thickness for a $\lambda/2$ oxide deposited on GaAs at the gap.

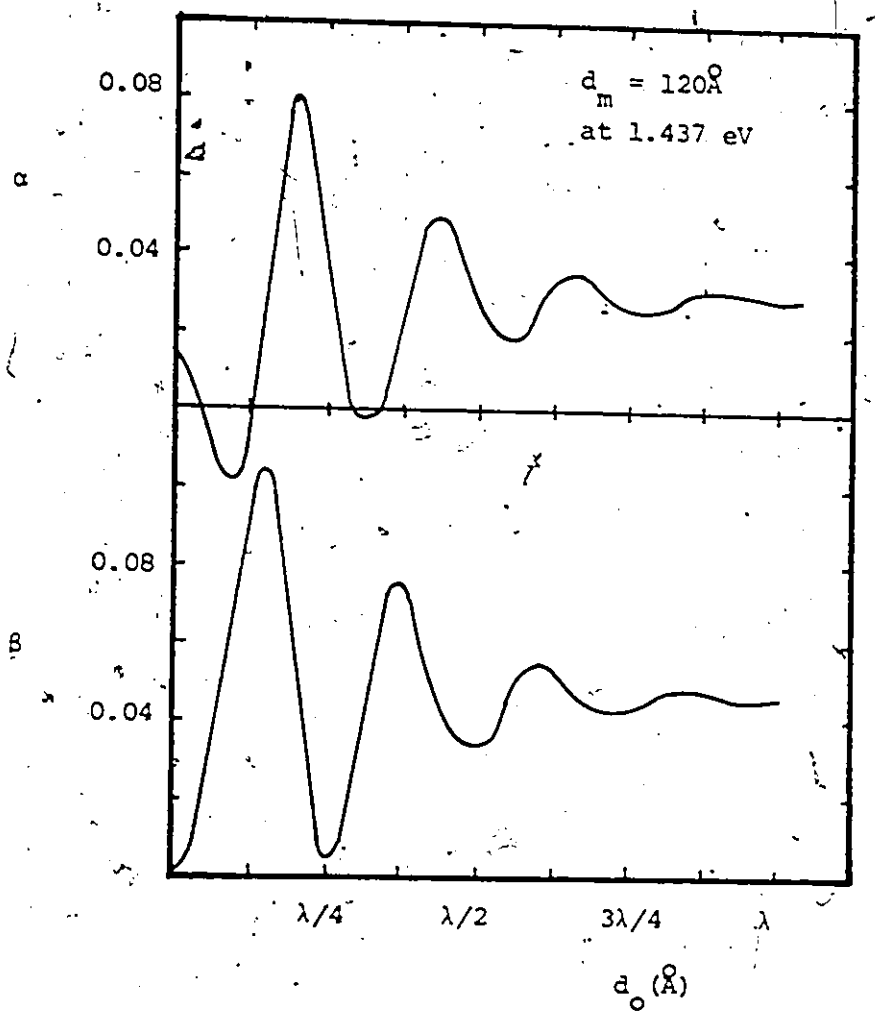

Figure A2-9. Showing the dependence of α, β on the SiO oxide thickness for an MOS sandwich with a 120Å Ni film at the gap of GaAs.

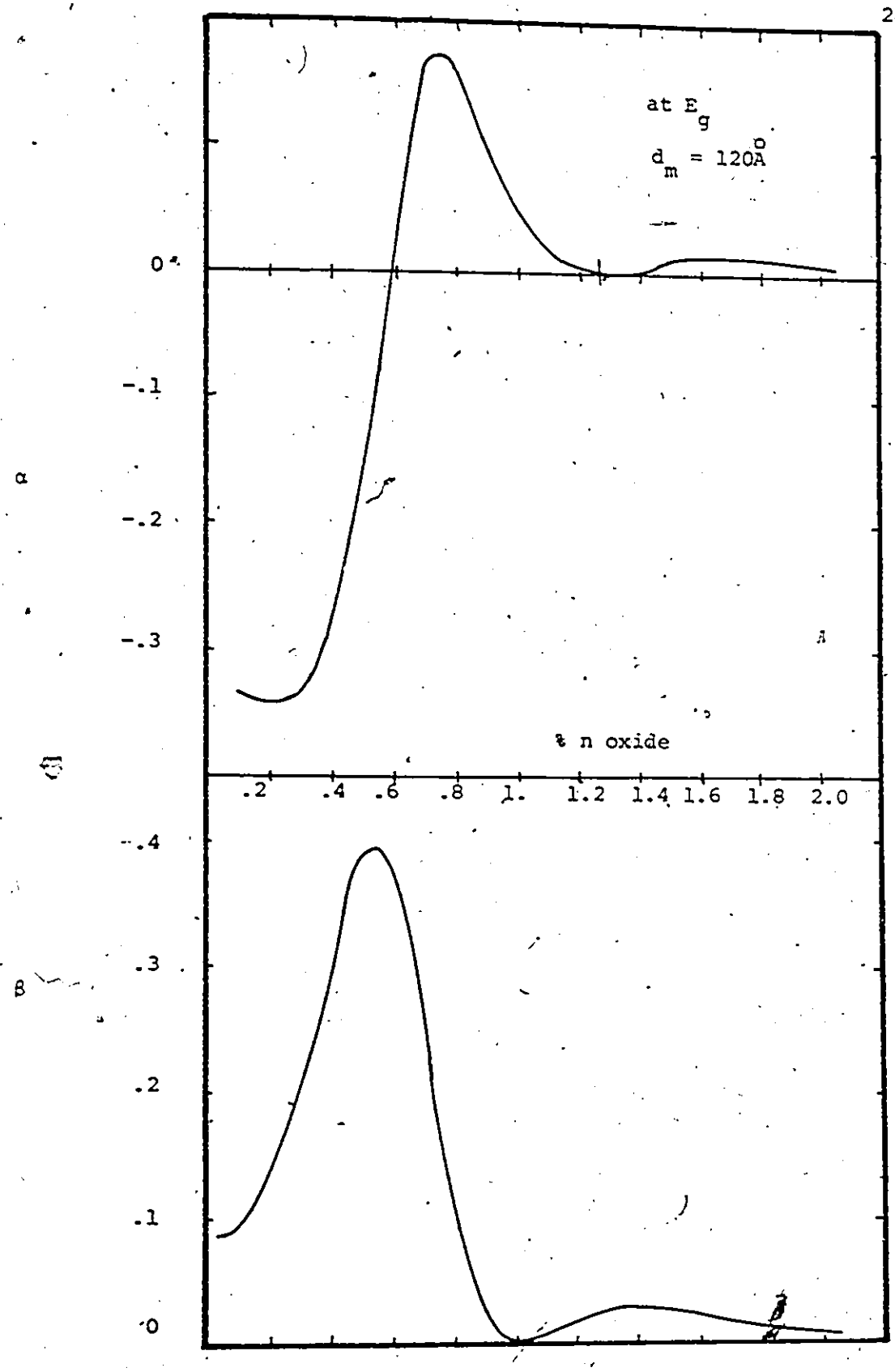

Figure A2-10. α, β dependence as a function of refractive index (exressed as % of that of SiO).

obtained at 1.437 eV should differ at other energies.

In fig. A2-10 a similar study at the gap of GaAs of the variation of α, β with the optical constants of the oxide is seen. It can be shown that for some choice of refractive index $\alpha << \beta$ (58% of n_o) or $\alpha >> \beta$ (100% n_o). It may also be noted that the large negative value of α at 40% or less of n_o results in a change in the direction of the peaks in SBER.

Conclusion - as a result, the choice of appropriate oxide parameters can be used as a device to obtain ΔR/R signals which are predominantly $\Delta\epsilon_{1s}$ or $\Delta\epsilon_{2s}$ in character. The coefficients (α, β respectively) can be calculated and the actual values of $\Delta\epsilon_{1s}$ and $\Delta\epsilon_{2s}$ can be found.

Throughout the experiments the oxide thickness (for SiO) of λ/2 is the one which can give most reliable optical transition measurements by the SBER technique.

When MOS devices are used it is therefore important to know the thickness of the oxide layers, an information which is more difficult to obtain with accuracy for Al_2O_3 oxide growth technique described in this work.

As one last point, this exercise demonstrates the importance of sample etching even for reflectance or EER measurements. Different material oxidizes at different rates and to different depths - if any correlation between results on materials is to be done, all surfaces must be atomically clean.

REFERENCES

1900

1D00 P. Drude, Ann. der Physik, 1, 566.

1905

1L05 H.A. Lorentz, Proc. Amsterdam Acad., 7, 684.

1919

1U19 G.G. Urasov, Zh. Russ. Fiz. Khim. Obsch., 51, 461.

1921

1U21 G.G. Urasov, Izv. Inst. Fiz. Khim. Anal., 1, 1

1928

1B28 F. Bloch, Zeit. Phys., 52, 555.

1S28 A. Sommerfeld, Zeit. Phys., 47, 1.

1929

1K29 H.A. Kramers, Phys. Zeit., 30, 522.

2K29 R. Kroenig, Phys. Rev., 30, 521.

1930

1B30 L. Brillouin, J. Phys. Rad., 1, 377.

1931

1N31 L. Nordheim, Ann. Phys., 9, 697.

1V31 J. Veszelka, Millberg u. huttenmann Alt. Kgl. Ungarn Hohschule, Sopron, 3, 193.

1934

1J34 H. Jones, Proc. Roy. Soc. A147, 400.

1R34 R. Robertson, J.J. Fox, A.E. Martin, Phil. Trans., A232, 463.

1936

1B36 L.P. Bouckaert, R. Smoluchowski, E. Wigner, Phys. Rev., 50, 58.

1M36 (see 1M58 for a later edition).

1938

1M38 T. Muto, Sci. Papers Inst. of Phys. and Chem. Res., 34, B77.

1939

1K39 W. Klemm; H. Stohr, Zeit. Anorg. Allgem. Chem., 241, 305.

1S39 H. Stohr, W. Klemm, Zeit. Allgem. Chem., 241, 305.

1940

1H40 C. Herring, Phys. Rev., 57, 1169.

1950

1J50 H. Jones, Phil. Mag. 41, 633.

1951

1L51 M. Lax, Rev. Mod. Phys., 23, 237.

2L51 J. Lawson, J. App. Phys., 22, 1444.

1Y51 T. Yamamoto (see ref. in 2L51)

1952

1W52 H. Welker, Zeit. Natur., 7A, 744.

1953

1L53 T.S. Liv, E.A. Peretti, Trans. Am. Soc. Metals 45, 677.

1P53 G.L. Pearson, C. Herring, Am. Phys. Soc., Stanford.

1V53 L. van Hove, Phys. Rev., 89, 1189.

1954 1B54 E. Burnstein, Phys. Rev., 93, 632.

1D54 T.M. Dauphinée, H. Preston-Thomas, Rev. Sci. Ins., 25, 884.

1H54 F. Herman, Phys. Rev., 95, 847.

1E54 R.J. Elliott, Phys. Rev., 96, 266.

2E54 R.J. Elliott, Phys. Rev., 96, 280.

1J54 E.R. Johnson, S.M. Christian, Phys. Rev., 95, 560.

1954 (continued)

1H54 F. Herman, Phys. Rev., 93, 1214.

1S54 C.S. Smith, Phys. Rev., 93, 42.

1955

1D55 G. Dresselhaus, P. Kip, C. Killel, Phys. Rev., 98, 368.

2D55 G. Dresselhaus, Phys. Rev., 100, 580.

1F55 O. G. Folberth, Zeit. Natur., 10A, 502.

1G55 M. Glicksman, Phys. Rev., 100, 1146.

1H55 F. Hemd , J. Electronics, 1, 103.

1K55 W. Koster, B. Thoma, Zeit. Metallk., 46, 293.

1P55 R.H. Parmenter, Phys. Rev., 97, 587.

1956

1G56 M. Glicksman, Phys. Rev., 102, 1496.

1K56 E. O. Kane, Phys. Chem. Sol., 1, 82.

2K56 E. O. Kane, Phys. Chem. Sol., 1, 249.

1P56 J.C. Phillips, Phys. Rev., 104, 1263.

1W56 H. Welker, H. Weiss,Sol. Stat. Phys., 3, 1.

2W56 H. Weiss,Zeit. Natur., 11a, 430.

1957

1A57 American Institute of Physics Handboook, McGraw-Hill, New York.

1B57 J. van der Boomgaard, K. Schol, Phillips Res. Rep., 12, 127.

1C57 J. Callaway, J. Electronics, 2, 330.

1957 (continued)

1H57 F. Herman, M. Glicksman and R.H. Parmenter, Prog. Semic., 2, 1.

1S57 M. Shafer, K. Weiser, J. Phys. Chem., 61, 1424.

2S57 L.G. Schulz, Advan. in Phys., 6, 101.

1958

1C58 M.H. Cohen, V. Heine, Advan. Phys., 7, 395.

1F58 O. Folberth, Zeit. Naturforsch, 13A, 856.

2F58 W. Franz, Zeit. Naturforsch, 13A, 484.

1G58 V.M. Glazov, D.A. Petrov, Izv. Akad. Nauk. SSSR Otd. Tekhn., 4, 125.

1K58 W. Koster, W. Ulrich, Zeit. Metallk, 49, 365.

2K58 J. Korriga, J. Phys. Chem. Sol., 7, 252.

3K58 W. Koster, W. Ulrich, Zeit. Metallk, 49, 365.

4K58 L.V. Keldysh, Sov. Phys. JETP., 7, 788.

1M58 N.F. Mott, H. Jones, "The Theory of the Properties of Metals and Alloys (Dover) pp. 170, 174.

1P58 R.H. Parmenter, J. Phys. Chem. Sol., 6, 6.

2P58 J.C. Phillips, Phys. Rev., 112, 685.

1W58 J.C. Woolley, B.A. Smith, Proc. Phys. Soc. (London) 72, 214.

1959

1A59 M.S. Abraham, R. Braunstein, F.D. Rosi, J. Phys. Chem. Sol., 10, 204.

1B59 I.I. Burdyan, Fiz. Tverd. Tela., 1, 1360.

2B59 I.I. Burdyan, B.T. Kolomietes, Fiz. Tverd. Tela., 1, 1165.

3B59 E. Burnstein, G.S. Pikus, R.F. Wallis, E. Blatt, Phys. Rev., 113, 15.

1O59 F. Oswald, Zeit. Natur., 14a, 374.

1P59 J.C. Phillips, L. Kleinman, Phys. Rev., 116, 287.

1S59 R.A. Smith, "Semiconductors", Cambridge University Press.

1960

1D60 J.F. Dewald in "Semiconductors" p. 727., N.B. Hannay ed., Reinhold.

1J60 H. Jones, "Theory of Brillouin Zones and Electronic States in Crystals", Intersc. Publish. Inc. New York.

1M60 J.F. Miller, H.L. Groering, R.C. Himes, J. Electrochem. Soc. 107, 527.

2M60 T.P. McLean, "The Absorption Edge Spectrum of Semiconductors", Progress in Semiconductors, 5, 53.

1P60 J. Pauling "Theory of the Chemical Bond". Cornell University Press, ch. 3-4.

1T60 J. Tauc, A. Abraham, Proc. Int. Conf. Semic. (Prague).

1961

1E61 H. Ehrenreich, J. App. Phys., 32, 2155.

1H61 N.F. Henry, H. Lipston, W.A. Wooster, "Interpretation of X-ray, Diffraction Photographs, p. 192, MacMillan.

1K61 J. Krebs et al.,"Uber Structur and Eingenshaffen der Halb - Metalle", XIV.

1T61 J. Tauc, A. Abraham, J. Phys. Chem. Sol., 20, 190.

1W61 J.C. Woolley, C.M. Gillet, J.A. Evans, Proc. Phys. Soc. (London) 77, 700.

1962

1B62 R. Braunstein, E.O. Kane, J. Phys. Chem. Sol., 23, 1423.

2B62 D. Brust, J.C. Phillips, F. Bassani, Phys. Rev. Letts., 9, 94.

1C62 M. Cardona, D.L. Greenaway, Phys. Rev., 125, 1291.

2C62 M. Cardona, Phys. Rev., 129, 69, 63.

1H62 N. Holonyak, S.F. Bevaqua, Appl. Phys. Letts. 1, 82,

2H62 W. Hume-Rothery, G.V. Raynor, "The Structure of Metals & Alloys" Institute of Metals, London

1L62 D. Long, Group # 46, J. Appl. Phys., 33, 1682.

1M62 T.S. Moss, A.K. Walton, B. Ellis, Exeter, Proc. Int. Conf. Semic.

1R62 M. Rubenstein, J.Electrochem. Soc., 109, 69 .

1S62 M. D. Sturge, Phys. Rev. 127 768, 62.

1962 continued

1T62 D.R. Turner, "The Electrochemistry of Semiconductors", P.J. Holmer ed., Acad. Press.

1U62 Umeda et al., J. App. Phys. Jap., 1, 277.

1W62 J.C. Woolley, "Comp. Semic". Reinholt chapter 1. ed. Willardson and Goering.

1963

1B63 F. Bassani, D. Brust, Phys. Rev., 131, 1524.

4B63 R.F. Brebrick, A.J. Strauss, Phys. Rev., 131, 104.

5B63 R.F. Brebrick, J. Phys. Chem. Sol., 24, 27.

1C63 M. Cardona, J. Phys. Chem. Sol., 24, 1547.

2C63 J. Callaway, Phys. Rev., 130, 549.

1D63 G.B. Dubrovskii, Sov. Phys. Sol. Stat., 5, 669.

2D63 A. Dauson, J. Appl. Phys., 34, 3083.

1K63 S.M. Ku, J.F. Black, Sol. Stat. Er., 6, 505.

1H63 R.N. Hall, J. Electrochem. Soc., 110, 385.

2H63 J. Hubbard, Proc. Roy. Soc., A276, 238.

3H63 J.W. Hodby, Proc. Phys. Soc., 82, 324.

4H63 N. Holonyak, S.F. Bevacqua, Appl. Phys. Letts., 3, 47.

1M63 G.A. Mead, W.G. Spitzer, Phys. Rev. Letts., 11, 358.

1963 continued.

2M63 T.P. MacLean: "Semiconducttori", Enrico Fermi School of Physics, p. 480.

3M63 R. Mazelski: "Non-Stoichiometric Compounds", Am. Chem. Soc. p. 210,

1T63 K. Tharmalingham , Phys. Rev., 130, 2204.

1964

1A64 F.B. Alexander, Appl. Phys. Letts., 4, 13.

1B64 J.L. Beeby, Phys. Rev., 135, A130.

2B64 J.L. Beeby, Proc. Phys. Soc., A279, 82.

3B64 P. Brust, Phys. Rev., 134, A133.

1C64 M. Cardona, 3rd Int. Conf. on the Phys. of Semic., (02-0) p. 181, Paris.

2C64 J. Callaway: "Energy Band Theory", Acad. Press, New York.

3C64 J. Callaway, Phys. Rev., 134, A998.

4C64 M. Cardona, Phys. Rev., 133, A1685.

5C64 J.B. Conlin, Phys. Rev., 137, A1282.

1F64 G.E. Fenner, Phys. Rev., 134A, 1113,; 137A, 1000, 1965.

1M64 E.K. Muller, J.L. Richards, J. Appl. Phys., 35, 1233.

2M64 O. Madelung: "Physics of III-V Compounds", Wiley.

3M64 T.D.F. Marple, J. App. Phys., 35, 1241.

1S64 W.G. Spitzer, C.A. Mead, Phys. Rev., 133, A872.

1964 continued.

4S64 B.O. Seraphin, Proc. Int. Conf. on the Phys. of Semic., (Paris).

1Y64 F. Yonezawa, Proc. Theo. Phys., 31, 357.

1W64 J.C. Woolley, A.G. Thompson, Con. J. Phys., 42, 2030.

2W64 J.C. Woolley, J.W. Warner, J. Electrochem. Soc.,

3W64 J.C. Woolley, J.W. Warner, Con. J. Phys., 42, 1879.

4W64 J.C. Woolley, K.W. Blazey, J. Phys. Chem. Sol., 25, 713.

1965

1A65 S.S. Abagyan, Sov. Phys. Sol. Stat., 6, 2266.

1B65 T.K. Bergestresser, Phys. Rev. Letts., 15, 662.

2B65 M.L. Belle, Fiz. Tve. Tela., 7, 606.

1H65 O.S. Heavens: "Optical Properties of Thin Solid Films", Dover.

1N65 D. Nikolic, Brit. J. Appl. Phys., 16, 1075.

1P65 M. Pilkuhn, H. Rupprecht, J. Appl. Phys., 36, 684.

1R65 M. Rubenstein, J. Electrochem. Soc., 112, 426.

1S65 E.A. Stern, Physics 1, 255.

2S65 J.C. Slater, "Quantum Theory of Molecules in Solids"
vol. 2 - MacGraw-Hill Book Company, New York.

3S65 B.O. Seraphin, N. Bottka, Phys. Rev., 139, A560.

4S65 K.L. Shaklee, F.H. Pollak, M. Cardona, Phys. Rev. Letts., 15, 883.

5S65 B.O. Seraphin, R.B. Hess, Phys. Rev. Letts., 14, 138.

6S65 B.O. Seraphin, R.B. Hess, N. Bottka, Appl. Phys. Letts., 6, 134.

1965 continued.

7S65 B.O. Seraphin, Phys. Rev., Phys. Rev., 140, A1716.

8S65 B.O. Seraphin, R.B. Hess, N. Bottka, J. Appl. Phys., 36, 2242.

1W65 J.C. Woolley, A.G. Thompson, M. Rubenstein, Phys. Rev. Letts., 15, 670.

2W65 E.W. Williams, Sol. Stat. Comm., 3, 195.

3W65 J.C. Woolley, P. Nikolic, J. Electrochem. Soc., 112, 82.

1966

1A66 D.E. Aspnes, Phys. Rev., 147, 554.

1B66 (see ref. 3B66)

2B66 J.F. Black, S.M. Ku, J. Electrochem. Soc., 113, 249.

3B66 D. Long, "Semiconductors and Semimetals", Willardson and Beer ed., Vol. I, Ch. 5.

4B66 Batz, Sol. Stat. Comm., 5, 985.

5B66 Batz, Sol. Stat. Comm., 4, 241.

1C66 M.L. Cohen, T.K. Bergestresser, Phys. Rev., 141, 789.

2C66 M. Cardona, P. McEleroy, E.H. Pollak, K.L. Shaklee, Sol. Stat. Comm., 4, 319.

3C66 M. Cardona, F.H. Pollak, Phys. Rev., 142, 530.

4C66 R.W. Conrad, C.E. Jones, E.W. Williams, J. Electrochem. Soc., 113, 287.

5C66 M. Cardona, K.L. Shaklee, F.H. Pollak, Proc. Phys. Soc. Jap., Suppl. 21, 20.

1D66 J. Dimmock, Phys. Rev. Letts., 26, 1193.

1966 continued.

1F66 J. Tauc ed., "Enrico Fermi Summer School: "Optical Properties of Solids".

1H66 E.F. Hockings, I. Kudman, T.E. Seidel, C.M. Schmelz, E.F. Steigmeier, J. Appl. Phys., 37, 2879.

2H66 F. Herman, R.L. Kortum, C.D. Kuglin, R.A. Short, Phys. Rev. Letts., 11, 541.

1K66 S.M. Ku, J.F. Black, J. Appl. Phys., 37, 3733.

2K66 S.G. Krioturn, V.V. Sobolov, S.D. Shutov, Inorg. Mat., 2, 687.

1L66 Lin, Kleinman, Phys. Rev., 142, 478.

1N66 K. Norr, J. Electrochem. Soc., 113, 66.

1P66 F.H. Pollak, C.W. Higginbotham, M. Cardona, Proc. Int. Conf. on Phys. of Semic., Kyoto.

2P66 F.H. Pollak, C.W. Higginbotham, M. Cardona, J. Phys. Soc. Jap., 21S, 20.

3P66 F.H. Pollak, M. Cardona, J. Phys. Chem. Sol., 27, 423.

1S66 E.A. Stern, Phys. Rev., 157, 544.

2S66 P. Soven, Phys. Rev., 151, 539.

3S66 B.O. Seraphin, N. Bottka, Phys. Rev., 145, 628.

4S66 B.O. Seraphin, J. Appl. Phys., 37, 721.

1T66 A.G. Thompson, J.C. Woolley, M. Rubenstein, Can. J. Phys. 44, 2927.

2T66 A.G. Thompson, M. Cardona, K.L. Shaklee, J.C. Woolley, Phys. Rev., 146, 601.

3T66 J.J. Tietjen, J.A. Amick, J. Electrochem. Soc., 113, 724.

1966 continued.

1Y66 F. Yonezawa, T. Matsubora, Proc. Theo. Phys., 35, 357.

2Y66 F. Yonezawa, T. Matsubora, Proc. Theo. Phys., 35, 759.

1967

1A67 P.W. Anderson, "Proc. Int. School of Physics: Enrico Fermi". course # 37.

2A67 D.E. Aspnes, Phys. Rev., 153, 972.

3A67 D.E. Aspnes, Phys. Stat. Sol., 23 K79.

4A67 J.A. Aboaf, J. Electrochem. Soc., 114, 948.

1C67 M. Cardona, K.L. Shaklee, F.H. Pollak, Phys. Rev., 154, 696.

2C67 M.L. Cohen, Lin, Saslow, Sol. Stat. Comm., 5, 893.

1D67 G. Dresselhous, Phys. Rev., 166, 649.

1H67 C.W. Higginbotham, F.H. Pollak, M. Cardona, Sol. Stat. Comm., 5, 513.

1F67 R.A. Forman, M. Cardona: "II-VI Semic. compounds" ed., D.G. Thomas, p. 100, Benjamin.

2F67 A. Frova, P.J. Boddy, Phys. Rev., 153, 606.

1L67 R. Ludecke, W. Paul, II-VI Semic, Comp., ed., D.G. Thomas, p. 123, Benjamin.

1M67 T. Matsubora, F. Yonezawa, Proc. Theo. Phys., 37, 1346.

2M67 J. Muir, J. Phys. Chem. Sol., 28, 1009.

1N67 P. Nikolic, Brit. J. Appl. Phys., 18, 897.

1P67 C.R. Pidgeon, S.H. Grooves, J. Feinleib, Sol. Stat. Comm. 5, 677.

1967 continued.

2P67 R.J. Phelan, J. Dimmock, Appl. Phys. Letts., 10, 55.

1R67 H. Rupprecht, J.M. Woodall, G. Petitt, Appl. Phys. Letts., 11, 81.

2R67 V. Rehn, D.S. Kyser, Phys. Rev. Letts., 18, 848

1S67 P. Soven, Phys. Rev., I56, 809.

2S67 B.O. Seraphin, Surface Science, 8, 399.

3S67 A. J. Strauss, Phys. Rev. 157, 608, 67.

1T67 D.W. Taylor, Phys. Rev., 156, 1017.

2T67 A.G. Thompson, J.C. Woolley, Con. J. Phys., 45, 2597.

3T67 A.G. Thompson, J.C. Woolley, Bull. Am. Phys.Soc., 12, 639.

4T67 A. Tauber, J. Appl. Phys., 38, 3714.

5T67 A. Tauber, J. Appl. Phys., 37, 4855.

1W67 J.C. Woolley, M.B. Thomas, A.G. Thompson, Can. J. Phys., 46, 157.

2W67 Willardson and Beer ed., "Semiconductors and Semimetals" vol. 1, ch. 1 and 2.

3W67 Willardson and Beer ed., "Semiconductors and Semimetals" vol. 3, Acad. Press, Ch. 4-6.

4W67 J.C. Woolley, J. W. Wagner, Mod. Res. Bull. 2, 1055.

1968

1A68 D.E. Aspnes, M. Cardona, Phys.Rev., 173, 714.

2A68 D.E. Aspnes, P. Handler, D.F. Blossey, Phys. Rev., 166, 921.

1B68 J.G. Broerman, J. Phys. Chem. Sol., 29, I147

1D68 P.J. Dean, G. Kaminski, R.B. Zetterstrom, Phys. Rev., 181, 1149.

2D68 J.R. Dixon, R.F. Bris, Phys. Rev., 176, 942.

1G68 S. Grooves, W. Paul, Phys. Rev. Letts., 20, 55.

2G68 J.G. Gay, L.T. Klander Jr., Phys. Rev., 172, 811.

3G68 D.L. Greenaway, G. Hacbecke: "Optical Properties and Band Structure of Semiconductors", Pergammon.

1H68 Y. Hamakawa, P. Handler, F.A. Germano, Phys. Rev., 167, 709.

2H68 C.W. Higginbotham, F.H. Pollak, M. Cardona, Proc. Int. Conf. of Phys: of Semic. (Moscow) p. 51, vol. 1.

1K68 J.S. Kline, F.H. Pollak, M. Cardona, Helv, Phys. Acta. 172, 816.

2K68 C.C.Y Kwan, A.G. Thompson, J.C. Woolley, Can. J. Phys., 46, 2733.

1L68 D. Long, "Energy Bands in Semiconductors.", Interscience, N.Y.

2L68 R. Ludecke , J. Appl. Phys., 39, 4028.

1M68 E. Matagui, A.G. Thompson, M. Cardona, Phys. Rev., 176, 958.

1O68 Y. Onodera, Y. Toyozawa, J. Phys. Soc. Jap., 24, 341.

1P68 F.H. Pollak, C.W. Higginbotham, M. Cardona, Proc. Int. Conf. on Phys. Semic. Moskow,.

1R68 H.D. Rees, J. Phys. Chem. Sol., 29, 143.

1968 continued.

1V68 B. Velicky, S. Kirkpatric, H. Ehrenreich, Phys. Rev., 175, 747.

1W68 J.C. Woolley, M.J. Aubin, Can. J. Phys., 46, 1191.

2W68 J.C. Woolley, E.H. van Tongerloo, Can. J. Phys., 46, 1199.

3W68 E.W. Williams, V. Rehn, Phys. Rev., 172, 798.

4W68 Willardson and Beer ed., "Physics of III-V Compounds." Vol. 4, Acad. Press.

5W68 J.C. Woolley, O. Berolo, Mat. Res. Bull., 3, 445.

1969

1A69 M.J. Aubin, M.G. Thomas, E.H. van Tongerloo, J.C. Woolley, Can. J. Phys., 47, 631.

1B69 R.L. Bowers, G.D. Mahon, Phys. Rev., 185, 1073.

1C69 W.E. Coderre (thesis) University of Ottawa.

2C69 M. Cardona: "Modulation Spectroscopy", Sol. Stat. Physics Series - Suppl 11. Acad. Press.

1H69 F. Herman "Methods in Computational Physics, Energy Bands of Solids", vol. 8. Acad. Press (New York).

2H69 R.D. Hudson Jr., "Infrared System Engineering", Ch. 2 to ch. 4., John Wiley.

1J69 D. Jones, A.H. Lettington, Bull. Am. Phys. Soc., 14, 329.

2J69 D. Jones, A.H. Lettington, Sol. Stat. Comm., 7, 7319.

1K69 D.S. Kyser, V. Rehn, Bull. Am. Phys. Soc., 14, 415.

1969 continued

1P69 M.B. Panish, S. Sumski, J. Phys. Chem. Sol., 30, 129.

2P69 M.B. Panish, H.C. Casey Jr., J. Appl. Phys., 40, 4910.

1S69 P. Soven, Phys. Rev., 178, 1136.

2S69 S.M. Sze: "Physics of Semiconductor Devices" ch. 6, John Wiley

1T69 A.G. Thompson, J.E. Rowe, M. Rubenstein, J. Appl. Phys., 40, 3280.

1W69 S.A. Wilson, A.D. Yotte, Advances in Physics Series.

1970

1E70 E.N. Economu, M.H. Cohen, Mat. Res. Bull., 5, 577.

1F70 A. Frova, D.E Aspnes, Phys. Rev., B2, 1037.

1H70 W.A. Harrison: "Sol. State Theory". McGraw-Hill.

2H70 J.N. Hodgson: "Optical Absorption and Dispersion in Solids" Pergammon.

1O70 A. Onton, "10th Int. Conf. on the Phys. of Semic.", Massachusetts, p. 107.

1P70 J.C. Phillips, Rev. Mod.Phys., 42, 317.

1S70 D. Stroud, H. Ehrenreich, 10th Inter. Conf. on Phys. of Semic., 1970, session Th-Pb-2

2S70 J.L. Shay, Phys. Rev., B2, 803.

3S70 A.J. Strauss, "Optical Properties of IV-VI Compouds" (Proceedings) Acad. Press.

1970

1V70 S.S. Vishnubathla, B. Eyglunent, J.C. Woolley, Can. J. Phys., 47, 1661.

2V70 B. Velický, K. Levin, Phys. Rev., B2, 938.

3V70 J.A. Van Vechten, T.K. Bergestresser, Phys. Rev., B1, 3351.

1Z70 R.L. Zucca, Y.R. Shen, Phys. Rev., B1, 2668.

1971

1B71 O. Berolo, J.C. Woolley, Can. J. Phys., 49, 1335.

2B71 A. Ben-Reuven, Phys. Rev., A4, 2115.

3B71 D. Brust, Sol. Stat. Comm. 9, 481.

1C71 V. Capek, Phys. Stat. Sol., 43b, 61.

2C71 F. Cyrot-Lackmann, J. Phys. C., 4, L75.

3C71 J.E. Carner, M.T. Duffy, J. App. Phys., 42, 4350.

4C71 C. Cairns, - Optics lab supervisor, N.R.C., (private communication).

5C71 J.E. Carnes, M.T. Duffy, J. Appl. Phys., 43, 4350.

1D71 D. Demars, (private communication).

1F71 J.E. Fisher, REv. Sci. Inst., 42, 872.

1H71 J.F. Hunter, G. Ball, D.J. Morgan, Sol. Stat. Phys., 45b, 679.

1K71 E.O. Tauc, Phys. Rev., B4, 1917.

2K71 R. Krieger, (private communication).

3K71 E.J.M. Kendall, Sol. Stat. El. 14, 791.

1971 continued

1L71 P. Lawaetz, Phys. Rev., B4, 3460.

1M71 P.J. Melz, I.B. Ortenburger, Phys. Rev., B3, 3257.

1N71 N. Nagosima, Jap. J. Appl. Phys., 10, 1119.

1O71 H. Overhof, Phys. Stat. Sol. b45, 315.

1R71 D. Richardson, R.K.W. Vinsoma, Phys. Letts., 36A, 3.

2R71 D. Richardson, J. Phys. C.: Proc. Phys. Soc. (London) 4, L289.

1S71 G.M. Stocks, R.W. Williams, J.S. Faulkner, Phys. Rev. Letts. 26, 253.

2S71 G.B. Stringfellow, P.E. Greene, J. Electrochem. Soc., 118, 805.

1T71 M.B. Thomas, J.C. Woolley, Can. J. Phys., 49, 2052.

2T71 A.G. Thompson, J.W. Wagner, J. Phys. Chem. Soc., 32, 2613.

1W71 G.G. Wepfer, T.C. Collins, R.N. Euwema, Phys. Rev., B4, 1296.

2W71 J.P. Walter, M.L. Cohen, Phys. Rev. Letts., 26, 17.

1972

1A72 D.E. Aspnes, Phys. Rev. Letts., 28, 168.

2A72 D.E. Aspnes, Phys. Rev. Letts., 28, 913.

3A72 quoted in 2A72 as to be published.

4A72 C. Alibert, G. Bordure, A.L. Augier, J. Chevalier, Phys. Rev., B6, 1301.

1972 continued

1B72 O. Berolo, J.C. Woolley, "Spin Orbit Splitting in III-V Alloys" Proc 11th Int. Conf. on the Phys. of Semic., Warsaw.

1D72 G. Dionne, J.C. Woolley, J. Electrochem. Soc., 119, 784.

2D72 G. Dionne, J.C. Woolley, Phys. Rev., B6, 3898.

1F72 W. Fahrner et al., Appl. Phys. Letts. 21, 329.

2F72 H. Fetterman, J. Waldman, C.H. Wolfe, Sol. Stat. Comm. 11, 375.

1M72 D.A. Metha et al., J. Appl. Phys., 43, 4633.

1O72 O. Kuyanne, Jap. J. Appl. Phys., 11, 1002.

1P72 S.F. Pond, P. Handler, Phys. Rev., B6, 2248.

1R72 S. Rosenbaum, Ph.D. Thesis, University of Ottawa.

2R72 D. Richardson, J. Phys. C., 5, L27.

1S72 D. Stroud, Phys. Rev., B5, 3366.

2S72 B.O. Seraphin, "Modulation Techniques" (North Holland).

3S72 R. Sittig et al., Phys. Stat. Sol., a12, 663.

4S72 J.B. Stringfellow, J. Phys. Chem. Sol., 33, 165.

1V72 J.A. VanVechten, O. Berolo, J.C. Woolley, Phys. Rev. Letts., 29, 1400,

1972 continued

4V72 Van Vechten (private communication).

1W72 M. Wekowsky, R. Braunstein, Rev. Sci. Inst., 43, 399.

1973

1A73 D.E. Aspnes, A.A. Studna, Surface Science, 37, 631.

1B73 O. Berolo, J.C. Woolley, J. Van Vechten ,(to be published), "Effective mass in semiconductor alloys"

1G73 M. Gratton, J.C. Woolley, J. Electron. Mat.

2G73 R. Glinski, O. Berolo, J.C. Woolley, (to be published).

1M73 A. Moritani, K. Tanigushi, C. Hamapuchi, J. Nakai, J. Phys. Soc. Jap., 34, 79.

1P73 F. Prat, J.C. Woolley, June meeting, CAP transactions.

1R73 R. Senechal, (private communication).

1W73 J.C. Woolley, P. Devlin, June meeting, CAP transactions.